Scuola Internazionale Superiore di Studi Avanzati - Trieste

SISSA

Doctoral Thesis

Dark Matter Indirect Detection and Collider Search: the Good and the Bad

Author:
Giorgio Busoni

Supervisor:
Dott. Andrea De Simone

A thesis submitted in fulfilment of the requirements for the degree of Doctor of Philosophy

in

Theoretical Particle Physics

July 2015

SISSA - Via Bonomea 265 - 34136 TRIESTE - ITALY

"The missing link in cosmology is the nature of dark matter and dark energy."

Stephen Hawking

SISSA

Abstract

Physics Sector
Theoretical Particle Physics

Doctor of Philosophy

Dark Matter Indirect Detection and Collider Search: the Good and the Bad

by Giorgio Busoni

In this work I aim to point out some theoretical issues and caveats in DM search. In the first chapters I review the evidence for DM existence, the DM candidates and the different kinds of DM experimental search. The bulk of the work investigates three different topics. In the first topic, concerning neutrino from the Sun, I show the fact that evaporation does not allow to probe part of the parameter space, in the low mass range. In the second one, I show that, like in the case of the detected positron excess, that could be explained both by DM or by astrophysical source, even a possible excess of antiprotons could suffer from the same kind of degeneracy. In the third part, I consider DM search at collider. I point out some problems about using the EFT low-energy approximation at LHC, arising from the fact that the experimental bounds and the average energy of collisions at LHC are of the same order of magnitude. Afterward, to take this fact into account, I propose a method to rescale experimental bounds, and I review an alternative way of analyzing experimental results, that is using Simplified Models. Finally, I also show which is the part of the parameter space for both Simplified Models and EFT giving the DM the right relic abundance, in the case of thermal freeze-out.

Acknowledgements

I want to thank the students, the teachers, and the administrative staff of SISSA, for the last four years what I have spent there. It is a very pleasant place to study, and it definitely helped me to develop and achieve my goal.
A special thank goes to my Advisor, Andrea De Simone. He helped me to find the right attitude to enter the world of research, as well as to learn new skills.
I would like to say thank you to my friends and my girlfriend as well, because they have always supported me morally and given me the strength I needed.
Finally, a special thank and gratitude is entitled to my family, for the support I received from them, not only in the last four years, but even more since I was born. They are really unique and I think I am very lucky to have them.

Contents

Thus is dedicated to my grandmother, who not only taught me to love science, but was a life teacher as well.

Chapter 1

Introduction

1.1 The Standard Model of Particle Physics and Recent Discoveries

The Standard Model (SM) of Particle Physics is a very successful theory, delivering high-precision theoretical estimates for experimental data, and it describes the quantum nature of the Weak, Electromagnetic and Strong Forces. The Gauge group of the theory is $SU(2) \times U_Y(1) \times SU(3) \rightarrow U_{em}(1) \times SU(3)$. The spontaneous symmetry breaking of the Gauge group allows for the W and Z bosons to be massive, and it can be explained by the existence of a Spin 0, neutral Boson, called the Higgs Boson, which was recently discovered at the LHC [1, 2].

1.1.1 Theoretical Hints for Beyond the Standard Model Physics

Indeed, the SM also suffers from some theoretical problems, regarding, for instance, the origin of the flavour structure and the radiative corrections to the Higgs boson mass. Here, I list some of the main theoretical questions which are still open:

- **The Higgs hierarchy problem**
- **The new physics flavour problem**
- **Neutrino masses:** neutrinos don't have a mass in the SM, but there is experimental evidence that they oscillate, and this implies that they have, indeed, non-zero masses [3].
- **The Strong CP problem**

- **The hierarchy problem of fermion family masses:** the fermion spectrum suggests some form of family symmetry, but it is not clear why masses span so many orders of magnitude, in the interval from 10^{-2} eV for neutrinos to 200 GeV for the top quark.
- **Charge quantization:** why the magnitudes of the proton and electron electric charges are the same, implying the electrical neutrality of ordinary matter, has not been understood yet.
- **Gauge Couplings Unification**
- **The Cosmological Constant problem**
- **The number of free parameters:** SM has around 20 free parameters, (masses, mixing angles, couplings and so on). A theory with a minimal number of parameters would look more natural.
- **Gravity:** SM and gravity cannot produce a consistent theory of quantum gravity.

1.1.1.1 The Higgs Hierarchy Problem

By combining the three fundamental constants, the speed of light c, Planck's constant h, and Newton's gravitational constant G_N, one can find a combination of them that has dimensions of mass, called the Planck Mass $M_{\rm Pl} \equiv \sqrt{hc/G_N} \simeq 1.2 \times 10^{19}$ GeV. We normally expect dimensionful parameters like a mass to be either 0, if dictated by a symmetry, or of the order of $M_{\rm Pl}$. In the SM, electroweak symmetry is broken, and the Higgs boson mass is not enforced to be zero, therefore we would expect $m_h \sim M_{\rm Pl}$. The higgs hierarchy problem is the question of why $m_h \sim 100$ GeV $\ll M_{\rm Pl}$.

This problem is enhanced in the SM by quantum corrections. The physical mass of the SM Higgs boson is $m_h^2 = m_{h\,0}^2 + \Delta m_h^2$, where $m_{h\,0}^2$ is the tree-level mass, and Δm_h^2 is made up of the sum of several terms arising from 1-loop diagrams. The one arising from the diagram with Higgs particle in the loop is:

$$\Delta m_h^2 \sim \frac{\lambda^2}{16\pi^2} \int^{\Lambda} \frac{d^4p}{p^2} \sim \frac{\lambda^2}{16\pi^2}\Lambda^2 \tag{1.1}$$

where the integral is over the momenta of particles in the loop, the Higgs self coupling λ is a dimensionless parameter of $\mathcal{O}(1)$ dimensionless coupling, and Λ is the energy scale at which the SM is no longer valid. The other 1-loop diagrams with a gauge boson of a fermion running in the loop give contributions still proportional to Λ^2, but with negative signs in the case of fermions. Because of this, Δm_h^2 is proportional to Λ^2, with a dimensionless coefficient that, in the standard model, has a negative sign overall. As

it would be natural to expect $\Lambda \sim M_{\rm Pl}$, this implies that $m^2_{h\,0}$ and Δm^2_h need to cancel to 1 part in 10^{36} to give the correct physical Higgs mass, which is hardly believable.

The higgs hierarchy problem would be solved if $\Lambda \lesssim 1$ TeV, and this would mean that there is new physics at the weak scale $m_{\rm weak} \sim 100$ GeV $-$ TeV. This is why usually any attempt to fix the higgs hierarchy problem implies the existence of new particles with mass of order $m_{\rm weak}$. The higgs hierarchy problem is one of the main motivations for dark matter candidates such as WIMPs, weakly-interacting massive particles, that are the topics of Sec. 2.1.1.

1.1.1.2 The New Physics Flavor Problem

Solving the higgs hierarchy problem by adding new particles with mass of order $m_{\rm weak}$, however, may generate new problems, like changing the level of the violation pattern of some of the symmetries present in the standard model, like baryon number, lepton number, flavor, or CP.

This implies that not all solutions to the higgs hierarchy problem are acceptable. For example, among SUSY theories, those that predict very heavy or degenerate squarks and sleptons spectra in a natural way are favored, because these kind of spectra naturally suppress flavor-changing neutral currents below current constraints. This problem is relevant for WIMPs Direct Detection, as discussed in Sec. 2.2.1, and motivates further dark matter models, like light gravitino dark matter or hidden sector dark matter models, reviewed in [4].

1.1.1.3 The Neutrino Mass Problem

Fermion mass terms in QFT lagrangian couple left- and right-handed fields together. The SM, however, does not include right-handed neutrino fields (and therefore not even neutrino mass terms), because they would be standard model singlets. Because of this, all neutrinos are massless in the SM. However, we know from experimental evidence that neutrinos undergo flavor oscillations [3, 5], and this in turn implies that the three neutrinos have a non-degenerate spectra, and so at least two of them have a non-zero mass. Neutrino mixing is one of the best proofs that the SM of particle physics is not a complete theory, and this problem motivates sterile neutrino dark matter, discussed in Sec. 2.1.2.5.

1.1.1.4 The Strong CP Problem

The SM does not include any symmetry that forbids the existence of a term

$$\frac{g_3^2\theta_3}{32\pi^2}\epsilon^{\mu\nu\rho\sigma}G^{\alpha}_{\mu\nu}G^{\alpha}_{\rho\sigma} \tag{1.2}$$

in the lagrangian, where g_3 is the coupling of the strong interactions, θ_3 is a dimensionless parameter, $\epsilon^{\mu\nu\rho\sigma}$ is the totally anti-symmetric 4-index tensor, and $G_{\mu\nu}$ is the gluon field strength, and therefore this term would be expected to be there, and the parameter θ_3 would be expected to be of order $\theta_3 \sim 1$, as it is a dimensionless parameter. However, this term contributes to CP-violating (but flavor-conserving) observables, such as the electric dipole moment (EDM) of the neutron d_e, and $\theta_3 \sim 1$ would imply $d_e \sim 10^{-16}\ e$ cm. The neutron EDM has not been observed yet, but actual constraints already imply $d_e < 2.9 \times 10^{-26}\ e$ cm [6]. This is, therefore, another fine-tuning problem, of 1 part in 10^9, and it motivates axions as dark matter candidates, to be discussed in Sec. 2.1.2.1.

1.1.1.5 Other Problems

Here I briefly introduce the remaining problems listed previously. The *SM flavor problem* is the puzzle of why the fermion masses are distributed along so many orders of magnitude. Grand unification theories, that try to interpret the strong, weak, and electromagnetic interactions as different manifestations of a single underlying force, thus solving part of the listed problems, like charge quantization and gauge coupling unification, fail to solve some of the others, like the SM flavor problem itself.

Eventually, note that there is another dimensionfull parameter in the SM, other than m_h: the lagrangian also contains the term $\bar{\Lambda}^4$, called vacuum energy term, that is of the same kind as the cosmological constant term, and therefore it contributes to dark energy and the cosmological constant. Equation (1.3) in Sec. 1.2 states that the measured value for this term is $\Lambda \simeq (2.76\,\text{meV})^4$, but, on the other hand, if $\bar{\Lambda} \simeq M_{\text{Pl}}^4$, then this value has to cancel with some other contributions to 1 part in 10^{122} to yield the experimental value, giving rise to a fine-tuning which is even worse than the higgs hierarchy problem. This is the *cosmological constant problem*. Although a unified solution to the cosmological constant and higgs hierarchy problem would be very desirable, at the moment the scientific community thinks that there is very little hint (if any) that they are related, and we will assume they are decoupled in this work.

1.2 Experimental Evidence for Dark Matter

The ΛCDM model, named after a non-zero cosmological constant and a relevant portion of cold Dark Matter, is nowadays considered the standard cosmological model and is almost universally thought to be the best description of the present experimental results. This model relies on several assumptions: the universe is assumed to be homogeneous, isotropic and flat, on cosmological scales, to be governed by the laws of Einstein's General Relativity and to be composed by stable particles known in the SM of particle physics, plus two additional ingredients: Dark Energy and Dark Matter. The assumption about flatness has, unfortunately, no theoretical *a priori* motivations, and this is one of the main problems of the theory, and is called *the flatness problem* (nowadays, the most commonly accepted solution to this problem is cosmic inflation, the idea that the universe went through a brief period of extremely rapid expansion in the first fraction of a second after the Big Bang). However, hints for flatness were given by a huge amount of experimental measurements; defining ρ_c as the critical energy density for making up a flat Universe (at the moment) and ρ as the energy density of the universe (today), we experimentally find that $\Omega = \rho/\rho_c = 1 \pm \mathcal{O}(10^{-3})$ [7]. Moreover, the same experiments (plus some others) show clear evidence for the existence of the two other ingredients, beside the known matter content (built up mainly by baryons): Dark Energy and Dark Matter. These are two very different entities and is still not clear at all whether they could have a common origin or be somehow connected. Dark Energy is a sort of negative pressure distributed across all the Universe, causing the Universe's accelerated expansion and, unlike matter, it does not cluster; its effect can be expressed by a cosmological constant term $\Lambda g^{\mu\nu}$ in Einstein's equations. Dark Matter (DM) behaves instead, from the gravitational point of view, like usual matter but, unlike baryons, it is dissipationless, which means that it does not emit, absorb nor diffuse light. Its interaction with photons is reduced or completely absent, thus, it is very difficult to detect it with the usual astronomical tools, and this is the reason it was dubbed 'dark'. By including these dark ingredients, which have not yet been verified experimentally, Cosmology works remarkably well. The data consistently indicate the presence of a large Dark Energy component Ω_Λ to the energy budget of the Universe, and to a Dark Matter contribution Ω_{DM} that dominates over the other known forms of matter.

The latest Wilkinson Microwave Anisotropy Probe WMAP 9-year fit [7, 9] (previous data from 7-year fit giving similar results can be found in [8, 10, 11] and are summarized Fig.1.1.) ΛCDM model yields:

$$\Omega_\Lambda = 0.718; \Omega_{DM} = 0.236; \Omega_b = 0.046 \tag{1.3}$$

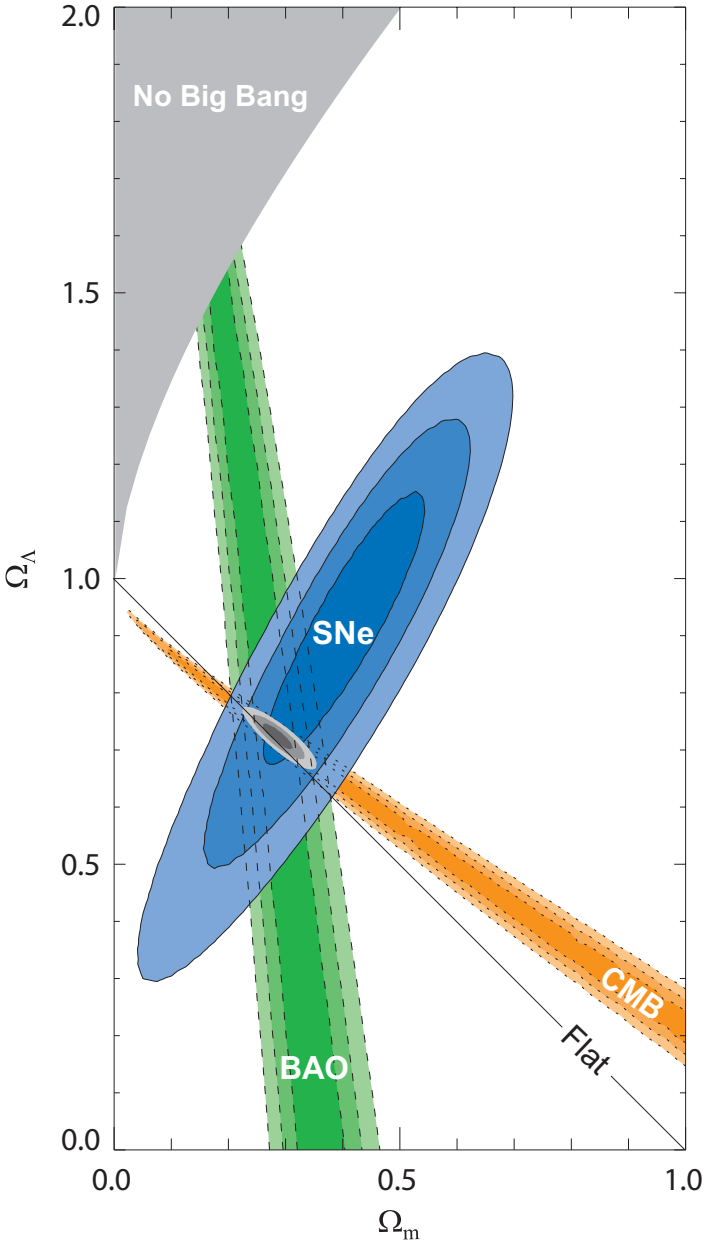

FIGURE 1.1: *68.3%, 95.4% and 99.7% confidence level contours on* Ω_Λ *and* $\Omega_M = \Omega_{DM} + \Omega_b$ *obtained from the Supernova Cosmology Project Collaboration: Cosmic Microwave Background, Baryonic Acoustic Oscillations and the SuperNovae Surveys as well as their combinations, extracted from [8].*

where Ω_b is the baryon contribution to the total energy density, which is the only relevant contribution among the known particles. In the rest of this section, we focus on the experimental motivations and evidence for Dark Matter. We also provide motivations for its key properties: dark, dissipationless, cold, and non-baryonic.

1.2.1 Galaxy Rotation curves

Some of the first and most compelling evidence for the presence of non visible matter comes from galaxy rotation curves. The centripetal acceleration of stars within a galaxy is expected to be (in the approximation of circular orbits)

$$\frac{v(r)^2}{r} = \frac{G_N M(r)}{r^2} \tag{1.4}$$

thus yielding a circular velocity

$$v(r) = \sqrt{\frac{G_N M(r)}{r}} \tag{1.5}$$

where G_N is Newton's gravitational constant and

$$M(r) = 4\pi \int \rho(r) r^2 \, \mathrm{d}r. \tag{1.6}$$

is the mass contained inside a sphere of radius r, $\rho(r)$ being the mass density profile. Most of the visible material in these galaxies is concentrated in the central part, so the angular rotation of stars is expected to slow down at large radii, reproducing the classical Keplerian behavior $v(r) \propto 1/\sqrt{r}$ for an object in the optical disk. On the other hand, observations show a nearly constant behaviour for the rotation speed, as shown in Fig.1.2. An approximately constant $v(r)$ implies that $M(r) \propto r$ i.e. $\rho(r) \propto 1/r^2$, if we believe Newton's gravitational law to be valid in this situation. Given such velocities, galaxies should not be able to remain bounded and pull themselves apart, unless an additional mass other than the luminous one is present as well [12].

There is another possible explanation for the galactic rotation curves, which is the MOND paradigm. Modified Newtonian Dynamics (see [16, 17]), a modification of Newtonian gravity in the low acceleration limit, is not definitely ruled out despite the Dark Matter assumption is by far the most favored.

1.2.2 Velocity Dispersion in Galaxy Clusters

There are a few other ways to measure the mass of galaxy clusters, and one of them involves, for instance, the use of the virial theorem. By using it, one can infer the gravitational potential from the observed distribution of radial velocities

$$\langle U \rangle = -2\langle T \rangle \tag{1.7}$$

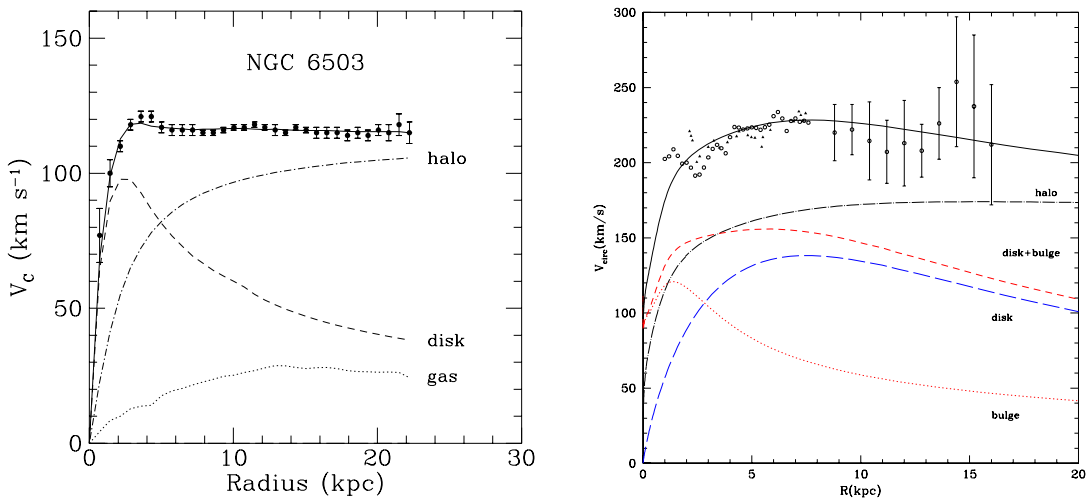

FIGURE 1.2: Left panel: *rotation curve for the spiral galaxy NGC6503 from Ref. [13, 14]. The points are the measured circular rotation velocities as a function of distance from the center of the galaxy. The dashed and dotted curves are the contribution to the rotational velocity due to the observed disk and gas, respectively, and the dot-dash curve is the estimated contribution from the dark halo needed to fit the data.* Right panel: *Milky Way's rotation curve from Ref. [15].*

where U and T are the potential and kinetic energies, respectively, and $\langle\rangle$ denotes time average. The total cluster's mass to the mass obtained in this way provides a hint to infer that the visible mass is not enough to cause the internal cluster dynamics, and that some not visible mass is needed.

1.2.3 Gravitational Lensing

Another experimental evidence of the existence of DM comes from gravitational lensing (see [12]). Light propagates along geodesics, which deviate from straight lines when passing inside strong gravitational fields. When the deflection of light is caused by a very strong gravitational field (and so by a large gravitational mass that plays the part of the 'lens' present in between a the source and the observer), this effect is easily noticeable and is called 'strong lensing' (see Fig.1.3); If the source is located exactly behind a symmetric massive object, a complete 'Einstein Ring' appears (as you can see in the bottom left panel of Fig.1.3); in more complicated cases, when the symmetry is partially broken, one can still observe arcs or multiple images of the same source (as you can see in the bottom right panel of Fig.1.3). The mass distribution of the lens can then be reconstructed by the measurement of the distribution of the deflecting mass. Comparing the measured mass of the lens with the one inferred by its luminosity, a mismatch is found again. The conclusion is once more that a large part of the galaxies is actually made of Dark Matter. Another phenomena that provides a way of measuring the mass present in a certain part of the sky is 'weak lensing' (see Fig.1.4). While

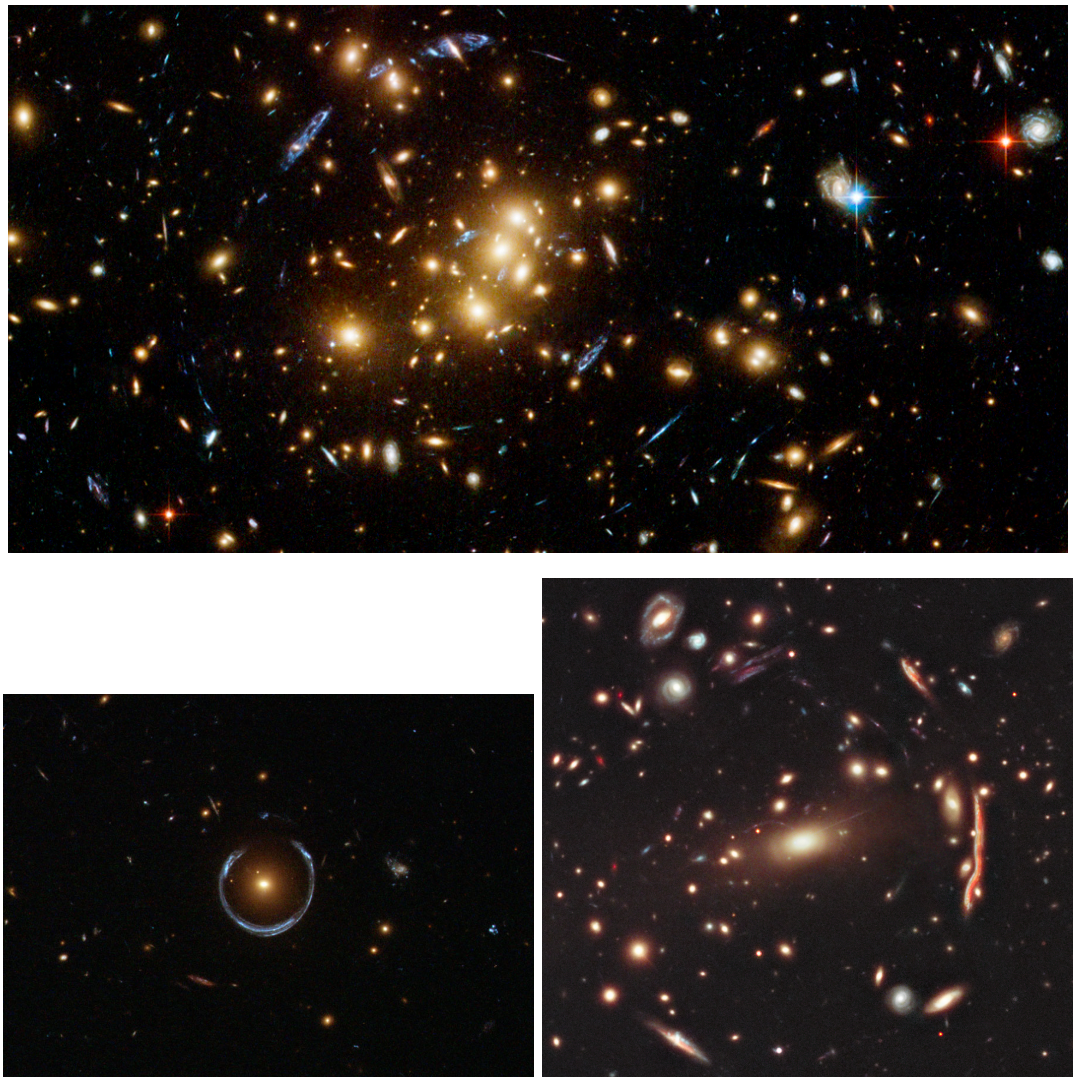

FIGURE 1.3: *Examples of strong lensing.* Top panel: *Many of the brightest blue images are of a single ring-like galaxy which happens to line-up behind the giant cluster of galaxies CL0024+1654. Cluster galaxies here typically appear yellow and, together with the cluster's Dark Matter, act as a gravitational lens.* Bottom Left panel: *the Luminous Red Galaxy LRG 3-757 acting as lens on a much more distant blue galaxy. Here the alignment is so precise that the background galaxy is distorted into a horseshoe (a nearly complete ring), so that it is now called 'the Cosmic Horseshoe'.* Bottom Right panel: *the cluster MACS J1206.2-0847 lensing the image of a yellow-red background galaxy into the huge arc on the right.*

the methods outlined above take into account single gravitationally bound objects, like galaxies and cluster of galaxies, this technique analyzes a large number of independent galaxies in a statistical fashion. Weak lensing occurs when the light passes inside a gravitational field that is not strong enough to cause visible effects like in strong lensing, but still strong enough to cause a slight deflection. Even if the distortion of individual sources cannot be seen because it is too small, it is possible to make a statistical analysis. Indeed the presence of some mass along the line of sight generates a coherent 'shear' distortion, that can be measured averaging over a large number of galaxies [12], while if

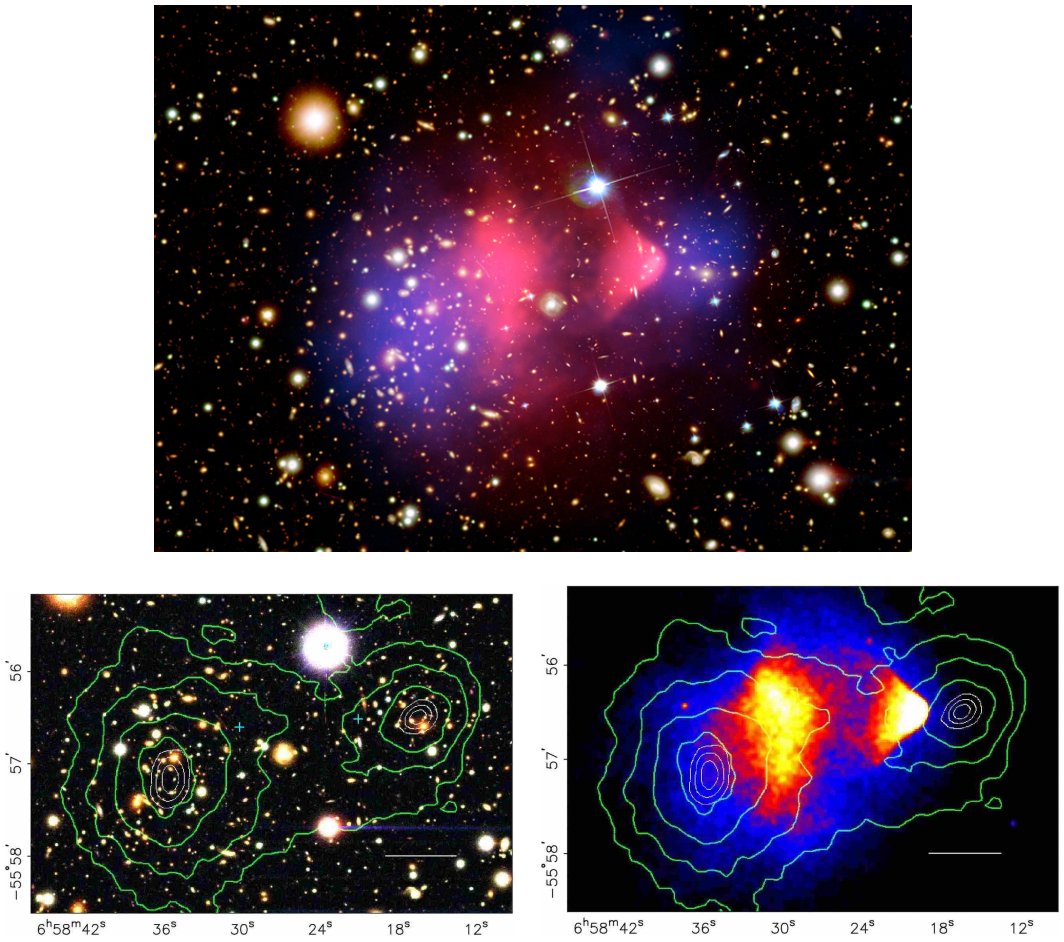

FIGURE 1.4: *Examples of weak lensing.* Top panel: *The Bullet Cluster 1E 0657-56, shown here in a composite image. The background image shows the location of galaxies, with most of the larger yellow galaxies associated with one of the colliding clusters. The overlaid red features show X-ray emission from hot, intra-cluster gas; the gas cloud at the right emerges distorted into the distinctive bullet-shape from the collision. The overlaid blue features show a reconstruction of the total mass from measurements of gravitational lensing. This appears coincident with the locations of the galaxies, implying it has a similarly small interaction cross section. However, there is more mass than that present in the optical galaxies and X-ray gas combined; this, plus the clear separation of the center of the potential well from the gas, otherwise considered to be the bulk gravitational component of the cluster, is considered strong evidence for the existence of Dark Matter.* Bottom panels: *Direct evidence for Dark Matter in the bullet cluster 1E0657-56. In this plot reproduced from [18]: the visible matter (red and yellow), observed in optical wavelengths (*left*) and X-rays (*right*) by the CHANDRA satellite, only contributes little to the total mass of the two colliding clusters (density contours in green). This total mass has been measured by gravitational lensing with VLT and Hubble satellite.*

no significant mass is present, and the universe has no preferred directions, one would expect their shapes to be uncorrelated, and the average to vanish. From the observed shear field, one can get the projected mass distribution.

The most extraordinary example of mass discrepancy in clusters is the so-called Bullet

Cluster 1E 0657-56 [18–20], consisting of 2 colliding clusters of galaxies and shown in Fig.1.4. Strictly speaking, the name "Bullet Cluster" refers to the smaller sub-cluster, which moves away from the larger one. By analyzing the weak lensing effect, the gravitational potential of the system was mapped in [18], showing that it does not trace the plasma distribution (that constitutes the dominant baryonic mass of this system), but rather the distribution of galaxies. The center of the total mass is found to lie 8σ away from the center of the baryonic mass, requiring a very big amount of dark mass to be located near the galaxies. The Bullet Cluster is one of the strongest proofs of existence of DM, also because it is believed to be very hard to explain it using the MOND alternative (see, however, [17]).

1.2.4 Evidence from Large Scale Structures (LSS)

On large scales, the Universe shows a hierarchical structure (galaxies are gathered into clusters, clusters are part of superclusters, and superclusters are arranged into large-scale sheets, filaments and voids, see Fig.1.5), as revealed by large-scale surveys such as the 2-degree Field Galaxy Redshift Survey (2dFGRS, [21]) and the Sloan Digital Sky Survey (SDSS, [22]). Structure formation strongly depends on the presence of Dark Matter or a modification of gravitational dynamics with respect to the predictions of General Relativity.

Dark Matter plays a key role in structure formation because it interacts only gravitationally. As a result, it begins to collapse into Dark Matter halos well before ordinary matter; the latter, indeed, has relevant interactions with photons in the primordial plasma, that prevent it from clumping due to the pressure force they exert. At the time of recombination, baryons promptly fall in the potential wells created by the Dark Matter halos. Without Dark Matter, baryons would clump much slower and galaxy formation would occur much later in the Universe than is observed.

Large-scale cosmological 'N-body' simulations, like e.g. the Millennium simulation [23], show that the observed LSS of luminous matter could have been formed only if a substantial amount of Dark Matter was present. Moreover, they show that most of the Dark Matter must be both nondissipative (to collapse before luminous matter, as explained before) and non-relativistic ('cold'). To explain the latter statement, we can say that relativistic ('hot') DM would have a very large free-streaming length, so that it would free-stream out of galaxy-sized overdense regions. This would imply that only very large structures can form early, while smaller structures form from fragmentation of larger ones, and this is called top-down hierarchy. Nowadays, galaxies at very high redshift have been observed, and so we think that galaxies are older than superclusters. For

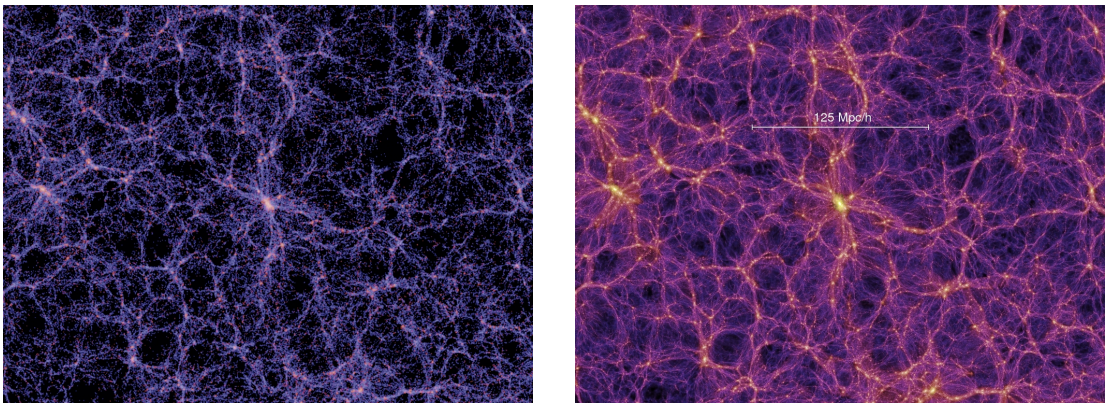

FIGURE 1.5: *The millennium simulation* Left panel: *visible matter distribution* Right panel: *Dark Matter distribution.*

this reason, cold species are preferred, as their non-relativistic speed gives them a short free-streaming length, which allows galaxies to form before larger structures, leading to a hierarchical structure formation, with smaller structures merging in larger ones, in accordance with N-body simulations. A third possibility, dubbed 'warm' DM because it has a velocity between that of hot and cold DM, was proposed in order to solve some problems of the cold DM paradigm (see e.g. [24]). Despite beeing slower than hot DM, its free-streaming length would still be too large and it would suppress the formation of small structures: for example, a warm DM particle with a mass of 1 KeVand an abundance that matches the correct Dark Matter density, has a free-streaming length of order of galaxy scales [25]. A lower bound on the mass of the warm DM particles is around the KeV scale [26] (the same is also done for hot particles, such as neutrinos [8]). However, Cold Dark Matter (CDM) remains the standard paradigm.

1.2.5 Evidence from Cosmology

Studying the history of the Universe offers some very powerful tools to probe its contents. During the evolution of the hot particle soup after the Big Bang, indeed, some relics where produced. These relics should still be present nearly unaltered today, and their presence gives us information about the state of the Universe at the time of their formation.

Surely, the most well-known and most important relic of the early Universe is the Cosmic Microwave Background Radiation (CMB). This is made of photons that were emitted during recombination, when free protons and electrons composing the primordial hot plasma became bound to form electromagnetically neutral hydrogen atoms, thus allowing photons to freely propagate across the universe. The CMB was detected in 1964 for the first time and is seen to have a perfect black body spectrum corresponding to a

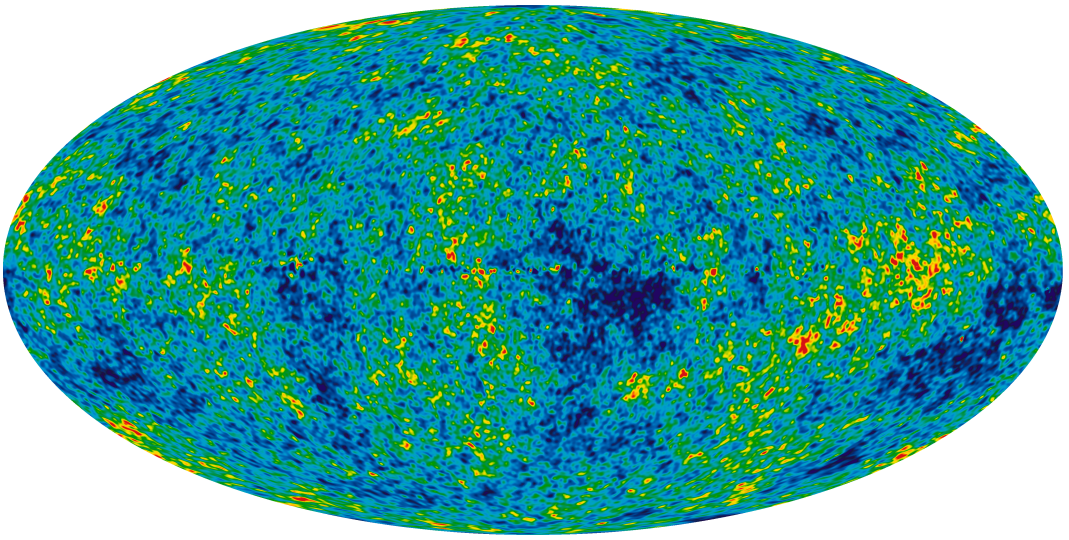

FIGURE 1.6: *The detailed, all-sky picture of the infant universe from nine years of WMAP [8] data. The image reveals 13.7 billion year old temperature fluctuations (shown as colour differences) that correspond to the seeds that grew to become the galaxies. This image shows a temperature range of* $\pm 200mK$.

temperature of $T_{CMB} = 2.725K$ [27, 28]. CMB also contains a lot of information about the state of the Universe at the time of recombination (when the universe was about 378.000 years old), allowing to fit several cosmological parameters (see e.g. [8]). The presence of overdensities and underdensities in the primordial plasma before recombination translates into anisotropies in the angular distribution of temperatures in the CMB, shown in Fig.1.6. For this reason, one can obtain, from CMB anisotropies, information on the distribution of baryon and matter in the Universe at the time of recombination. The angular distribution of CMB anisotropies is a function of the angular position in the sky θ,

$$\frac{T(\theta) - T_{CMB}}{T_{CMB}} = \frac{\delta T}{T_{CMB}}(\theta) = \sum_{l=2}^{\infty} a_{lm} Y_{lm}(\theta) \tag{1.8}$$

and therefore can be written as a infinite series of the spherical harmonics $Y_{lm}(\theta)$. The monopole $l = 0$ and the dipole $l = 1$ are skipped in the definition because these correspond to the CMB mean temperature and to the anisotropy due to the motion of the Earth relative to the CMB rest frame, respectively. One then defines the variance C_l of a_{lm} as

$$C_l = \langle |a_{lm}|^2 \rangle = \frac{1}{2l+1} \sum_{m=-l}^{l} |a_{lm}|^2 \tag{1.9}$$

as this is the variable with a physical meaning (C_l, for example, is a rotationally invariant quantity, while the a_{lm} are not). If the temperature fluctuations are assumed to be Gaussian , all of the information contained in the CMB map are expressed by the spectrum of the C_l, usually displayed as $l(l+1)C_l T_{CMB}^2/2\pi$ (see Fig.1.7). This is an

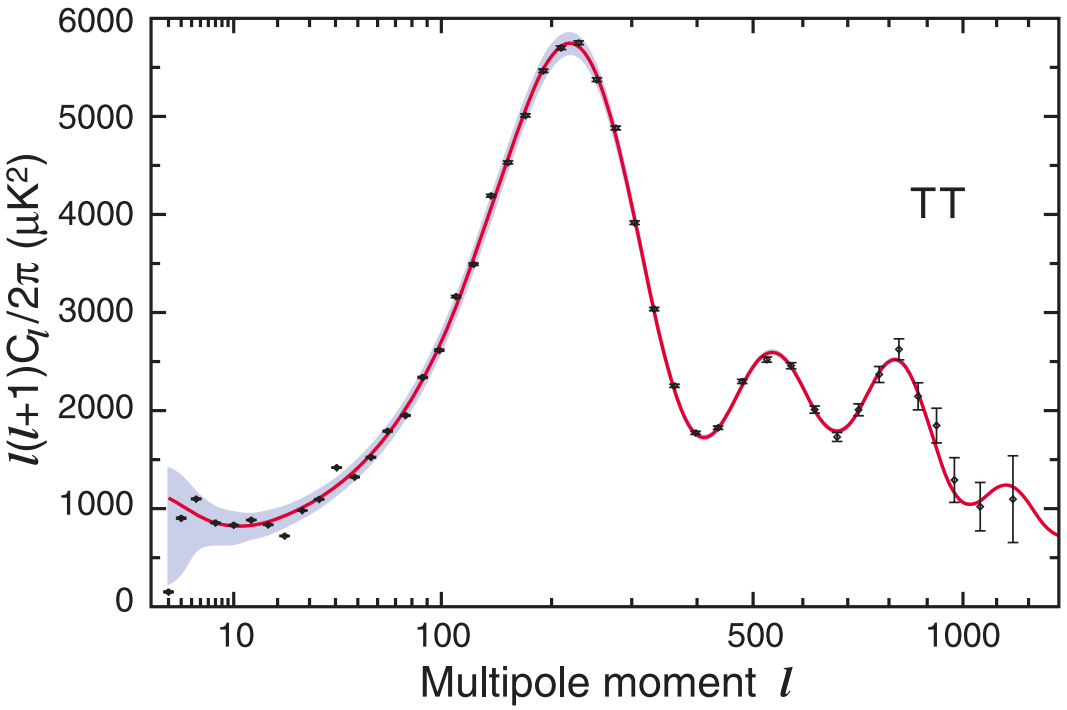

FIGURE 1.7: *The nine-year WMAP TT angular power spectrum. The WMAP data are in black, with error bars, the best fit model is the red curve, and the smoothed binned cosmic variance curve is the shaded region. The first three acoustic peaks are well-determined. Taken from [9].*

oscillating spectrum featuring a number of peaks that were generated by the acoustic oscillations of the plasma before recombination and photon decoupling. Pressure/density waves where generated in the primordial plasma by the presence of two opposite forces: the gravitational attraction and the pressure of photons. These acoustic waves compressed and rarefied the primordial plasma, thus generating temperature fluctuations whose imprint remained encoded in the CMB. Oscillation modes that are caught at maxima or minima of their oscillation at the time of recombination correspond to peaks in the power spectrum. The first peak, occurring at $l \simeq 200$, represents the oscillation mode that compressed the primordial plasma only once before recombination happened. The second peak represents the oscillation mode of a single full cycle, compressing and then rarefying the plasma, before recombination, the third peak the mode that compressed, rarefied and then compressed again, and so on. Therefore the odd peaks are related with the compression of the plasma, and it results that they are enhanced by an increase of baryon density Ω_b. Instead, the even peaks are associated with plasma rarefaction, and do not depend on Ω_b. Thus, with the addition of baryons the odd peaks are enhanced over the even peaks. Because of this it is possible to estimate the baryon density from the ratio between the first two peaks. Fits to the CMB power spectrum allow to determine even more ΛCDM model parameters, and the results are the values reported in Equation (1.3) at the beginning of this chapter. The CMB

experimental data gives and independently confirms the large discrepancy between the baryon and matter density, suggesting a dominant (cold) Dark Matter component. The last important hint for dark matter comes from Big Bang Nucleosynthesis (BBN). BBN offers a very reliable probe of the early Universe, as this phenomenon is quite well understood and it is based on Standard Model physics. BBN Predictions of the abundance of light elements (which are essentially: D, ^{3}He, ^{4}He, and ^{7}Li) are in good agreement with the abundances inferred from observations. The major problem here is that primordial abundances get altered by stellar nucleosynthesis which also produces heavy elements. The reaction rates for the formation of light elements depend on the density of baryons n_b, which is usually expressed normalized to the relic black body photon density as $\eta = n_b/n_\gamma$. All the light-element abundances (see Fig.1.8) can be explained with $\eta \simeq 5.1 - 6.5 \cdot 10^{-10}$. As the photon density n_γ gets fixed by CMB measurements, this implies that $\Omega_b \simeq (0.019 - 0.024)h^{-2}$, where $h \simeq 0.721$ is the present Hubble parameter. Therefore BBN also confirms the value of Ω_b as measured by WMAP, Equation (1.3) in an independent way. Comparing this value with the total amount of matter in the Universe, we come again to the conclusion that a dominant Dark Matter component should exist.

To summarize, LSS, CMB and BBN all consistently agree that the observed baryonic matter constitutes only one part out of four or five of the total amount of matter contained in the universe, and that the missing part should be constituted by some cold matter that does not interact with light. The CMB, together with observations of Type Ia supernovae, imply the further presence of a Dark Energy component, responsible for the Universe's accelerated expansion today, which contributes the 72% of the total energy density. In fact, one can get the value of Ω_λ fitting the CMB, because the position of CMB peaks depends on it [8, 10, 11], and distant supernovae are apparently dimming, indicating that the expansion of the Universe is accelerating [29, 30]. All these observations are in remarkable mutual agreement and conspire to paint an entirely self-consistent picture of the Universe.Nevertheless, we still ignore the fundamental nature of both Dark Energy and Dark Matter.

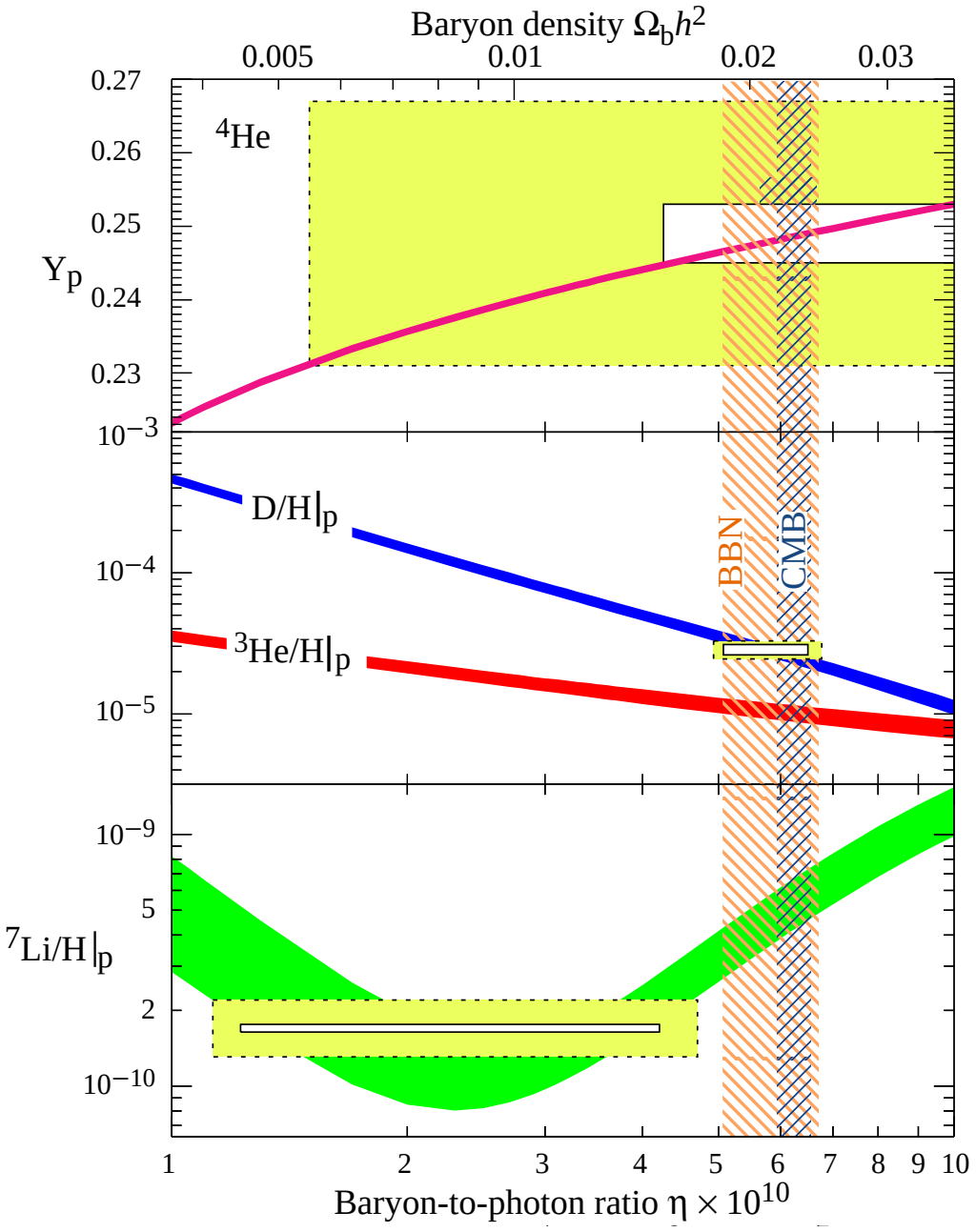

FIGURE 1.8: *The abundances of ^4He, D, ^3He, and ^7Li as predicted by the standard model of Big-Bang nucleosynthesis (Y_p indicates the ^4He mass fraction). The bands show the 95% CL range. Boxes indicate the observed light element abundances (smaller boxes: $\pm 2\sigma$ statistical errors; larger boxes: $\pm 2\sigma$ statistical and systematic errors). The narrow vertical band indicates the CMB measure of the cosmic baryon density, while the wider band indicates the BBN concordance range (both at 95% CL). Taken from [11].*

Chapter 2

Dark Matter Candidates and Experimental Searches

2.1 Dark Matter Candidates

The DM mass $m_{\rm DM}$ is expected to lie within the range

$$10^{-28}\,\text{eV} < m_{\rm DM} < 10^{24}\,\text{Kg} \tag{2.1}$$

This plot illustrates the mass range of some plausible DM candidates:

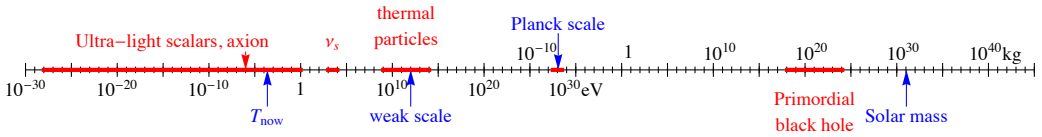

FIGURE 2.1: Possible Scales and relative DM candidates. Thanks to A. Strumia.

The Planck scale, $M_{\rm Pl} \approx 1.2 \cdot 10^{19}\,\text{GeV}$, is the ultimate boundary of particle physics: elementary particles with mass $m_{\rm DM} > M_{\rm Pl}$ are black holes because their wavelength $1/m_{\rm DM}$ is smaller than the Swartzchild radius $m_{\rm DM}/M_{\rm Pl}^2$. The DM mass could be above or below $M_{\rm Pl}$: we do not know if DM physics is astrophysics or particle physics.

The DM candidate considered in the work is the WIMP, but I will review here the other possible candidates. For a more complete review concerning them, you can check [4], on which this section is based on.

2.1.1 WIMP Dark Matter

WIMPs (Weakly Interacting Massive Particles) are particle physics DM candidates whose mass lies in the range $m_{\text{weak}} \sim 10\ \text{GeV} - \text{TeV}$ and the only interact through the weak force.

Using partial-wave unitarity of the S-matrix, Griest and Kamionkowski [31] derived an upper bound of 340 TeV (240 TeV) on the mass of a stable Majorana (Dirac) fermion which was once in thermal equilibrium. WIMPs are the most studied dark matter candidates at the moment, as they are predicted in many particle physics theories, such as SUSY, they may solve the hierarchy problem, naturally produce the correct relic density, and they may be detected in many ways. In this section, we discuss their production through thermal freeze out and their implications for direct detection Sec. 2.2.1, indirect detection Sec. 2.2.2, and particle colliders Sec. 2.2.3.
What is called 'WIMP miracle' is the fact that, if a WIMP exists and is stable, it is naturally produced with a relic density of the order of that required for dark matter. Because of this, WIMPs are usually believed to be excellent dark matter candidates.

The observed DM energy density may be produced as a thermal relic of the Big Bang [32–35]. The evolution of a thermal relic's number density is described quantitatively by the Boltzmann equation

$$\frac{dn}{dt} = -3Hn - \langle \sigma_A v \rangle \left(n^2 - n_{\text{eq}}^2 \right) \ , \tag{2.2}$$

where n is the number density of the dark matter particle X, H is the Hubble parameter, $\langle \sigma_A v \rangle$ is the thermally averaged annihilation cross section for the processes $XX \rightarrow$ SM SM, where SM denotes SM particles, and n_{eq} is the dark matter number density in thermal equilibrium. On the right-hand side of (2.2), the first term accounts for dilution from expansion. The n^2 term arises from processes $XX \rightarrow$ SM SM which destroy X particles, and the n_{eq}^2 term arises from the reverse process SM SM $\rightarrow XX$, which creates X particles. This process is shown in Fig. 2.2. Initially, when the early Universe has a very high density and a temperature well above the WIMP mass, all particles are in thermal equilibrium. When the Universe has cooled down to a temperature T below the dark matter particle's mass m_X, the number of dark matter particles drops exponentially as $e^{-m_X/T}$, being Boltzmann suppressed. Eventually, the DM number density does not go to zero, but rather converges to a fixed value, because the Universe is also expanding. In fact, because of expansion, the dark matter number density becomes so low that the DM interaction rate goes to zero as they cannot find each other to annihilate themselves. This is what is called "'freeze out"': when their number asymptotically tends to a constant, this is their thermal relic density. Note that after freeze out, even though interactions that change the number of DM particles are negligible, interactions that can

efficiently exchange energy between DM and other SM particles, such as $XSM \rightarrow$ X SM, may still be active.

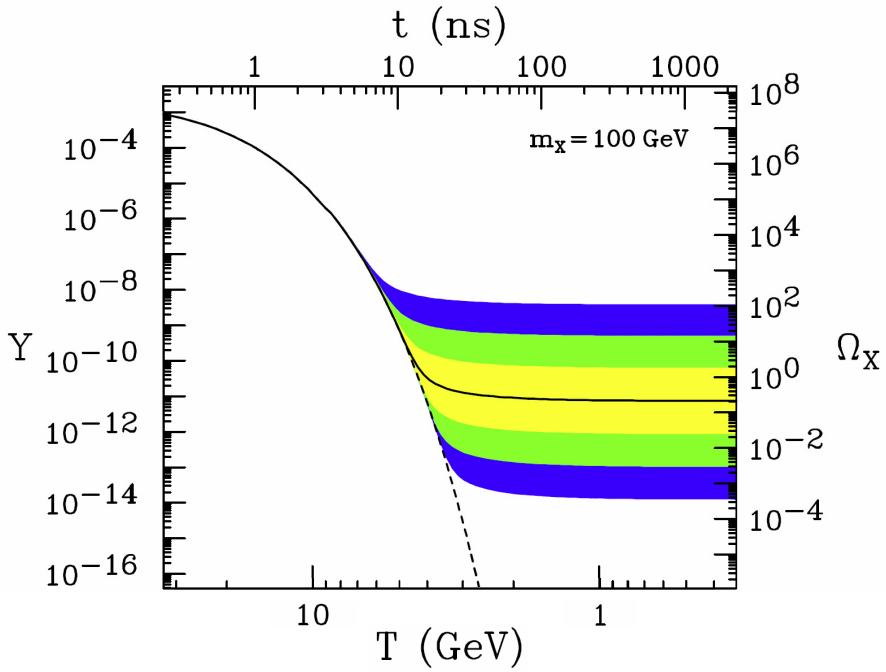

FIGURE 2.2: The comoving number density Y (left) and resulting thermal relic density (right) of a 100 GeV, P-wave annihilating dark matter particle as a function of temperature T (bottom) and time t (top). The solid contour is for an annihilation cross section that yields the correct relic density, and the shaded regions are for cross sections that differ by 10, 10^2, and 10^3 from this value. The dashed contour is the number density of a particle that remains in thermal equilibrium. Taken from [4].

The Boltzmann equation can be solved numerically. Here we present a rough analytical analysis of the solution. Defining freeze out to be the time when $n\langle\sigma_A v\rangle = H$, we have

$$n_f = \frac{H_f}{\langle\sigma_A v\rangle} \sim (m_X T_f)^{3/2} e^{-m_X/T_f}, \tag{2.3}$$

$$H \sim \frac{T^2}{M_{\rm Pl}}, \tag{2.4}$$

$$n_f \sim \frac{T_f^2}{M_{\rm Pl}\langle\sigma_A v\rangle}, \tag{2.5}$$

where the subscripts f denote quantities at freeze out. The ratio $x_f \equiv m_X/T_f$ appears in the exponential, and is, therefore, highly insensitive to the dark matter's properties and may be considered a constant; a typical value is $x_f \sim 20$. The thermal relic density is, then,

$$\Omega_X = \frac{m_X n_0}{\rho_c} \sim \frac{m_X T_0^3}{\rho_c}\frac{n_f}{T_f^3} \sim \frac{x_f T_0^3}{\rho_c M_{\rm Pl}}\langle\sigma_A v\rangle^{-1} \sim \Omega_{DM}\frac{3\cdot 10^{26} cm^3/s}{\langle\sigma_A v\rangle}, \tag{2.6}$$

where ρ_c is the critical density and the subscripts 0 denote present day quantities. We

see that the thermal relic density is insensitive to the dark matter mass m_X and inversely proportional to the annihilation cross section $\langle \sigma_A v \rangle$.

Even though Ω_X does not depend on m_X directly, the DM mass is the only relevant mass scale to determine the annihilation cross section in many theories. In these cases, one can write $\langle \sigma_A v \rangle$ using dimensional considerations as

$$\sigma_A v = k \, \frac{g_{\text{weak}}^4}{16\pi^2 m_X^2} \, (1 \text{ or } v^2) \, , \tag{2.7}$$

where the presence of the factor v^2 depends on whether it is an S- or P-wave annihilation, respectively, and higher-order terms in v have been neglected. The constant $g_{\text{weak}} \simeq 0.65$ is the weak interaction gauge coupling, and $k = \mathcal{O}(1)$ parametrises deviations from this estimate.

The only free parameters in this parametrization are k and m_X. The results are shown in Fig. 2.3. The width of the band comes from considering both S- and P-wave annihilation, and from letting k vary from $\frac{1}{2}$ to 2. A particle that gives the correct dark matter is predicted to have mass in the range $m_X \sim 100 \text{ GeV} - 1 \text{ TeV}$; a particle that makes up 10% of dark matter has mass $m_X \sim 30 \text{ GeV} - 300 \text{ GeV}$. This is the WIMP miracle: weak-scale particles make excellent dark matter candidates. In this rough analysis, many details have been neglected, for example, there are models for which k may differ up to one order of magnitude from the range of values considered here. Nevertheless, the WIMP miracle implies that it is very easy to obtain viable WIMP dark matter candidates, and it is at present the main reason to think that central problems in particle physics and astrophysics may in fact be related. Note also that, in addition to the motivations arising from the hierarchy problem, the WIMP miracle provides an independent strong motivation for new particles at the weak scale.

2.1.2 Other candidates

Here We present some other candidates for the dark matter.

2.1.2.1 Axions

The QCD vacuum has a rather complex structure, because the gluon field can be a pure gauge field at spatial infinity [36]. The pure gauge boundary condition introduces some degree of freedom in the choice of the boundary field, which translates into similar freedom in the choice of the QCD vacuum. Because of this vacuum structure, the QCD

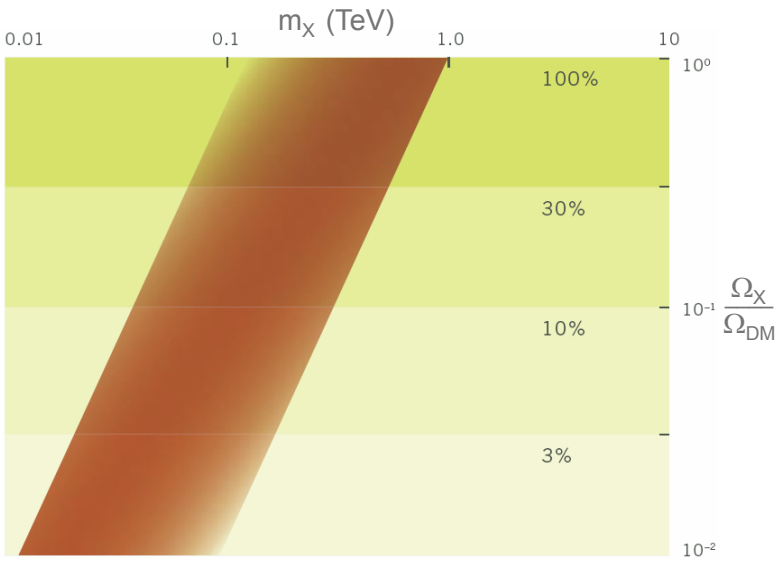

FIGURE 2.3: A band of natural values in the $(m_X, \Omega_X/\Omega_{\rm DM})$ plane for a thermal relic X, where $\Omega_{\rm DM} \simeq 0.23$ is the required total dark matter density. Taken from [4].

Lagrangian picks up an additional effective term

$$\mathcal{L}_\theta = \theta \frac{g_s^2}{32\pi^2} G_a^{\mu\nu} \tilde{G}_{\mu\nu}^a \tag{2.8}$$

Here, g_s is the strong coupling constant, $G_a^{\mu\nu}$ is the QCD field strength tensor for the ath gluon, and $\tilde{G}_{\mu\nu}^a$ is its dual. Unlike the rest of the QCD Lagrangian, $\mathcal{L}_\theta$ does not conserve CP. As we have said in section 1.1.1.4, this is a problem called "'strong CP problem"' because the strong interaction is known empirically to conserve CP rather well. Observations constrain the vacuum angle θ to be less than 10^{-9} [36]. The existence of an additional spontaneously-broken, global chiral $U(1)$ symmetry of the SM Lagrangian, known as the Peccei-Quinn symmetry [37], may solve the "'strong CP problem"'. The Axion is the Goldstone boson of this broken symmetry (see e.g. [38]).

The Axion solution originates by introducing a new pseudoscalar field a with coupling

$$\mathcal{L}_a = -\frac{g_3^2}{32\pi^2} \frac{a}{f_a} \epsilon^{\mu\nu\rho\sigma} G_{\mu\nu}^\alpha G_{\rho\sigma}^\alpha \ , \tag{2.9}$$

where f_a is the Axion decay constant. The Axion potential has a minimum that naturally sets the field to a value $a = \theta f_a$ which cancels $\mathcal{L}_\theta$, whatever the value of θ is, thus solving the "'strong CP problem"'. The Axion's mass and interactions are model dependent, but they can be calculated as function of f_a up to model dependent factors that are typically $\mathcal{O}(1)$. The Axion's mass is

$$m_a = \frac{\sqrt{m_u m_d}}{m_u + m_d} m_\pi f_\pi \frac{1}{f_a} \approx 6 \ \mu\text{eV} \left(\frac{10^{12} \ \text{GeV}}{f_a} \right), \tag{2.10}$$

where $m_u \simeq 4$ MeV, $m_d \simeq 8$ MeV, and $m_\pi \simeq 135$ MeV are the up quark, down quark, and pion masses, and $f_\pi \simeq 93$ MeV is the pion decay constant. Axions interact with gluons, through the term of (2.9), and also with fermions. At loop-level, the lagrangian also gets an interaction term

$$\mathcal{L}_{a\gamma\gamma} = -g_\gamma \frac{\alpha}{\pi} \frac{a}{f_a} \vec{E} \cdot \vec{B} \equiv -g_{a\gamma\gamma}\, a\, \vec{E} \cdot \vec{B} \ , \tag{2.11}$$

where α is the fine-structure constant and g_γ is a model-dependent parameter. In the case of two well-known possibilities, the KSVZ [39, 40] and DFSZ [41, 42] Axions, g_γ is -0.97 and 0.36, respectively. The Axion's mass is bounded by several independent constraints. The coupling of (2.11) implies that Axions decay with lifetime

$$\tau(a \to \gamma\gamma) = \frac{64\pi}{g_{a\gamma\gamma}^2 m_a^3} \simeq \frac{8.8 \times 10^{23} \text{ s}}{g_\gamma^2} \left(\frac{\text{eV}}{m_a} \right)^5 \ . \tag{2.12}$$

This implies $m_a \lesssim 20$ eV, if we want them to be stable on timescales of the Universe. Axions may be produced in stars and then escape, leading to a new source of energy loss. The longevity of red giants and the observed length of the neutrino pulse from Supernova 1987a require $f_a \gtrsim 10^9$ GeV, implying $m_a \lesssim 10$ meV [43].

Axions are expected to interact very weakly with ordinary particles, and this implies that they were not in thermal equilibrium in the early Universe. Their relic density calculation is uncertain but it is possible to find an acceptable range where Axions satisfy constraints and represent a possible dark matter candidate [44].

There are several possible production mechanisms for Axion dark matter. Unfortunately, if Axions were produced thermally, they would have a relic density of $\Omega_a^{\text{th}} \sim 0.22\,(m_a/80 \text{ eV})$ and this, together with (2.12), implies that Axions produced in this way cannot simultaneously reproduce the right relic density and be stable on cosmological timescales.

There are, however, several non-thermal production mechanisms linked to the rich cosmological history of the Axion field [45–49].

The allowed ranges for the Axion mass and decay constant are:

$$\begin{aligned} 10^{12} \text{ GeV } \theta_i^{-2} \gtrsim \quad & f_a \quad \gtrsim 10^9 \text{ GeV} \\ 6\ \mu\text{eV } \theta_i^2 \lesssim \quad & m_a \quad \lesssim 6 \text{ meV} \ , \end{aligned} \tag{2.13}$$

where θ_i is an arbitrary constant that is less than or of the order of 1.

The lower bound on m_a arises from requiring that Axions don't overclose the Universe. Any choice in the allowed windows allows the Axion to generate 100% of the expected

amount of DM. However, differently from the WIMP case, there is no *a priori* reason for the Axion mass and decay constant to lie exactly in this range of values.

One may note that, in the cases where $\theta_i \ll 1$, the allowed ranges for m_a and f_a enlarge, and the possibility $f_a \simeq m_{\rm GUT} \simeq 10^{16}$ GeV may be allowed: this provides an avenue for anthropic selection [50, 51]. In this case, unfortunately, Axions would be undetectable in the near future.

2.1.2.2 SIMP

The ΛCDM model is very successful in explaining the formation and evolution of cosmic structures, but it still has some problems and one of them is called "'the Cusp Problem"' (see, *e.g.* [52]). Numerical simulations using the ΛCDM model result in density profiles for DM that have a cusp towards the center of the galaxy. These results are challenged by observations, that would instead predict flat core profiles for DM density. The inclusion in the simulations of baryonic effects may reduce the discrepancies, but is not clear if this would be enough to reconcile simulations with observations, or whether it would be necessary to change the physics of the DM sector. SIMPs [53] are Strongly Interacting Massive Particles which could form colourless bound states [54] and hide their strong interactions. For instance, self-interacting DM with a strength [55–62]

$$0.1 \text{ cm}^2/\text{g} \lesssim \left.\frac{\sigma_{\rm scatter}}{m_{\rm DM}}\right|_{\rm obs} \lesssim 10 \text{ cm}^2/\text{g} \tag{2.14}$$

can help in solving the observed discrepancies. Constraints from the Bullet Cluster [20, 63, 64] and from halo shapes [58–60] place an additional upper bound on the DM self-interacting cross section (at velocities greater than 300 km/s)

$$\frac{\sigma_{\rm scatter}}{m_{\rm DM}} \lesssim 1 \text{ cm}^2/\text{g}\,. \tag{2.15}$$

2.1.2.3 Asymmetric Dark Matter

The main reason for studying Asymmetric DM [65] comes from observing the following relation between the observed DM and Visible Matter (VM) abundances [7, 66]

$$\Omega_{\rm DM} \simeq 5\,\Omega_{\rm VM}\ , \tag{2.16}$$

where Ω denotes, as usual, the ratio between the mass density of a given component and the critical density. This similarity would suggest some kind of common origin for these two components. We know that the density of VM was originated from the baryon

asymmetry of the universe: for some reason, a tiny excess of baryons B over antibaryons $\bar{B}$ developed during the early universe [7, 66]

$$\eta(B) \equiv \frac{n_B - n_{\bar{B}}}{s} \simeq 10^{-10} \ , \tag{2.17}$$

where number densities are denoted n, and s is entropy density.[1] After all the antibaryons were annihilated with the baryons, the remaining small excess of baryons formed the baryonic matter we can see in the universe. Baryogenesis may suggest that a similar process happened for DM as well, with a similar origin for the generated excess which generated a similar amount of excess, that translates into the similar amounts of DM and Visible Matter.

Therefore, Asymmetric DM, in analogy with WIMP, naturally generates the right relic abundance (even though with another mechanism), but it also features a natural explanation of why VM and DM have very similar abundances (in WIMP models this is usually a coincidence, you can check [67–69] for some attempts to solve this). The standard WIMP scenario is also rather strongly constrained by direct, indirect and collider DM searches [70–72].

Asymmetric DM is one of a number of well-motivated alternatives to the WIMP solution. A downturn of ADM is that is does not feature the strong connection between the freeze-out process and the various kinds of searches. It is also undetectable through Indirect detection, because DM particle-antiparticle annihilations are obviously irrelevant today, as there are not antiparticle left to generate such process and other processes like co-annihilations with other particles, such as nucleons, are possible, but they are not a required feature of ADM. Usually ADM models can be tested by using direct detection and collider searches, but, unfortunately, ADM models usually contain parameters that do not affect cosmic abundances, so that we have no theoretical hint of their value, thus making such searches less effective for this kind of models.

As in most ADM models, DM and baryon number densities are similar. To satisfy the observed relation of Eq. (2.16), it is then necessary for DM particles to have a mass similar to the proton or just slightly higher, typically in the range 1-15 GeV, but this varies depending on the precise model. There are various experiments that support a mass in the this range, the DAMA+DAMA/LIBRA [73, 74], CoGeNT [75, 76], CRESST [77] and CDMS [78]. These results are, however, in tension with other experiments, such as LUX, [79] which instead exclude this part of the parameter space. Certain kinds of ADM models may reconcile these positive results, even if with some

[1] The asymmetry in a charge X is generally defined by $\eta(X) \equiv \sum_i X_i(n_i - n_{\bar{i}})/s$ where i denotes a species carrying X-charge of X_i. An asymmetry normalized in this way is useful because it remains constant during the isentropic expansion of the Universe.

tension with null searches [80–85]. The two main differences from WIMP-style DM to archive such reconciliation are the nature of the DM-Nucleon interaction, and the DM velocity dispersion. An altered velocity dispersion relation could be explained by non-negligible DM self interactions, thus solving the small-scale structure problems (like the "'cusp problem"') of the collisionless ΛCDM paradigm. Finally, a full ADM explanation for Eq. (2.16) would require an explanation for the required DM mass scale: even though it is not difficult to produce a model where the baryon and DM number densities are similar, it is way more difficult to produce models where the required DM mass is generated naturally.

The idea that the Universe may contain a dark, relic, asymmetric component has been considered for many years. One of the older ideas is that of mirror matter [83, 86–100], where duplicates of the Standard Model form the dark sector (subsequent observations have ruled out the specific scenarios of Refs. [91] and [92]). Another relatively early idea was to consider DM a neutral techni-baryon [101, 102] whose stability was enforced by an analog of baryon number conservation.

2.1.2.4 Lightest Kaluza-Klein particle

New physics at weak scale may be due to extra dimensions. The origin of this idea is quite old, in fact it was introduced for the first time in a work of Kaluza and Klein in 1920's [103]. The concrete realization of their original idea is nowadays excluded, but there are many modern descendants, two of the most famous being universal extra dimensions (UED) [104] and large extra dimensions (ADD) [105–110].

In UED, the additional dimensions have a size $R \lesssim 10^{-18}$ m [104] and all particles can propagate into them, while in ADD, the size of the dimensions can be up to $R \sim 10^{-4} m$ [111, 112], as only KK-particles (but not standard model ones) can propagate into the new dimensions. In the simplest extra dimensions model, there is one extra dimension of size R compactified on a circle (for ADD, usually at least 2 or 3 additional dimensions are necessary due to astrophysical bounds, even though there are some ways to avoid them [113]). Every particle allowed to enter the additional dimensions has an infinite number of Kaluza-Klein (KK) excitation levels n with mass $\sim nR^{-1}$. Couplings in extra dimensions models become non-perturbative at an energy scale well below $M_{\rm Pl}$, thus they could be an interesting low energy description of a more complete theory that solves the hierarchy problem and that is well defined up to $M_{\rm Pl}$.

UED models usually preserve a discrete parity called KK-parity, and this implies that the lightest KK particle (LKP) is stable and a viable dark matter candidate [114, 115].

2.1.2.5 Sterile Neutrinos

We have introduced the neutrino mass problem in 1.1.1.3.

Neutrinos could be given a mass by adding right-handed neutrinos $\nu^\alpha \equiv \nu_R^\alpha$ and a coupling term to the higgs, so that they get a mass in the same way as all other particles. SM symmetries imply that a right-handed neutrino would be a Sm singlet and it must have no SM gauge interactions. Because of this, it is also possible to add a so-called Majorana mass term for the two right-handed neutrinos, which are therefore gauge-invariant.

The SM lagrangian is therefore extended to include N sterile neutrinos by adding

$$\mathcal{L}_{\nu_R} = \bar{\nu}^\alpha i \not{\partial} \nu^\alpha - \left(\lambda^\nu_{i\beta} \bar{L}^i \nu^\beta \tilde{\phi} + \text{h.c.}\right) - \frac{1}{2} M_{\alpha\beta} \bar{\nu}^\alpha \nu^\beta \ , \tag{2.18}$$

where $\lambda^\nu_{i\beta}$ are the neutrino Yukawa couplings, $M_{\alpha\beta}$ is the Majorana mass matrix, and $\alpha, \beta = 1, \ldots, N$, where $N \geq 2$ so that at least two neutrino states are massive. After electroweak symmetry breaking, the Higgs field gets a vacuum expectation value, and the neutrino masses are the eigenvalues of the complete $(3+N)\times(3+N)$ neutrino mass matrix

$$m_\nu = \begin{pmatrix} 0 & \lambda_{i\beta}\langle\phi\rangle \\ \lambda^*_{\alpha j}\langle\phi\rangle & M_{\alpha\beta} \end{pmatrix} . \tag{2.19}$$

Mass eigenstates are linear combinations of left and right neutrinos; the ones that are predominantly left are usually called "'active"', while the ones that are predominantly right are called "'sterile"' neutrinos.

One can explain neutrino masses in a natural way, supposing $\lambda^\nu \sim \mathcal{O}(1)$ and $M \sim 10^{12} - 10^{16}\,\text{GeV} \gg \langle\phi\rangle$ (near m_{GUT}; this mechanism is, in fact, common in Grand Unification Theories [116]), obtaining N large neutrino masses $\sim M$, and three small neutrino masses $\sim {\lambda^\nu}^2 \langle\phi\rangle^2 / M$. For $M \sim 10^{14}$ GeV, near the grand unification scale, one gets the desired light neutrino masses. Unfortunately, sterile neutrinos are beyond the range of experiments and are not viable dark matter candidates in this case [117, 118].

Given the fact that yukawa couplings in the SM span a large range ($\mathcal{O}(10^{-6}) - \mathcal{O}(1)$), there is no reason to enforce $\lambda^\nu \sim \mathcal{O}(1)$. If $\lambda^\nu \ll 1$, one may obtain light sterile neutrinos, which can be dark matter candidates.

For $\lambda^\nu \sim 10^{-11}$, sterile neutrino masses are in the KeV range, allowing them to be a viable warm dark matter candidate, with the correct relic abundance (see e.g. [119]). It is also possible to make sterile neutrinos viable cold dark matter candidates.

2.1.2.6 MACHOs and Primordial Black Holes

Till now we have reviewed the most common DM candidates coming from particle physics. DM could also consist of yet-undetected astrophysical objects, called Massive Compact Halo Objects (MACHOs), like large planets, small dead stars or stray black holes, which would not emit light and would therefore be invisible. As we have already discussed in Sec. Sec. 1.2, any DM explanation using baryonic astrophysical objects created after BBN, like the rest of astrophysical objects (which are pretty natural expectations), contradicts the bounds from BBN and CMB.
Since the first proposal on MACHOs , several surveys (named EROS-1 and -2 [120–122], MACHO [123–125], OGLE-1...-3 [126, 127] etc) have tried to detect MACHOs through the search for microlensing signals from stars in the Magellanic clouds, which are one of the nearest and best known environments just outside our Galaxy. Gravitational microlensing happens when a MACHO crosses the line of sight towards some background star: when this happens the light of this star is lensed and, despite the fact that effects like multiple imaging (like in strong lensing Sec. 1.2.3) or shear (like in weak lensing Sec. 1.2.3) are too small to be detected, its flux towards the Earth temporarily increases by detectable amounts. The results from these surveys are consistent with BBN and CMB; in fact, most of them have only found upper limits on the fraction of halo dark mass consisting of massive objects.

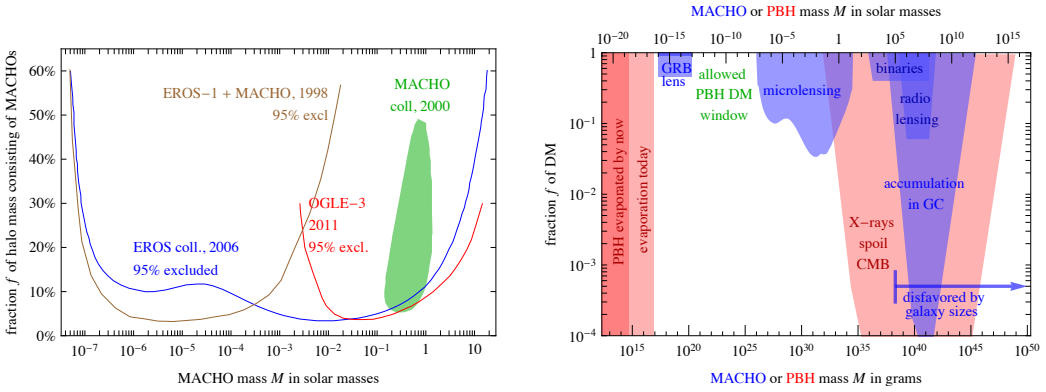

FIGURE 2.4: MACHO searches. Left: Results of microlensing surveys towards the Magellanic Clouds: the bounds on the fraction f of the Milky Way halo's mass which can consist of MACHOs, as a function of the object's mass M, together with the region identified by the MACHO collaboration in 2000. Right: A collection of bounds on the fraction f of DM consisting of massive astrophysical objects. The blue bounds apply to any MACHO, including Primordial Black Holes (PBH). The red bounds only to PBHs. Thanks to A.Strumia.

The detailed bounds are reported in the left panel of Fig.2.4. A selection of further constraints other than those from microlensing are illustrated in the right panel of Fig.2.4

(purple region).
In sum, the various observational and dynamical bounds leave only some small regions open for MACHOs. However, let us recall that DM explanations with MACHOs of any mass which have formed after BBN is forbidden by BBN and CMB. The only way to avoid these constraints is to consider MACHOs that have formed before BBN, since, in this case, their material is subtracted from the baryonic budget before BBN, thus not affecting it. This is the case of primordial black holes (PBHs).
The formation of PBHs is not predicted by standard cosmology. The expected mass of a PBH is generically $M \approx 10^{15}(t/10^{-23}sec)g \simeq 5 \cdot 10^{-19}(t/10^{-23}sec)M_{\odot}$, where t is the time of formation of the PBH. A very large range of masses is possible: for $t \sim 10^{-43}sec$, we get $M \sim M_{\rm Pl} \sim 10^{-5}\,$g, while if they were generated just before BBN $t \approx 1sec$, they could have a mass of $M \approx 10^{5}M_{\odot}$, of the order of supermassive BHs.
Because of their nature, PBHs are subject to several additional constrains compared to traditional MACHOs (see the red region in Fig.2.4). These additional limits are caused by two main reasons. The first one is that PHBs should be big enough not to be evaporated (or be about to evaporate). Black holes, due to quantum fluctuations, emit the "'Hawking Radiation"', a black body radiation of $T_{BH} = (8\pi G_N m_{\rm DM})^{-1}$, for a total radiated power of $W = (15360\pi G_N^2 m_{\rm DM}^2)^{-1}$, thus losing energy, i.e. mass, at this rate. Consequently, BHs have a lifetime of $\tau_{BH} = 5120\pi G_N^2 m_{\rm DM}^3$. If we want this lifetime to be longer than the age of the Universe, we get $M \gtrsim 10^{-19}M_{\odot}$ (a detailed computation not neglecting accretion gives indeed $M > 2.5{\cdot}10^{-19}M_{\odot}$). PBHs that would be currently evaporating are also excluded, as they would emit unobserved Hawking Radiation of $T \sim 80\,$MeV. This further increases the minimum-allowed PHB mass to $M \gtrsim 2 \cdot 10^{-17}M_{\odot}$. The second reason is that PHBs, like any other BHs, accrete material, emitting X-rays. This rules out PHBs with masses in the range $10^{-1} - 10^{15}M_{\odot}$, as X-rays emitted from these PHBs would ionize matter, spoiling CMB. To recap, by superimposing PBHs limits on the MACHOs limits (which apply to PBHs as well), as one can see from the right panel of Fig.2.4 , PBHs with mass

$$10^{-13}M_{\odot} \lesssim m_{\rm DM} \lesssim 10^{-7}M_{\odot} \tag{2.20}$$

are viable DM candidates.

2.2 Experimental Search for WIMP

We now go back on the candidate that we consider in this work, the WIMP. There are three different kinds of DM searches, that use different assumptions and approaches to

detect DM. They can be summarized in the picture below:

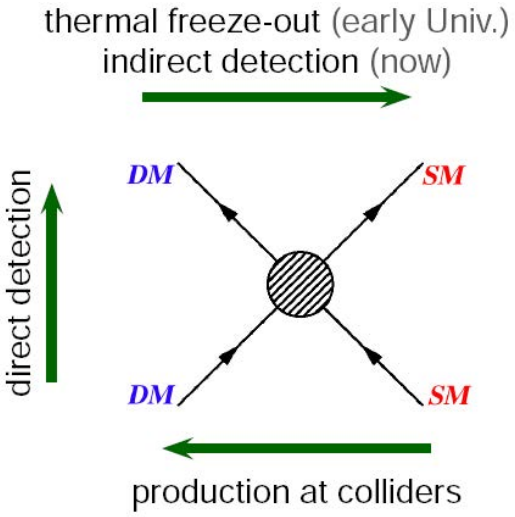

FIGURE 2.5: Principal kinds of DM searches.

Direct Detection is a kind of search that looks for interactions of DM with known matter, which is atomic nuclei. To do this, huge detectors are built and they look for tiny amounts of energy $\mathcal{O}(\text{KeV})$ that could be deposited in the detector in case a particle of DM interacts with one of the atomic nuclei of the detector.
Instead Indirect Detection searches for dark matter by trying to detect its annihilation products. Any annihilation product that is not stable would decay to a stable particle in far less time than to travel to us. So, the particles with which we measure the fluxes to investigate DM are only (anti)protons, electrons, positrons, neutrinos, gamma rays, and a few others. For more detailed information about Direct and Indirect Searches, you can check [128] on which the two following subsections are based.
Finally, DM could be produced in pairs at Collider, by collisions of SM particles. For this to be possible, the Collider has to operate at energies higher than twice the dark matter mass. In the case of LHC, this fact limits the searches at $\mathcal{O}(\text{TeV})$.

2.2.1 Direct Search

The original idea of Drukier and Stodolsky [129] to try to detect neutrinos by exploiting their elastic scattering was the starting point for direct searches, as this detection method could be applied to elastic scattering of WIMP on nuclei as well (Goodman and Witten [130]). Further studies tried to determine detectable DM candidates, DM halo model in the galaxy, detector details and possible DM signatures, one of the latter being annual modulation: the earth motion around the sun produces a modulation of the signal. Since then, there were many improvements, both theoretically and experimentally. On the theoretical side, the main efforts were about refining the calculation

of all the data entering the prediction of event rates. On the experimental side, the main improvements were about noise reduction, increasing detector size and precision in reconstructing events. Thanks to these efforts, noise levels below 1 event per kg and year have now been reached. In this section [131], I will briefly review predictions for signal event rates and signatures, considering specific input and constraints from particle physics and from astrophysical and cosmological measurements.

2.2.1.1 Prediction of event rates

The differential rate for WIMP elastic scattering off nuclei can be expressed as:

$$\frac{dR}{dE_R} = N_N \frac{\rho_0}{m_{\rm DM}} \int_{v_{\rm min}}^{v_{\rm max}} d\mathbf{v}\, f(\mathbf{v})\, v\, \frac{d\sigma}{dE_R}\,, \tag{2.21}$$

where N_N is the number of the target nuclei, $m_{\rm DM}$ is the WIMP mass, ρ_0 is the local WIMP density in the galactic halo, $\mathbf{v}$ and $f(\mathbf{v})$ are the WIMP velocity and velocity distribution function in the Earth frame and $d\sigma/dE_R$ is the WIMP-nucleus differential cross section. The energy that is transferred to the recoiling nucleus is:

$$E_R = \frac{p^2}{2m_N} = \frac{\mu_N^2 v^2}{m_N}(1-\cos\theta), \tag{2.22}$$

where p is the momentum transfer, θ is the scattering angle in the WIMP-nucleus center-of-mass frame, m_N is the nuclear mass and μ_N is the WIMP-nucleus reduced mass:

$$\mu_N = \frac{m_N \cdot m_{\rm DM}}{m_N + m_{\rm DM}}. \tag{2.23}$$

The lower bound in the integral over the velocity distribution is:

$$v_{\rm min} = \sqrt{\frac{m_N E_{th}}{2\mu_N^2}}\,, \tag{2.24}$$

where E_{th} is the energy threshold of the detector (the minimum deposited energy that the detector can efficiently detect), while the upper bound in the integration $v_{\rm max}$ is the escape WIMP velocity in the Earth reference frame. The simplest velocity distribution we can consider for the DM is a Maxwell-Boltzmann distribution in the galactic rest frame. In this case, the Maxwellian velocity dispersion can be obtained from experimental data and has a value $\sigma_v \approx 270\,{\rm km\,s^{-1}}$. The escape velocity from the galaxy is $\mathrm{v}_{esc} \approx 544\,{\rm km\,s^{-1}}$. These parameters will be discussed in more detail in section 2.2.1.3.

To provide an idea of the typical value of the event rate, I provide a numerical example. I assume $m_{\rm DM} = m_N = 100\,{\rm GeV}$, and that $\langle v\rangle = 220\,{\rm km\,s^{-1}} = 0.75\cdot 10^{-3}{\rm c}$. The mean recoiling energy is:

$$\langle E_R\rangle = \frac{1}{2} m_{\rm DM}\langle v\rangle^2 \sim 30\ {\rm keV}. \tag{2.25}$$

Assuming a local dark matter density of $\rho_0 = 0.3\,{\rm GeV\,cm^{-3}}$, the number density of WIMPs is $n_0 = \rho_0/{\rm m}_W$, and their flux on Earth:

$$\phi_0 = n_0 \times \langle v\rangle = \frac{\rho_0}{m_{\rm DM}} \times \langle v\rangle = 6.6\times 10^4\ {\rm cm^{-2}s^{-1}}. \tag{2.26}$$

An electroweak-scale interaction will have an elastic scattering cross section from the nucleus of the order of σ_{WN} $\sim$$10^{-38}{\rm cm}^2$, leading to a rate for elastic scattering:

$$R \sim N_N \times \phi_0 \times \sigma_{WN} = \frac{N_A}{A\cdot kg} \times \frac{\rho_0}{m_{\rm DM}} \times \langle v\rangle \times \sigma_{WN} \sim 0.13\,{\rm events\ kg^{-1}year^{-1}}, \tag{2.27}$$

where N_N is the number of target nuclei, N_A is the Avogadro number and A is the atomic mass number of the target nucleus. It can also be expressed as:

$$R \sim 0.13\ \frac{\rm events}{\rm kg\ year}\left[\frac{A}{100}\times\frac{\sigma_{WN}}{10^{-38}\,{\rm cm^2}}\times\frac{\langle v\rangle}{220\,{\rm km\,s^{-1}}}\times\frac{\rho_0}{0.3\,{\rm GeVcm^{-3}}}\right]. \tag{2.28}$$

2.2.1.2 Input from particle and nuclear physics

The WIMP-nucleus speed is equal to the earth speed relative to the galactic center, which is of the order of $220\,{\rm km\,s^{-1}}$, and the average momentum transfer is:

$$\langle p\rangle \simeq \mu_N\langle v\rangle \tag{2.29}$$

which is in the range between $\sim 6\,{\rm MeV} - 70\,{\rm MeV}$ for values of $m_{\rm DM}$ in the range $10\,{\rm GeV} - 1\,{\rm TeV}$. Hence, the elastic scattering occurs in the extreme non-relativistic regime and therefore the scattering will be isotropic in the center of mass frame. The de Broglie wavelength corresponding to a momentum transfer of $p = 10\,{\rm MeV}$ is:

$$\lambda = \frac{h}{p} \simeq 20\,{\rm fm} > 1.25\,{\rm fm}\ A^{1/3} \tag{2.30}$$

which is larger than the diameter of most nuclei, apart from the heaviest ones. This implies that the scattering amplitudes on individual nucleons will then sum up coherently, and decoherence effects will be important only for heavy nuclei and/or WIMPs.

The differential WIMP-nucleus cross section can be expressed as the sum of the spin-independent (SI) and spin-dependent (SD) terms (if DM is a scalar the SD term will be zero):

$$\frac{d\sigma_{WN}}{dE_R} = \frac{m_N}{2\mu_N^2 v^2}\left[\sigma_{SI}F_{SI}^2(E_R) + \sigma_{SD}F_{SD}^2(E_R)\right], \tag{2.31}$$

where σ_{SI} and σ_{SD} are the cross sections in the zero momentum transfer limits, F_{SI} and F_{SD} are the nuclear form factors, that depend on the recoil energy and

$$\sigma_{SI} = \frac{4\mu_N^2}{\pi}\left[Zf_p + (A-Z)f_n\right]^2, \tag{2.32}$$

$$\sigma_{SD} = \frac{16\mu_N^2}{\pi}\frac{J+1}{J}\left[a_p\langle S_p\rangle + a_n\langle S_n\rangle\right]^2 \tag{2.33}$$

with f_p, f_n and a_p, a_n being the effective WIMP-couplings to neutrons and protons in the spin-independent and spin-dependent case, respectively. These parameters depend on the details of DM nature and interactions with SM particles, and are not known *a priori*.What is usually done is to express them in terms of the WIMP-proton cross section σ_p and express the experimental limits as a function of σ_p and m_{DM}. $\langle S_p, S_n\rangle = \langle N|S_{p,n}|N\rangle$ are the expectation values of total proton and neutron spin operators in the limit of zero momentum transfer, and they have be determined by using detailed nuclear model calculations. One example is the "'odd group"' nuclear model described in [132]. The equation 2.32 reduces to

$$\sigma_{SI} = \frac{\mu_N^2}{\mu_p^2}A^2\sigma_p \tag{2.34}$$

in the case of isospin-conserving interactions ($f_p = f_n$). Here μ_p indicates the WIMP-proton reduced mass. The equation 2.33 instead can be simplified to

$$\sigma_{SD} = \frac{4}{3}\frac{\mu_N^2}{\mu_p^2}\frac{J+1}{J}\langle S_{p,n}\rangle\sigma_{n,p} = \frac{4}{3}\frac{\mu_N^2}{\mu_p^2}\frac{J+1}{J}\langle S_{p,n}\rangle\sigma_p \tag{2.35}$$

by using the nuclear "'odd group"' model and isospin conservation in the second equality. In the nuclear odd group model only one of $\langle S_p\rangle, \langle S_n\rangle$ are non-zero, this is why the formula 2.35 contains only one of them. The nuclear form factor is taken as the Fourier transform of the nucleon density and can be expressed as a function of momentum transfer p [133]:

$$F_{SI}^2(p) = \left(\frac{3j_1(pR_1)}{pR_1}\right)^2 \exp(-p^2s^2), \tag{2.36}$$

where j_1 is a spherical Bessel function, $s \simeq 1$ fm takes into account nuclear skin thickness and $R_1 = \sqrt{R^2 - 5s^2}$ with $R \simeq 1.25A^{1/3}$ fm. Note that the nuclear form factor is normalized as $F(0) = 1$. In the spin-dependent case, the form factor is defined as:

$$F_{SD}^2(p) = \frac{S(p)}{S(0)}, \tag{2.37}$$

where the spin-structure functions $S(p)$ are commonly decomposed into isoscalar $a_0 = a_p + a_n$ and isovector $a_1 = a_p - a_n$ couplings:

$$S(p) = a_0^2 S_{00}(p) + a_0 a_1 S_{01}(p) + a_1^2 S_{11}(p), \tag{2.38}$$

obtaining the pure isoscalar term S_{00}, the pure isovector term S_{11} and the interference term S_{01}. Once again the expectation values $\langle S_p, S_n \rangle$ of the structure functions $S(p)$ are based on the nuclear [134–141]. Ref. [141] uses, for the first time, chiral effective field theory (EFT) currents [142, 143] to calculate WIMP-nucleon couplings. It's easy to notice that, while the spin-independent cross section increases with the nucleon mass number (scaling as $\propto A^2$ until decoherence effects coming from the nuclear form factor start to play a significant role), the spin-dependent cross section does not, so we expect then it to be generally smaller, and only relevant for nuclei with odd mass number A.

2.2.1.3 Input from astrophysics

The astrophysical parameters that are needed to calculate the expected events rate are the earth rotation speed around the galactic center, the escape speed from the galaxy at the position of the earth, the WIMP velocity distribution $f(\mathbf{v})$ and the local dark matter density ρ_0. Of these, only the latter two may induce a considerable uncertainty in the predicted event rates and alter the inferred scattering cross section and WIMP mass.[2] In the so-called standard halo model (SHM), which describes an isotropic, isothermal sphere of collisionless particles with density profile $\rho(r) \propto r^{-2}$, the velocity distribution is Maxwellian:

$$f(\mathbf{v}) = \frac{1}{\sqrt{2\pi}\sigma_v} \exp\left(-\frac{\mathbf{v}^2}{2\sigma_v^2}\right), \tag{2.39}$$

where the velocity dispersion is related to the local circular speed v_c as $\sigma_v = \sqrt{3/2} v_c$. Since the velocity distribution extends to infinity in the SHM, it has to be truncated at the measured local escape velocity v_{esc}, such that $f(\mathbf{v}) = 0$ for $v \geq v_{esc}$. Dark matter particles with speeds larger than $v_{esc}(r) = \sqrt{|\phi(r)|}$, where $|\phi(r)|$ is the gravitational potential, will not be gravitationally bound to the galaxy. The parameters used in the SHM are $\rho_0 = 0.3\,\mathrm{GeV\,cm^{-3}} = 5 \cdot 10^{-25}\,\mathrm{g\,cm^{-3}} = 8 \cdot 10^{-3} M_\odot\,\mathrm{pc^{-1}}$, $v_c = 220\,\mathrm{km\,s^{-1}}$ and a local escape speed of $v_{esc} = 544\,\mathrm{km\,s^{-1}}$. The underlying assumption is that the space and velocity distribution of the dark matter have reached a stable state and are smooth. Both these hypothesis are confirmed by high-resolution DM simulations of the Milky Way halo, but only down to kpc-scales, while Direct Detection probes sub-milliparsec scales.

[2] For a more complete analysis of the relevant astrophysical parameters, see [144].

2.2.1.4 Predicted signatures

To better discriminate the DM detection from background noise, it is desiderable to identify the features of the DM signal. One ingredient is the shape of the recoiling energy spectrum, that, as detailed in the previous subsections, depends both on m_N and $m_{\rm DM}$: for $m_{\rm DM} \ll m_N$, $E_R \propto m_{\rm DM}^2$ and for $m_{\rm DM} \gg m_N$, the recoil energy spectrum is independent of the WIMP mass. This means that the WIMP mass can be determined most accurately when $m_{\rm DM} \sim m_N$, and that having multiple experiments with different targets m_N can help provide better constraints on m_W [145].

Two other ingredients that add characteristic features to DD signals come from the Earth's motion through the galaxy. This motion induces both a seasonal modulation of the total event rate [146, 147] and a forward-backward asymmetry of the signal [148, 149]. The differential rate in the SHM can be written in a first approximation as:

$$\frac{dR}{dE_R}(E_R, t) \simeq \frac{dR}{dE_R}(E_R)\left[1 + \Delta(E_R)\cos\frac{2\pi\,(t - t_0)}{T}\right] \tag{2.40}$$

where $\mathrm{T} = 1\,\mathrm{year}$ and the phase is $t_0 = 150\,\mathrm{d}$. ΔE is negative at small recoil energies and positive for large recoil energies, meaning that the differential event rates peak in winter for small recoil energies, and in summer for larger recoils energies [150]. The energy E_{cr} at which $\Delta(E_{cr})$ is also referred to as the crossing energy. This fact can be used, in principle, to determine the mass of the WIMP [151] (as the value of $\Delta(E_{cr})$ depends both on m_N and $m_{\rm DM}$), requiring, however, very low values for E_{th}.

A stronger signature would be given by the ability to detect the axis and direction of the recoil nucleus thanks to the forward-backward asymmetry.

2.2.1.5 Backgrounds

The minimization and identification of the background noise is one of the main challenges for direct DM search experiments. The main background sources include environmental radioactivity and cosmic rays and their secondaries, among many others. [3]. Ultimately, DD searches sensitivity may reach the neutrino floor (see fig Fig. 2.6) [153].

[3] For an excellent review, refer to [152].

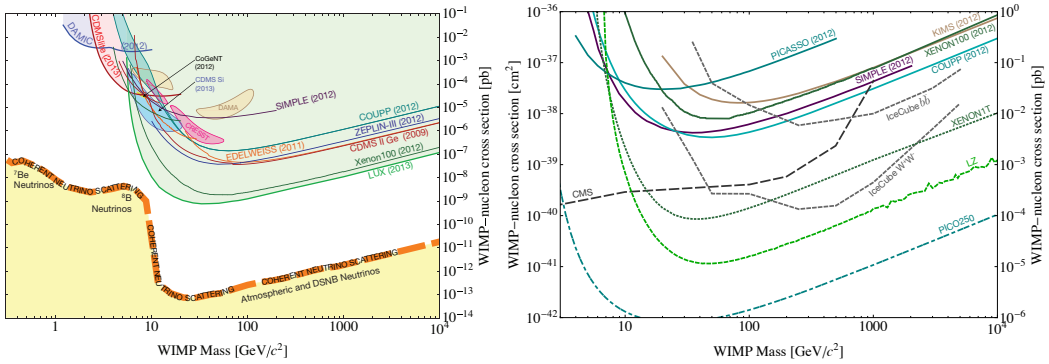

FIGURE 2.6: Left: WIMP discovery limit (thick dashed orange) compared with current limits and regions of interest. The dominant neutrino components for different WIMP mass regions are labeled. Progress beyond this line would require a combination of better knowledge of the neutrino background, annual modulation, and/or directional detection. We show 90% confidence exclusion limits from DAMIC [154] (light blue), SIMPLE [155] (purple), COUPP [156] (teal), ZEPLIN-III [157] (blue), EDELWEISS standard [158] and low-threshold [159] (orange), CDMS II Ge standard [160], low-threshold [161] and CDMSlite [162] (red), XENON10 S2-only [163] and XENON100 [164] (dark green) and LUX [79] (light green). The filled regions identify possible signal regions associated with data from CDMS-II Si [78] (light blue, 90% C.L.), CoGeNT [165] (yellow, 90% C.L.), DAMA/LIBRA [74] (tan, 99.7% C.L.), and CRESST [77] (pink, 95.45% C.L.) experiments. The light green shaded region is the parameter space excluded by the LUX Collaboration. Taken from [153]. Right: A compilation of WIMP-nucleon spin-dependent cross section limits (solid curves) and projections (dot and dot-dashed curves) for US-led direct detection experiments that are expected to operate over the next decade. Taken from [166].

2.2.2 Indirect Search

The indirect searches for DM are based on identifying excesses in fluxes of cosmic rays with respect to their presumed astrophysical backgrounds. Stable Standard Model particles may be the end product of the annihilation, or decay, of DM in the galactic halo or in the Sun. In this case, such particles would then propagate in the galaxy and reach us. Promising sources are usually the most dense regions, such as the galactic center, the inner halo of our galaxy, the center of the Sun. However in some of these regions it is usually very complicated to understand the underlying astrophysics, to correctly estimate the astrophysical background. So it may happen that the best detection opportunities, i.e. the regions with the best signal to background ratio, don't come necessarily from the most dense regions. The SM particles giving the best information are photons, neutrinos and stable antiparticles: positrons and anti-protons (also, maybe, anti-deuteron). Antiparticles usually deliver good information because there is very little antimatter in the universe and astrophysical processes should produce very tiny amounts of it.

- **Photons.** They freely propagate in the galaxy, and they deliver information in the energy and angular distributions. However the DM is electrically neutral, so

its annihilation or decay to photons should be subdominant (either by loops or secondary radiation). the astrophysical background is also difficult to estimate.

- **Positrons.** Positrons diffuse in the galaxy losing energy due to: syncroton emission, Coulumb scattering, ionization, bremsstrahlung and inverse Compton scattering. The contribution is dominated by the nearby regions of the galaxy, and they deliver informations only witht the energy spectrum. Below a few GeV, solar activity effect is important.

- **Anti-protons.** Energy losses for Antiprotons are much smaller than for positrons, the only important process being scattering on matter. Therefore even regions of the galaxy that are very far away can contribute to their flux at the Earth, and this increases its astrophysical uncertainties due to the DM halo profile. Like positrons, only the energy spectrum delivers information and below few GeV solar activity effects are important.

- **Neutrinos.** High-energy $\mathcal{O}(\,\mathrm{TeV})$ neutrinos can freely propagate in the galaxy, and also through dense matter of stars and planets. Neutrinos detection is difficult, their fluxes can be measured indirectly via the detection of charged particles (e.g. muons) produced by a neutrino interaction in the surroundings (water, rocks, etc) of the detector. The detector can partially reconstruct the original energy of the incoming neutrino. Same sources are photons, plus the center of Sun and Earth itself.

The scope of this section is to schematically present the *status* of the field of indirect DM detection [167].

DM Indirect Detection (ID) is one of the possible ways to detect DM in the scenarios where DM is a thermal relic, that has a weak scale annihilation cross section to SM particles. In this class of models falls the WIMP and all "'dark forces"' models. In some other cases, instead, DM detection using ID would be very disfavored or impossible. Such cases include assuming a different cosmological history [168], or considering particles that interact so weakly that would have never reached thermal equilibrium [169, 170].Finally, another suggestion is that of asymmetric DM [101]. In this case, as we have already stated in 2.1.2.3 annihilations of DM particles are not possible for lack of target antipartices (even if there were some theoretical models with DM anti-DM oscillations that would fix this problem [171, 172]).

2.2.2.1 Charged cosmic rays

It has been known for a couple of decades that there is an excess of positrons in charged cosmic rays, at the TeV and sub-TeV scale:

- Data from the PAMELA satellite [173] has shown a steep rise of the positron fraction $e^+/(e^+ + e^-)$ above 10 GeV up to 100 GeV (further extended up to 300 GeV [174]), compatible with hints from HEAT [175] and AMS-01 [176].
- These results have been confirmed independently by the FERMI satellite [177] for energies up to 200 GeV.
- The $\bar{p}/p$ energy spectrum from PAMELA [178–180] has instead shown no excess compared with the predicted background for energies up to 350 GeV.
- Results from the FERMI satellite [181] have confirmed the presence of an excess with respect to the expected background for positrons, but also showed that the $e^+ + e^-$ spectrum is following a simple power law.
- The HESS telescope confirmed the results for the $e^+ + e^-$ energy spectrum seen by FERMI for energies above 600 GeV [182]. This spectrum follows a simple power law and eventually becomes steeper at energies of a few TeV.
- The AMS-02 experiment has confirmed the previous results concerning the positron fraction rise with an even higher precision [183]. In april 2015, it also released preliminary results regarding proton and antiproton fluxes. The $\bar{p}/p$ ratio features an excess for energies above ~ 50 GeV, but it is shown that such excess is within the uncertainty of the astrophysical background [184].

The data are displayed in fig. 2.7, together with the expected astrophysical background in the case pf $\bar{p}/p$. The uncertainties of the latter ones play a significant role, as they are needed to identify whether what looks like an excess is real or not. There have been numerous attempts to explain the positron fraction, the main explanation being a background modification or a new primary source, either astrophysical or DM. Explanations involving background modifications, like [185] are nowadays disfavored, in light of the measure of pure e^- fluxes by PAMELA and FERMI [186, 187].

The positron fraction rise is therefore a very important result because it implies the existence of a source of primary e^+ (and e^-) other than the known astrophysical ones. The new source can be either of astrophysical nature, e.g. one or more pulsar(s), supernova remnants, etc [187], or annihilating (decaying) DM.

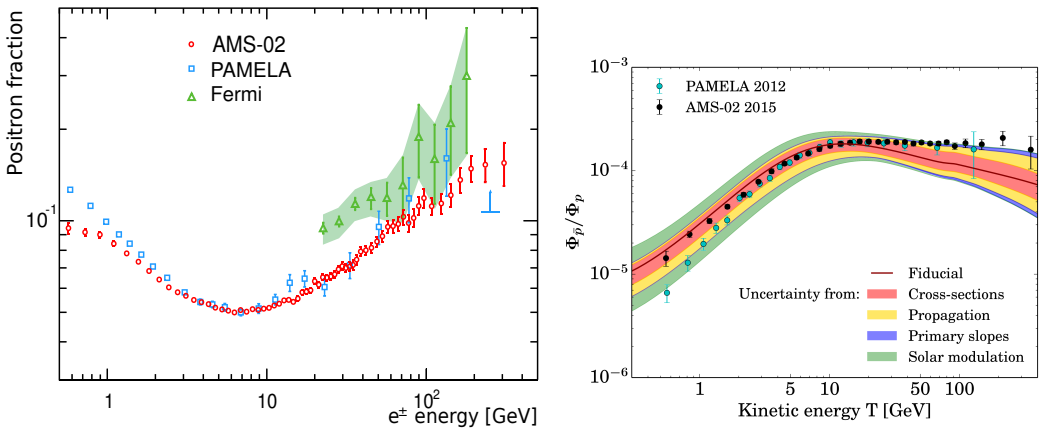

FIGURE 2.7: A compilation of recent and less recent data in charged cosmic rays, superimposed on plausible but uncertain astrophysical backgrounds from secondary production. Left: positron fraction (taken from [183]). Right: $\bar{p}/p$ ratio, with astrophysical background and its uncertainty (taken from [184]).

If DM particles of the DM halo in the Milky Way annihilate into pairs of SM particles (such as $b\bar{b}$, $\mu^+\mu^-$, $\tau^+\tau^-$, W^+W^- and so on), then these annihilation products, after decay, showering and hadronizing would produce fluxes of energetic cosmic rays: $e^-, e^+, \bar{p}$ (and also γ-rays, ν...), denoted dN_f/dE. The exact shape of the resulting spectra depends on the primary particle, the open channels and their Branching Ratios. Generically, however, they feature a bump-like shape, with a high energy cutoff at the DM particle mass and a soft tail at lower energies. In fig. 2.9 you can find some examples of such spectra for the best-fit DM candidate. From the quality of the fits in fig. 2.9 it looks quite normal to try to interpret the positron excess in terms of DM. Charged particles in the galaxy undergo a random walk in the turbulent galactic magnetic fields. An effective description of their propagation is given by the transport equation, that takes into account diffusion, synchrotron radiation energy losses, Inverse Compton Scattering and nuclear spallation and fragmentation. The transport equation for the number density per unit energy $n(\vec{r}, t, p)$ is

$$\begin{aligned}\frac{\partial n(\vec{r},t,p)}{\partial t} = \; & q(\vec{r},t,p) + \vec{\nabla}\cdot\left(D_{xx}\vec{\nabla}n - \vec{V}_c n\right) + \frac{\partial}{\partial p}\left(p^2 D_{pp}\frac{\partial}{\partial p}\left(\frac{n}{p^2}\right)\right) \\ & - \frac{\partial}{\partial p}\left(\dot{p}n - \frac{p}{3}(\vec{\nabla}\cdot\vec{V}_c)n\right) - \frac{1}{\tau_{sp}}n - \frac{1}{\tau_f}n \end{aligned} \tag{2.41}$$

where $D_{xx}(D_{pp})$ is the diffusion coefficient in position (momentum) space, and it is usually taken to be a power-law

$$D_{xx} = K_0 p^\alpha \tag{2.42}$$

Notable choices are $\alpha = 1/3$ (Kolmogorov) or $\alpha = 1/2$ (Kraichnan). $\vec{V}_c$ is the convection velocity and it is usually taken to be along the z axis $\vec{V}_c = sign(z)V_c\hat{z}$, τ_{sp} is the mean

time for nuclear spallation process to occur, and τ_f is the mean time for nuclear fragmentation process to occur. The coefficient D_{pp} determines the diffusive reacceleration and it is proportional to D_{xx}^{-1}. The $\dot{p}$ term encodes energy losses, and $q(\vec{r}, t, p)$ is the source term. In case of DM annihilations, its value is

$$q(\vec{r}, t, p) = \frac{1}{2}\left(\frac{\rho_{DM}(\vec{r}, t)}{m_{\rm DM}}\right)^2 \sum_f \langle \sigma_A v \rangle_f(p) \frac{dN_f}{dE}(p) \tag{2.43}$$

After solving the transport equation, the corresponding fluxes can be calculated as

$$\Phi = \beta \frac{n}{4\pi} \tag{2.44}$$

where β is the particle speed in units of the speed of light. $\rho(\vec{x})$ is the DM density profile in the galactic halo. The choice of the latter is one of the main open problems in ID. In eq. (2.45), you can find a list of the most common DM halo profiles used. A plot of them and a table of the values of their parameters can be found in fig. 2.8. These profiles are coming from theoretical models, numerical simulations or direct observations. As can be seen in fig. 2.8, all profiles are normalized at the same value at the location of the earth (≈ 0.3 GeV/cm^3) and only significantly differ in the core of the galaxy. Navarro-Frenk-White (NFW) and Einasto exibit a cusp in the center, while isothermal and Burkert feature a central core (we talked briefly about the CUSP problem in 2.1.2.2). As all the profiles have similar values in the outer region $r \gtrsim 5\,$kpc, observables that depend mostly on the local DM density will not be very affected by the choice of the profile. Other observables that are sensitive to DM density and can propagate efficiently through all the galaxy are, instead, affected the most (e.g. gamma rays observations of regions close to the GC).

$$\begin{aligned}
\text{NFW}: \quad \rho_{\rm NFW}(r) &= \rho_s \frac{r_s}{r}\left(1+\frac{r}{r_s}\right)^{-2} \\
\text{Einasto}: \quad \rho_{\rm Ein}(r) &= \rho_s \exp\left\{-\frac{2}{\delta}\left[\left(\frac{r}{r_s}\right)^{\delta} - 1\right]\right\} \\
\text{Isothermal}: \quad \rho_{\rm Iso}(r) &= \frac{\rho_s}{1+(r/r_s)^2} \\
\text{Burkert}: \quad \rho_{\rm Bur}(r) &= \frac{\rho_s}{(1+r/r_s)(1+(r/r_s)^2)} \\
\text{Moore}: \quad \rho_{\rm Moo}(r) &= \rho_s \left(\frac{r_s}{r}\right)^{1.16}\left(1+\frac{r}{r_s}\right)^{-1.84}
\end{aligned} \tag{2.45}$$

Eq. (2.41) is usually solved numerically in a cylindrical space that sandwiches the galactic plane, with height $2L$ and radius $R = 20\,$kpc. The location of the solar system corresponds to $\vec{x}_\odot = (r_\odot, z_\odot) = (8.33\,\text{kpc}, 0)$. Boundary conditions force n_f to vanish

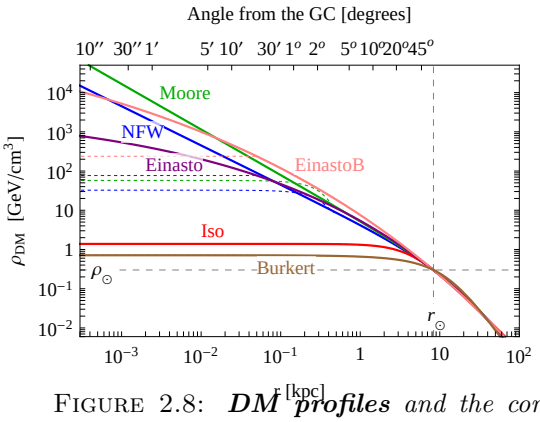

DM halo	δ	r_s [kpc]	ρ_s [GeV/cm^3]
NFW	–	24.42	0.184
Einasto	0.17	28.44	0.033
EinastoB	0.11	35.24	0.021
Isothermal	–	4.38	1.387
Burkert	–	12.67	0.712
Moore	–	30.28	0.105

FIGURE 2.8: ***DM profiles*** *and the corresponding parameters to be plugged in the functional forms of eq. (2.45). Taken from [188].*

on the surface of the cylinder, outside of which the charged cosmic rays freely propagate and escape. Estimates of the values of the propagation parameters α, K_0, V_c and L are obtained from a variety of (ordinary) cosmic ray models and data, such as the B/C ratio.

We can use Eq. (2.41) to get an idea of the behavior of the background. For heavy charged cosmic rays (protons, C), whose source is a power-law injection spectrum $q \propto p^{-\beta_{inj}}$. We can neglect everything except the diffusion, so

$$\Phi_{prim} \propto p^{-\beta_{obs,prim}}, \beta_{obs,prim} = \alpha + \beta_{inj} \tag{2.46}$$

We can iterate the procedure to calculate the secondaries spectrum (antiprotons, B)

$$\Phi_{sec} \propto p^{-\beta_{obs,sec}}, \beta_{obs,sec} = \alpha + \beta_{obs,prim} \tag{2.47}$$

the fit of the B/C ratio provides a measure for α and other diffusion model parameters, and gives excellent predictions for $\bar{p}$ in agreement with data.

The case of electrons/positrons is more complex. Being much lighter than protons, their energy losses cannot be neglected. For primaries, we get:

$$\Phi_{e^-} \propto p^{-\beta_{obs,e^-}}, \beta_{obs,e^-} = \begin{cases} \alpha + \beta_{inj,e} & (diffusion) \\ 1 + \beta_{inj,e} & (energy losses) \end{cases} \tag{2.48}$$

so the spectrum power law will have a break somewhere. Secondary positrons are generated in spallation of protons on hydrogen, so we get

$$\Phi_{e^+} \propto p^{-\beta_{obs,e^+}}, \beta_{obs,e^+} = \begin{cases} \alpha + \beta_{inj,p} & (diffusion) \\ 1 + \beta_{inj,p} & (energy losses) \end{cases} \tag{2.49}$$

and the ratio of the two fluxes is approximately

$$\frac{\Phi_{e^+}}{\Phi_{e^-}} \propto p^{-(\beta_{ijn,p}-\beta inj,e^-)-\alpha} \tag{2.50}$$

decreases with energy. The datasets listed at the beginning of this section determine the properties of the DM particle needed to interpret them in terms of annihilations:

- ▷ $m_{\rm DM} \sim \mathcal{O}(\,\text{TeV})$, in order to reproduce the feature in the $e^+ + e^-$ spectrum.
- ▷ Dm should be *Leptophilic*, i.e. annihilating nearly exclusively into leptonic channels, otherwise the $\bar{p}/p$ spectrum would feature a strong excess similar to the positrons.
- ▷ $\langle\sigma v\rangle \gtrsim 10^{-23}\,\text{cm}^3/\,\text{s} \gg \langle\sigma v\rangle_{th}$ DM should have an annihilation cross section much larger than the thermal one, in order to reproduce the bump observed in the positron fraction and the $e^+ + e^-$ flux.

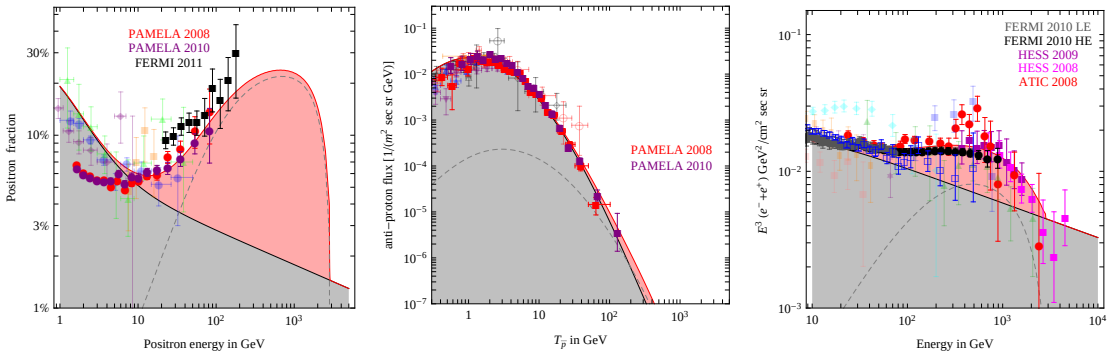

FIGURE 2.9: Charged cosmic ray data interpreted in terms of Dark Matter annihilations: the flux from the best fit DM candidate (a 3 TeV DM particle annihilating into $\tau^+\tau^-$ with a cross section of $2 \cdot 10^{-22}\,\text{cm}^3/\text{sec}$) is the lower dashed line and is summed to the supposed background, giving the pink flux which fits the data. Left: positron fraction. Center: antiproton flux. Right: $e^+ + e^-$ flux. Taken from [167].

Fig. 2.10 illustrates these features. On the left, one can see that a DM of $m_{\rm DM} \sim 3\,\text{TeV}$ annihilating to $\tau^+\tau^-$ has the best χ^2; other leptonic channels (e.g. $\mu^+\mu^-$) still give good fits, while all other annihilations channels (quarks, vector bosons and Higgs) are significantly disfavored. The required annihilation cross section as a function of the DM mass is shown in fig. 2.10 (right) in units of the thermal one. For the best fit, the value of the cross section is $2 \cdot 10^{-22}\ \text{cm}^3/\,\text{s}$, about 6000 times the thermal one.
In fig. 2.10 (center), one can see a small antiproton flux originated by the DM candidate annihilations to $\tau^+\tau^-$. This flux is originated by electroweak corrections [191]: the τ can radiate an EW gauge boson, which then decays into other SM particles, including antiprotons. EW corrections are particularly important for large DM mass. They tend to

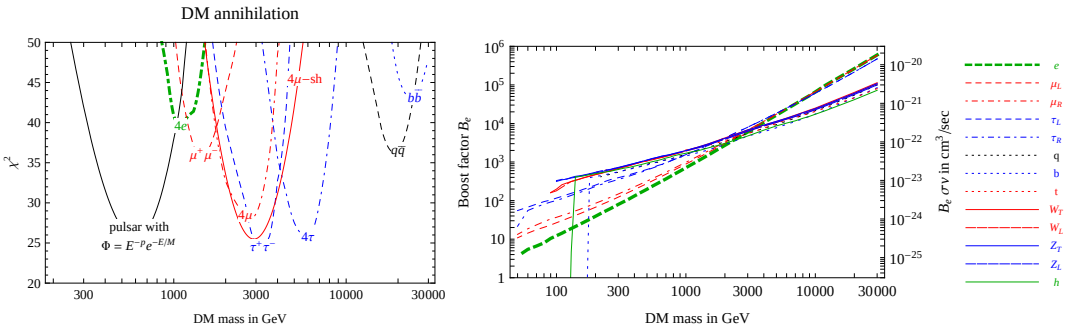

FIGURE 2.10: Left: Global fit of different DM annihilation channels to the PAMELA, FERMI and HESS data. The labels on each curve indicate the primary annihilation channel (figure from [189] (2009); the fit results remain essentially valid even through the subsequent data updates; the four-lepton lines refer to exotic channels. Right: Values of $B_e \cdot \sigma v$ (right axis) and of the boost factor B_e (left axis, for $\sigma v = 3\ 10^{-26}\text{cm}^3/\text{sec}$) needed to fit the data (figure from [190]). Taken from [167].

alter the spectrum by softening it and by enhancing it in the low energy region [192], and in the cases where their addition opens up s-wave annihilation, they can also significantly increase the total cross section [193].

Finally, it is worth noting that there are only 2 possible options for the positron fraction rise: to be caused by DM or not. In the latter case, it would constitute a huge background that would make it probably impossible to detect any possible additional DM signal on the top of it. With this in mind, the antiproton channel looks like the best one to look at to constrain (or detect) a DM signal [194].

2.2.2.2 Photons

For energies above $\mathcal{O}(\,\text{GeV})$, the current main experiments are the FERMI satellite [195–203] which has an excellent sensitivity to gamma rays spanning a range of energies from 30 MeV to 300 GeV; the HESS telescope [204–212] with a sensitivity mainly between 10 GeV and 10 TeV, and the ground-based Imaging Atmospheric Čerenkov Telescopes (IACT).

Without going into the details of each single analysis, the overall common conclusions of almost all the studies cited above is: no anomalous signals are detected, therefore upper bounds on DM annihilation cross section can be derived. Fig. 2.11 shows results from FERMI and the effect of different choices of the DM halo profile on them.

2.2.2.3 Neutrinos

Neutrinos can be produced in DM annihilations as well. Like γ-rays, they propagate straight through the galaxy, but, while, on one hand, they also have the advantage that

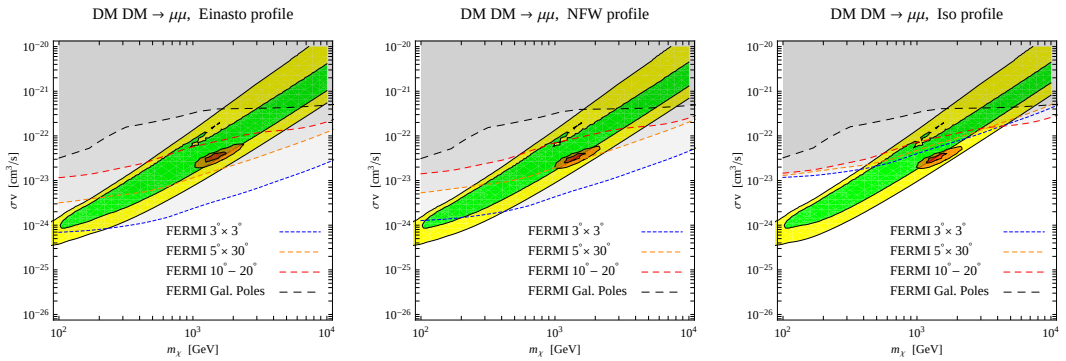

FIGURE 2.11: Illustration of a typical dependence of GH γ-ray bounds on the choice of DM profile. Having fixed the particle physics model, we change the DM profile of the MW from Einasto (left) to NFW (center) to Isothermal (right). For the most shallow profiles the gamma ray bounds from the inner regions are lifted and the PAMELA+FERMI+HESS fit area (orange) is reallowed. Figure from [213]. Taken from [167].

they can propagate across long lengths of dense matter with little interaction, on the other hand, they also have the disadvantage that their detection is more difficult and has limitations in the choice of targets. Neutrinos are observed at huge Čerenkov detectors located underground. Neutrinos can interact with the material in the surroundings of the detectors, generating charged particles that emit Čerenkov light when traveling across the experiment. From this light it is possible to understand the energy and direction of the charged particles, and from these it is possible to partially reconstruct the original energy and direction of the parent neutrino. The main background for this search are atmospheric muons. To avoid this, experiments select only upgoing tracks.

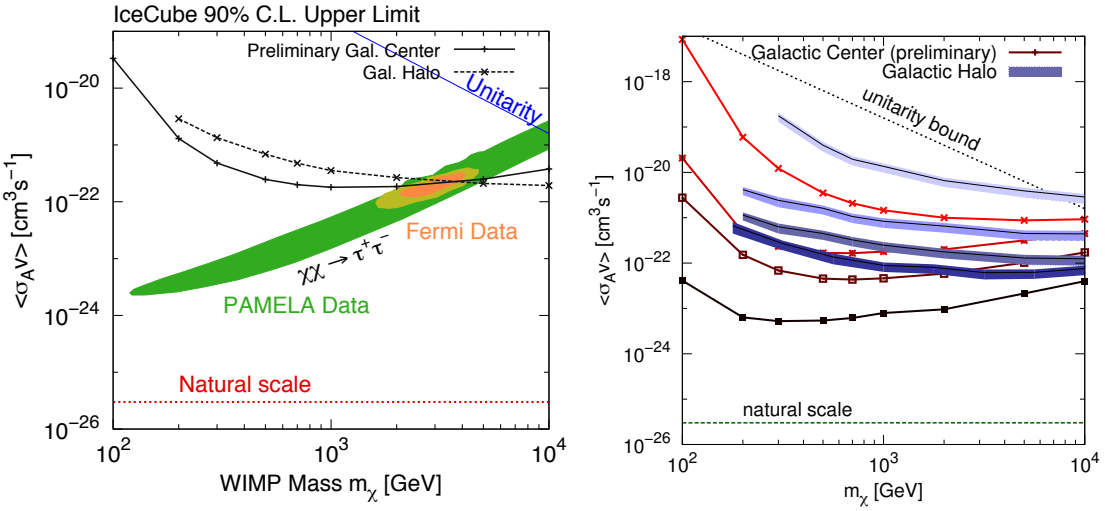

FIGURE 2.12: Left: constraints on the DM annihilation cross section from ICECUBE's observation of the Galactic Halo, comparing with the fit regions of charged CRs (figure from [214] or [215]). Right: a compilation of current constraints from ICECUBE, from the GC and the galactic halo (figure from [214]). Taken from [167].

Experiments look for neutrinos, in analogy with γ-rays, from the GC or the GH and from satellite galaxies or clusters of galaxies (even if, in the latter two, the sensitivities are not comparable with those for γ-rays). Additional targets for neutrino searches are also the center of the Sun and the Earth. Under the same assumptions of DD, i.e. that WIMP can scatter on nuclei of DD detectors, DM should also scatter on astrophysical objects. WIMP may lose energy by scattering on nuclei of stars and become gravitationally bound. Being bound inside the star, it would undergo subsequent scatterings and thermalize [216, 217]. Eventually, DM may annihilate in couples. This should happen in the Sun (and in the Earth) as well! This also happens in the GC, the only difference being the lower capture rates in the Sun, mainly due to lower local DM density. If the total mass of captured WIMPs is not too high, their presence would not affect the physics of the Sun much (though small modifications might be relevant for Solar Helioseismology [218–221]). Some fraction of the energy released in WIMP annihilations can escape as neutrinos, and these could be easily distinguished from solar neutrinos, the former being $\mathcal{O}(\,\mathrm{GeV})$, whereas the latter being $\mathcal{O}(\,\mathrm{MeV})$ [222]. The only background in that portion of solar neutrino spectrum would come from cosmic rays interactions with the corona, and this is expected to be low [223]. The main background would come instead from atmospheric muons and neutrinos, produced by interactions of cosmic rays with the Earth's atmosphere. This background can be substantially reduced by selecting upgoing events [224]. While DD limits have very limited model dependency (essentially the ratio f_p/f_n for SI, and the nuclear model $\langle S_{p,n}\rangle$ for SD), limits from neutrinos in the Sun are much more model-dependent, as expected neutrino yield depends on annihilation branching fractions of the WIMP [225]. Some channels produce more neutrinos than others, and with different spectra. DM annihilating directly to neutrinos would produce two monocromatic neutrinos per annihilation, while, for example, neutralino DM would produce multiple secondary neutrinos, coming from the interactions of primary quarks and gauge bosons with solar matter [226]. Moreover, this kind of search depends more than others on the low scale features of DM velocity distributions [227], such that also perturbations due to planets might be relevant [228]. SuperKamiokande [189, 229], ICECUBE [215] and Amanda, have looked for neutrino signals from th GC, without finding any. Therefore, this imposes limits on the relevant DM properties. Fig. 2.12 collects a sample of them from ICECUBE. Usually, such constraints are sightly less stringent than the ones frm γ-rays. They are, however, less dependent on m_{DM}: the lower DM density (e.g. in the GC) is partly compensated by the higher detection cross section the neutrinos have at higher energies. Therefore, neutrino constraints become somewhat competitive with γ-ray bounds at large DM masses. No signal was found from the center of the Sun as well. As we have already explained, this imposes constraints on σ_p. Bounds were presented by ICECUBE and AMANDA [214, 230, 231], SuperKamiokande [229, 232, 233], ANTARES [234–236] and

by the Baksan experiment [237]. Remarkably, such bounds are competitive with those from the dedicated DD for SD, while for SI, they are several orders of magnitude weaker, except for very low m_{DM} where the sensitivity in the Sun is higher thanks to the fact that the principal target is hydrogen, which is much lighter than usual targets for DD.

2.2.3 Collider Search

If DM is a stable neutral particle, it can only be produced in pairs at colliders. The reach of this kind of search is thus limited by energies accessible by the collider (the energy of the collider must be bigger than $\sqrt{s} > 2m_{\mathrm{DM}}$).

2.2.3.1 Production at colliders

There are two main categories of colliders.

- Electron colliders e^+e^-

In a circular collider beam of radius R, the main energy loss of the beam is due to synchrotron radiation. The power emitted is: $P = \beta\frac{dE}{dx} = (2/3)e^2\beta^4\gamma^4/R^2$, where $\gamma = E/m$. The maximal energy of the beam is therefore

$$\frac{E_{max}}{m_e} \simeq 6\dot{1}0^5\sqrt{\frac{R}{5\,\mathrm{km}}}\left(\frac{dE/dx|_{max}}{m_ec^2/10\,\mathrm{cm}}\right)^{1/4} \tag{2.51}$$

This sets a limit for the maximum energy reachable by an electron in a circular collider of about $E_{max} \sim 300\,\mathrm{GeV}$. The dependence on the collider parameters is rather weak, so in order to increase the energy, one has to build linear colliders, for which the maximal energy is set by the length L.

$$E_{max} \sim L\left.\frac{dE}{dx}\right|_{max} \sim 1\,\mathrm{TeV}\frac{L}{100\,\mathrm{km}}\frac{dE/dx|_{max}}{\mathrm{MeV/\,cm}} \tag{2.52}$$

- Hadron colliders: pp (LHC) or $p\bar{p}$ (Tevatron).

In this case, the synchrotron radiation is negligible and the main problem is generating a magnetic field B strong enough to get a radius R:

$$E_{max} = QRB = 15\,\mathrm{TeV}\frac{Q}{e}\frac{R}{5\,\mathrm{km}}\frac{B}{10T} \tag{2.53}$$

Hadron colliders can reach higher energies, but they have additional problems. Protons are not elementary particles, so the true elementary processes happen at lower energies.

Let the two quarks/gluons that interact at the elementary level have a fraction of the total energy of the two protons $x_1, x_2 \lesssim 0.1$. The energy of the elementary process is then $\hat{s} = s x_1 x_2$. Hadron colliders also imply a large QCD background due to the usual large value of QCD cross sections.

2.2.3.2 Detection at colliders

The end products of the collisions pass through a series of detectors (Tracking chamber, Electromagnetic calorimeter, Hadron calorimeter, Muon chamber) which record their passage. Only stable or long-lived particles are able to reach the detectors.

- **Photons.** Being stable neutral particles, they are not seen by the tracking chamber, and they get absorbed by the Electromagnetic calorimeter, which can measure their energy.
- **Electrons.** As they are stable charged particles with tiny mass, they get identified in the tracking chamber where the direction of their momentum is measured, and in the Electromagnetic calorimeter, where they are absorbed and their energy is measured.
- **Muons.** They are charged like the electron, but they have higher mass, so after the tracking chamber (where the direction of the momentum is measured), they go through the Electromagnetic calorimeter without being absorbed. They then continue in the Hadron calorimeter, where they are checked to distinguish them from spurious events, and in the muon chamber, where their momentum is measured again more precisely.
- Quarks and gluons. They undergo hadronization and showering before reaching the detectors, forming jets. Only $p, n, \pi^{\pm}$ reach it before decaying. Particles in the jet pass through the tracking chamber, where the direction of the momentum of the charged ones is measured, then through the Electrogmagnetic calorimeter, where the electrons that are part of the jet are stopped and their energy is measured, and they finally reach the Hadron calorimeter, where the remaining particles are stopped and their energy is measured.
- Neutrinos. Neutrinos escape all the detectors, without being identified by any of them. Therefore, the look like missing momentum: the sum of the transverse momenta of visible particles in the event is not zero.

2.2.3.3 Kinematic collider variables

A convenient coordinate system for colliders is the cylindrical one, whose $\hat{z}$ axis coincides with the beam line, and the angular variables θ, ϕ map the detector barrel. The rapidity y of a particle with momentum $p^\mu = (E, p_x, p_y, p_z)$ is defined as

$$y = \frac{1}{2} \ln \frac{E + p_z}{E - p_z} \tag{2.54}$$

The effect of a boost along the $\hat{z}$ axis of a speed β is just a shift $\delta y = \operatorname{arctanh}(\beta)$ in the rapidity. The pseudo-rapidity is defined as

$$\eta = -\ln \tan \frac{\theta}{2} \tag{2.55}$$

Th pseudorapidity coincides with the rapidity for massless particles and is a good approximation of rapidity also for massive particles whose energy is much higher than their mass. The transverse momentum is the momentum in the direction orthogonal to the beam

$$\vec{p_{\mathrm{T}}} = \vec{p} \sin\theta = \frac{\vec{p}}{\cosh \eta} \tag{2.56}$$

The missing transverse momentum in an event with visible momenta $\vec{p_{\mathrm{T}}}$ is

$$p_T^{miss} = \not{p}_T = -\sum \vec{p_{\mathrm{T}}} \tag{2.57}$$

and the missing transverse energy (or missing ET or MET) is the magnitude of it: $E_T^{miss} = \not{E}_T = |\not{p}_T|$.

2.2.3.4 DM signatures at Hadron Colliders and LHC

Having in mind what we said about Hadron collider problems in 2.2.3.1, the maximum DM mass that can be searched at LHC is not $\sqrt{s}/2$, but rather $\mathcal{O}(\text{ TeV})$, and to suppress the background, one has to, first of all, to choose the topology of the process he wants to use to search for a DM signal, then one has to select appropriate jet tagging and set reasonable cuts in the jet kinematic variables (p_{T}, η) and angular distributions.
The simplest thing one can think of is to simply produce DM in pairs from the initial colliding protons. However, this would provide just totally invisible events, with only MET in the final state. So, an interesting possibility to consider is the Initial State Radiation of some SM particle, providing a handle over the simple MET signal to look for. The most used topology for DM search is Mono-Jet+$\not{E}_T$. This corresponds to a partonic process

$$q\bar{q} \to \chi\bar{\chi} + g, qg \to \chi\bar{\chi} + q, gg \to \chi\bar{\chi} + g \tag{2.58}$$

Variations of this are the mono-photon+$\not{E}_T$, mono-$W/Z + \not{E}_T$ or mono-higgs+$\not{E}_T$ processes, where the radiated object from the initial state is either a photon, an electroweak gauge boson or higgs boson. The interaction vertex between quarks and DM is usually modeled using an effective operator (EFT). This approach has the advantage that it does not depend on the UV physics of the complete model for the dark particles, and that it has the minimal number of parameters (m_{DM}, Λ). To optimize the signal-to-background ratio, Monojet search [238–241] commonly use event selection criteria similar to:

- Events must feature a high value of E_T^{miss}
- Only a maximum of 2 jets are allowed in the event. The second jet is allowed to increase the magnitude of the signal and the signal-to-background ratio.
- The most energetic jet has to be hard $p_{\mathrm{T}} > 200, 400, 600, 800\,\mathrm{GeV}$
- The second jet, if present, is allowed to be soft $p_{\mathrm{T}} > 60\,\mathrm{GeV}$
- The rapidity of the jets has to lie in the region where the detectors are most efficient, usually $\eta < 2$ for hard jets and $\eta < 4 \div 4.5$ for soft jets
- Any other useful criteria to minimize misidentification of the event, such as lepton veto.

After specifying the EFT operators to consider, one can calculate the theoretical cross section and the expected number of events, and compare it with the observed number of events, provided that one can estimate the background. The region of the parameters space where

$$\chi^2 = \frac{(N_{obs} - N_{bkg} - N_{DM}(\Lambda, m_{\mathrm{DM}}))^2}{N_{DM}(\Lambda, m_{\mathrm{DM}}) + N_{bkg} + \sigma_{bkg}^2} > 2.71 \tag{2.59}$$

is excluded at 90% confidence level. To set bounds efficiently, it is thus necessary to estimate the background as precisely as possible.

2.2.3.5 Background Estimation

The main background process for this search is irreducible and it comes from $pp \to j(j) + Z.z \to \nu\bar{\nu}$. The other main source of background is reducible and comes from $pp \to j(j) + W, W \to l\nu$, where l is a charged lepton (τ, e, or μ in decreasing order of importance). If, for some reason, the lepton is not detected (for example, if it is outside detector acceptance, or is missed because of reconstruction inefficiencies), or if a hadronic τ decay is reconstructed as a single jet, this also leads to Monojet signature. The Z and W boson plus jet(s) backgrounds, collectively referred to in the following as *electroweak backgrounds*, are determined in a data-driven way:

1. Control regions are defined by explicitly selecting electrons or muons while keeping the same jet and missing transverse energy selection criteria as in the signal regions. Four processes containing electrons or muons are considered: $W \to e\nu$+jets, $W \to \mu\nu$+jets, $Z \to e^+e^-$+jets, $Z \to \mu^+\mu^-$+jets. Corrections are made for contamination of these control samples from processes other than Z or W decays.

2. Correction factors are then applied to account for differences in trigger and kinematic selection criteria between the control and signal regions. The control-to-signal region transfer factors, which are multiplied by the number of control-region events obtained in the previous step to yield the background estimate, are obtained using both data and simulation.

In this approach, the modelling of the jet and missing transverse energy kinematics of the electroweak backgrounds is obtained directly from data. Further experimental uncertainties that impact background prediction, such as the jet energy scale (JES) and resolution (JER) [242], the trigger efficiency, and the luminosity measurement [243, 244], are minimised by this approach.

SR process	$Z \to \nu\bar{\nu}$+jets	$W \to \tau\nu$+jets $W \to \mu\nu$+jets	$W \to e\nu$+jets	$Z \to \tau^+\tau^-$+jets $Z \to \mu^+\mu^-$+jets
CR process	$W \to e\nu$+jets $W \to \mu\nu$+jets $Z \to e^+e^-$+jets $Z \to \mu^+\mu^-$+jets	$W \to \mu\nu$+jets	$W \to e\nu$+jets	$Z \to \mu^+\mu^-$+jets

TABLE 2.1: Overview of processes in the control regions (CR) used to estimate background contributions to processes in the signal regions (SR). Taken from [238].

I here report examples from [238] of typical CR/SR and background estimates, together with the results of the search. For more details about background estimations, refer to [238]. The four signal regions defined in this search are reported in table 2.2. An

Signal regions	SR1	SR2	SR3	SR4
Common requirements	Data quality + trigger + vertex + jet quality + $\lvert\eta^{\text{jet1}}\rvert < 2.0$ + $\lvert\Delta\phi(\mathbf{p}_{\text{T}}^{\text{miss}}, \mathbf{p}_{\text{T}}^{\text{jet2}})\rvert > 0.5$ + $N_{\text{jets}} \leq 2$ + lepton veto			
$E_{\text{T}}^{\text{miss}}$, $p_{\text{T}}^{\text{jet1}}$ >	120 GeV	220 GeV	350 GeV	500 GeV

TABLE 2.2: Definition of the four overlapping signal regions SR1–SR4. *Data quality*, *trigger*, *vertex*, and *jet quality* refer to the selection criteria discussed in the main text. Taken from [238].

example of systematic and statistical uncertainties [238] on all background estimates are given in table 2.3.

Source	SR1	SR2	SR3	SR4
JES/JER/missing transverse energy	1.0	2.6	4.9	5.8
MC Z/W modelling	2.9	2.9	2.9	3.0
MC statistical uncertainty	0.5	1.4	3.4	8.9
$1 - f_{\mathrm{EW}}$	1.0	1.0	0.7	0.7
Muon scale and resolution	0.03	0.02	0.08	0.61
Lepton scale factors	0.4	0.5	0.6	0.7
Multijet BG in electron CR	0.1	0.1	0.3	0.6
Di-boson, top, multijet, non-collisions	0.8	0.7	1.1	0.3
Total systematic uncertainty	3.4	4.4	6.8	11.1
Total data statistical uncertainty	0.5	1.7	4.3	11.8

TABLE 2.3: Relative systematic uncertainties for all signal regions (in percent). Individual contributions are summed in quadrature to derive the total numbers. The MC statistical uncertainty is included in the total systematic uncertainty. Taken from [238].

An example overview of all backgrounds [238] is given in table 2.4 (cf. table 2.1 for the definition of the control regions).

	SR1	SR2	SR3	SR4
$Z \to \nu\bar{\nu}$+jets	63000 ± 2100	5300 ± 280	500 ± 40	58 ± 9
$W \to \tau\nu$+jets	31400 ± 1000	1853 ± 81	133 ± 13	13 ± 3
$W \to e\nu$+jets	14600 ± 500	679 ± 43	40 ± 8	5 ± 2
$W \to \mu\nu$+jets	11100 ± 600	704 ± 60	55 ± 6	6 ± 1
$t\bar{t}$ + single t	1240 ± 250	57 ± 12	4 ± 1	-
Multijets	1100 ± 900	64 ± 64	8^{+9}_{-8}	-
Non-coll. Background	575 ± 83	25 ± 13	-	-
$Z/\gamma^* \to \tau\tau$+jets	421 ± 25	15 ± 2	2 ± 1	-
Di-bosons	302 ± 61	29 ± 5	5 ± 1	1 ± 1
$Z/\gamma^* \to \mu\mu$+jets	204 ± 19	8 ± 4	-	-
Total Background	124000 ± 4000	8800 ± 400	750 ± 60	83 ± 14
Events in Data (4.7fb^{-1})	124703	8631	785	77
$\sigma_{\mathrm{vis}}^{\mathrm{obs}}$ at 90% [pb]	1.63	0.13	0.026	0.0055
$\sigma_{\mathrm{vis}}^{\mathrm{exp}}$ at 90% [pb]	1.54	0.15	0.020	0.0064
$\sigma_{\mathrm{vis}}^{\mathrm{obs}}$ at 95% [pb]	1.92	0.17	0.030	0.0069
$\sigma_{\mathrm{vis}}^{\mathrm{exp}}$ at 95% [pb]	1.82	0.18	0.024	0.0079

TABLE 2.4: Overview of predicted SM background and observed events in data for 4.7fb^{-1} for each of the four signal regions. The total uncertainty quoted is the quadratic sum of statistical and systematic uncertainties. Observed and expected 90% and 95% CL upper limits on the non-SM contribution to all signal regions are also given in terms of limits on visible cross sections ($\sigma_{\mathrm{vis}} \equiv \sigma \times A \times \epsilon$). The 90% CL upper limits are given to facilitate comparisons with other experiments. Taken from [238].

Distributions from all four visible decay modes used to determine the background in SR1 are shown in figure 2.13.

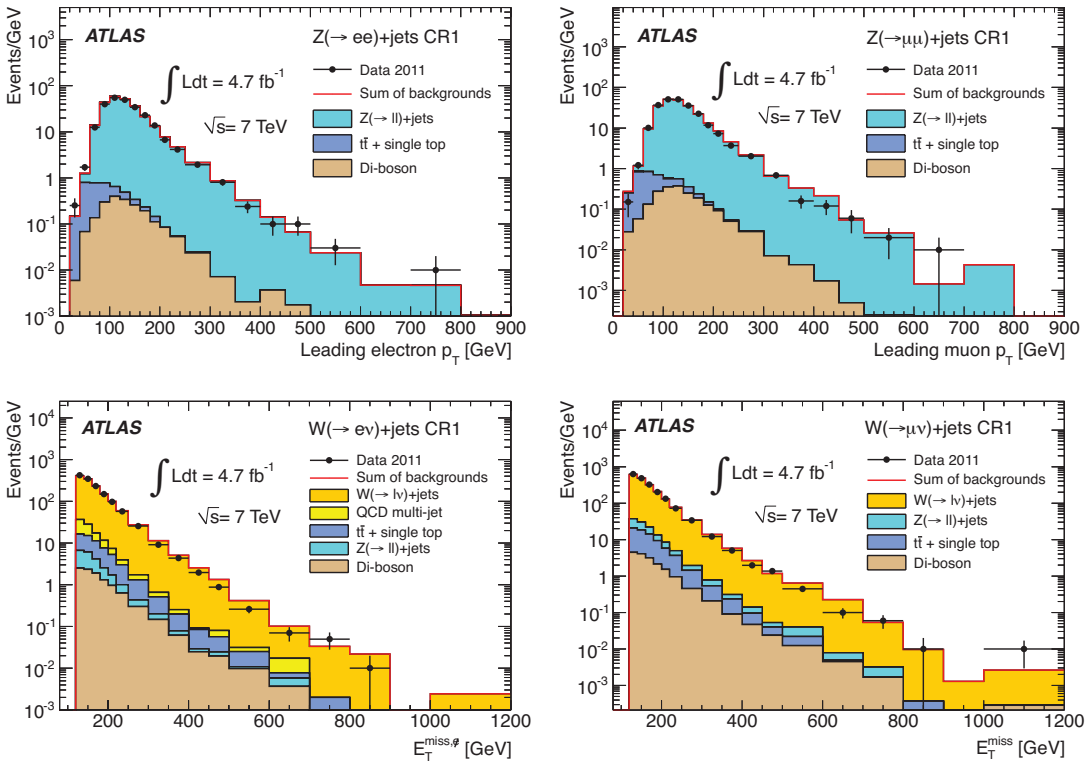

FIGURE 2.13: Kinematic distributions in the control regions corresponding to SR1 (labelled CR1) are shown. The upper row is the leading electron and muon p_{T} distribution for $Z \to e^+e^-$+jets (left) and $Z \to \mu^+\mu^-$+jets (right) and shows distributions after SR1 cuts on jets and $E_{\mathrm{T}}^{\mathrm{miss}}$. The lower row is the missing transverse momentum distribution $E_{\mathrm{T}}^{\mathrm{miss},\not{e}}$ for $W \to e\nu$+jets (left) and missing transverse energy for $W \to \mu\nu$+jets (right) also after SR1 jet and $E_{\mathrm{T}}^{\mathrm{miss}}$ cuts. Taken from [238].

2.2.3.6 Results

Lower limits (90% CL) on the suppression scale $\Lambda = M_*$ are shown in figure 2.15 for all considered operators, as a function of the DM mass $m_{\mathrm{DM}} = m_\chi$. For any given mass m_{DM}, limits on lambda are derived from cross section limits. The displayed values are the best within the four signal regions. Theoretical values of the event yields have been calculated for $10\,\mathrm{GeV} < m_{\mathrm{DM}} < 1300\,\mathrm{GeV}$ and extrapolated down to $m_{\mathrm{DM}} = 1\,\mathrm{GeV}$. Such extrapolations are valid since the variations of cross section and kinematic distributions for low mass WIMP are negligible in Monojet events at LHC. The effect of $\pm 1\sigma$ variations on the expected limit due to statistical fluctuations and experimental uncertainties is shown as a grey band. The impact of the theoretical uncertainties is represented by dotted red $\pm 1\sigma$ lines on either side of the observed limit. The nominal observed limit line excluding theoretical uncertainties is the final result. Numeric values of the lower limits on Λ (90% and 95% CL) are listed in table 2.5. These lower limits are flat up to $m_{\mathrm{DM}} = 100\,\mathrm{GeV}$ and start to get worse around $m_{\mathrm{DM}} = 200\,\mathrm{GeV}$ for

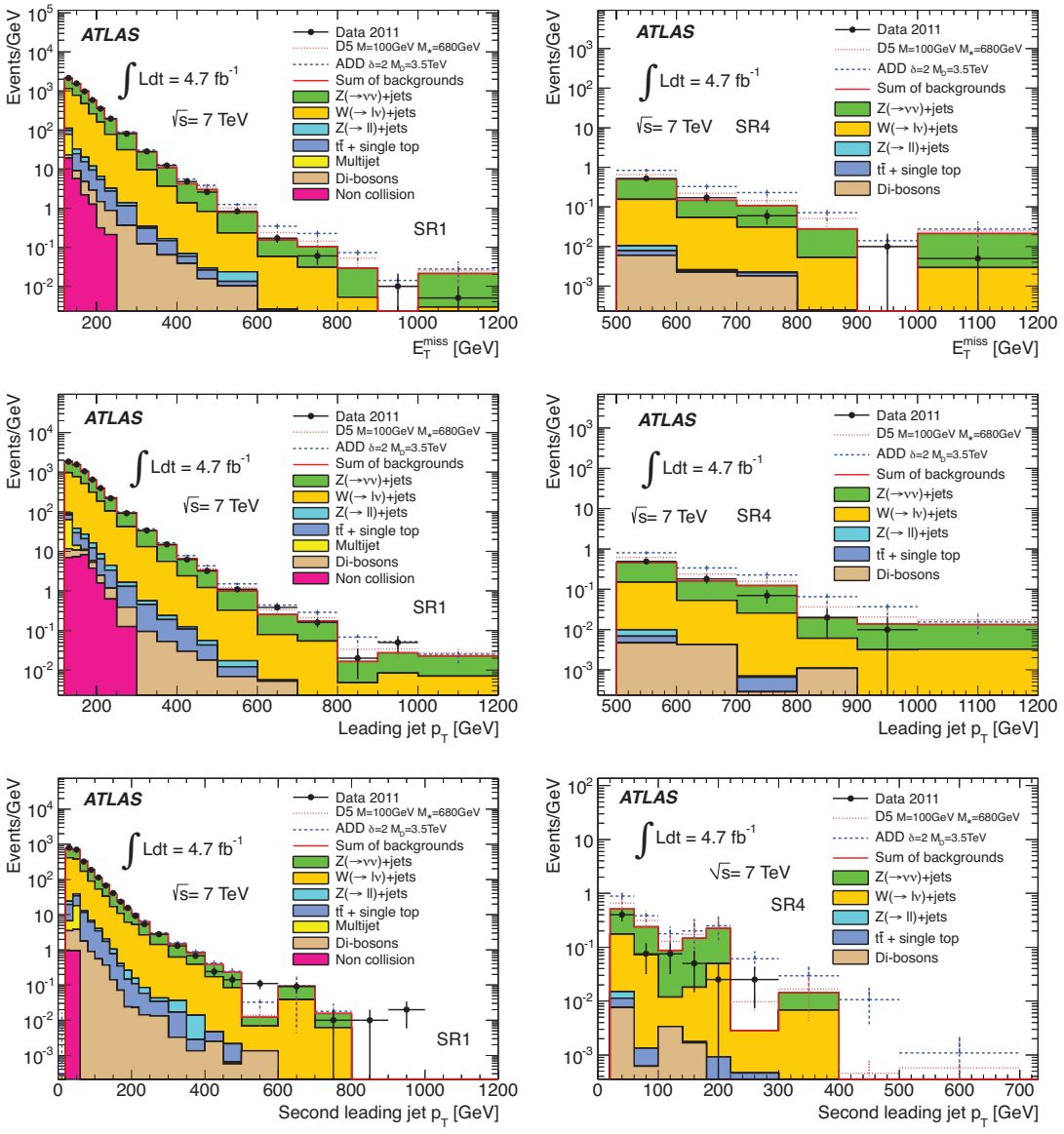

FIGURE 2.14: Kinematic distributions for signal regions SR1 on the left and SR4 on the right. Signal distributions for ADD and WIMP samples for cross sections equal to the excluded values are drawn as dashed lines on top of the predicted background distributions. The electroweak backgrounds are determined in bins of the variable that is plotted. Taken from [238]

all considered operators. Note that the Λ limits for D1 are much smaller due to the additional factor m_q/Λ in the definition of the operator (see table 5.1).

The regions where the EFT approach breaks down [245] are the light-grey regions in the bottom-right corner in all plots of figure 2.15[4]. All the limits on Λ set in this analysis [238] are well above this line, except for very high masses $m_{\mathrm{DM}} > 1300\,\mathrm{GeV}$. The validity of the EFT approach will be the main topic of chapter 5.

[4]Compared to ref. [245], the valid region of D1 shown here accounts for the factor of m_q in the definition of D1 (see table 5.1).

m_χ	D1	D5	D8	D9	D11
1	30 (29)	687 (658)	687 (658)	1353 (1284)	347 (335)
5	30 (29)	687 (658)	687 (658)	1353 (1284)	347 (335)
10	30 (29)	687 (658)	687 (658)	1353 (1284)	347 (335)
50	30 (29)	682 (653)	666 (638)	1338 (1269)	343 (331)
100	29 (28)	681 (653)	650 (623)	1310 (1243)	334 (322)
200	27 (26)	658 (631)	595 (570)	1202 (1140)	331 (319)
400	21 (20)	571 (547)	475 (455)	943 (893)	301 (290)
700	14 (14)	416 (398)	311 (298)	629 (596)	232 (223)
1000	9 (9)	281 (269)	196 (188)	406 (384)	171 (165)
1300	6 (6)	173 (165)	110 (106)	240 (227)	118 (114)

TABLE 2.5: ATLAS 90% (95%) CL observed lower limits on the suppression scale M_* as a function of WIMP mass m_χ. All values are given in GeV and correspond to the nominal observed limit excluding theoretical uncertainties. The signal regions with the best expected limits are quoted in all cases, SR3 is used for D1, D5 and D8, SR4 for D9 and D11. Taken from [238].

Thermal relic lines taken from [245] are also shown in Figure 2.15. These lines correspond to the values of $\Lambda, m_{\rm DM}$ that yield the correct amount of the relic density abundance [8], in the absence of other interactions. Cases where displayed limits on Λ are above such lines exclude DM annihilating only by using the considered operator. Relic density considerations to drive LHC search will be discussed in section 6.2.

2.3 Motivations for this work

The reason to study DM was given in Chapter 1. There are so many different and independent hints for its existence, that many physicist don't try to answer the question "'Does DM exist?"', but rather "'What is the nature of DM, and how is DM related to the known physics?"', giving its existence for granted. However, searches for DM are not an easy task, both experimentally and theoretically. From the experimental point of view, increasing the precision and acceptance of detectors, and minimizing the background noise are the main problems, as we have seen in section 2.2. To avoid to get wrong conclusions, it is important to understand all the possible problems that could affect the flow that brings you from experimental results to exclusion limits and/or DM detection claims. This work tries to individuate and analyze some of these problems, concerning ID and collider searches, and is based on the papers published, together with other authors, along the four years of my Ph.D. studies [246–252].

In Chapter 3, we will investigate the effects of DM evaporation in the Sun on DM seaches that measure neutrinos from the sun, which we talked about in section 2.2.2.3. This process together with capture and annihilation, determines the number of DM trapped

inside the Sun and so the total DM annihilation rate, but it is usually neglected because it is exponentially suppressed for heavy DM. However, as DD experiments efficiency in placing limits on σ_p decreases dramatically at low DM masses $m_{\rm DM} \lesssim 10\,{\rm GeV}$ (due to the use of heavy targets $> 10\,{\rm GeV}$, and the energy threshold E_{th} of detectors), and as the region around $m_{\rm DM} \sim 3\,{\rm GeV}$ is believed to be interesting, as there were some claims for DM with a mass around that value of mass in the recent past, it would be very tempting to use neutrino searches from the Sun to probe that part of parameter space and improve DD limits on σ_p for such low DM masses. Unfortunately, we show that in this region, evaporation (that is the process where a DM bounded gravitationally is made free by scattering on a nucleus) is important, and taking it into account make the neutrino flux due to DM annihilations independent of σ_p, so no bound on this parameter can be extracted from experimental data for such low DM masses.

In Chapter 4 we discuss another important aspect of ID: the possibility to distinguish whether a signal is generated by DM or by astrophysical searches. This is already a very well known problem for positrons (as discussed in section 2.2.2.1), for which both explanations are possible (though the astrophysical one seems actually to be preferred among the scientific community) and other independent searches in different channels are required to understand which of the two is the true origin of the signal. In particular, we argue that a possible DM signal in the antiproton channel could not be distinguished by astrophysical sources like SuperNova Remnants (SNR).

In Chapter 5, that is the main part of this work, we point out what is now considered a problem in the scientific community of the field, that is the limited validity of using EFT in DM searches at colliders. EFT is used in collider searches to analyze, for example, results from Monojet events and put constrains on the EFT operator suppression scale Λ, as a function of $m_{\rm DM}$. The advantage of it is that this approach is pretty model independent, as it is possible to show that any UV model where DM is coupled to SM in some way, would reduce in the low energy limit to an EFT operator that is a linear combination of a very limited set. Even if the low energy limit condition (that lets us legitimately use EFT) is surely fulfilled in DD for $\mathcal{O}(\,{\rm GeV})$ DM, and is probably fulfilled as well for ID, we show in Chapter 5 that this is not the case for collider searches at LHC, and we propose a method to rescale current limits to take into account this fact.

Finally, in Chapter 6 we briefly analyse what was proposed to be the next step to analyse experimental results from collider searches, that solves the EFT validity problem at the cost of introducing some model-dependency and enlarging the parameter space by adding a few more parameters: Simplified Models. The final Chapter 7 draws the conclusions about this work.

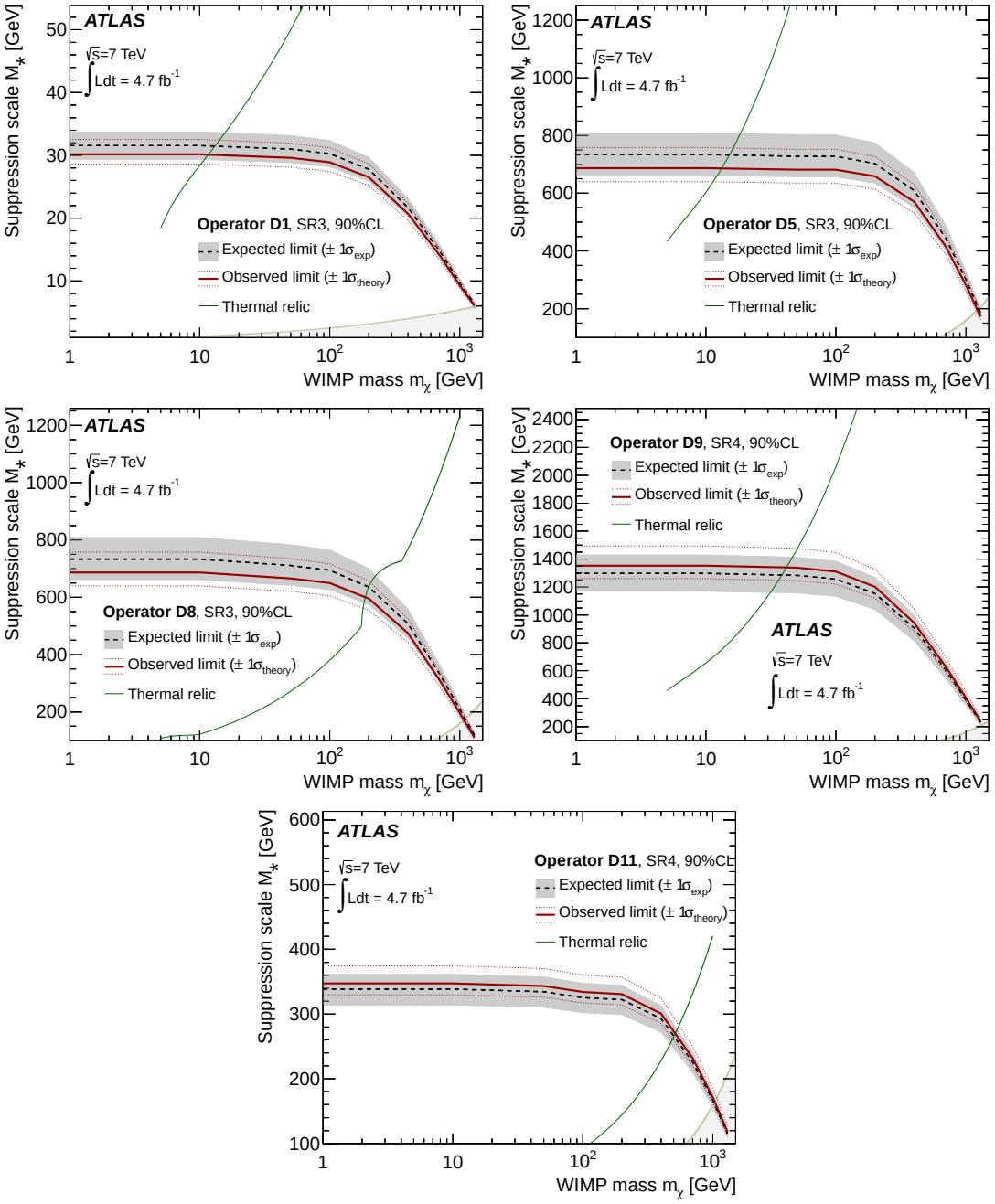

FIGURE 2.15: ATLAS lower limits at 90% CL on M_* for different masses of χ—the region below the limit lines is excluded. Observed and expected limits including all but the theoretical signal uncertainties are shown as dashed black and red solid lines, respectively. The grey $\pm 1\sigma$ band around the expected limit is the variation expected from statistical fluctuations and experimental systematic uncertainties on SM and signal processes. The impact of the theoretical uncertainties is shown by the thin red dotted $\pm 1\sigma$ limit lines around the observed limit. The M_* values at which WIMPs of a given mass would result in the required relic abundance are shown as rising green lines (taken from [245]), assuming annihilation in the early universe proceeded exclusively via the given operator. The shaded light-grey regions in the bottom right corners indicate where the effective field theory approach breaks down [245]. The plots for D1, D5, D8 are based on SR3, those for D9 and D11 on SR4. Taken from [238].

Chapter 3

Dark Matter from Solar Neutrinos

3.1 Introduction

The indirect searches for the Dark Matter (DM) component of the Universe are primarily based on identifying excesses in fluxes of cosmic rays, such as positrons, anti-protons, neutrinos, etc; these stable Standard Model particles may be the end product of the annihilation (or decay) of DM in the galactic halo or in the Sun. Among the different ongoing search strategies, the search for the annihilation products of DM in the Sun is particularly interesting. In fact, the DM particles trapped in the core of the Sun may annihilate into anything, but only neutrinos would be able to escape the surface and reach the Earth. The role of neutrinos in DM searches of this type is then very special.

The indirect searches for DM in the Sun are tightly linked to direct detection searches, which are sensitive to the cross section for DM scattering off the nucleons of heavy nuclei (e.g. σ_p for protons). In fact, suppose that DM annihilates into several final states j, with branching ratios BR_j, and producing a differential number of neutrinos per annihilation $\mathrm{d}N_j/\mathrm{d}E_\nu$; then, the flux of neutrinos of DM origin arriving at Earth is given by

$$\frac{\mathrm{d}\Phi_\nu}{\mathrm{d}E_\nu} = \frac{\Gamma_A}{4\pi R^2} \sum_j \mathrm{BR}_j \frac{\mathrm{d}N_j}{\mathrm{d}E_\nu} \tag{3.1}$$

where R is the Sun-Earth distance, Γ_A is the rate of annihilations per unit time

$$\Gamma_A = \frac{1}{2} A_\odot N_\chi^2 \,, \tag{3.2}$$

N_χ is the number of DM particles in the Sun, and the annihilation coefficient $A_\odot$ will be defined and discussed later, see Eq. (3.5). Since N_χ depends on how many DM particles got trapped in the Sun, and hence generically depends on σ_p, observational limits on the flux Φ_ν translate into limits on σ_p, which can be competitive with those of direct detection searches.

This situation dramatically changes in the case of light DM, with mass around GeV. The number N_χ becomes independent of σ_p when the capture process goes in equilibrium with the evaporation, and annihilation is negligible. As a consequence, the experimental bounds on the neutrino flux from the Sun cannot be translated anymore into constraints on σ_p and the link between neutrino flux and DM-nucleon scattering cross section disappears. We also find simple and accurate fitting functions for all the relevant processes concerning DM in the Sun: annihilation, capture and evaporation.

The interest in $\mathcal{O}$(GeV) neutrinos as probes of DM has been recently reinvigorated by the proposal to consider the production in the Sun of muons and charged pions as products of DM annihilations, and their subsequent decay at rest [253, 254]. These neutrinos can be easily detected by neutrino telescopes based on water Cherenkov detectors, such as Super-Kamiokande [229, 232]. One should also keep in mind that the energy to distinguish neutrinos originated by DM in the Sun is bounded from below; in fact, for DM masses below $\sim$ 100 MeV, the detection process is based on inverse β-decay $\bar{\nu}_e + p \to e^+ + n$, of which e^+ gets identified. The distribution of e^+ is mostly isotropic (see e.g. Ref. [255]), and the angular resolution is typically not good enough to extract information on the arrival direction. Therefore, it is not possible to distinguish neutrinos from DM annihilations in the Sun from those from the galactic halo, whose flux is much bigger [256, 257]. While we will not commit ourselves to any specific model for GeV-scale DM, this situation can be realized in the context e.g. of asymmetric DM [258] or in explicit models such as the one in Ref. [259].

The rest of the chapter is organized as follows. In Section 3.2 we will briefly discuss the relevant processes for DM inside the Sun, and then turn to compute the total number of the DM inside the Sun in Section 3.3. Our concluding remarks are in Section 3.4.

3.2 Relevant processes of DM in the Sun

The DM inside the Sun undergoes several processes: it gets captured, via the energy losses from scattering with the nuclei; it annihilates, whenever two DM particles meet; or it can even evaporate, if the collisions with nuclei make it escape the Sun. The total number of DM inside the Sun is thus determined by the interplay of these three

processes. Let us discuss them in more detail (see also Ref. [128] for a previous analysis of these processes, and Ref. [260] for a recent update in the regime where evaporation is not important).

3.2.1 Annihilation

The first important process to consider is the annihilation of two DM particles inside the Sun, and we want to compute the rate for this process (we follow closely the discussion in Ref. [261]). We approximate the phase space distribution of the DM trapped in the Sun by a global temperature T_χ and the local gravitational potential $\phi(r)$, defined with respect to the solar core, as

$$\phi(r) = \int_0^r \frac{G_N M_\odot(r')}{r'^2} \mathrm{d}r' \,, \tag{3.3}$$

where G_N is Newton's constant and $M_\odot(r) = 4\pi \int_0^r r'^2 \rho_\odot(r') \mathrm{d}r'$ is the solar mass within radius r. Throughout the chapter we use the density profile $\rho_\odot(r)$ from the solar model AGSS09 [262]. The DM number density is determined by solar gravitational potential and scales as

$$n_\chi(r) = n_0 e^{-m_\chi \phi(r)/T_\chi} \,, \tag{3.4}$$

where n_0 is the density at the core. The annihilation coefficient $A_\odot$ in Eq. (3.2) is defined as

$$A_\odot \equiv \langle \sigma v_{rel} \rangle_\odot \frac{\int_{\mathrm{Sun}} n_\chi(r)^2 \, \mathrm{d}^3 r}{\left[\int_{\mathrm{Sun}} n_\chi(r) \, \mathrm{d}^3 r\right]^2} \,, \tag{3.5}$$

where the thermally-averaged annihilation cross section $\langle \sigma v_{rel} \rangle_\odot$ is assumed to be independent on the DM position in the Sun, and we assume the number density of DM particles equal to that of antiparticles. The factor of 1/2 in Eq. (3.2) simply avoids double counting of pairs in the annihilation.

To compute the annihilation coefficient $A_\odot$, we need to know T_χ, which is obtained as follows. The average DM orbit radius $\bar{r}$ is the mean value of the DM distance from the center of the Sun,

$$\bar{r}(m_\chi) = \frac{\int_{\mathrm{Sun}} r \, n_\chi(r) \mathrm{d}^3 r}{\int_{\mathrm{Sun}} n_\chi(r) \mathrm{d}^3 r} \,, \tag{3.6}$$

and it depends on the DM mass (see Fig. 3.1, left panel). The temperature of the population of DM particles trapped in the Sun, or DM temperature T_χ for brevity, is taken to be the local solar temperature at the DM mean orbit:

$$T_\chi = T_\odot(\bar{r}) \,, \tag{3.7}$$

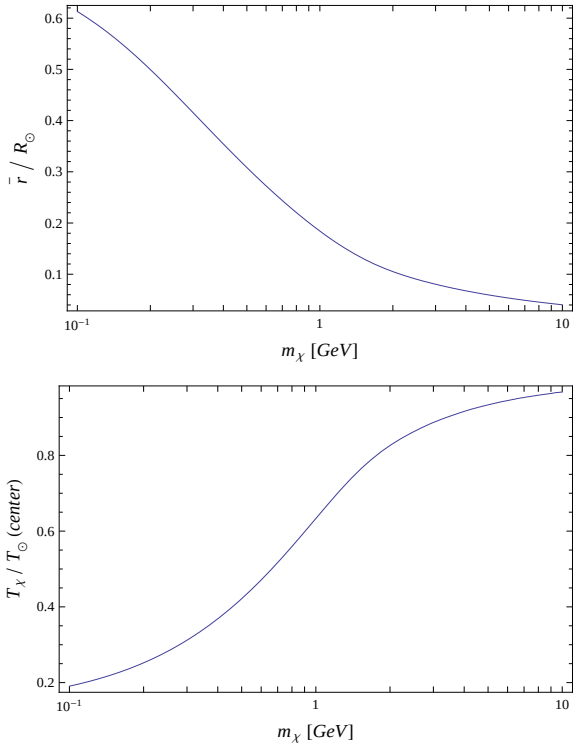

FIGURE 3.1: Left panel: *The average orbit radius $\bar{r}$, normalized to the solar radius, as a function of the DM mass.* Right panel: *The temperature of the population of DM particles trapped in the Sun T_χ, normalized to the central solar temperature, as a function of the DM mass.*

and it depends on m_χ through $\bar{r}$. The dependence of T_χ on the DM mass is shown in the right panel of Fig. 3.1. If the DM particles are heavier than a few GeV, they get trapped near the solar core and the corresponding $\bar{r}$ will be very small. As a consequence, the DM temperature T_χ will be close to the central solar temperature. In the limit where the DM is much heavier than the nucleon mass $m_\chi \gg m_N$, the DM temperature will approach the solar temperature at the center. The determination of T_χ, and hence the annihilation coefficient, for DM masses of a few GeV (or less) requires taking into account the full solar density profile, as the DM orbit can span a wide region inside the Sun and the approximation of constant solar density is no longer valid.

For the annihilation coefficient $A_\odot$ we find the following fitting function

$$A_\odot \simeq 2.91\, e^{-1.34\left[\log\left(\frac{20\,\mathrm{GeV}}{m_\chi}\right)\right]^{1.14}} \left(\frac{\langle\sigma_{\rm ann} v\rangle_\odot}{3\times 10^{-26}\mathrm{cm}^3/\mathrm{s}}\right) \times 10^{-55}\,\mathrm{s}^{-1}\,, \tag{3.8}$$

valid in the range $0.1\,\mathrm{GeV} \leq m_\chi \leq 10$ GeV, to better then 9%. In Fig. 3.2, we show the comparison between our numerical results with Eqs. (16) of Ref. [263] for $\langle\sigma_{\rm ann} v\rangle_\odot = 3\times 10^{-26}\mathrm{cm}^3/\mathrm{s}$. They are consistent with each other up to $m_\chi = 1$ TeV, except for $m_\chi \leq 2$ GeV, which is due to the breakdown of the constant density approximation.

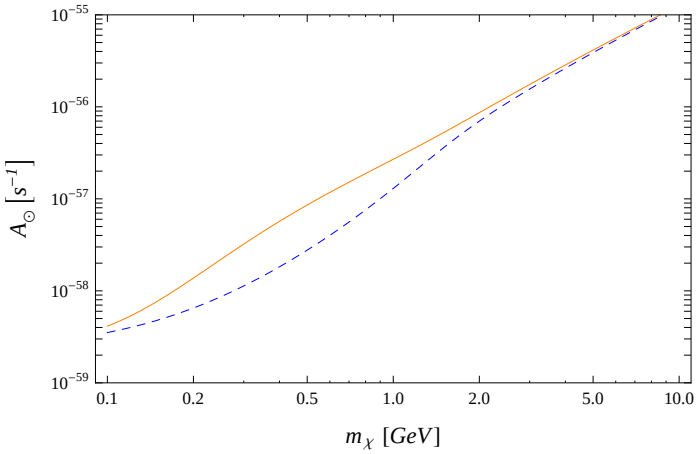

FIGURE 3.2: *The annihilation coefficient $A_\odot$ for $\langle\sigma v_{rel}\rangle_\odot = 3\times10^{-26}\,\mathrm{cm}^3/\mathrm{s}$ (orange solid line). We compare with Eq. (16) of Ref. [263] (blue dashed line): $A_\odot = (\sqrt{2}/\pi\bar{r})^3\langle\sigma_{\mathrm{ann}}v\rangle_\odot$.*

In the following, we will only consider the case where the annihilation cross section is velocity-independent (s-wave annihilations). As a reference value for the thermally average cross section in the Sun today we take $\langle\sigma_{\mathrm{ann}}v\rangle_\odot = 3\times10^{-26}\,\mathrm{cm}^3/\mathrm{s}$, although the actual value depends on the effective degrees of freedom at the freeze-out temperature, which in turn depends on the DM mass (see e.g. Ref. [264]). The case of pure p-wave annihilations results in a smaller annihilation cross section today than at freeze-out. We will not explore this case thoroughly, although in our analysis we will vary the annihilation cross section with respect to its reference value.

3.2.2 Capture

The other relevant processes occurring in the Sun are capture and evaporation. A DM particle can collide with nuclei and lose energy when it traverses the Sun. If the final velocity of the DM particle after the collision is less than the local escape velocity $v_e(r)$, then it gets gravitationally trapped. This capture process makes the popoulation of DM particles in the Sun grow. However, the captured DM particles may scatter off energetic nuclei and be ejected, whenever the DM velocity after the collision is larger than the local escape velocity. This process is called evaporation. The formalism to describe capture and evaporation is the same, apart from the requirement on the final velocity to be larger or smaller than v_e.

The local escape velocity is defined as $v_e(r) \equiv \sqrt{2\,[\phi(\infty)-\phi(r)]}$, where $\phi(r)$ is the local gravitational potential in Eq. (3.3). The basic quantity is the rate per unit time $R_i^{\pm}(w \to v')$ at which a single DM particle of velocity w scatters to a final velocity between v' and $v'+\mathrm{d}v'$, off a thermal distribution of nuclei i with number density

n_{N_i}, mass m_{N_i} and temperature $T_{N_i} = T_\odot(r)$. The plus (minus) sign refers to whether the final velocity is larger (smaller) than the initial one. This quantity has been first computed in Ref. [265], under the assumption of isotropic, velocity-independent DM-nucleus cross section σ_i, and we provide the details of the calculation in Appendix A.1. The scattering rate per unit time results to be (see Eqs. (A.12)-(A.13))

$$\begin{aligned} R_i^{\pm}(w \to v')\mathrm{d}v' &= \frac{\sigma_i n_{N_i}}{w}\frac{\mu_{+,i}^2}{\mu_i}\left[[\mathrm{Erf}(\alpha_{+,i}) - \mathrm{Erf}(\pm\alpha_{-,i})]\right. \\ &+ \left. e^{-\frac{m_\chi(v'^2-w^2)}{2T_{N,i}}}\left[\mathrm{Erf}(\beta_{+,i}) - \mathrm{Erf}(\pm\beta_{-,i})\right]\right] v'\mathrm{d}v' \end{aligned} \tag{3.9}$$

where $\mathrm{Erf}(x)$ is the error function and

$$\begin{aligned} \alpha_{\pm,i} &\equiv \sqrt{\frac{m_{N_i}}{2T_{N_i}}}\left(\mu_{+,i}v' \pm \mu_{-,i}w\right), \quad \beta_{\pm,i} \equiv \sqrt{\frac{m_{N_i}}{2T_{N_i}}}\left(\mu_{-,i}v' \pm \mu_{+,i}w\right), \\ \mu_i &\equiv \frac{m_\chi}{m_{N_i}}, \qquad\qquad \mu_{\pm,i} \equiv \frac{\mu_i \pm 1}{2}. \end{aligned} \tag{3.10}$$

The rate per unit time is simply related to the differential scattering cross section $\mathrm{d}\sigma_i$ by $R_i(w \to v')\mathrm{d}v' = n_{N_i} w\, \mathrm{d}\sigma_i$. The rates per unit time $\Omega^{\pm}_{v_e,i}(w)$ are simply obtained by appropriate integrations over the final DM velocity

$$\Omega^{-}_{v_e,i}(w) = \int_{\frac{|\mu_{-,i}|}{\mu_{+,i}}w}^{v_e} R_i^{-}(w \to v')\mathrm{d}v', \tag{3.11}$$

$$\Omega^{+}_{v_e,i}(w) = \int_{v_e}^{+\infty} R_i^{+}(w \to v')\mathrm{d}v'. \tag{3.12}$$

The lower integration limit in Eq. (3.11) is the minimal final velocity simply set by kinematics. The rate $\Omega^{-}_{v_e,i}$ is what controls capture, while $\Omega^{+}_{v_e,i}$ controls evaporation. We discuss here the capture process and defer evaporation to the next subsection.

The local capture rate of DM per unit volume at radius r, due to nucleus i of mass m_{N_i}, can be written as [217, 225]

$$\frac{dC_{\odot,i}}{dV} = \int_0^{u_i^{\max}} \mathrm{d}u \frac{f_{v_\odot}(u)}{u} w \Omega^{-}_{v_e,i}(w), \tag{3.13}$$

where u is the DM velocity at infinity, $w(r) = \sqrt{u^2 + v_e(r)^2}$ is the local DM velocity inside the Sun before the scattering, and $u_i^{\max} \equiv v_e\sqrt{\mu_i}/|\mu_{-,i}|$ corresponds to a DM scattering with a final velocity equal to v_e.

The function $f_{v_\odot}(u)$ is the velocity distribution of DM particles seen by an observer moving at the velocity of the Sun $v_\odot \simeq 220$ km/s, with respect to the DM rest frame. The velocity distribution of DM particles in the galactic halo, in their rest frame, is

approximated by a Maxwell-Boltzmann $f_0(u)$ with a velocity dispersion v_d

$$f_0(u) = \frac{\rho_\chi}{m_\chi}\frac{4}{\sqrt{\pi}}\left(\frac{3}{2}\right)^{3/2}\frac{u^2}{v_d^3}e^{-3u^2/(2v_d^2)}\,, \tag{3.14}$$

where $\rho_\chi \simeq 0.3\,\mathrm{GeV/\,cm^3}$ is the average mass density of DM in the halo. We will set $v_d = 270$ km/s. By making a Galilean transformation of velocity $v_\odot$, it is straightforward to derive the distribution $f_{v_\odot}(u)$

$$f_{v_\odot}(u) = \frac{\rho_\chi}{m_\chi}\sqrt{\frac{3}{2\pi}}\frac{u}{v_\odot v_d}\left[\exp\left(-\frac{3(u-v_\odot)^2}{2v_d^2}\right) - \exp\left(-\frac{3(u+v_\odot)^2}{2v_d^2}\right)\right]. \tag{3.15}$$

In the Sun, the solar temperature is much smaller than the escape energy $(1/2)m_\chi v_e^2$ of a DM particle, so for capture it suffices to deal with the zero-temperature limit. We checked that taking into account the finite-temperature corrections would reduce the capture rate by less than 10% with respect to the one computed for $T_{N_i} = 0$.

In the limit $T_{N_i} = 0$, and for elastic isospin-invariant contact interactions between DM and nuclei, simple analytical formulae can be derived. The scattering rate per unit time for nucleus i is

$$R_i^-(w \to v')\mathrm{d}v' = 2\frac{n_{N_i}\sigma_i}{w}\frac{\mu_{+,i}^2}{\mu_i}v'\mathrm{d}v'\,. \tag{3.16}$$

and the total rate (3.11) becomes

$$\Omega_{v_e,\mathrm{H}}^-(w) = \frac{\sigma_\mathrm{H} n_{N_\mathrm{H}}}{w}\left(v_e^2 - \frac{\mu_{-,\mathrm{H}}^2}{\mu_\mathrm{H}}u^2\right), \tag{3.17}$$

which is valid only for Hydrogen (H). In fact, for scatterings with heavier elements one should take into account the decoherence effect. One simple way to do so is to multiply the scattering rate R by a form factor $|F_i(E_R)|^2$, depending on the recoil energy, which is the difference between the energies of the DM particle before and after the collision $E_R = (1/2)m_\chi(w^2 - v'^2)$. So for Hydrogen $|F_\mathrm{H}(E_R)|^2 = 1$, while for heavier elements we consider the simple exponential form factor [217, 225, 266]:

$$|F_i(E_R)|^2 = \exp(-E_R/E_i), \quad E_i = 3/(2m_{N_i}R_i^2)\,, \quad R_i = [0.91\,(m_{N_i}/\mathrm{GeV})^{1/3} + 0.3]\ \mathrm{fm}\,, \tag{3.18}$$

which has the advantage of making possible a simple analytical integration of Eq. (3.11), to get

$$\Omega_{v_e,i}^-(w) = \frac{\sigma_i n_{N_i}}{w}\frac{(\mu_i+1)^2}{2m_\chi\mu_i}E_i\left[e^{-m_\chi u^2/(2E_i)} - e^{-m_\chi w^2\mu_i/(2\mu_{+,i}^2E_i)}\right]. \tag{3.19}$$

We checked that using the more accurate Helm-Lewin-Smith form factor [133, 267, 268],

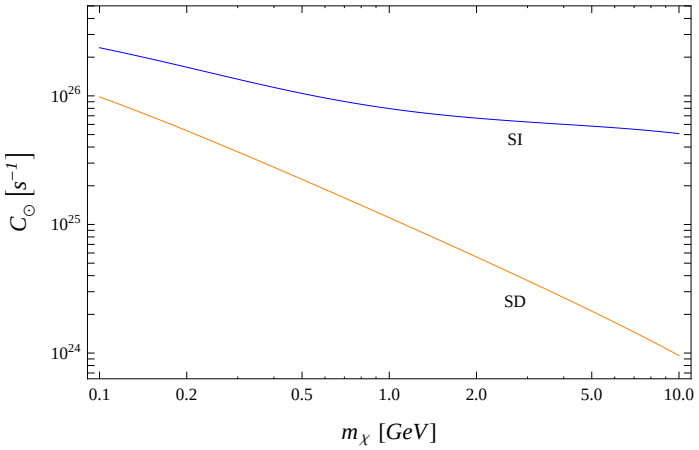

FIGURE 3.3: *The capture rate $C_\odot$ for $\sigma_p = 10^{-40}\text{cm}^2$ for SD and SI.*

the capture rate would differ by less than 2% in the mass range considered, and the corresponding number of DM particles (to be discussed in the next section) by less than 1%, for $m_\chi \leq 10$ GeV.

Finally, the total capture rate inside the Sun is obtained by integrating Eq. (3.13), with (3.15), (3.17) and (3.19), over the solar volume and summing over the different nuclear species in the Sun

$$C_\odot = \sum_i \int_{\text{Sun}} \frac{dC_{\odot,i}}{dV} \text{d}^3 r, \tag{3.20}$$

where i refers to the nucleus i. The quantity of phenomenological interest is the DM-proton scattering cross section σ_p, which is related to the cross section σ_i on the nucleus i (with mass number A_i) by

$$\sigma_i = \sigma_p A_i^2 \frac{m_{N_i}^2}{m_p^2} \frac{(m_\chi + m_p)^2}{(m_\chi + m_{N_i})^2}\,, \tag{3.21}$$

and we assume equal couplings of the DM to protons and neutrons. The generalization to account for different DM-nucleon couplings is straightforward. For spin-independent (SI) DM-nucleus interactions, we have an enhancement of the cross section from constructive interference between nucleons inside the nucleus i. Therefore, we have included contributions from the most important elements up to Ni. On the other hand, for spin-dependent (SD) interactions, only Hydrogen is considered since another dominant element, Helium, has spin zero. So, the capture rate for SD interactions is computed using Eqs. (3.13) and (3.17) with $\sigma_\text{H} = \sigma_p$ and unit form factor $|F_\text{H}(E_R)|^2 = 1$. The capture rates we obtained are shown in Fig. 3.3, for the SD and SI cases. Our results are in very good agreement with those of Ref. [263].

We find the following simple fitting functions for the capture rate corresponding to SD and SI DM-nucleus interactions

$$C_\odot \simeq 3.57\, e^{1.34\left[\log\left(\frac{20\,\mathrm{GeV}}{m_\chi}\right)\right]^{0.86}} \left(\frac{\sigma_p}{10^{-40}\mathrm{cm}^2}\right) \times 10^{23}\,\mathrm{s}^{-1}\,, \qquad \text{(SD)} \quad (3.22)$$

$$C_\odot \simeq 5.27\, e^{3.73\times10^{-2}\left[\log\left(\frac{20\,\mathrm{GeV}}{m_\chi}\right)\right]^{2.23}} \left(\frac{\sigma_p}{10^{-40}\mathrm{cm}^2}\right) \times 10^{25}\,\mathrm{s}^{-1}\,, \qquad \text{(SI)} \quad (3.23)$$

valid in the range $0.1 \leq m_\chi \leq 10$ GeV, with an accuracy better than 3% and 6%, respectively.

3.2.3 Evaporation

As highlighted in the previous subsection, the formalism for describing evaporation is identical to that for capture. However, contrarily to capture, the evaporation is highly sensitive to the temperature of the distribution of nuclei in the Sun, and therefore we now need to work in the finite temperature regime $T_{N_i} \neq 0$. Also, we willl work in the regime where the Sun is optically thin with respect to the DM particles, and we do not consider the refinements of the calculations in the optically thick regime [269–271]

The evaporation rate per unit volume at radius r is given by

$$\frac{\mathrm{d}E_{\odot,i}}{\mathrm{d}V} = \int_0^{v_e} f_\odot(w)\Omega^+_{v_e,i}(w)\mathrm{d}w, \tag{3.24}$$

with $\Omega^+_{v_e,i}$ given by Eq. (3.12). We will approximate the velocity distribution $f_\odot(w)$ of the population of DM particles trapped in the Sun, as a Maxwell-Boltzmann distribution, depending on the DM mass and temperature

$$f_\odot(w) = n_\chi \frac{4}{\sqrt{\pi}} \left(\frac{m_\chi}{2T_\chi}\right)^{3/2} w^2 e^{-m_\chi w^2/(2T_\chi)}\,. \tag{3.25}$$

The approximation of thermal distribution is valid for DM mass $m_\chi \sim 1$ GeV, while the actual DM distribution deviates from the thermal distribution for larger masses. We use the results of [265] to account for the corrections due to a non-thermal distribution. The total evaporation rate per DM particle is obtained by integrating Eq. (3.24) over the solar volume and divide by the total number of DM particles in the Sun

$$E_\odot = \frac{\sum_i \int_{\mathrm{Sun}} \frac{dE_{\odot,i}}{dV} \mathrm{d}^3 r}{\int_{\mathrm{Sun}} n_\chi(r)\, \mathrm{d}^3 r} \tag{3.26}$$

Again, for SD interactions, only Hydrogen is considered but for SI interactions, we include all the elements up to Nickel, using the solar model AGSS09 [262].

There is a simple analytical approximation of Eq. (3.26) [265, 269], which is valid for $m_\chi/m_N > 1$

$$E_\odot^{\rm approx} \simeq \frac{8}{\pi^3}\sqrt{\frac{2m_\chi}{\pi T_\odot(\bar{r})}}\frac{v_e(0)^2}{\bar{r}^3}e^{-\frac{m_\chi v_e(0)^2}{2T_\odot(\bar{r})}}\Sigma_{\rm evap}, \tag{3.27}$$

where $v_e(0)$ is the escape velocity at the solar center. The quantity $\Sigma_{\rm evap}$ is the sum of the scattering cross sections of all the nuclei within a radius $r_{95\%}$, where the solar temperature has dropped to 95% of the DM temperature. The derivation of Eq. (3.27) is sketched in Appendix A.2. We present our numerical results for $E_\odot$ in Fig. 3.4. Notice that for $m_\chi \gtrsim 4$ GeV the evaporation rate drops rapidly. We found that the approximated formula $E_\odot^{\rm approx}$ of Eq. (3.27) is off by a factor $\lesssim 4$ with respect to the full numerical result, in the relevant region $2 \lesssim m_\chi \lesssim 5$ GeV, in agreement with what stated in Ref. [269].

For the evaporation rate for SI and SD DM-nucleus interactions, we find the following simple fitting functions

$$E_\odot \simeq 1.09\, e^{-34.97\left(\frac{1\,\rm GeV}{m_\chi}\right)^{0.0467}-9.25\left(\frac{m_\chi}{1\,\rm GeV}\right)^{0.95}}\left(\frac{\sigma_p}{10^{-40}\rm cm^2}\right)\times 10^9\,\rm s^{-1}, \tag{SI}$$

$$E_\odot \simeq 5.13\, e^{-39.6\left(\frac{1\,\rm GeV}{m_\chi}\right)^{0.077}-8.92\left(\frac{m_\chi}{1\,\rm GeV}\right)^{0.97}}\left(\frac{\sigma_p}{10^{-40}\rm cm^2}\right)\times 10^{11}\,\rm s^{-1}, \tag{SD}$$

which reproduce the full numerical results with an accuracy better than 14% and 10%, respectively, in the range $0.5 \leq m_\chi \leq 8$ GeV. For heavier DM masses, the evaporation is completely negligible.

3.3 Results

3.3.1 The number of DM particles in the Sun

We have now all the tools to determine the number of DM particles in the Sun, which depends on the DM mass m_χ, its annihilation cross section $\langle\sigma_{\rm ann}v\rangle_\odot$ and its scattering cross section with proton σ_p. The time evolution of the number N is described by the simple differential equation [128]

$$\frac{{\rm d}N(t)}{{\rm d}t} = C_\odot - E_\odot N(t) - A_\odot N(t)^2\,, \tag{3.30}$$

whose solution, evaluated at the age of the Sun $t_\odot$, is

$$N(t_\odot) = \sqrt{\frac{C_\odot}{A_\odot}}\cdot\frac{\tanh(kt_\odot/\tau)}{k+\frac{1}{2}E_\odot\tau\tanh(kt_\odot/\tau)} \equiv N_\chi, \tag{3.31}$$

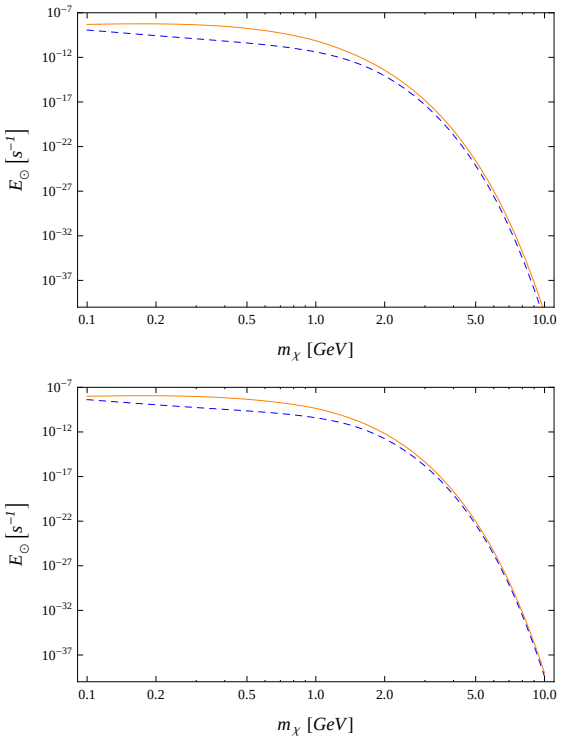

FIGURE 3.4: *The evaporation rate $E_\odot$, for $\sigma_p = 10^{-40}\text{cm}^2$ (orange solid line) for SD* (left panel) *and SI* (right panel)*. We compare it to the simple analytical approximation $E_\odot^{\text{approx}}$ in Eq. (3.27) (blue dashed line).*

where $\tau \equiv 1/\sqrt{C_\odot A_\odot}$ and $k \equiv \sqrt{1 + (E_\odot \tau/2)^2}$.

Depending on the DM mass and cross sections, the different processes have different relevances, and ultimately two regimes are possible: capture and annihilation are in equilibrium, or capture and evaporation are in equilibrium. For the cross sections of interest, $\sigma_p \gtrsim 10^{-42}\,\text{cm}^2$, the quantity $kt_\odot/\tau$ is always bigger than one meaning that the equilibrium condition is always fulfilled. When evaporation is negligible, $E_\odot \tau \ll 1$, then $k \simeq 1$ and the number N_χ simply reduces to

$$N_\chi \simeq \sqrt{\frac{C_\odot}{A_\odot}}\,\tanh(t_\odot/\tau) \simeq \sqrt{\frac{C_\odot}{A_\odot}}\,. \tag{3.32}$$

In this situation the capture and annihilation processes are in equilibrium. On the other hand, in the opposite regime $E_\odot \tau \gg 1$, the annihilation becomes negligible and the equilibrium is attained by capture and evaporation and the number of DM particles becomes

$$N_\chi \simeq \frac{C_\odot}{E_\odot} \tag{3.33}$$

becomes independent of the DM-nucleus cross section.

The main parameter determining whether evaporation is relevant or not is the DM mass.

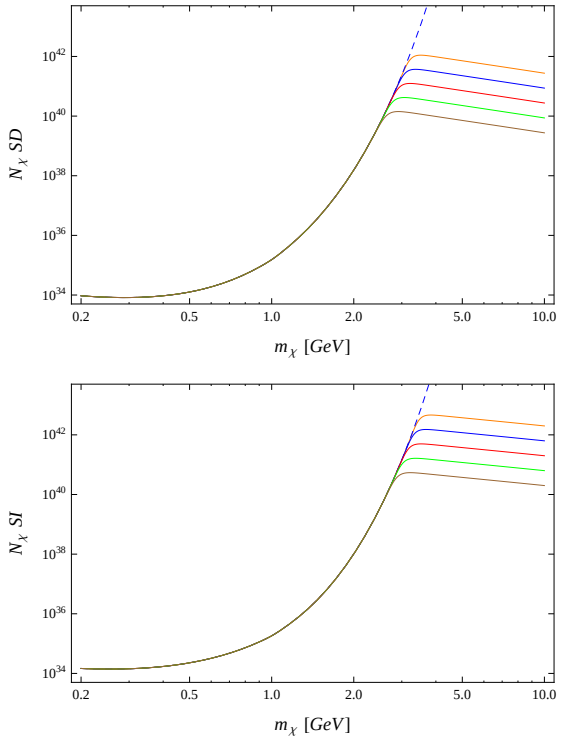

FIGURE 3.5: *The number of DM particles in the Sun N_χ, as a function of the DM mass, for SD* (left panel) *and SI* (right panel)*, for different values of the DM-proton cross section $\sigma_p = 10^{-40}, 10^{-39}, 10^{-38}, 10^{-37}, 10^{-36}\,\mathrm{cm}^2$ (from bottom to top). We have set $\langle\sigma_{\rm ann} v\rangle_\odot = 3 \times 10^{-26}\mathrm{cm}^3/\mathrm{s}$. We also show the curve (blue dashed line) corresponding to $C_\odot/E_\odot$, which N_χ tends to when the evaporation-capture equilibrium is reached.*

Since the evaporation drops rapidly for about $m_\chi \gtrsim 4$ GeV, so we expect that in this regime annihilation and capture are in equilibrium; however, for lighter DM, the capture goes in equilibrium with evaporation.

In Fig. 3.5, we show N_χ as a function of m_χ for different values of σ_p, in the range $10^{-40} \div 10^{-36}\mathrm{cm}^2$. Notice that N_χ tends to the curve $C_\odot/E_\odot$, corresponding to when the equilibrium between capture and evaporation is attained, and the number of DM particles does not depend on σ_p anymore. Notice also that the maximum of N_χ occurs around $m_\chi \sim 3$ GeV because below this value the evaporation is important, yielding fewer N_χ, and above that the number of DM particles passing through the Sun decreases as $\rho_\odot/m_\chi \simeq 0.3\,\mathrm{GeV\,cm}^{-3}/m_\chi$.

3.3.2 The minimum testable DM mass

In order to characterize how evaporation affects N_χ, one can define two quantities with dimension of a mass: the "evaporation" mass $m_{\rm evap}$ and the "minimum" mass $m_{\rm min}$. First, the evaporation mass is defined as the mass for which the inverse of the evaporation rate is equal to the age of the Sun $t_\odot \simeq 4.7 \times 10^9$ yrs, i.e., $E_\odot(m_{\rm evap}) \equiv 1/t_\odot$ [269].

Second, we introduce the mass $m_{\rm min}$, corresponding to the DM mass for which N_χ approaches the equilibrium value $C_\odot/E_\odot$, which is independent of σ_p. Quantitatively,

$$\left| N_\chi(m_{\rm min}) - \frac{C_\odot}{E_\odot} \right| \equiv 0.1\, N_\chi(m_{\rm min})\,, \tag{3.34}$$

where we arbitrarily chose 10% as a satisfactory level of N_χ approaching $C_\odot/E_\odot$. The standard lore regarding $m_{\rm evap}$ is that the evaporation rate becomes negligible when $m_\chi \geq m_{\rm evap}$; on the other hand, for $m_\chi \leq m_{\rm evap}$, the annihilation rate becomes negligible. As a consequence, one would expect that for $m_\chi \leq m_{\rm evap}$ the capture and evaporation processes are in equilibrium and the number of DM particles in the Sun can be approximated by the equilibrium value in Eq. (3.33), which does not depend on σ_p. What we want to point out here is that it is actually $m_{\rm min}$ (and not $m_{\rm evap}$) which qualifies the inability of extracting constraints on σ_p, since the number of DM particles N_χ is not sensitive to σ_p anymore, for $m_\chi \leq m_{\rm min}$.

We have found some simple fits of of $m_{\rm min}$ as a function of σ_p and $\langle\sigma_{\rm ann} v\rangle_\odot$

$$m_{\rm min} \simeq \left[2.5 + 0.15 \log_{10}\left(\frac{\sigma_p}{10^{-40}\,{\rm cm}^2}\right) - 0.15 \log_{10}\left(\frac{\langle\sigma_{\rm ann} v\rangle_\odot}{3\cdot 10^{-26}\,{\rm cm}^3/{\rm s}}\right)\right] {\rm GeV} \tag{3.35}$$

$$m_{\rm min} \simeq \left[2.7 + 0.15 \log_{10}\left(\frac{\sigma_p}{10^{-40}\,{\rm cm}^2}\right) - 0.15 \log_{10}\left(\frac{\langle\sigma_{\rm ann} v\rangle_\odot}{3\cdot 10^{-26}\,{\rm cm}^3/{\rm s}}\right)\right] {\rm GeV} \tag{3.36}$$

which are valid to better than 1%, in the interval: $10^{-42}\,{\rm cm}^2 \leq \sigma_p \leq 10^{-30}\,{\rm cm}^2$, $3\times 10^{-27}\,{\rm cm}^3/{\rm s} \leq \langle\sigma_{\rm ann} v\rangle_\odot \leq 3\times 10^{-25}\,{\rm cm}^3/{\rm s}$. In these intervals, the evaporation mass is always greater than $m_{\rm min}$.

A simple argument to understand the positive correlation between $m_{\rm min}$ and σ_p goes as follows. First of all, in the regime where capture and evaporation are the relevant processes, the larger m_χ, the more difficult is for nuclei to expel DM particles, so N_χ is larger. Then, increasing σ_p leads to more DM particles captured by the Sun, so larger N_χ. Therefore, $m_{\rm min}$ turns out to be larger.

In Fig. 3.6, we plot $m_{\rm min}$ in the (σ_p, m_χ) plane. The plot shows the region of parameter space where it is not possible to contrain σ_p with neutrino data from the Sun. For comparison, we also show some of the exclusion curves obtained in the analysis of Super-K data of Refs. [254, 263]. For instance, for $m_\chi \lesssim 4\,{\rm GeV}$, data on neutrinos from the Sun are not able to provide information on the DM-proton scattering cross section below $\sigma_p \lesssim 10^{-31}\,{\rm cm}^2$. On the other hand, for a given value of the scattering cross section there is a minimum DM mass (see Eqs. (3.35)-(3.36)) which can be probed by neutrino fluxes from the Sun. Increasing (decreasing) the annihilation cross section $\langle\sigma_{\rm ann} v\rangle_\odot$ leads to a smaller (bigger) $m_{\rm min}$ at fixed σ_p, as confirmed by Eqs. (3.35)-(3.36); the effect of

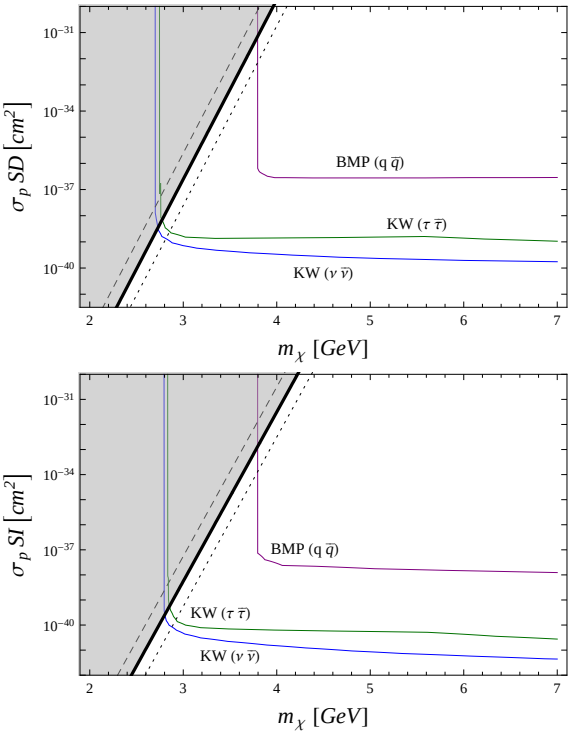

FIGURE 3.6: *The region in the* (m_χ, σ_p) *plane* (shaded area) *which is not testable by detectors of neutrinos from the Sun, as discussed in the text, for SD* (left panel) *and SI* (right panel) *interactions. The thick black line corresponds to* $m_{\rm min}$ *for the reference annihilation cross section* $\langle\sigma_{\rm ann}v\rangle_\odot = 3\times10^{-26}$ cm^3/s*, the dotted (dashed) black lines correspond to* $\langle\sigma_{\rm ann}v\rangle_\odot = 0.1\,(10)$ *times the reference value. For comparison, we also show the exclusion curves obtained in Ref. [254] (BMP) for* $\mathrm{DM\,DM} \to q\bar{q}$*, and in Ref. [263] (KW) for* $\mathrm{DM\,DM} \to \tau\bar{\tau}, \nu\bar{\nu}$*.*

varying the annihilation cross section by a factor of 10 with respect to its reference value is also shown in Fig. 3.6.

3.4 Conclusions

In this chapter we have considered the implications of the presence of GeV-scale DM in the Sun, the relevant processes it is subject to, and the constraints which can be placed on its properties, namely mass and cross sections, using neutrino data. We can summarize our main results as follows:

- for DM masses below about 4 GeV the effect of evaporation cannot be neglected, and we provide handy and accurate fitting functions for all the relevant processes of light DM in the Sun: annihilation Eq. (3.8), capture Eqs. (3.22)-(3.23) and evaporation Eqs. (3.28)-(3.29);
- we point out a limitation on extracting cross section bounds when evaporation is important; we provide expressions for the minimum DM mass below which the

number of DM particles in the Sun does not depend on σ_p, Eqs. (3.35)-(3.36), and the link with DM direct detection bounds disappears;

- we identify the region of the parameter space $(m_\chi, \sigma_p, \langle\sigma_{\rm ann} v\rangle_\odot)$ (see Fig. 3.6) which is not accessible by data on neutrino fluxes from the Sun.

Chapter 4

Antiprotons from Indirect detection

4.1 Introduction

In the years 2006-2009, the PAMELA collaboration satellite measured the flux of cosmic ray antiparticles observed on Earth. Its results [173, 179], also confirmed by AMS-02 [272], have shown a rise in the positron fraction at energies above 10 GeV . Such a rise is not compatible with the predictions of the standard model of cosmic rays acceleration and propagation, in which energetic protons (primaries) accelerated by astrophysical sources as SuperNova Remnants (SNR) [273, 274] interact with hydrogen and helium nuclei of the interstellar gas, generating antiparticles (secondaries). Futhermore, one could argue that an increase with energy of the positron fraction in cosmic rays most likely requires a primary source of electron-positron pairs [186].

An exciting possibility is that the rise is due to Dark Matter (DM) particles annihilating or decaying in the galactic disk, producing a flux of antiparticles that eventually reaches Earth in addition to standard cosmic rays. Such interpretation gives the interesting possibility to explain at the same time also the gamma-ray excess from the galactic center, as in Ref. [275]. This interpretation has however some drawbacks. First, the fact that no anomalous signal is seen in antiprotons data in the same range of energies puts severe constraints on DM properties [276] and tends to favour the so-called leptophylic models, in which DM only couples to leptons. In this scenario, antiprotons data can also be used to constrain DM properties [277, 278], since the positrons and antiprotons fluxes are correlated thanks to the electroweak corrections [192, 193, 279, 280]. Secondly, to fit the PAMELA and the AMS-02 data with a DM model, one usually needs a high cross section $\langle \sigma v \rangle \sim 10^{-22}\,\mathrm{cm}^3\,\mathrm{s}^{-1}$, much higher than the reference value of $3 \times 10^{-26}\,\mathrm{cm}^3\,\mathrm{s}^{-1}$

expected for a stable thermal relic. In order to justify this discrepancy, one can rely on several possible, albeit ad-hoc, explanations: introduce a boost factor, possibly due to clumpiness of the dark matter halo [281, 282] or to the presence of a narrow resonance just below the threshold [190, 283, 284]; invoke non-perturbative effects operating at small velocities that can enhance the present day thermal cross section [285–292] or otherwise discard the standard thermal relic picture for DM particles.

Of course, one may invoke astrophysical sources as an explanation for the positron rise. It has been known since a long time that a rise in the positron fraction can be due to the production of $e^{\pm}$ in pulsars [293]. In particular, young nearby pulsars plus a diffuse background of mature pulsars can fit PAMELA positrons data [294, 295]. The intrinsic degeneracy between the pulsar and the DM interpretation of PAMELA and AMS-02 data cannot be broken by positron data alone [296]; nevertheless the two scenarios can be distinguished by a future positive signal in the antiprotons channel since antiprotons are not expected to arise from pulsars.

In this work, made before the release of the antiproton data from the AMS-02 collaboration [184], we were trying to address the legitimate question that is whether a possible antiproton signal above the expected background would lead to a degeneracy problem between a possible DM origin and an astrophysical origin. As a benchmark model for the astrophysical source of antiprotons we take the one discussed in Ref. [297] to explain the rise of positrons and subsequently in Ref. [298] to predict the antiproton flux. The excess of positrons is due to secondary products of hadronic interactions inside the same SuperNova Remnants (SNR) that accelerate cosmic rays. Primary protons accelerated in shock regions of SNRs can undergo hadronic interactions not only at late times after diffusion in the galaxy, but also when they are still in the acceleration region. These interactions will produce a flux of antiparticles that will in turn be accelerated by the same sources of the standard primary cosmic rays, and will then give an additional cosmic ray flux at Earth with a spectral shape different from that of standard secondaries. A generic prediction of the model is a flattening and eventually a weak rise of the antiparticle-over-particle ratio in both positrons and antiprotons channel [298]. What makes this mechanism particularly interesting is that it does not need any new source of antiparticles (since positrons and antiprotons are generated by the same primary protons that accelerate in SNR) and that it predicts similar signals both in positrons and in antiprotons, precisely as many DM model do. This leads to a possible degeneracy in the shape of signals of very different origin, thus weakening the discriminating power of AMS-02.

The goal of this chapter is precisely to study this possible degeneracy by using the projected sensitivity of AMS-02 for the antiproton channel under the assumption that

the measurements of AMS-02 will show a significant antiproton excess above the background. We will assume in turn that this excess is due either to DM annihilation or to SNR and investigate whether the signal can be mimicked by SNR and DM annihilation, respectively. Our conclusions will be pessimistic: the expected sensitivity of an experiment like AMS-02 may not be able to disentangle the two possible sources.

The chapter is organized as follows. In Section 4.2 we review the basics of the mechanism for primary antiprotons from SNR and recall some results which will be used in the following. In Section 4.3, some standard material about the background of secondary antiprotons and their propagation is recalled, while in Section 4.4 we briefly discuss the possible antiproton contribution from DM. Then, in Section 4.5 we turn to investigate the degenercies which may arise in the interpretation of a putative signal in antiprotons eventually measured by AMS-02. We first assume the signal is due to DM and we try to fit it with SNR, and subsequently we analyse briefly the possibilty of a SNR signal intepreted as a DM. Finally, our conclusions are summarized in Section 4.6.

4.2 Antiprotons accelerated in supernova remnants

Here we briefly recall the basics of the astrophysical mechanism leading to primary antiprotons and we refer to the original papers, Refs. [297, 298], for further details. In particular, Ref. [298] derived the analytical prescription for the ratio $\bar{p}/p$ that we will use for our analysis. Simulations were also performed in Ref. [299].

Antiproton production inside the accelerator is described by the source function

$$Q_{\bar{p}}(E) = 2 \int_{E}^{E_{\rm max}} \mathrm{d}\mathcal{E} N_{\rm CR}(\mathcal{E}) \sigma_{p\bar{p}}(\mathcal{E}, E) n_{\rm gas} c, \tag{4.1}$$

where c is the speed of light, $N_{\rm CR}$ is the spectrum of protons inside the source, $n_{\rm gas}$ is the gas density in the shock region and $\sigma_{p\bar{p}}(\mathcal{E}, E)$ is the differential cross section for a proton of energy $\mathcal{E}$ to produce an antiproton of energy E in pp scattering, that we parametrize as in Refs. [300–302].

The energy $E_{\rm max}$ is the maximum energy of a proton accelerated in the SNR at the age relevant for this mechanism. We will treat $E_{\rm max}$ as a free parameter in our analysis. The factor of 2 comes from the fact that, in pp collisions, an antineutron can be produced with equal probability than an antiproton (in the isospin symmetry limit); they will then decay into an antiproton, contributing equally to the final flux. For that, we are assuming that the characteristic size of the SNR is larger than the mean path travelled by a neutron before decay.

After being produced, the antiprotons undergo acceleration around the shock region. The $\bar{p}/p$ flux ratio at this stage is [298]

$$\left.\frac{J_{\bar{p}}(E)}{J_p(E)}\right|_{\rm SNR} \sim 2\, n_1\, \epsilon\, c\, [\mathcal{A}(E) + \mathcal{B}(E)]\,, \tag{4.2}$$

where

$$\mathcal{A}(E) = \gamma \left(\frac{1}{\xi} + r^2\right) \int_m^E {\rm d}\omega\, \omega^{\gamma-3} \frac{D_1(\omega)}{u_1^2} \int_\omega^{E_{\rm max}} {\rm d}\mathcal{E}\, \mathcal{E}^{2-\gamma} \sigma_{p\bar{p}}(\mathcal{E}, \omega) \tag{4.3}$$

and

$$\mathcal{B}(E) = \frac{\tau_{\rm SN} r}{2E^{2-\gamma}} \int_E^{E_{\rm max}} {\rm d}\mathcal{E}\, \mathcal{E}^{2-\gamma} \sigma_{p\bar{p}}(\mathcal{E}, E). \tag{4.4}$$

The two terms $\mathcal{A}$ and $\mathcal{B}$ account for the antiparticles that are produced in the acceleration region and for the ones that are produced in the inner region of the SNR. In the above expressions, n_1 and u_1 are the background gas target density and the fluid velocity in the upstream region of the shock, fixed as in Ref. [298] to $2\,{\rm cm}^{-3}$ and $0.5 \times 10^{-8}\,{\rm cm/s}$, respectively.

The factor ξ in the $\mathcal{A}$ term gives the fraction of proton energy carried away by the produced secondary antiproton, which is here taken to be constant with energy. The validity of this assumption is discussed in Ref. [299]. In this work, we keep it as a constant and we consider it as a second free parameter for our analysis.

Both $\mathcal{A}$ and $\mathcal{B}$ include r, which is the compression factor of the shock, defined as the ratio of the fluid velocity upstream and downstream, and $\tau_{\rm SN}$ is the typical SNR age. The index γ gives the slope of the spectrum in momentum space, and it is related to the shock compression factor by $\gamma = 3r/(r-1)$. As we aim at comparing the SNR $\bar{p}/p$ ratio with the ones generated by DM annihilation, our choice is to make sure that our choice for r is consistent with the ones for the background antiproton spectrum (see also discussion below) and satisfies the relation $r = (2+\gamma_{\rm pr})/(\gamma_{\rm pr}-1)$, where $\gamma_{\rm pr} = 2-\gamma$ is the nuclei source spectral index for the Cosmic Ray (CR) propagation model, as defined in Ref. [303]; we then fix $r = 3.22$, which is consistent with $\gamma_{\rm pr} = 2.35$ of both KRA and THK models of propagation (cf. Table 4.1).

The $\epsilon = 1.26$ factor in front of Eq. (4.2) accounts for the fact that $\bar{p}$ production happens not only in pp collisions, but also in collisions with heavier nuclei, depending on the chemical composition of the gas and it is fixed as in Ref. [298]. The diffusion coefficient upstream the shock D_1 is given by

$$D_1(E) = \left(\frac{\lambda_c c}{3\mathcal{F}}\right) \left(\frac{E}{eB\lambda_c}\right)^{2-\beta}, \tag{4.5}$$

where, using the same notation as in [298], e is the unit charge, B is the magnetic field, $\mathcal{F} \sim (\Delta B/B)^2$ is the ratio of power in turbulent magnetic field over that in the ordered one, λ_c is the largest coherence scale of the turbulent component, and β is the index that characterizes the spectrum of B fluctuations. Following Ref. [298] we assume a Bohm-like diffusion index $\beta = 1$ and set $\mathcal{F} = 1/20$ and $B = 1\,\mu$G. In this way the expression for D_1 symplifies to

$$D_1(E) \simeq 3.3 \times 20 \times 10^{22}\, E_{\rm GeV}\, {\rm cm}^2\, {\rm s}^{-1}. \tag{4.6}$$

Note that this diffusion coefficient can be different from the one assumed in propagating particles through the galaxy, since it refers only to the acceleration region near the shock. Instead, diffusion in the galaxy affects in the same way both primary protons and antiprotons, so that the modifications in their spectra cancel out in the ratio. The flux ratio on Earth is then given by Eqs. (4.2), (4.3) and (4.4). All in all, we have used all parameters as in Ref. [298], except r (which, again, is chosen to be consistent with our choice of the propagation model).

As for the parameters to vary in our following analysis, we have chosen $E_{\rm max}$ and ξ: we checked that they are the parameters having the largest impact on our estimate of the flux ratio. We have solved the equations above numerically in order to estimate the ratio (4.2) and we have checked that our results match the ones in Ref. [298] for the same choice of parameters. Note that for the analysis we have not used the expression for the background illustrated in Ref. [298], but rather the one obtained from the DRAGON[304] numerical code, as illustrated in the next section. Finally, we have neglected energy losses, which are not relevant for antiprotons, and solar modulation, which has negligible effect for $E \gtrsim 10\,$GeV, to which we restrict our analysis.

4.3 Secondary antiprotons

As summarized above, the standard source of antiprotons in cosmic rays is the spallation of primary protons (*i.e.* protons accelerated in SNR) with nuclei of the interstellar medium (ISM). In a scenario in which the mechanism outlined in section 4.2 is operative, the total antiproton flux ratio would be given by the secondary component computed in this section, plus the primary component given by Eq. (4.2).

In general, the propagation of Cosmic Rays through the galaxy is regulated by the diffusion equation (see for instance Ref. [304])

$$\frac{\partial N_i}{\partial t} - \nabla \cdot (D\nabla - \mathbf{v}_c) N_i + \frac{\partial}{\partial p}\left(\dot{p} - \frac{p}{3}\nabla \cdot \mathbf{v}_c\right) N_i - \frac{\partial}{\partial p} p^2 D_{pp} \frac{\partial}{\partial p} \frac{N_i}{p^2} =$$

$$= Q_i(p,r,z) + \sum_{j>i} v\, n_{\rm gas}(r,z)\sigma_{ij}N_j - v\, n_{\rm gas}\sigma_i^{\rm in}(E_k)N_i, \tag{4.7}$$

where $N_i(p,\mathbf{x})$ is the number density of the i-th nuclear species, p is its momentum (not to be confused with the symbol for the proton) and v its velocity. D is the diffusion coefficient in the galaxy in real space, while D_{pp} is the diffusion coefficient in momentum space, that describes the diffusive reacceleration of CRs in the turbulent galactic magnetic field. The cross sections $\sigma_i^{\rm in}$ and σ_{ij} are the total inelastic cross section onto the ISM gas and the cross section for production of species i by fragmentation of species j, respectively. E_k is the kinetic energy of the particle under consideration. The ISM gas density is given by $n_{\rm gas}$ and $\mathbf{v}_c$ is the convection velocity. Finally, $Q_i(p,r,z)$ is the source function that describes the injection of primary CRs in the galaxy. The diffusion coefficients are parametrized as

$$D(\rho,R,z) = D_0\left(\frac{v}{c}\right)^{\eta} e^{|z|/z_t}\left(\frac{\rho}{\rho_0}\right)^{\delta} \tag{4.8}$$

and

$$D_{pp} = \frac{4}{3\delta(4-\delta^2)(4-\delta)}\frac{v_A^2 p^2}{D}, \tag{4.9}$$

where (R,z) are the usual cylindrical coordinates, z_t is the half-height of the cylindrical diffusion box, $\rho = pv/(Ze)$ is the particle rigidity and v_A is the Alfvén velocity.

To compute the secondary antiproton flux, we have assumed a spectrum of primary protons from SNR of the form $Q_p \sim \rho^{-\gamma_{\rm pr}}$, and then solved the diffusion Eq. (4.7) numerically using the public avaiable DRAGON code [304].

In the present work, we have considered two propagation models, namely KRA and THK, defined from the choice of propagation parameters and injection spectra illustrated in Table II of Ref. [303], found by looking for good fits to B/C data and PAMELA proton data. We report the values in Table 4.1 for convenience. We have not considered other propagation models here, as we expect different choices will not change dramatically our main conclusions.

To constrain DM models and some SNR parameters, the antiproton ratio data with energy larger than 10 GeV is applied. Since the relative high energy, solar modulation and the factors η and v_A in the propagation models do not play important role.

4.4 Antiprotons from DM

The production of CR's by DM annihilation is controlled by three factors: the density of DM particles in the galaxy, the details of the annihilation process (annihilation channel

Model	z_t	δ	$D_0(10^{28}\,\mathrm{cm^2\,s^{-1}})$	η	$v_A(\mathrm{km\,s^{-1}})$	γ	v_c
KRA	4 kpc	0.50	2.64	-0.39	14.2	2.35	0
THK	10 kpc	0.50	4.75	-0.15	14.1	2.35	0

TABLE 4.1: Diffusion parameter values used to propagate the secondary antiproton flux and the DM originated flux. No solar modulation is included.

and fragmentation functions) and finally propagation to Earth. The DM density profile of the Milky Way is rather uncertain, and this fact reflects in an uncertainty of $\mathcal{O}(\lesssim 1)$ order of magnitude in the resulting flux at Earth [194]. As a reference DM halo density profile, we have used the Navarro-Frenk-White (NFW) [305] profile

$$\rho_{\mathrm{NFW}}(r) = \frac{\rho_s}{(r/r_s)(1+r/r_s)^2}, \tag{4.10}$$

with $r_s = 24.42\,\mathrm{kpc}$ and $\rho_s = 0.184\,\mathrm{GeV\,cm^{-3}}$ and the isothermal profile [14]

$$\rho_{\mathrm{ISO}}(r) = \frac{\rho_s}{1+(r/r_s)^2}, \tag{4.11}$$

with $r_s = 4.38\,\mathrm{kpc}$ and $\rho_s = 1.387\,\mathrm{GeV\,cm^{-3}}$. The propagation of cosmic rays is still controlled by Eq. (4.7), with the source term $Q_{\bar{p}}$ now given by

$$Q_{\bar{p}}(\vec{r},t,p) = \frac{1}{2}\left(\frac{\rho_{\mathrm{DM}}(\vec{r})}{m_{\mathrm{DM}}}\right)^2 \frac{\mathrm{d}N_{\bar{p}}}{\mathrm{d}E}\langle\sigma v\rangle\,, \tag{4.12}$$

where $\langle\sigma v\rangle$ is the DM annihilation cross section and $\mathrm{d}N_{\bar{p}}/\mathrm{d}E$ is the number of antiprotons of a given energy E per DM annihilation. We have computed the antiproton flux at Earth using DRAGON [303] for various models of annihilating DM, as summarized in Table 4.2 and including electroweak corrections [192]. The models have been chosen so that they are not excluded by present antiproton data [194]. The diffusion parameters are still the ones given in Table 4.1.

In calculating the flux we include secondary antiprotons obtained from the scattering of primary proton with the interstellar gas.

4.5 Investigating the degeneracies: fit DM signal using SNR model

Our aim is to test whether a putative signal in the ratio of $\bar{p}/p$ eventually observed by AMS-02 leads to degeneracies in the interpretation of its origin: DM or astrophysics? To this end, we produce a set of mock AMS-02 data through a set of benchmark DM models

Name	Final state	Propagation model	DM mass (TeV)	σv_0 (cm^3/s)	Profile
bKN	$b\bar{b}$	KRA	3	7×10^{-25}	NFW
muKN	$\mu^+\mu^-$	KRA	4	8×10^{-23}	NFW
muKI	$\mu^+\mu^-$	KRA	4	1×10^{-22}	ISO
WKN	W^+W^-	KRA	3	7×10^{-25}	NFW
bTN	$b\bar{b}$	THK	3	7×10^{-25}	NFW
muTN	$\mu^+\mu^-$	THK	4	8×10^{-23}	NFW
muTI	$\mu^+\mu^-$	THK	4	1×10^{-22}	ISO
WTN	W^+W^-	THK	3	7×10^{-25}	NFW

TABLE 4.2: DM annihilation models considered in this analysis.

and ask if these data could be interpreted as due to SNR, based on the astrophysical mechanism described in section 4.2 (and using the same propagation model).

As we mentioned already, we consider as free parameters in the SNR model the fraction of proton energy carried away by the antiproton ξ, and the energy cutoff E_{max}. In order to investigate possible degeneracies, we have performed the following steps:

- obtain the CR background expected for $\bar{p}/p$ using DRAGON, as described in section 4.3;
- produce mock data for AMS, as described in the following;
- create a grid in the plane (E_{max}, ξ), in a range of values of 1 TeV $< E_{\mathrm{max}} <$ 10 TeV and $0.1 < \xi < 0.5$ [297, 298];
- solve Eq. (4.2) numerically in order to get the ratio of $\bar{p}/p$ from SNR, as described in section 4.2 on the grid, assuming the same cosmic ray background as the one used for DM models;
- calculate the χ^2, summed on each bin for a given mock dataset, between the DM mock flux and the SNR flux. We have performed this calculation on every point of the grid to get a function $\chi^2(E_{\mathrm{max}}, \xi)$;
- estimate the minimum of the χ^2 for each mock dataset. Then, assuming a Gaussian distribution, the confidence contours in the plane (E_{max}, ξ) are plotted. The area within the contours will give us a measure of the degeneracy between DM and SNR interpretation of the mock data.

To create the mock data, we have considered a series of benchmark (fiducial) DM models and calculate the corresponding mock data for all of them, assuming a propagation method for Cosmic Rays (KRA or THK) and a DM halo profile. In particular, we

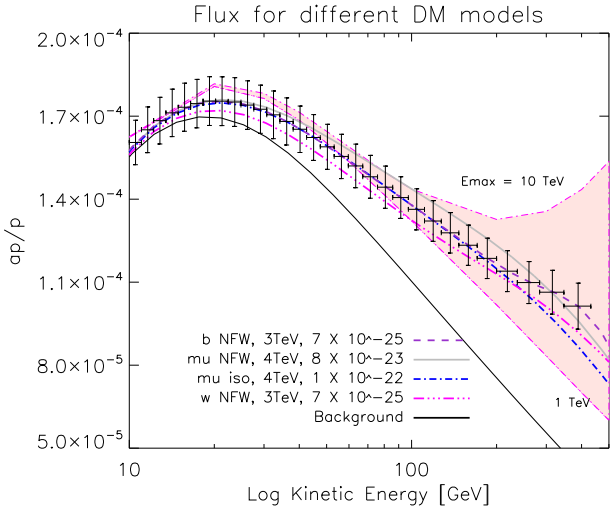

FIGURE 4.1: The flux of $\bar{p}/p$ is plotted as a function of the kinetic energy for different DM models. The labels in the legend refer to annihilation channel, the DM halo profile, DM mass and annihilation cross section (in units of cm^3/s), respectively. The background from Cosmic Rays is shown in solid black line. For the first model we also overplot the corresponding mock data. The pink band corresponds to the region spanned by SNR when $\xi = 0.17$, as in [297] and 1 TeV $< E_{\mathrm{max}} <$ 10 TeV. The propagation model used is KRA.

have studied non-relativistic DM annihilating into two standard model (SM) fermions or gauge bosons with 100% branching ratio, such as $\chi\chi \to b\bar{b}$, $\chi\chi \to \mu^+\mu^-$, and $\chi\chi \to W^+W^-$. Their cross sections are chosen in such a way that they are consistent with the current PAMELA antiproton flux [179] and also not excluded by the other indirect detection observations: the positron fraction from PAMELA [173] and AMS-02 [272], Fermi LAT's gammay ray observation of dwarf galaxies [306] and diffuse background [201]. The DM benchmark models with different final states, annihliation cross section and density profiles are listed in Tab. 4.2.

To generate the AMS-02 mock data, we have first set the width of the energy bins based on the detector energy resolution to be [307]

$$\Delta E/E = (0.042(E/\mathrm{GeV}) + 10)\,\%. \tag{4.13}$$

The mock data have as central value of $\bar{p}/p$ the one of the benchmark model in the centre of each bin. Uncertainties around each point have been calculated by summing up in quadrature systematic and statistical errors for the $\bar{p}/p$ ratio. The statistical error is approximately given by [194, 308]

$$\frac{\Delta(\bar{p}/p)^{\mathrm{stat}}}{\bar{p}/p} \sim \frac{\Delta N_{\bar{p}}^{\mathrm{stat}}}{N_{\bar{p}}} = \frac{1}{\sqrt{N_{\bar{p}}}}. \tag{4.14}$$

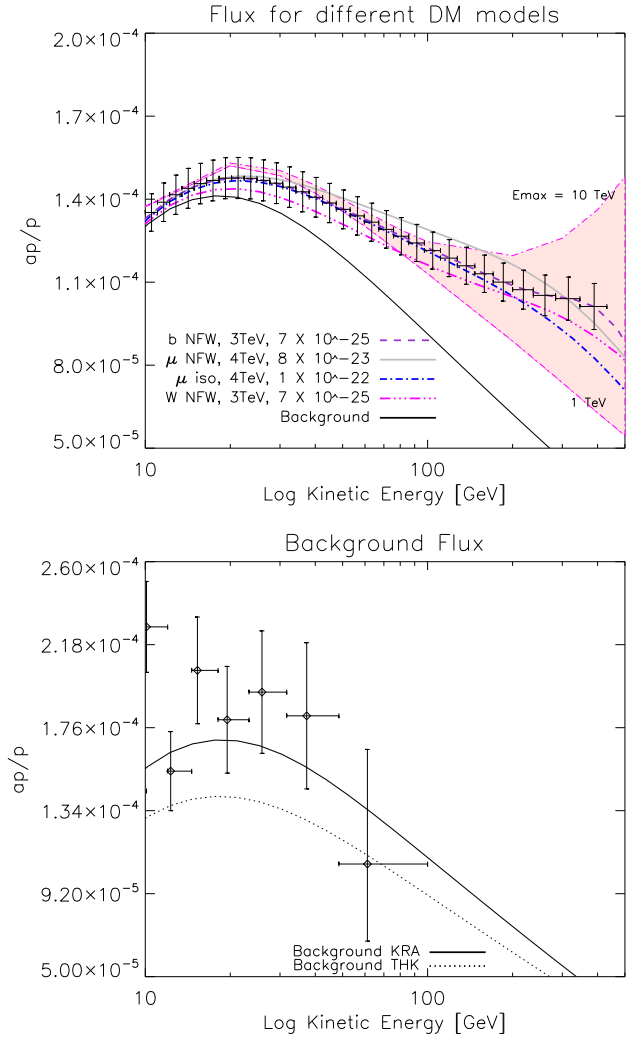

FIGURE 4.2: Same as Fig.4.1 but with THK propagation model. In the lower panel we show PAMELA data [179] as compared to the same background curve as in Fig.4.1 for KRA and to the upper panel of this Figure for THK. We keep the same range as in the other panel to facilitate the comparison.

We have fixed the relative systematic error to be $\Delta N_{\bar{p}}^{\rm syst}/N_{\bar{p}} = 10\%$. Here $N_{\bar{p}}$ is the expected number of antiproton events per bin and is related to the specification parameters of the experiment via the relation $N_{\bar{p}} = \epsilon\ a_{\bar{p}}\ \Phi_i \Delta E \Delta t_i$. In particular, we have set the efficiency $\epsilon_i = 1$, the geometrical acceptance of the instrument $a_{\bar{p}} = 0.2\, m^2$ sr and a reference operation time $\Delta t_i = 1$ yr. The flux Φ_i is the $\bar{p}$ flux in the centre of the bin i, while ΔE is the energy resolution for our binning, as found in Eq. (4.13). Mock data are plotted in Fig. 4.1 for KRA and Fig. 4.2 for THK propagation models. They extend up to $E_k \simeq 400\,$GeV; having a higher energy reach would probably improve the discrimination between DM and SNR models.

We are now able to quantify the capability of the SNR to reproduce possible antiproton fluxes generated by the DM models (as forecasted for the AMS-02). The SNR fluxes are

calculated on the grid of values $(E_{\rm max}, \xi)$. Confidence contours in the plane $(E_{\rm max}, \xi)$ are shown in Fig. 4.3 and Fig. 4.4 for all benchmarks DM models in Tab. 4.2. Different colours represent 1σ to 5σ contours. We have assumed for simplicity a Gaussian distribution. Fig. 4.3 shows results for the four DM models in Tab. 4.2 whose propagation follows the KRA prescription. We see that for all annihilation channels (b, μ, W) there can be degeneracy between the corresponding DM model and SNR flux. A point in the grey region indicates that for those choice of $\xi, E_{\rm max}$ the SNR flux is compatible (and therefore degenerate) with mock data based on a DM hypothesis at 5σ. In particular, lower values of $E_{\rm max}$ allow for a larger degeneracy in all cases investigated here. The b- and W-channels seem to prefer larger values of ξ (with relative minimum at the edge of the grid) while the μ-channel has a minimum χ^2 for lower values of ξ. Notice though that the tendency towards lower values of ξ disappears when we change DM profile (Fig. 4.3, panel (c)) or when we change the propagation model, as in (Fig. 4.4, panel (b)). The values of the minimal χ^2 and number of degrees of freedom for all cases is shown in Tab.(4.3) for all models considered in the analysis.

There is indication that some portion of parameter space might be excluded by data on boron to carbon ration, as shown in [309]. However, we cannot make a direct comparison with the results of this paper because of a different choice of parameters. In particular our case corresponds indeed to $n_{gas} = 2\,{\rm cm}^{-3}$, $B = 1\mu G$ and $v = 0.5 \times 10^{-8}\,{\rm cm/\,s}$, which can be compared with Fig.3 of their analysis (upper panel) for $K_B = 20$. We are however fixing r = 3.22 as explained in our Section (4.2) for consistency with the background spectrum. The paper [309] uses instead r = 4.

Name	Minimum χ^2
bKN	6.1
muKN	6.3
muKI	6.7
WKN	21.0
bTN	5.6
muTN	5.6
muTI	8.6
WTN	8.6

TABLE 4.3: χ^2 values for the models considered in this analysis. In all cases the number of degrees of freedom is N = 30 (data points) - 2 (parameters) = 28.

Finally, we have investigated the degeneracy following the inverse logic with respect to the analysis done so far; instead of assuming a DM benchmark model and test whether we can find a combination of (ξ, E_{max}) that fit our mock data, we reversed the procedure: we first produced a set of mock AMS-02 data through a benchmark SNR model and asked if these data could be interpreted as originated from DM models (using the

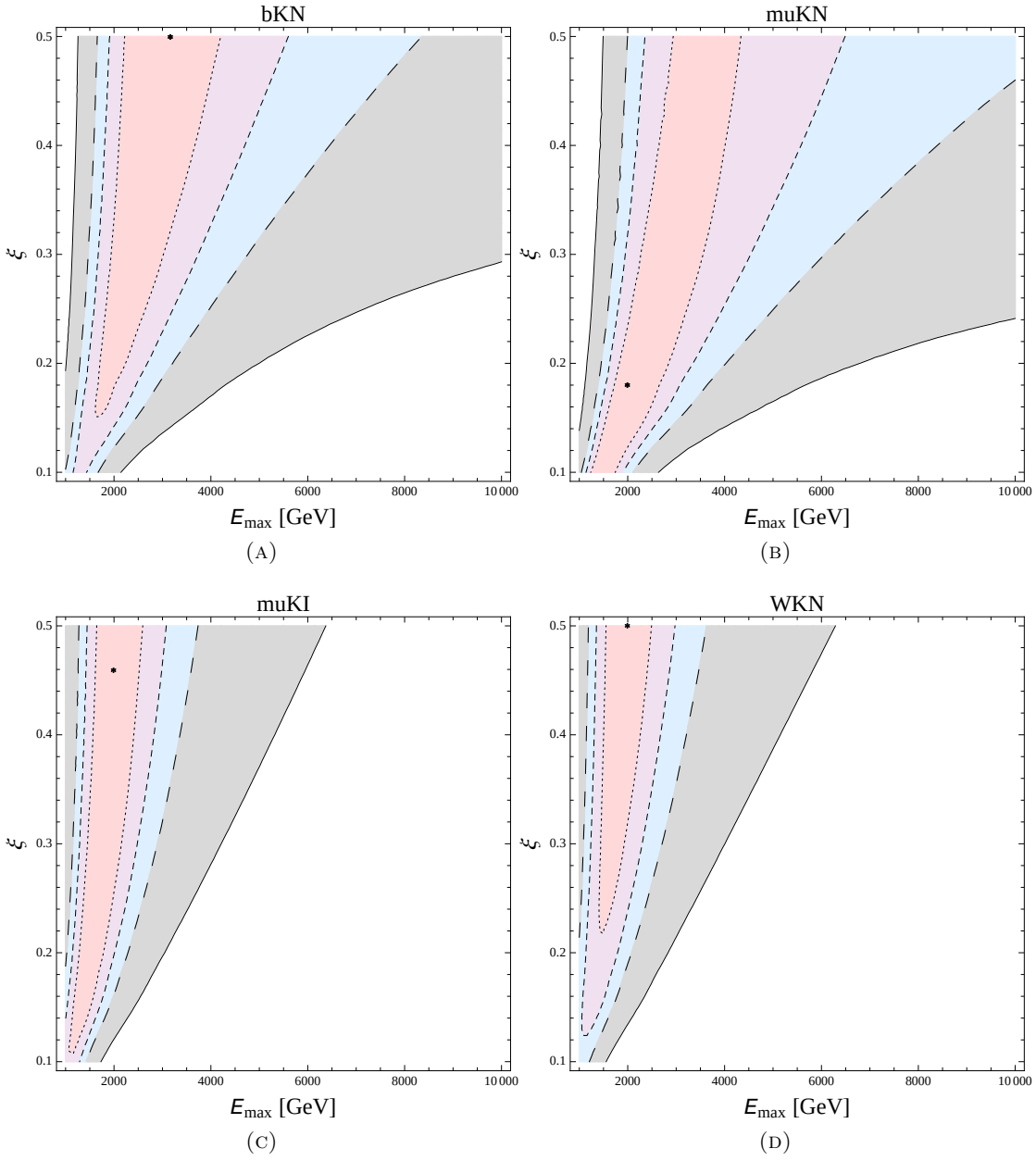

FIGURE 4.3: Confidence contours for different DM models with propagation KRA. The names of the models refer to the ones given in Table 4.2. Colours indicate 1, 2, 3, 5 σ contours. The black dot corresponds to the minimum χ^2 value (relative minimum within the chosen grid).

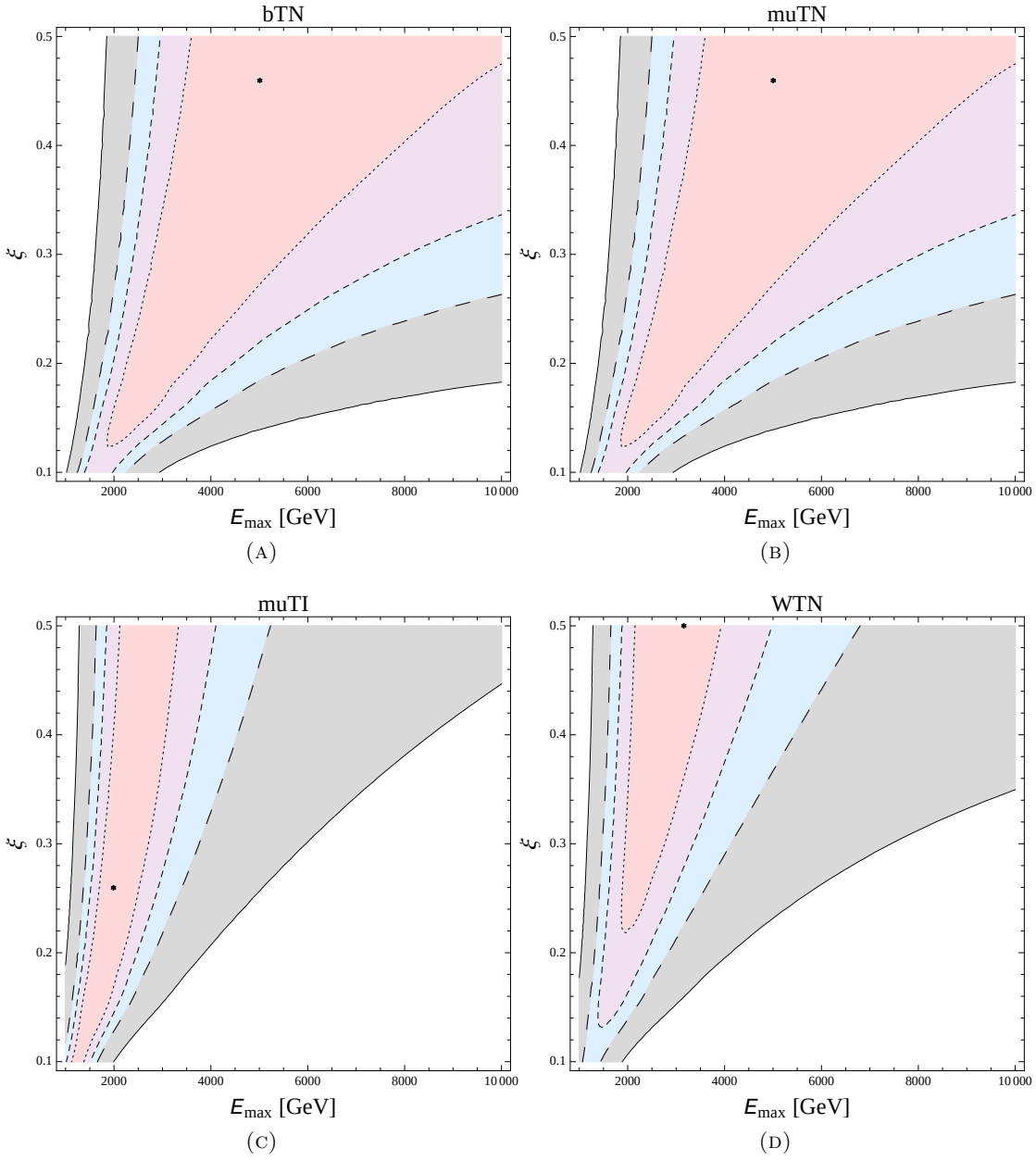

(A) (B) (C) (D)

FIGURE 4.4: Confidence contours for different DM models with propagation THK. The names of the models refer to the ones given in Tab. 4.2. Colours indicate 1, 2, 3, 5 σ contours. The black dot corresponds to the minimum χ^2 value (relative minimum within the chosen grid).

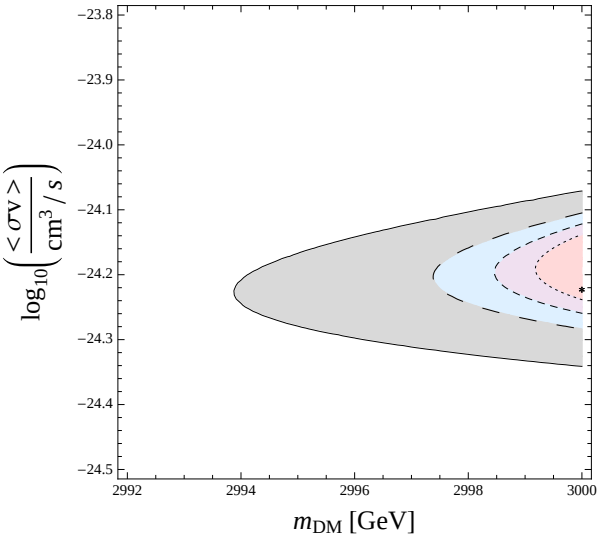

FIGURE 4.5: Confidence contours in the parameter space $(\langle\sigma v\rangle, M)$, for the $b\bar{b}$ annihilation channel and with KRA propagation model, as obtained fixing $E_{max} = 2500$ GeV and $\xi = 0.14$ in the SNR benchmark model. The (relative) minimum χ^2 within the grid for this case is 9.1 for 28 degrees of freedom. Colours indicate 1, 2, 3, 5 σ contours.

same propagation model). As expected, also in this case it is possible to find some degeneracy. In Fig. 4.5 we show an example of such a degeneracy, which, for the chosen SNR benchmark model and DM annihilation channel, peaks around a very small range in mass. This is in agreement with the value found in model bKN. The extension of the degeneracy does not vary much with the annihilation channels.

4.6 Conclusions

Finding indirect signatures of DM is certainly one of the main targets of many current experimental efforts. Nevertheless, even in the optimistic case in which a signal above the expected background is found (and this doesn't seem to be the case in preliminary analysis [184]), the most pressing question is whether such a signal can be ascribed to DM annihilation (or decay) beyond any reasonable doubt. This is a legitimate question as there are astrophysical sources which can mimic a signal, the best example being pulsars which can generate a positron excess. In this chapter we have investigated this degeneracy problem focussing our attention on the antiproton signal. Indeed, antiprotons may be generated as secondaries accelerated in supernova remnants and we have shown that a potential signal from DM annihilation can be mimicked by such an astrophysical source.

Chapter 5

Dark Matter Search at Collider using Effective Field Theories

5.1 Introduction

In order to avoid the overwhelming model-dependence introduced by the plethora of DM models discussed in the literature, DM searches at the LHC have made use of the Effective Field Theory (EFT) [70, 245, 310–318]. This approach is a very powerful and economical way to grasp the main features of a physical process, only in terms of the degrees of freedom which are excited at the scale of the process. EFT techniques are successfully applied in many branches of physics, and in particular they have become a standard way to present experimental results for DM searches.

However, as far as collider searches are concerned, with the LHC being such a powerful machine, it is not guaranteed that the events used to constrain an effective interaction are not occurring at an energy scale larger than the cutoff scale of the effective description. In other words, some (or many) events of DM production may occur with such a high momentum transfer that the EFT is not a good description anymore. The question about the validity of the EFT for collider searches of DM has become pressing (see also Refs. [245, 248–250, 319–325]), especially in the perspective of analysing the data from the future LHC run at (13-14) TeV.

In order to clarify this point better, let us consider a simple example, which will be the *leitmotiv* throughout this work. Let us consider DM to be a fermion, whose interactions with quarks are mediated by a heavy scalar particle S through the Lagrangian

$$\mathscr{L}_{\rm UV} \supset \frac{1}{2}M^2 S^2 - g_q \bar{q} q S - g_\chi \bar{\chi}\chi S \,. \tag{5.1}$$

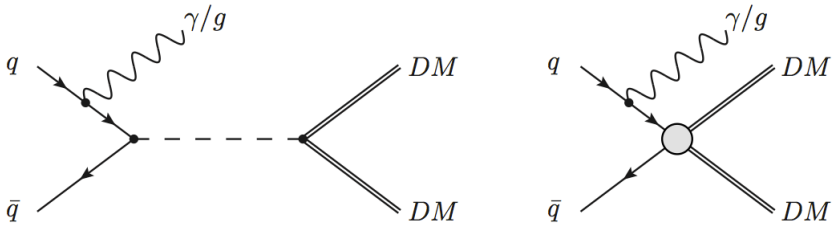

FIGURE 5.1: *The Feynman diagrams for DM pair production with ISR of a photon or jet, for a model with scalar exchange* (left panel) *and its effective operator* (right panel). *We omitted the diagrams where the radiation is emitted from the anti-quark.*

At energies much smaller than M the heavy mediator S can be integrated out, resulting in a tower of non-renormalizable operators for the fermionic DM interactions with quarks. The lowest-dimensional operator has dimension six

$$\mathcal{O}_S = \frac{1}{\Lambda^2}(\bar{\chi}\chi)(\bar{q}q)\,, \tag{5.2}$$

and the matching condition implies

$$\frac{1}{\Lambda^2} = \frac{g_\chi g_q}{M^2}\,. \tag{5.3}$$

The Feynman diagrams for the processes under consideration are depicted in Fig. 5.1. The processes where a quark-jet is emitted from an initial gluon also contribute to the signal, but are suppressed by a factor of about 4 at 8 TeV LHC with respect to the gluon emission, and for simplicity we will not consider them in this chapter. The procedure of integrating out the heavy mediator and retaining the operator of lowest dimension can be viewed in terms of the expansion of the heavy particle propagator

$$\frac{1}{Q_{\rm tr}^2 - M^2} = -\frac{1}{M^2}\left(1 + \frac{Q_{\rm tr}^2}{M^2} + \mathcal{O}\left(\frac{Q_{\rm tr}^4}{M^4}\right)\right)\,, \tag{5.4}$$

where only the leading term $1/M^2$ is kept. The higher-order terms in the expansion correspond to higher-dimensional operators. It is obvious that retaining only the lowest-dimensional operator is a good approximation as long as

$$Q_{\rm tr}^2 \ll M^2 \sim \Lambda^2 \tag{5.5}$$

Thus, the parameter $Q_{\rm tr}/M$ characterizes the goodness of the truncation of the tower of effective operators to the lowest dimensional ones. A DM production event occurs at an energy at which the EFT is reliable as long as $Q_{\rm tr} < M$, where $Q_{\rm tr}$ is the momentum transfer in the process; this, together with the condition of perturbativity of the couplings

$g_{q,\chi} < 4\pi$, implies

$$\Lambda > \frac{Q_{\rm tr}}{\sqrt{g_q g_\chi}} > \frac{Q_{\rm tr}}{4\pi}\,. \tag{5.6}$$

If, in addition, one assumes the momentum transfer to occur in the s-channel, then kinematics imposes $Q_{\rm tr} > 2m_{\rm DM}$, so Eq. (5.6) becomes

$$\Lambda > \frac{m_{\rm DM}}{2\pi}\,. \tag{5.7}$$

This is a very minimal requirement which is refined event-by-event by the stronger condition Eq. (5.6), which depends on $m_{\rm DM}$ through $Q_{\rm tr}$. It is clear that the details of condition (5.6) depend on the values of the couplings in the UV theory. In the following, for definiteness, we will mostly identify the mass of the new degrees of freedom M with the suppression scale of the operator Λ. This is equivalent to consider couplings in the UV theory of $\mathcal{O}(1)$. So, we will deal with the condition (but we will discuss also the impact of taking couplings larger than 1)

$$Q_{\rm tr} \lesssim \Lambda\,. \tag{5.8}$$

In Ref. [248] we have started the discussion of the limitations to the use of the EFT approach for DM searches at the LHC by adopting a toy model where the heavy mediator is exchanged in the s-channel and by introducing a few quantities which quantify the error made when using effective operators to describe processes with very high momentum transfer. Our criteria indicated up to what cutoff energy scale, and with what precision, the effective description is valid, depending on the DM mass and couplings. In the following sections (5.2,5.3,5.4 and 5.5), taken on [249] we significantly extend our previous work along four different directions:

1. we consider the full list of operators connecting fermion DM to quarks and corresponding to integrating out the heavy mediator in the s-channel;
2. we provide analytical results for the validity of the EFT description for both $\sqrt{s} = 8$ TeV and 14 TeV;
3. we follow a MonteCarlo approach to assess the validity of the EFT and compare this fully numerical results with the analytical calculations;
4. we apply our results to revisit the current experimental bounds on the effective operator scale; by requiring that only the events which are "safe" from the EFT point of view should be considered, the bounds get weakened.

The rest of the chapter is organized as follows. In Section 5.3 we present and discuss the results of our analytical approach to assess the validity of EFT. In Section 5.4, the

fully numerical approach is described and the results are compared with the analytical calculations. In Section 5.5 we analyze the impact of the limitation of the validity of the EFT for the current limits from the LHC searches. In section 5.6 we repeat a similar analysis for EFT operators coming from low energy expansions of t-channel mediators. Finally, we draw our conclusions in Section 5.7. The details of the analytical results can be found in the Appendix B.1.

5.2 S-Channel: An estimate of the momentum transfer

Many LHC searches for DM are based on the idea of looking at events with missing energy plus a single jet or photon, emitted from the initial state. At the parton level the process is described by

$$q(p_1) + \bar{q}(p_2) \to \chi_1(p_3) + \chi_2(p_4) + \text{jet}(k)\,. \tag{5.9}$$

Let us see what happens if the energy exchanged is in the s-channel. Notice that, in the cases where the heavy mediator is exchanged in the t- or u-channels, one can always Fierz-rotate the corresponding non-renormalizable operator to give rise to (a set of) operators where the momentum is transferred in the s-channel. However, the basis of operators considered in experimental searches corresponds to s-channel mediation only.

In the pp center of mass frame, the proton momenta take the explicit form $P_1 = (\sqrt{s}/2, 0, 0, \sqrt{s}/2)$, $P_2 = (\sqrt{s}/2, 0, 0, -\sqrt{s}/2)$, where s is the center-of-mass energy. Ignoring the small transverse momenta of the partons, we can write the constituent quark momenta as fractions of these four-vectors

$$p_1 = x_1 P_1, \qquad p_2 = x_2 P_2\,. \tag{5.10}$$

The four-momentum of the jet (assuming it is massless) is given in terms of transverse momentum $p_{\rm T}$, pseudo-rapidity η and azimuth angle ϕ by

$$k = (p_{\rm T}\cosh\eta, p_{\rm T}\cos\phi, p_{\rm T}\sin\phi, p_{\rm T}\sinh\eta)\,. \tag{5.11}$$

If the production of the DM takes place through the s-channel, then in the propagator it will appear the quantity $Q_{\rm tr}^2 - M^2$, where

$$Q_{\rm tr}^2 = (p_1 + p_2 - k)^2 = x_1 x_2 s - \sqrt{s}\, p_{\rm T}\left(x_1 e^{-\eta} + x_2 e^{\eta}\right)\,. \tag{5.12}$$

The condition that $Q_{\rm tr}^2 > 0$ is equivalent to the condition that the energy of the jet should be smaller than the energy of the parton it is emitted from. The expression

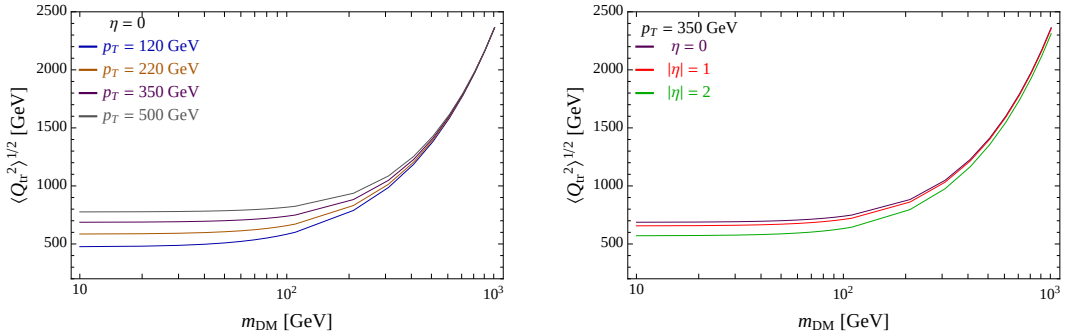

FIGURE 5.2: *The momentum transfer in the s-channel in Eq. (5.12), weighted with PDFs, as a function of* $m_{\rm DM}$*, for different choices of* $p_{\rm T}, \eta$ *of the radiated jet. We considered* $\sqrt{s} = 8\,\text{TeV}$.

(5.12) is maximized at the rapidity value $e^{2\eta} = x_1/x_2$ corresponding to $Q^2_{\rm tr}\big|_{\rm max} = x_1 x_2 s - 2\sqrt{s}\, p_{\rm T}\sqrt{x_1 x_2}$.

To assess the validity of the EFT, we first adopt a procedure which, albeit not rigorous, gives an idea of the error one might make in adopting the EFT. The advantage of this procedure is that it is model-independent in the sense that it does not depend on the particular UV completion of the EFT theory. A simple inspection of the expansion (5.4) tells us that the EFT is trustable only if $Q^2_{\rm tr} \ll M^2$ and we take for the typical value of $Q_{\rm tr}$ the square root of the averaged squared momentum transfer in the s-channel, where the average is computed properly weighting with PDFs [326, 327]

$$\langle Q^2_{\rm tr}\rangle = \frac{\sum_q \int {\rm d}x_1 {\rm d}x_2 \left[f_q(x_1) f_{\bar q}(x_2) + f_q(x_2) f_{\bar q}(x_1)\right] \theta(Q_{\rm tr} - 2m_{\rm DM}) Q^2_{\rm tr}}{\sum_q \int {\rm d}x_1 {\rm d}x_2 \left[f_q(x_1) f_{\bar q}(x_2) + f_q(x_2) f_{\bar q}(x_1)\right] \theta(Q_{\rm tr} - 2m_{\rm DM})}\,. \tag{5.13}$$

The integration in x_1, x_2 is performed over the kinematically allowed region $Q_{\rm tr} \geq 2m_{\rm DM}$ and we have set the renormalization and factorization scales to $p_{\rm T} + 2[m^2_{\rm DM} + p^2_{\rm T}/4]^{1/2}$, as often done by the LHC collaborations (see e.g. Ref. [240]). The results are plotted in Fig. 5.2 as a function of the DM mass $m_{\rm DM}$ and for different choices of $p_{\rm T}$ and η of the radiated jet. From Fig. 5.2 we see that the lower the jet $p_{\rm T}$, the lower the momentum transfer is, and therefore the better the EFT will work. The same is true for smaller DM masses. These behaviors, which are due to the fact we have restricted the average of the mometum transfer to the kinematically allowed domain, will be confirmed by a more rigorous approach in the next section. Notice that $\langle Q^2_{\rm tr}\rangle^{1/2}$ is always larger than about 500 GeV, which poses a strong bound on the cutoff scale Λ: when the coupling constants g_q and g_χ are close to their perturbative regime, from the condition (5.6) we get $\Lambda \gtrsim 50$ GeV, but when the couplings are of order unity, one gets a much stronger bound $\Lambda \gtrsim 500$ GeV.

5.3 S-Channel, Validity of the EFT: analytical approach

5.3.1 Operators and cross sections

The starting point of our analysis is the list of the 18 operators reported in Tab. 5.1 which are commonly used in the literature [310]. We have considered not only the operators connecting the DM fermion to quarks (D1-D10), but also those involving gluon field strengths (D11-D14). Furthermore, the operators can originate from heavy mediators exchange in the s-channel. For instance, the D1' (D5) operators may be originated by the tree-level s-channel exchange of a very heavy scalar (vector) boson S (V_μ), with lagrangians

$$\mathscr{L}_{\mathrm{D1'}} \supset \frac{1}{2}M^2S^2 - g_q\bar{q}qS - g_\chi\bar{\chi}\chi S\,, \tag{5.14}$$

$$\mathscr{L}_{\mathrm{D5}} \supset \frac{1}{2}M^2V^\mu V_\mu - g_q\bar{q}\gamma^\mu qV_\mu - g_\chi\bar{\chi}\gamma^\mu\chi V_\mu\,. \tag{5.15}$$

Notice the presence of the "primed" operators $D1'$–$D4'$, very similar to the ones often considered $D1$–$D4$, respectively, but with a different normalization, independent of the quark masses. In fact, they may arise from integrating out heavy scalars which do not take a vacuum expectation value and therefore do not give rise to quark masses. [1]

We have computed the tree-level differential cross sections in the transverse momentum p_{T} and rapidity η of the final jet for the hard scattering process with gluon radiation from the initial state $f(p_1)+\bar{f}(p_2)\to\chi(p_3)+\chi(p_4)+g(k)$, where f is either a quark (for operators D1-D10), or a gluon (for operators D11-D14). The results are conveniently written in terms of the momentum transfer in the s-channel

$$Q^2_{\mathrm{tr}} = (p_1+p_2-k)^2 = x_1x_2s - \sqrt{s}\,p_{\mathrm{T}}\left(x_1e^{-\eta}+x_2e^{\eta}\right)\,, \tag{5.17}$$

where x_1, x_2 are the fractions of momentum carried by initial partons and η, p_{T} are the pseudo-rapidity and the transverse momentum of the final state gluon, respectively. The expressions are of course valid for all admitted values of the parameters. It's only when integrated numerically over the PDFs and over η, p_{T} that the dependence on these

[1] A normalization proportional to the quark mass is common in many models motivated by flavour physics, but in general the coefficient Λ^3 at the denominator can have a different form. For example, if the effective operators come from a Naturalness-motivated new physics theory like Supersymmetry or Composite Higgs Models, assuming a $U(2)^3$ flavour symmetry [328, 329] the normalization would be

$$\lambda_{t,b}\frac{1}{\Lambda^2}\frac{m_q}{m_{t,b}} \tag{5.16}$$

where Λ is an energy scale of the order some TeV related to the Electroweak Symmetry Breaking and $m_{t,b}, \lambda_{t,b}$ are the mass and the Yukawa coupling with the Higgs of the top/bottom quark, depending on whether the quark q is up-like or down-like. In the present work, we will be agnostic about this point, and we will keep both the primed and unprimed operators into account on the same footing as all others.

Name	Operator	Coefficient
D1	$\bar{\chi}\chi\ \bar{q}q$	m_q/Λ^3
D1'	$\bar{\chi}\chi\ \bar{q}q$	$1/\Lambda^2$
D2	$\bar{\chi}\gamma^5\chi\ \bar{q}q$	im_q/Λ^3
D2'	$\bar{\chi}\gamma^5\chi\ \bar{q}q$	i/Λ^2
D3	$\bar{\chi}\chi\ \bar{q}\gamma^5 q$	im_q/Λ^3
D3'	$\bar{\chi}\chi\ \bar{q}\gamma^5 q$	i/Λ^2
D4	$\bar{\chi}\gamma^5\chi\ \bar{q}\gamma^5 q$	m_q/Λ^3
D4'	$\bar{\chi}\gamma^5\chi\ \bar{q}\gamma^5 q$	$1/\Lambda^2$
D5	$\bar{\chi}\gamma_\mu\chi\ \bar{q}\gamma^\mu q$	$1/\Lambda^2$
D6	$\bar{\chi}\gamma_\mu\gamma^5\chi\ \bar{q}\gamma^\mu q$	$1/\Lambda^2$
D7	$\bar{\chi}\gamma_\mu\chi\ \bar{q}\gamma^\mu\gamma^5 q$	$1/\Lambda^2$
D8	$\bar{\chi}\gamma_\mu\gamma^5\chi\ \bar{q}\gamma^\mu\gamma^5 q$	$1/\Lambda^2$
D9	$\bar{\chi}\sigma_{\mu\nu}\chi\ \bar{q}\sigma^{\mu\nu} q$	$1/\Lambda^2$
D10	$\bar{\chi}\sigma_{\mu\nu}\gamma^5\chi\ \bar{q}\sigma^{\mu\nu} q$	i/Λ^2
D11	$\bar{\chi}\chi\ G^{\mu\nu}G_{\mu\nu}$	$\alpha_s/4\Lambda^3$
D12	$\bar{\chi}\gamma^5\chi\ G^{\mu\nu}G_{\mu\nu}$	$i\alpha_s/4\Lambda^3$
D13	$\bar{\chi}\chi\ G^{\mu\nu}\tilde{G}_{\mu\nu}$	$i\alpha_s/4\Lambda^3$
D14	$\bar{\chi}\gamma^5\chi\ G^{\mu\nu}\tilde{G}_{\mu\nu}$	$\alpha_s/4\Lambda^3$

TABLE 5.1: *Operators used throughout this work. The nomenclature is mostly taken from Ref. [245].*

values comes in. We obtain

$$\left.\frac{\mathrm{d}^2\hat{\sigma}}{\mathrm{d}p_\mathrm{T}\mathrm{d}\eta}\right|_{D1'} = \frac{\alpha_s}{36\pi^2}\frac{1}{p_\mathrm{T}}\frac{1}{\Lambda^4}\frac{\left[Q_\mathrm{tr}^2-4m_\mathrm{DM}^2\right]^{3/2}\left[1+\frac{Q_\mathrm{tr}^4}{(x_1x_2s)^2}\right]}{Q_\mathrm{tr}} \tag{5.18}$$

$$\left.\frac{\mathrm{d}^2\hat{\sigma}}{\mathrm{d}p_\mathrm{T}\mathrm{d}\eta}\right|_{D4'} = \frac{\alpha_s}{36\pi^2}\frac{1}{p_\mathrm{T}}\frac{1}{\Lambda^4}Q_\mathrm{tr}\left[Q_\mathrm{tr}^2-4m_\mathrm{DM}^2\right]^{1/2}\left[1+\frac{Q_\mathrm{tr}^4}{(x_1x_2s)^2}\right] \tag{5.19}$$

$$\left.\frac{\mathrm{d}^2\hat{\sigma}}{\mathrm{d}p_\mathrm{T}\mathrm{d}\eta}\right|_{D5} = \frac{\alpha_s}{27\pi^2}\frac{1}{p_\mathrm{T}}\frac{1}{\Lambda^4}\frac{\left[Q_\mathrm{tr}^2-4m_\mathrm{DM}^2\right]^{1/2}\left[Q_\mathrm{tr}^2+2m_\mathrm{DM}^2\right]\left[1+\frac{Q_\mathrm{tr}^4}{(x_1x_2s)^2}-2\frac{p_\mathrm{T}^2}{x_1x_2s}\right]}{Q_\mathrm{tr}} \tag{5.20}$$

$$\left.\frac{\mathrm{d}^2\hat{\sigma}}{\mathrm{d}p_\mathrm{T}\mathrm{d}\eta}\right|_{D8} = \frac{\alpha_s}{27\pi^2}\frac{1}{p_\mathrm{T}}\frac{1}{\Lambda^4}\frac{\left[Q_\mathrm{tr}^2-4m_\mathrm{DM}^2\right]^{3/2}\left[1+\frac{Q_\mathrm{tr}^4}{(x_1x_2s)^2}-2\frac{p_\mathrm{T}^2}{x_1x_2s}\right]}{Q_\mathrm{tr}} \tag{5.21}$$

$$\left.\frac{\mathrm{d}^2\hat{\sigma}}{\mathrm{d}p_\mathrm{T}\mathrm{d}\eta}\right|_{D9} = \frac{2\alpha_s}{27\pi^2}\frac{1}{p_\mathrm{T}}\frac{1}{\Lambda^4}\frac{\sqrt{Q_\mathrm{tr}-4m_\mathrm{DM}^2}\left[Q_\mathrm{tr}^2+2m_\mathrm{DM}^2\right]}{Q_\mathrm{tr}} \times\left[1+\frac{Q_\mathrm{tr}^4}{(x_1x_2s)^2}+4p_\mathrm{T}^2\left(\frac{1}{Q_\mathrm{tr}^2}-\frac{1}{x_1x_2s}\right)\right] \tag{5.22}$$

$$\begin{aligned}\left.\frac{\mathrm{d}^2\hat{\sigma}}{\mathrm{d}p_\mathrm{T}\mathrm{d}\eta}\right|_{D11} = {}& \frac{3\alpha_s^3}{256\pi^2\Lambda^6}\frac{(x_1x_2s)^3}{(Q_\mathrm{tr}^2-x_1x_2s)^2}\frac{(Q_\mathrm{tr}^2-4m_\mathrm{DM}^2)^{3/2}}{p_\mathrm{T}Q_\mathrm{tr}}\left[1-4\frac{Q_\mathrm{tr}^2-p_\mathrm{T}^2}{x_1x_2s}\right.\\ &+\frac{8Q_\mathrm{tr}^4+21p_\mathrm{T}^4}{(x_1x_2s)^2}-2Q_\mathrm{tr}^2\frac{5Q_\mathrm{tr}^4+4Q_\mathrm{tr}^2p_\mathrm{T}^2+5p_\mathrm{T}^4}{(x_1x_2s)^3}\\ &\left.+Q_\mathrm{tr}^4\frac{8Q_\mathrm{tr}^4+8Q_\mathrm{tr}^2p_\mathrm{T}^2+5p_\mathrm{T}^4}{(x_1x_2s)^4}-4Q_\mathrm{tr}^8\frac{Q_\mathrm{tr}^2+p_\mathrm{T}^2}{(x_1x_2s)^5}+\frac{Q_\mathrm{tr}^{12}}{(x_1x_2s)^6}\right]\end{aligned} \tag{5.23}$$

$$\left.\frac{\mathrm{d}^2\hat{\sigma}}{\mathrm{d}p_{\mathrm{T}}\mathrm{d}\eta}\right|_{D12} = \frac{3\alpha_s^3}{256\pi^2\Lambda^6}\frac{(x_1x_2s)^3}{(Q_{\mathrm{tr}}^2-x_1x_2s)^2}\frac{Q_{\mathrm{tr}}\sqrt{Q_{\mathrm{tr}}^2-4m_{\mathrm{DM}}^2}}{p_{\mathrm{T}}}\left[1-4\frac{Q_{\mathrm{tr}}^2-p_{\mathrm{T}}^2}{x_1x_2s}\right.$$
$$+\frac{8Q_{\mathrm{tr}}^4+21p_{\mathrm{T}}^4}{(x_1x_2s)^2}-2Q_{\mathrm{tr}}^2\frac{5Q_{\mathrm{tr}}^4+4Q_{\mathrm{tr}}^2p_{\mathrm{T}}^2+5p_{\mathrm{T}}^4}{(x_1x_2s)^3}$$
$$\left.+Q_{\mathrm{tr}}^4\frac{8Q_{\mathrm{tr}}^4+8Q_{\mathrm{tr}}^2p_{\mathrm{T}}^2+5p_{\mathrm{T}}^4}{(x_1x_2s)^4}-4Q_{\mathrm{tr}}^8\frac{Q_{\mathrm{tr}}^2+p_{\mathrm{T}}^2}{(x_1x_2s)^5}+\frac{Q_{\mathrm{tr}}^{12}}{(x_1x_2s)^6}\right] \tag{5.24}$$

$$\left.\frac{\mathrm{d}^2\hat{\sigma}}{\mathrm{d}p_{\mathrm{T}}\mathrm{d}\eta}\right|_{D13} = \frac{3\alpha_s^3}{256\pi^2\Lambda^6}\frac{(x_1x_2s)^3}{(Q_{\mathrm{tr}}^2-x_1x_2s)^2}\frac{(Q_{\mathrm{tr}}^2-4m_{\mathrm{DM}}^2)^{3/2}}{p_{\mathrm{T}}Q_{\mathrm{tr}}}\left[1-4\frac{Q_{\mathrm{tr}}^2}{x_1x_2s}\right.$$
$$+\frac{8Q_{\mathrm{tr}}^4+8Q_{\mathrm{tr}}^2p_{\mathrm{T}}^2+5p_{\mathrm{T}}^4}{(x_1x_2s)^2}-2Q_{\mathrm{tr}}^2\frac{5Q_{\mathrm{tr}}^4+6Q_{\mathrm{tr}}^2p_{\mathrm{T}}^2-3p_{\mathrm{T}}^4}{(x_1x_2s)^3}$$
$$\left.+Q_{\mathrm{tr}}^4\frac{8Q_{\mathrm{tr}}^4+8Q_{\mathrm{tr}}^2p_{\mathrm{T}}^2+5p_{\mathrm{T}}^4}{(x_1x_2s)^4}-4Q_{\mathrm{tr}}^8\frac{Q_{\mathrm{tr}}^2+p_{\mathrm{T}}^2}{(x_1x_2s)^5}+\frac{Q_{\mathrm{tr}}^{12}}{(x_1x_2s)^6}\right] \tag{5.25}$$

$$\left.\frac{\mathrm{d}^2\hat{\sigma}}{\mathrm{d}p_{\mathrm{T}}\mathrm{d}\eta}\right|_{D14} = \frac{3\alpha_s^3}{256\pi^2\Lambda^6}\frac{(x_1x_2s)^3}{(Q_{\mathrm{tr}}^2-x_1x_2s)^2}\frac{Q_{\mathrm{tr}}\sqrt{Q_{\mathrm{tr}}^2-4m_{\mathrm{DM}}^2}}{p_{\mathrm{T}}}\left[1-4\frac{Q_{\mathrm{tr}}^2}{x_1x_2s}\right.$$
$$+\frac{8Q_{\mathrm{tr}}^4+8Q_{\mathrm{tr}}^2p_{\mathrm{T}}^2+5p_{\mathrm{T}}^4}{(x_1x_2s)^2}-2Q_{\mathrm{tr}}^2\frac{5Q_{\mathrm{tr}}^4+6Q_{\mathrm{tr}}^2p_{\mathrm{T}}^2-3p_{\mathrm{T}}^4}{(x_1x_2s)^3}$$
$$\left.+Q_{\mathrm{tr}}^4\frac{8Q_{\mathrm{tr}}^4+8Q_{\mathrm{tr}}^2p_{\mathrm{T}}^2+5p_{\mathrm{T}}^4}{(x_1x_2s)^4}-4Q_{\mathrm{tr}}^8\frac{Q_{\mathrm{tr}}^2+p_{\mathrm{T}}^2}{(x_1x_2s)^5}+\frac{Q_{\mathrm{tr}}^{12}}{(x_1x_2s)^6}\right] \tag{5.26}$$

The reader can find the details of the derivation of Eqs. (5.18)-(5.26) in Appendix B.1. As for the other operators, we get

$$\left.\frac{\mathrm{d}^2\hat{\sigma}}{\mathrm{d}p_{\mathrm{T}}\mathrm{d}\eta}\right|_{D2'} = \left.\frac{\mathrm{d}^2\hat{\sigma}}{\mathrm{d}p_{\mathrm{T}}\mathrm{d}\eta}\right|_{D4'} \qquad \left.\frac{\mathrm{d}^2\hat{\sigma}}{\mathrm{d}p_{\mathrm{T}}\mathrm{d}\eta}\right|_{D3'} = \left.\frac{\mathrm{d}^2\hat{\sigma}}{\mathrm{d}p_{\mathrm{T}}\mathrm{d}\eta}\right|_{D1'} \qquad \left.\frac{\mathrm{d}^2\hat{\sigma}}{\mathrm{d}p_{\mathrm{T}}\mathrm{d}\eta}\right|_{D6} = \left.\frac{\mathrm{d}^2\hat{\sigma}}{\mathrm{d}p_{\mathrm{T}}\mathrm{d}\eta}\right|_{D8} \tag{5.27}$$

$$\left.\frac{\mathrm{d}^2\hat{\sigma}}{\mathrm{d}p_{\mathrm{T}}\mathrm{d}\eta}\right|_{D7} = \left.\frac{\mathrm{d}^2\hat{\sigma}}{\mathrm{d}p_{\mathrm{T}}\mathrm{d}\eta}\right|_{D5} \qquad \left.\frac{\mathrm{d}^2\hat{\sigma}}{\mathrm{d}p_{\mathrm{T}}\mathrm{d}\eta}\right|_{D9} = \left.\frac{\mathrm{d}^2\hat{\sigma}}{\mathrm{d}p_{\mathrm{T}}\mathrm{d}\eta}\right|_{D10} \tag{5.28}$$

in the limit of massless light quarks. The operators $D1$–$D4$ are simply related to $D1'$–$D4'$ by a straightforward rescaling

$$\left.\frac{\mathrm{d}^2\hat{\sigma}}{\mathrm{d}p_{\mathrm{T}}\mathrm{d}\eta}\right|_{D1,D2,D3,D4} = \left(\frac{m_q}{\Lambda}\right)^2 \left.\frac{\mathrm{d}^2\hat{\sigma}}{\mathrm{d}p_{\mathrm{T}}\mathrm{d}\eta}\right|_{D1',D2',D3',D4'} . \tag{5.29}$$

We checked that the differences between the cross sections for $D1'$–$D4'$ computed for $m_q \neq 0$ and those reported above assuming $m_q = 0$ are at the per-mille level, so the approximation $m_q = 0$ which we used in all our analytical calculations is justified. The cross sections for the UV completions of dim-6 operators, with s-channel exchange of a mediator of mass M_{med}, are simply obtained by the replacement $1/\Lambda^4 \to g_q^2 g_\chi^2/[Q_{\mathrm{tr}}^2 - M_{\mathrm{med}}^2]^2$.

In order to get the cross sections initiated by the colliding protons one needs to average over the PDFs. For example, for processes with initial state quarks

$$\left.\frac{\mathrm{d}^2\sigma}{\mathrm{d}p_{\mathrm{T}}\mathrm{d}\eta}\right|_{Di} = \sum_q \int \mathrm{d}x_1\mathrm{d}x_2[f_q(x_1)f_{\bar{q}}(x_2) + f_q(x_2)f_{\bar{q}}(x_1)] \left.\frac{\mathrm{d}^2\hat{\sigma}}{\mathrm{d}p_{\mathrm{T}}\mathrm{d}\eta}\right|_{Di} . \tag{5.30}$$

We have performed the analytical calculation only for the emission of an initial state gluon (identified with the final jet observed experimentally). The extension to include also the smaller contribution coming from initial radiation of quarks ($qg \to \chi\chi + q$) is done numerically in Section 5.4.

5.3.2 Results and discussion

In what regions of the parameter space $(\Lambda, m_{\mathrm{DM}})$ is the effective description accurate and reliable? The truncation to the lowest-dimensional operator of the EFT expansion is accurate only if the momentum transfer is smaller than an energy scale of the order of Λ, see Eqs. (5.8). Therefore we want to compute the fraction of events with momentum transfer lower than the EFT cutoff scale. To this end we define the ratio of the cross section obtained in the EFT with the requirement $Q_{\mathrm{tr}} < \Lambda$ on the PDF integration domain, over the total cross section obtained in the EFT.

$$R_\Lambda^{\mathrm{tot}} \equiv \frac{\sigma|_{Q_{\mathrm{tr}}<\Lambda}}{\sigma} = \frac{\int_{p_{\mathrm{T}}^{\mathrm{min}}}^{p_{\mathrm{T}}^{\mathrm{max}}} \mathrm{d}p_{\mathrm{T}} \int_{-2}^{2} \mathrm{d}\eta \left.\frac{\mathrm{d}^2\sigma}{\mathrm{d}p_{\mathrm{T}}\mathrm{d}\eta}\right|_{Q_{\mathrm{tr}}<\Lambda}}{\int_{p_{\mathrm{T}}^{\mathrm{min}}}^{p_{\mathrm{T}}^{\mathrm{max}}} \mathrm{d}p_{\mathrm{T}} \int_{-2}^{2} \mathrm{d}\eta \frac{\mathrm{d}^2\sigma}{\mathrm{d}p_{\mathrm{T}}\mathrm{d}\eta}}. \tag{5.31}$$

To sum over the possible p_{T}, η of the jets, we integrate the differential cross sections over values typically considered in the experimental searches. We consider $p_{\mathrm{T}}^{\mathrm{min}} = 500\,\mathrm{GeV}$ (as used in the signal region SR4 of [240]), $|\eta| < 2$ and the two cases with center-of-mass energies $\sqrt{s} = 8$ TeV and 14 TeV. For $p_{\mathrm{T}}^{\mathrm{max}}$ we used 1, 2 TeV for $\sqrt{s} = 8, 14$ TeV, respectively. The sum over quark flavours is performed only considering u, d, c, s quarks.

We first study the behavior of the ratio R_Λ^{tot}, as a function of Λ and m_{DM} The results are shown in Fig. 5.3. We show only results for representative operators $D1', D5, D9$. This ratio R_Λ^{tot} gets closer to unity for large values of Λ, as in this case the effect of the cutoff becomes negligible. The ratio drops for large m_{DM} because the momentum transfer increases in this regime. This confirms our precedent analysis of Ref. [248], that the EFT works better for large Λ and small m_{DM}. Notice also that, going from $\sqrt{s} = 8$TeV to $\sqrt{s} = 14$TeV, the results scale almost linearly with the energy, so for the same value of the ratio m_{DM}/Λ one obtains nearly the same R_Λ^{tot}.

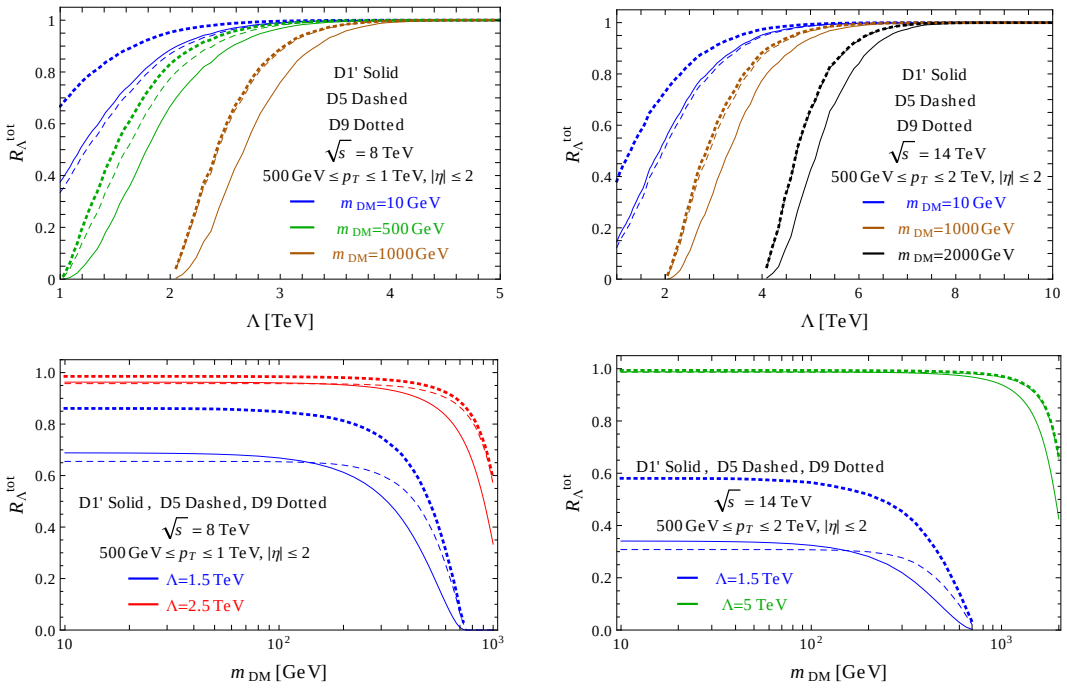

FIGURE 5.3: *The ratio $R_\Lambda^{\rm tot}$ defined in Eq. (5.31) for operators $D1'$ (solid lines), $D5$ (dashed lines) and $D9$ (dotted lines) as a function of Λ and $m_{\rm DM}$, for $\sqrt{s} = 8$ TeV (left panel) and 14 TeV (right panel).*

Next, we turn to study the contours of constant values of the quantity $R_\Lambda^{\rm tot}$, in the plane $(m_{\rm DM}, \Lambda)$. These contour curves for the different operators are shown in Fig. 5.4 for $\sqrt{s} = 8$ TeV and in Fig. 5.5 for $\sqrt{s} = 14$ TeV. The requirement that at least 50% of the events occur with momentum transfer below the cutoff scale Λ requires such a cutoff scale to be above $\sim$ 1TeV for $\sqrt{s} = 8\,$TeV, or above $\sim$ 2TeV for $\sqrt{s} = 14\,$TeV. Note also that the contours for $D1$–$D4$ differ by the corresponding contours for $D1'$–$D4'$ by $\mathcal{O}(1)$ factors, due to the different weighting of the quarks' PDFs. On the other hand, the experimental bounds on the scale of the operators $D1$–$D4$ are much lower (of the order of tens of GeV), as such operators experience an additional suppression of m_q/Λ. This means that the bounds on $D1$–$D4$ are not reliable from the point of view of EFT validity.

We stress once again that the precise definition of a cutoff scale for an EFT is only possible when the details of the UV completion are known. The most conservative regime is when the couplings of the UV theory reach their maximal values allowed by perturbativity. In such a situation, the requirement on the momentum transfer becomes $Q_{\rm tr} < 4\pi\Lambda$. We show the effect of varying the cutoff scale in Fig. 5.6, for the representative contour $R_\Lambda^{\rm tot} = 50\%$ of D5. As it should be clear, the variation of the cutoff scale is equivalent to a change of the unknown couplings of the UV theory. All the operators have very similar results, as the contours scale linearly with the cutoff. As a comparison, we show as a shaded area the region $\Lambda > m_{\rm DM}/(2\pi)$ often used as a

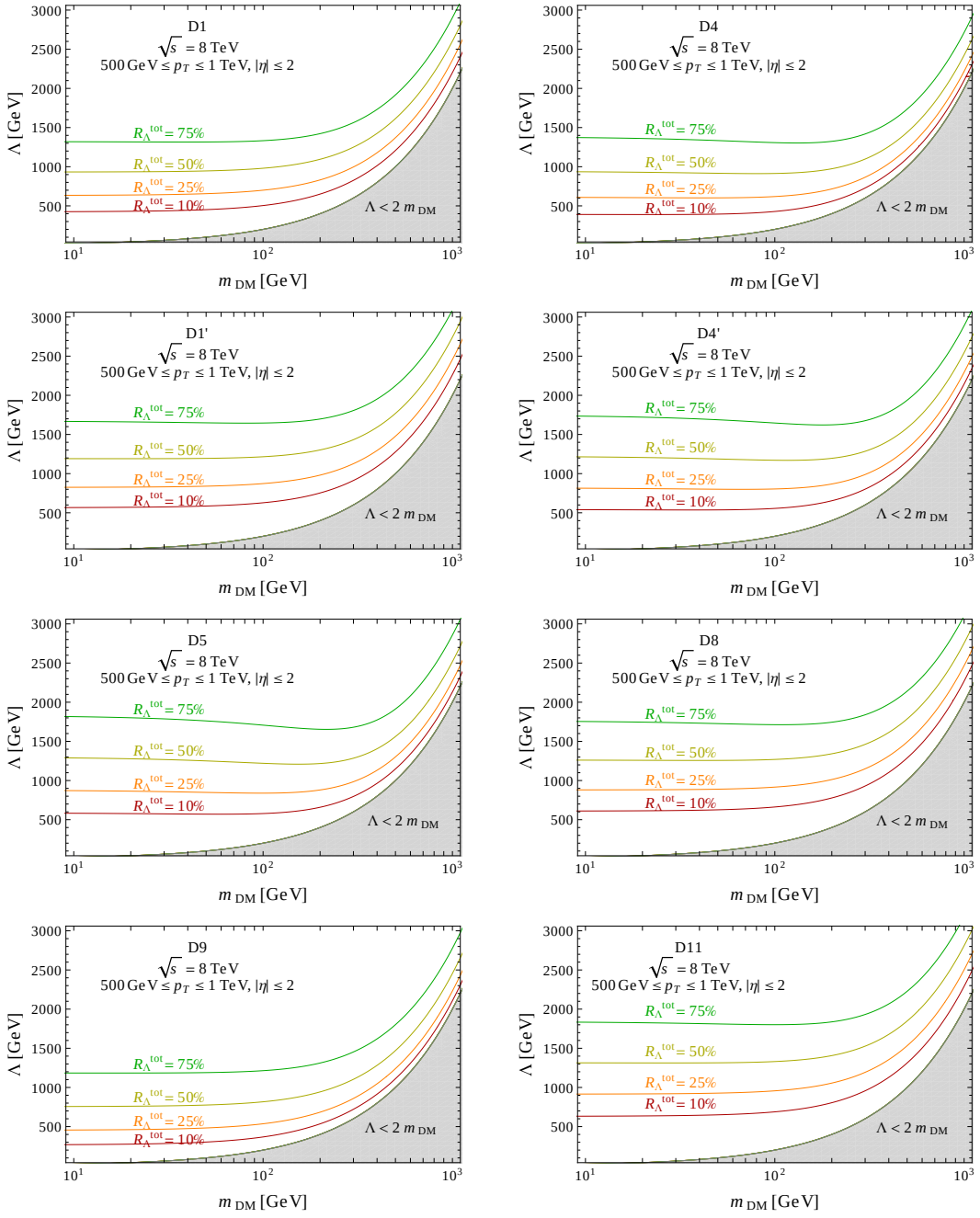

FIGURE 5.4: *Contours for the ratio* $R_\Lambda^{\rm tot}$*, defined in Eq. (5.31), on the plane* $(m_{\rm DM}, \Lambda)$*, for the different operators. We set* $\sqrt{s} = 8\text{TeV}, |\eta| \leq 2$ *and* $500\,\text{GeV} < p_{\rm T} < 1\,\text{TeV}$.

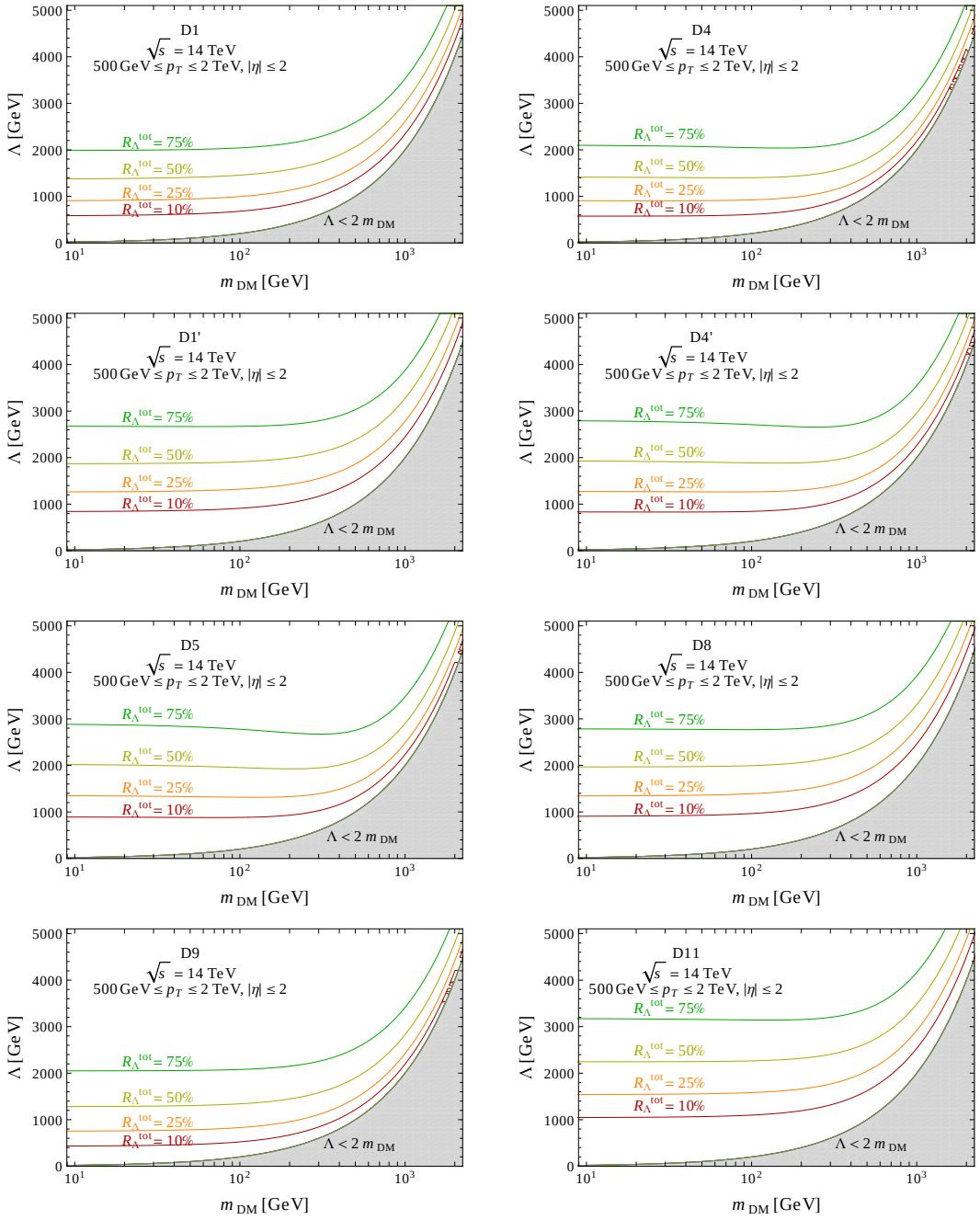

FIGURE 5.5: *Contours for the ratio* $R_\Lambda^{\rm tot}$*, defined in Eq. (5.31), on the plane* $(m_{\rm DM}, \Lambda)$*, for the different operators. We set* $\sqrt{s} = 14\text{TeV}, |\eta| \leq 2$ *and* $500\,\text{GeV} < p_{\rm T} < 2\,\text{TeV}$.

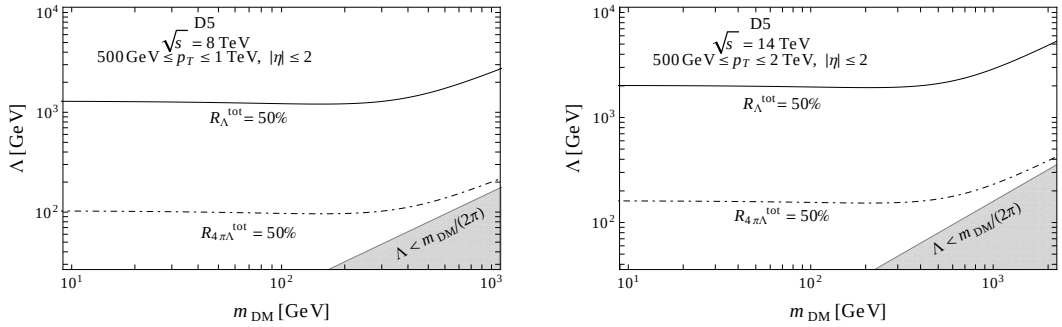

FIGURE 5.6: *50% contours for the ratio $R_\Lambda^{\rm tot}$ for the operator $D5$, varying the cutoff $Q_{\rm tr} < \Lambda$ (solid line) and $Q_{\rm tr} < 4\pi\Lambda$ (dot-dashed line). We have also shown the region corresponding to $\Lambda < m_{\rm DM}/(2\pi)$ (gray shaded area), often used as a benchmark for the validity of the EFT. We set $\sqrt{s} = 8$ TeV (left panel) and $\sqrt{s} = 14$ TeV (right panel).*

benchmark for the validity of the EFT (see Eq. (5.7)). The 50% contour is above such a region, meaning that the parameter space regions of validity of the effective operator approach is smaller than commonly considered.

To close this section let us comment on another question one may ask: what is the difference between interpreting data with an effective operator and with its simplest UV completion? This question has already been addressed in Ref. [248] for the operator $D1'$, by studying the ratio of the cross sections obtained with the UV theory and with the effective operator. For each of the operators in Table 5.1 one can write a simple UV-complete Lagrangian, see e.g. Eqs. (5.14)-(5.15). The very same analysis can be repeated for all the other operators and we checked that the same qualitative conclusions can be drawn. In particular, if Λ is not larger than a few TeV, interpreting the experimental data in terms of EFT or in terms of a simplified model with a mediator can make a significant difference.

5.4 S-Channel, Comparison with MonteCarlo Simulations

In order to perform an alternative check of our analytical results and to be able to compare to the experimental limits as close as possible, we present in this section the results of numerical event simulations.

5.4.1 Simulation and analysis description

We made use of MADGRAPH 5[330] to simulate pp collisions at $\sqrt{s} = 8$ TeV and $\sqrt{s} = 14$ TeV. Both PDF sets CTEQ6L1 and MSTW2008LO (discussed in Ref. [326, 327]) are employed. The PDF choice affects the cross section, but only minimally the acceptance.

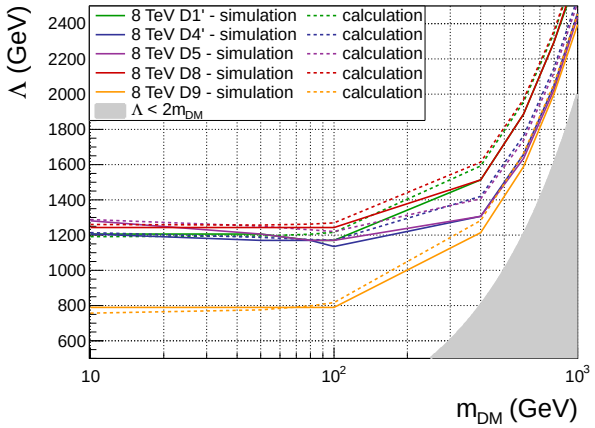

FIGURE 5.7: *Comparison of the contour* $R_\Lambda^{\text{tot}} = 50\%$ *for the analytical calculation (dashed line) and the simulation (solid line) for the different operators* $D1'$, $D4'$, $D5$, $D8$ *and* $D9$. *The results agree within less than 7 %.*

Hence, the change in contours of R_Λ^{tot} is negligible. Since MSTW2008LO is used for the analytical calculations, this set is also used where direct comparisons between simulation and calculation are shown. For the comparison to the experimental results, CTEQ6L1 is used instead. Only u, d, c, s quarks were considered, both in the initial and in the final state.

According to the event kinematics we have evaluated whether or not the conditions of validity discussed in Section 5.3 are fulfilled. Specifically, we have checked if Eqs. (5.6) and (5.7) are fulfilled, that is, if the following condition is satisfied

$$\Lambda > \frac{Q_{\text{tr}}}{\sqrt{g_q g_\chi}} > 2\frac{m_{\text{DM}}}{\sqrt{g_q g_\chi}}\,. \tag{5.32}$$

Samples of 20000 events were simulated for each operator, scanning DM mass values of 10, 50, 80, 100, 400, 600, 800 and 1000 GeV and cutoff scales of 250, 500, 1000, 1500, 2000, 2500 and 3000 GeV in the case of $\sqrt{s} = 8$ TeV collisions. When increasing the collision energy to $\sqrt{s} = 14$ TeV, the DM mass of 2000 GeV and cutoff scales of 4000 and 5000 GeV were added.

From the simulated samples the fraction of events fulfilling $\Lambda > Q_{\text{tr}}/\sqrt{g_q g_\chi}$ for each pair of DM mass and cutoff scale can be evaluated, if one assumes a certain value for the couplings $\sqrt{g_\chi g_q}$ connecting the cutoff scale Λ and the mediator mass M via $\Lambda = M/\sqrt{g_q g_\chi}$. As above, $g_q g_\chi$ was assumed to be 1.

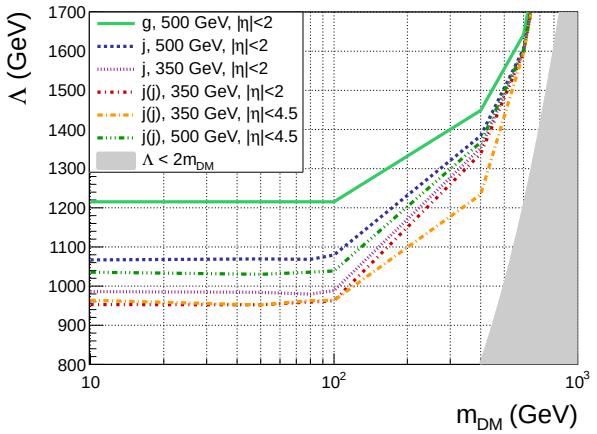

FIGURE 5.8: *The changes of the contour of* $R_\Lambda^{\text{tot}} = 50\%$ *are shown for several variations from the analytically calculated scenario to a scenario close to the cuts used in the ATLAS monojet analysis exemplarily for the operator* $D5$ *at* $\sqrt{s} = 8$ *TeV. In the legend, "g" means only gluon radiation, "j" stands for either quark- or gluon-initiated jets, "j(j)" means a second jet is allowed.*

5.4.2 Results

In order to confirm that analytical and numerical results are in agreement, Figure 5.7 shows a comparison for the operators $D1'$, $D4'$, $D5$, $D8$ and $D9$. The results were obtained for the scenario of one radiated gluon jet above 500 GeV within $|\eta| < 2$. The contours of $R_\Lambda^{\text{tot}} = 50\%$ from analytical and numerical evaluation agree within less than 7 %. The remaining differences could be due to the upper jet p_{T} cut not imposed during event simulation but needed for the analytical calculation, and the details of the fitting procedures.

Next, we vary the kinematical constraints step by step from the scenario considered in the analytical calculations, namely one radiated gluon jet above 500 GeV within $|\eta| < 2$, to a scenario closest to the analysis cuts applied in the ATLAS monojet analysis [240]. More specifically, the leading jet is allowed to come from either a gluon or a quark being radiated, the leading jet p_{T} cut is changed from 500 GeV to 350 GeV, a second jet is allowed and its range in η is enlarged to $|\eta| < 4.5$. No further cuts are applied at simulation level.

The effect of the variation of the cuts can be seen in Figure 5.8. Allowing not only for a gluon jet but also taking into account the possibility of a quark jet changes the R_Λ^{tot} contours appreciably. The change from lowering the p_{T} of the leading jet has a smaller effect. Allowing for a second jet and enhancing its rapidity range barely changes the R_Λ^{tot} contour, especially at large m_{DM} values.

$\sqrt{s} = 8$ TeV						$\sqrt{s} = 14$ TeV					
Op.	a	b	c	d	e	Op.	a	b	c	d	e
D1	1.32	787.13	1.39	1.08	1.53	D1	0.89	1017.37	1.45	1.28	1.24
D1'	1.30	1008.25	1.49	0.77	1.83	D1'	0.43	909.66	1.59	0.53	1.37
D4	1.65	702.93	1.14	0.65	1.75	D4	1.23	996.82	1.25	0.80	1.48
D4'	1.51	859.83	1.22	0.48	1.92	D4'	0.76	982.75	1.33	0.37	1.63
D5	1.54	816.83	1.18	0.50	1.85	D5	0.78	894.86	1.25	0.39	1.54
D8	1.23	964.62	1.50	0.91	1.59	D8	0.48	945.09	1.55	0.74	1.24
D9	1.43	681.92	1.15	1.02	1.35	D9	0.91	891.65	1.21	1.23	1.04
D11	1.23	1002.33	1.49	0.82	1.69	D11	0.68	1250.49	1.58	0.81	1.35

TABLE 5.2: *Coefficient for the fitting functions for $R_\Lambda^{\rm tot}$ in Eq. (5.33), in the cases $\sqrt{s} = 8$ and 14* TeV*. The fitting functions describe processes where quarks and/or gluons are radiated, the final state contains 1 or 2 jets, where the leading jet has minimum $p_{\rm T}$ of 350 GeV while the second jet is allowed to be within $|\eta| < 4.5$. See text for further details.*

If the collision energy is augmented to $\sqrt{s} = 14$ TeV, all the $R_\Lambda^{\rm tot}$ contours increase. As seen for $\sqrt{s} = 8$ TeV, moving to the scenario closer to the experimental analysis leads to contours that are at most $\sim 30\%$ lower in Λ.

After having extracted $R_\Lambda^{\rm tot}$ for each WIMP and mediator mass, a curve can be fitted through the points obtained in the plane of $R_\Lambda^{\rm tot}$ and Λ. The following functional form is used for this purpose

$$R_\Lambda^{\rm tot} = \left[1 - e^{-a\left(\frac{\Lambda - 2m_{\rm DM}}{b}\right)^c}\right]\left[1 - e^{-d\left(\frac{\Lambda + 2m_{\rm DM}}{b}\right)^e}\right]. \tag{5.33}$$

Further, the parameters are fitted for each DM mass separately. From these fits, the points denoting a cutoff scale where $R_\Lambda^{\rm tot}$ equals e.g. 50% can be extracted for each DM mass, and the lines of constant $R_\Lambda^{\rm tot}$ can be plotted in the usual limit-setting plane Λ vs. $m_{\rm DM}$. Table 5.2 collects the values of the fitting parameters for all operators except D12-D14, for which no experimental analysis exists.

5.5 S-Channel, Implications of the limited validity of EFT in DM searches at LHC

Figure 5.9 shows the experimental limits obtained from the ATLAS monojet analysis [240] in the plane (Λ, $m_{\rm DM}$), for the opearators D5, D8 and D11. The contours of $R_\Lambda^{\rm tot}$ for 25%, 50% and 75% are superimposed. The experimental limits are placed in a region where about 30% of the events can be expected to fulfill the EFT conditions - the exact number depends on the operator considered. Especially the limit on the gluon operator $D11$ seems questionnable. For comparison, dashed lines show the contours of $R_\Lambda^{\rm tot}$ for

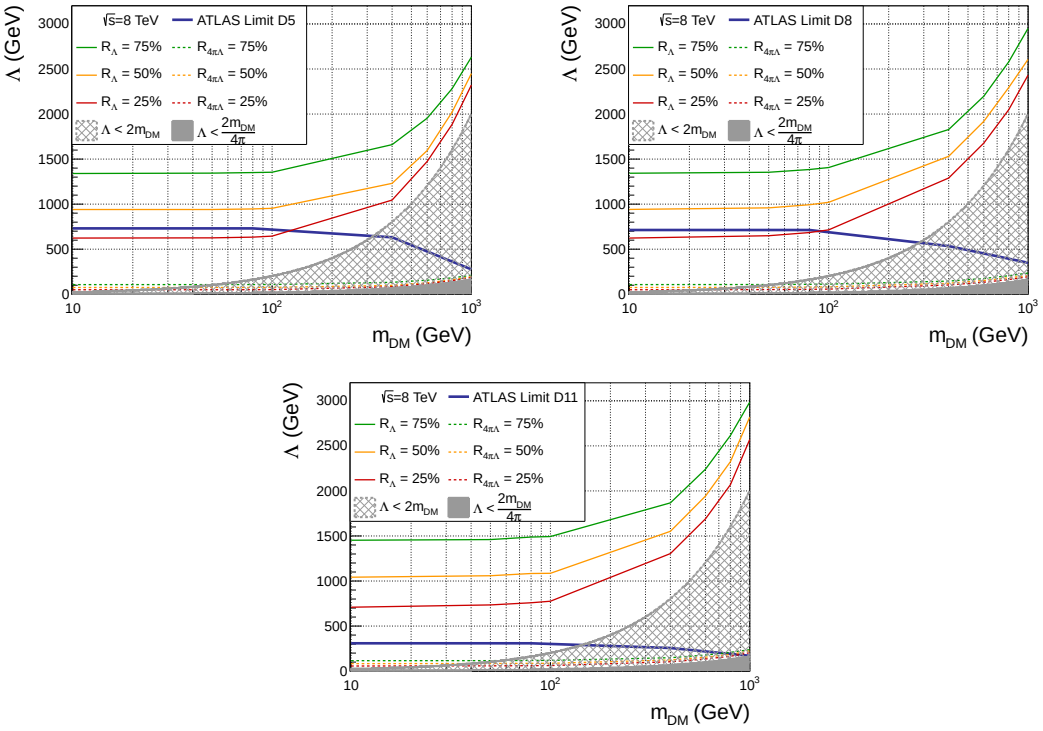

FIGURE 5.9: *25%, 50% and 75% contours for the ratio $R_\Lambda^{\rm tot}$, compared to the experimental limits from ATLAS [240] (blue line). Also indicated are the contours of $R_\Lambda^{\rm tot}$ in the extreme case when setting the couplings $\sqrt{g_q g_\chi} = 4\pi$ (dashed lines). Results are shown for different operators: D5 (upper left panel), D8 (upper right panel) and D11 (lower panel).*

the extreme case of couplings $\sqrt{g_q g_\chi} = 4\pi$, presenting the limiting case for which the theory is still considered perturbative.

Unfortuntately, there is no possibility to measure $Q_{\rm tr}$ in data, on an event-by-event basis. So the information on what is the fraction of the events to cut out comes from analytical computations or a numerical simulation, as we explained in this chapter. To assess the impact of the limited validity of the EFT on the current collider bounds, we adopt the procedure that relies on the assumption that the $p_{\rm T}$ (or MET) distributions with the $Q_{\rm tr}$ cut are simply a rescaling of those without the cut. A more refined study should account for possible kinematic shape changes with the jet transverse momentum and/or missing energy and DM mass[2].

Very naively, neglecting the statistical and systematical uncertainties, the number of signal events in a given EFT model has to be less than the experimental observation, $N_{\rm signal}(\Lambda, m_{\rm DM}) < N_{\rm expt}$. The cross section due to an operator of mass dimension d scale like $\Lambda^{-2(d-4)}$, so $N_{\rm signal}(\Lambda, m_{\rm DM}) = \Lambda^{-2(d-4)} \tilde{N}_{\rm signal}(m_{\rm DM})$, and the experimental

[2]Preliminary studies indicate that the method adopted in this chapter is quite reasonable for cuts with $Q_{\rm tr} < 750$ GeV or weaker [331].

lower bound in the scale of the operator becomes

$$\Lambda > \left[\tilde{N}_{\rm signal}(m_{\rm DM})/N_{\rm exp}\right]^{1/[2(d-4)]} \equiv \Lambda_{\rm expt.}\,. \tag{5.34}$$

Now, if we do not consider any information about the shapes of the $p_{\rm T}$ or MET distributions, the experimental bound only comes from the total number of events passing given cuts. The fact that a fraction of the events involve a transfer momentum exceeding the cutoff scale of the EFT means that the number of signal events for placing a limit gets reduced by a factor $R_\Lambda^{\rm tot}$. Therefore, actually $N_{\rm signal}(\Lambda, m_{\rm DM}) \to R_\Lambda^{\rm tot}(m_{\rm DM}) N_{\rm signal}(\Lambda, m_{\rm DM})$, so the new limit is found by solving the implicit equation

$$\Lambda > [R_\Lambda^{\rm tot}(m_{\rm DM})]^{1/2[(d-4)]}[N_{\rm signal}(m_{\rm DM})/N_{\rm exp}]^{1/[2(d-4)]} = [R_\Lambda^{\rm tot}(m_{\rm DM})]^{1/[2(d-4)]}\Lambda_{\rm expt} \tag{5.35}$$

and it turns out to be weaker than $\Lambda_{\rm expt}$. In Fig. 5.10 we show the new limits for the dim-6 operators D5, D8 and the dim-7 operator D11, for the conditions $Q_{\rm tr} < \Lambda, 2\Lambda, 4\pi\Lambda$, corresponding different choices of the UV couplings: $\sqrt{g_q g_\chi} = 1, 2, 4\pi$, respectively. The curves are obtained solving Eq. 5.35 with $R_\Lambda^{\rm tot}, R_{2\Lambda}^{\rm tot}, R_{4\pi\Lambda}^{\rm tot}$ respectively. The ATLAS bound reported is the 90%CL observed limit. The functions $R_\Lambda^{\rm tot}$ used are taken from the fitting functions described in Table 5.2, which include both quark and gluon jets, and the same cuts as the "Signal Region 3" used by ATLAS. As expected, the weaker is the condition on $Q_{\rm tr}$, the more the new limits approach the ATLAS bound. In the case of extreme couplings $\sqrt{g_q g_\chi} = 4\pi$, the condition on the momentum transfer is very conservative $Q_{\rm tr} < 4\pi\Lambda$. For D5 and D8, the new limit is indisinguishable from the ATLAS one, meaning that the experimental results are safe from the EFT point of view, in this limiting situation. For D11, even for extreme values of the couplings, the bound at large DM masses must be corrected. In general, for couplings of order one, the limits which are safe from the EFT point of view are appreciably weaker than those reported. We encourage the experimental collaborations to take this point into account when publishing their limits.

5.6 T-Channel, Validity of the EFT: analytical approach

5.6.1 Operators and cross sections

In this chapter we will consider the following effective operator describing the interactions between Dirac dark matter χ and left-handed quarks q

$$\mathcal{O} = \frac{1}{\Lambda^2}\,(\bar{\chi}P_L q)\,(\bar{q}P_R\chi)\,. \tag{5.36}$$

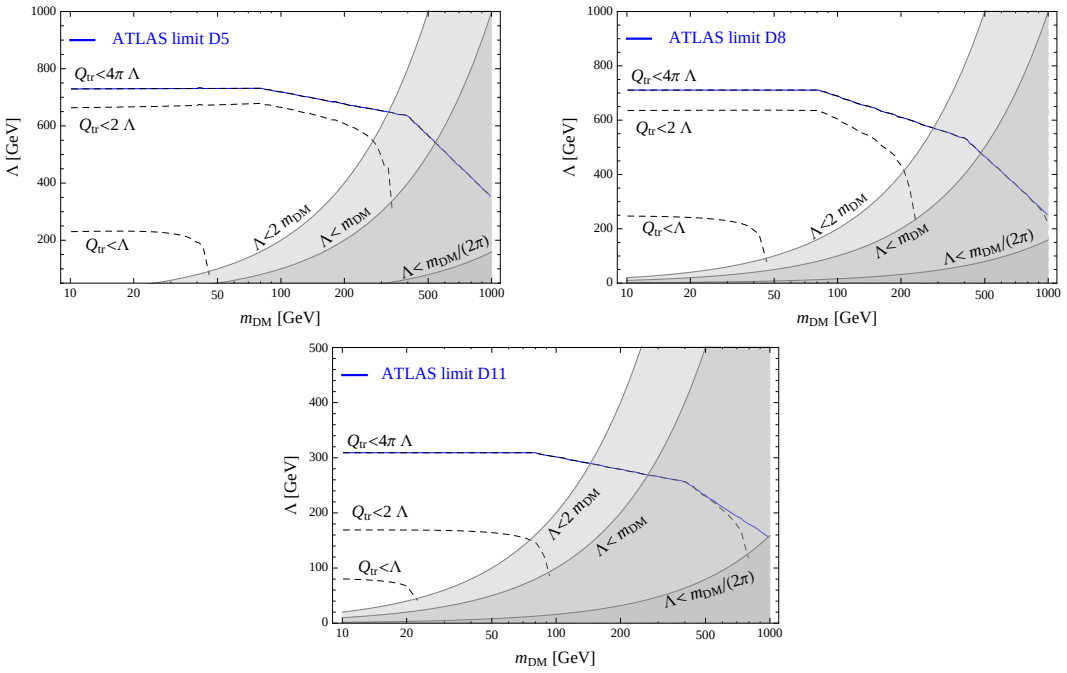

FIGURE 5.10: *The experimental limits by ATLAS [240] on the suppression scale Λ are shown as solid blue lines. The updated limits taking into account EFT validity are shown as dashed black lines, for $Q_{\rm tr} < \Lambda, 2\Lambda, 4\pi\Lambda$, corresponding to different choices of the UV couplings: $\sqrt{g_q g_\chi} = 1, 2, 4\pi$, respectively. The corresponding kinematical constraints (Eq. (5.32)) are denoted by gray bands. The different plots refer to different operators: D5 (upper left panel), D8 (upper right panel) and D11 (lower panel).*

Only the coupling between dark matter and the first generation of quarks is considered. Including couplings to the other generations of quarks requires fixing the relationships between the couplings and mediator masses for each generation, making such an analysis less general. In principle the dark matter can also couple to the right-handed quark singlet, switching P_R and P_L in the above operator. The inclusion of both of these operators does not modify our results, even if the two terms have different coupling strengths.

The operator in Eq. (5.36) can be viewed as the low-energy limit of a simplified model describing a quark doublet Q_L coupling to DM, via t-channel exchange of a scalar mediator S_Q,

$$\mathcal{L}_{\rm int} = g\,\bar{\chi} Q_L S_Q^* + h.c. \tag{5.37}$$

and integrating out the mediator itself. Since we consider only coupling to the first generation of quarks, $Q_L = (u_L, d_L)$. As an illustration, the $2 \to 2$ process $q\bar{q} \to \chi\bar{\chi}$ for this model is shown in Fig. 5.11. This model is popular as an example of a simple DM model with t-channel couplings, which exist also in well-motivated models such as supersymmetry where the mediator particle is identified as a squark, and the DM is a Majorana particle. Bell et al. [332] have used a version of this model with Majorana DM in place of Dirac DM, to test the prospects of Z-bosons as a potential search channel.

This has been followed up by a dedicated ATLAS search in this channel [333]. Refs [334–339] have also constrained this model, using both the standard monojet search channel as well as searching for multiple jets arising from direct mediator production. Refs [335, 339] found that collider constraints on this model were competitive if not stronger than direct detection constraints across most of the parameter space.

The t-channel operator in Eqn. (5.36) can be expressed as a sum of s-channel operators using Fierz transformations. For arbitrary Dirac spinors such as $\bar{q}_1$, q_2, $\bar{\chi}_1$, χ_2, and adopting in part the notation of [340], the Fierz transformation can be expressed as

$$(\bar{q}_1 X \chi_2)\,(\bar{\chi}_1 Y q_2) = \frac{1}{4}\sum_B \left(\bar{q}_1 X \Gamma^B Y q_2\right)\left(\bar{\chi}_1 \Gamma_B \chi_2\right), \tag{5.38}$$

where X, Y are some combination of Dirac-matrices, and $\Gamma^B = \{\not{1}, i\gamma_5, \gamma^\mu, \gamma_5\gamma^\mu, \sigma^{\mu\nu}\}$ and $\Gamma_B = \{\not{1}, -i\gamma_5, \gamma_\mu, -\gamma_5\gamma_\mu, \frac{1}{2}\sigma_{\mu\nu}\}$ form a basis spanning 4×4 matrices over the complex number field [340]. Due to the chiral coupling between the quarks and DM, most of the terms in the sum cancel, and we are left with

$$\begin{aligned}
\mathcal{O} &= \frac{1}{\Lambda^2}\,(\bar{\chi} P_L q)\;(\bar{q} P_R \chi) \\
&= \frac{1}{8\Lambda^2}\,(\bar{\chi}\gamma^\mu \chi)\;(\bar{q}\gamma_\mu q) \qquad (D5) \\
&+ \frac{1}{8\Lambda^2}\,(\bar{\chi}\gamma^\mu\gamma_5 \chi)\;(\bar{q}\gamma_\mu q) \qquad (D6) \\
&- \frac{1}{8\Lambda^2}\,(\bar{\chi}\gamma^\mu \chi)\;(\bar{q}\gamma_\mu\gamma_5 q) \qquad (D7) \\
&- \frac{1}{8\Lambda^2}\,(\bar{\chi}\gamma^\mu\gamma_5 \chi)\;(\bar{q}\gamma_\mu\gamma_5 q) \qquad (D8) \\
&= \frac{1}{2\Lambda^2}\,(\bar{\chi}\gamma^\mu P_R \chi)\;(\bar{q}\gamma_\mu P_L q)\,.
\end{aligned} \tag{5.39}$$

This is equivalent to a rescaled sum of the $D5$, $D6$, $D7$ and $D8$ operators [245]. Thus, it is interesting to see whether the EFT limit of the t-channel model under investigation has similar phenomenology to these s-channel operators. This is discussed in Section 5.7.

The standard search channel for such a scenario is missing energy ($E_{\mathrm{T}}^{\mathrm{miss}}$) plus a single jet, although particles such as Z-bosons [332, 333] are promising complementary search channels. The dijet+$E_{\mathrm{T}}^{\mathrm{miss}}$ channel is particularly promising for the simplified model in Eq. (5.37) since direct production of a pair of mediator particles can result in a strong dijet signal. In particular, Refs. [335, 338] found that in much of parameter space, the dijet signal from direct mediator production provides comparable or stronger constraints on the model than the traditional monojet signal. In the high-energy limit, the mediator particle has SM charges and can emit a gluon, photon or massive gauge boson. This channel is suppressed in the EFT limit and so is not considered here.

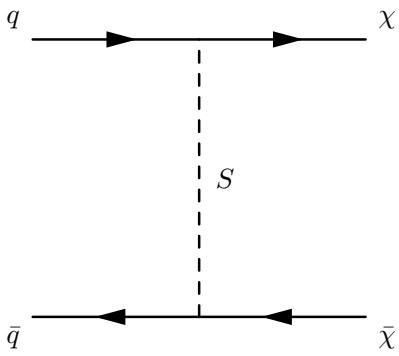

FIGURE 5.11: Illustrative $2 \to 2$ process for the UV-complete version of our effective operator.

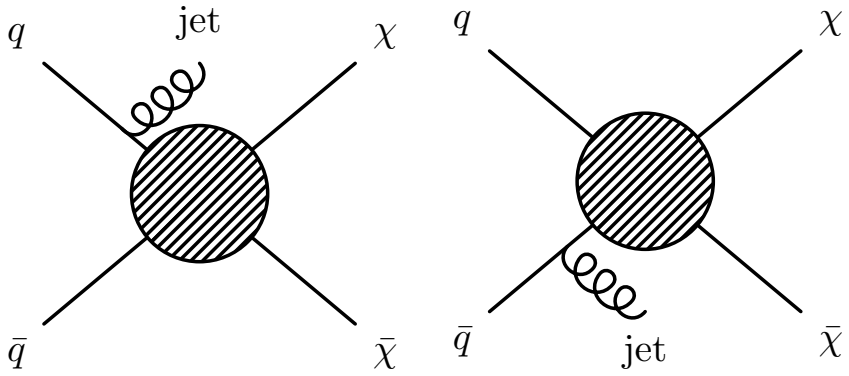

FIGURE 5.12: Search channel.

The dominant process contributing to the $E_{\mathrm{T}}^{\mathrm{miss}}$+ monojet signal is $q\bar{q} \to \chi\bar{\chi}g$. Representations of the EFT diagrams are shown in Fig. 5.12. We have calculated the differential cross section for these processes, with the results given in Appendix B.2 along with the corresponding matrix elements. In the same appendix we have also calculated the differential cross section for the other contributing processes, $qg \to \chi\bar{\chi}q$ and $g\bar{q} \to \chi\bar{\chi}\bar{q}$, which we found to be subdominant. In the full simplified model, the scalar mediator carries standard model charges and can emit gauge bosons, including gluons which would contribute to the $E_{\mathrm{T}}^{\mathrm{miss}}$+ monojet signal. This channel is neglected in this study, since we are testing whether the effective operator description of this model is internally consistent regardless of the UV completion.

In order to compute the cross section with proton initial states appropriate for LHC events, it is necessary to integrate over the parton distribution function (PDF) of the proton. For $q\bar{q}$ initial states, this is defined as

$$\sigma = \sum_{q} \int \mathrm{d}x_1 \mathrm{d}x_2 [f_q(x_1) f_{\bar{q}}(x_2) + f_q(x_2) f_{\bar{q}}(x_1)] \hat{\sigma}, \tag{5.40}$$

where $\hat{\sigma}$ is the total cross section for a process in the center of momentum frame. We have used the MSTW PDFs from Refs. [326, 327, 341], and checked that the our results

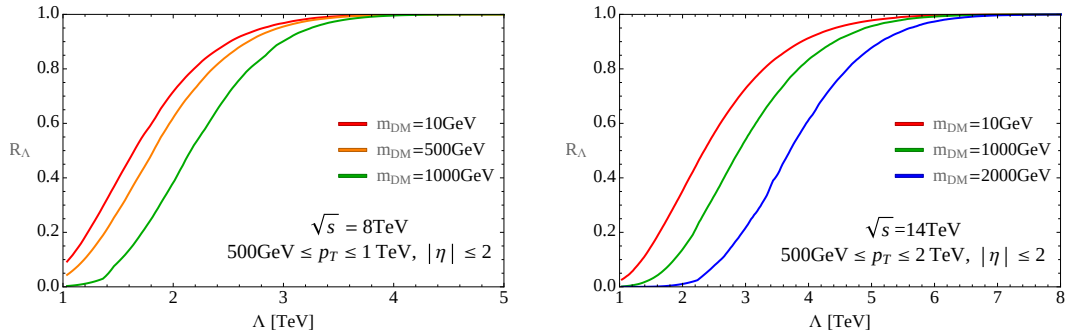

FIGURE 5.13: The ratio $R_\Lambda^{\rm tot}$ as a function of Λ for three choices of the DM mass, for $\sqrt{s} = 8$ TeV (left panel) and 14 TeV (right panel).

are not sensitive to the choice of leading or next-to-leading-order MSTW PDFs.

5.6.2 Results and discussion

Recall that our goal is to determine whether the EFT approximation is valid for the operator in Eqn. 5.36, in the standard search channel $q\bar{q} \to \chi\bar{\chi}+$ jet, when the coupling strength is at roughly the natural scale, $1 \lesssim g \lesssim 4\pi$. In this case, for any given event, the momentum of the mediator can only be neglected if $Q_{\rm tr}^2 \lesssim \Lambda^2$. To test this, we define the ratio of the cross section truncated so that all events pass the condition, to the total cross section:

$$R_\Lambda \equiv \frac{\sigma|_{Q_{\rm tr}<\Lambda}}{\sigma} = \frac{\int_{p_{\rm T}^{\rm min}}^{p_{\rm T}^{\rm max}} {\rm d}p_{\rm T} \int_{-2}^{2} {\rm d}\eta \left.\frac{{\rm d}^2\sigma}{{\rm d}p_{\rm T}{\rm d}\eta}\right|_{Q_{\rm tr}<\Lambda}}{\int_{p_{\rm T}^{\rm min}}^{p_{\rm T}^{\rm max}} {\rm d}p_{\rm T} \int_{-2}^{2} {\rm d}\eta \frac{{\rm d}^2\sigma}{{\rm d}p_{\rm T}{\rm d}\eta}}. \tag{5.41}$$

We have parameterised the cross section such that the final integration variables are the standard observables for jets observed at the LHC, namely the transverse momentum $p_{\rm T}$ and pseudorapidity η. The integration limits on these quantities are chosen to be comparable to those used in standard searches for WIMP DM by the LHC collaborations (see, for instance, Ref. [240]). For searches at center of mass energy $\sqrt{s} = 8$ TeV, $p_{\rm T}$ is integrated from 500 GeV to 1 TeV. For $\sqrt{s} = 14$ TeV, the integration range is instead 500 GeV to 2 TeV. In both cases, the pseudorapidity integration range is $|\eta| \leq 2$.

There are two values of $Q_{\rm tr}$, corresponding to jet emission from either the initial state quark or antiquark respectively. These are given in Appendix B.2.3. Mixing between diagrams makes it impossible to disentangle a single transferred momentum for any individual event, and so we require that for each event *both* values of $Q_{\rm tr}$ for that process satisfy the requirement that $Q_{\rm tr}^2 < \Lambda^2$.

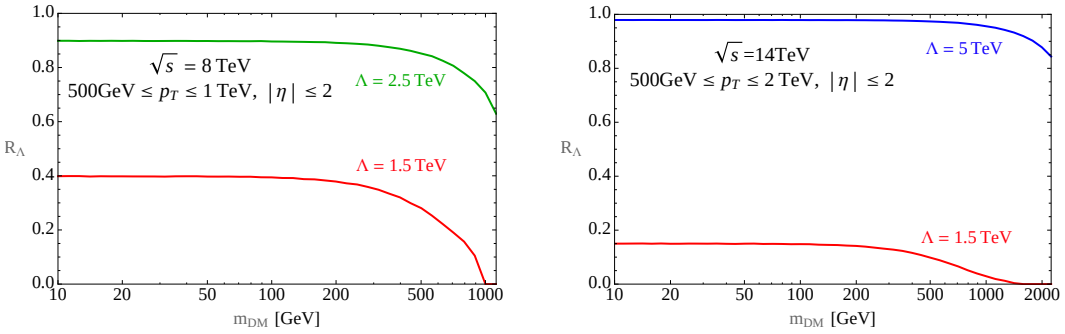

FIGURE 5.14: The ratio $R_\Lambda^{\rm tot}$ as a function of $m_{\rm DM}$ for two choices of Λ, for $\sqrt{s} = 8$ TeV (left panel) and 14 TeV (right panel).

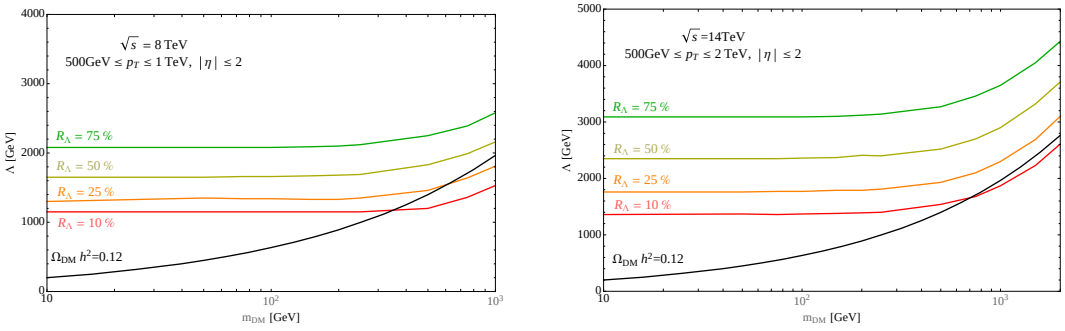

FIGURE 5.15: Contours for the ratio $R_\Lambda^{\rm tot}$, defined in Eq. (5.41), on the plane $(m_{\rm DM}, \Lambda)$. We set $\sqrt{s} = 8$TeV, $|\eta| \leq 2$ and $500\,{\rm GeV} < p_{\rm T} < 1$ TeV in the left panel, and $\sqrt{s} = 14$TeV, $|\eta| \leq 2$ and $500\,{\rm GeV} < p_{\rm T} < 2$ TeV in the right panel. The black solid curves indicates the correct relic abundance.

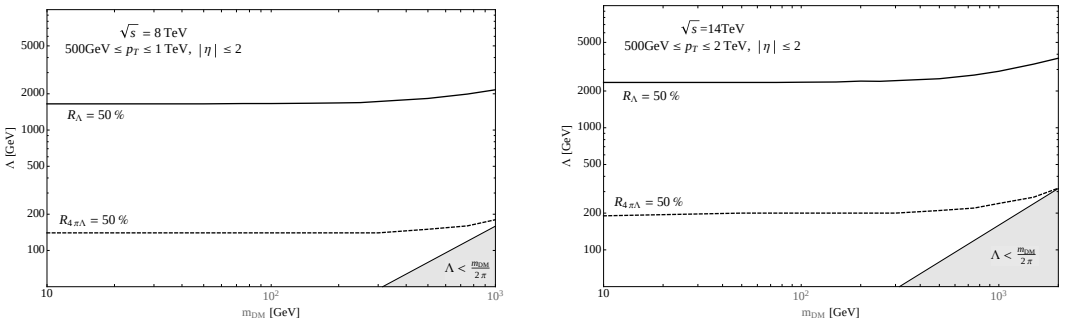

FIGURE 5.16: 50% contours for the ratio $R_\Lambda^{\rm tot}$, varying the cutoff $Q_{\rm tr} < \Lambda$ (solid line) and $Q_{\rm tr} < 4\pi\Lambda$ (dot-dashed line). We have also shown the region corresponding to $\Lambda < m_{\rm DM}/(2\pi)$ (gray shaded area), often used as a benchmark for the validity of the EFT. We set $\sqrt{s} = 8$ TeV (left panel) and $\sqrt{s} = 14$ TeV (right panel).

In Fig. 5.13 we show the behaviour of R_Λ as a function of Λ, at both $\sqrt{s}$ =8 and 14 TeV. Similarly, Fig. 5.14 shows R_Λ as a function of $m_{\rm DM}$ at the same center of mass energies. In Fig. 5.15 we instead plot isocontours of four fixed values of R_Λ as a function of both $m_{\rm DM}$ and Λ. Contrasted with the s-channel case [248, 249], the ratio has less DM mass dependence, being even smaller than in the s-channel case at low DM masses and larger at large DM masses, without becoming large enough to save EFTs.

In Fig. 5.15 we also show the curves corresponding to the correct DM relic density, assuming that interactions between the DM particle and the SM plasma were mediated by the operator (5.36). These were computed by using a semi-analytic solution to the Boltzmann equation [342] to find the values of $m_{\rm DM}$ and Λ that yield a DM abundance matching the observed value $\Omega_{\rm DM}h^2 \simeq 0.12$ [66]. Since we are dealing with Dirac DM, have included an additional factor of 2 in the expression for the relic density relative to the equation for Majorana DM in Ref. [342]. For given $m_{\rm DM}$, larger Λ leads to a smaller self-annihilation cross section and therefore to larger relic abundance. It is evident that the large-Λ region where the EFT is valid typically leads to an unacceptably large DM density. However, it may certainly be that additional annihilation channels and interactions, beyond those described by the operator (5.36) can enhance the cross section and decrease the relic abundance to fit the observations.

In the most optimistic scenario for EFTs, the coupling strength g takes the maximum value (4π) such that the model remains in the perturbative regime. In this case, a given constraint on Λ corresponds to a relatively larger value of M, such that the EFT is valid across a larger region. To demonstrate how our results depend on the coupling strength, in Fig. 5.16 we plot isocontours for $R = 50\%$, for two cases: **1)** the standard requirement that $Q_{\rm tr}^2 < \Lambda^2$, equivalent to requiring $g \simeq 1$, and **2)** requiring $Q_{\rm tr}^2 < (4\pi\Lambda)^2$, equivalent to requiring $g \simeq 4\pi$.

The grey shaded area indicates the region where $\Lambda < m_{\rm DM}/(2\pi)$. This is often used as a benchmark for the validity of the EFT approximation, since in the s-channel, $Q_{\rm tr}$ is kinematically forced to be greater than $2m_{\rm DM}$, leaving the EFT inherently invalid when $M < 2m_{\rm DM}$, which is equivalent to $\Lambda < m_{\rm DM}/(2\pi)$ for a coupling strength $g \simeq 4\pi$. Thus, in the s-channel the contours never cross this boundary. Interestingly this is not the case in the t-channel, since the kinematic constraints on $Q_{\rm tr}$ no longer apply. This indicates that at very large DM masses the EFT approximation can become safer than naively assumed - although in practice the ratio is still too low for EFTs to be of any practical use.

To gain a sense of whether this model is potentially observable at the LHC, and whether the effective operator model is still observable even after rescaling by R_Λ, we show in Figure 5.17 the integrated signal cross-section at $\sqrt{s} = 14$ TeV, using the same cuts as earlier. We can see even at relatively low dark matter masses, Λ must be smaller than $\sim$1 TeV before events can be expected to be produced after 25 fb^{-1}, at which point the effective operator approach has entirely ceased to be a valid approximation. At higher luminosities the model will begin to become more observable for a greater range of Λ.

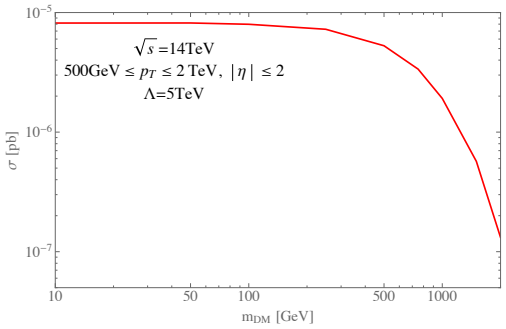

FIGURE 5.17: Cross section for the monojet process under consideration, before applying R_Λ cuts. Note that $\sigma \propto \Lambda^{-4}$.

5.6.3 Comparison with MonteCarlo Simulations

As a check, it is interesting to compare our analytical results to fully numerical results. We have reproduced Fig. 5.13 using numerical simulations of the LHC events at truth level, i.e., simulating events as they would be produced in truth without simulating how they would be observed by the ATLAS or CMS detectors.

The t-channel EFT model from Eqn. 5.36 was constructed using FeynRules [343], and the resultant Feynman rules were exported into MADGRAPH 5[330]. The process of interest, $pp \to \chi\bar{\chi}+$ jet, was simulated at a center-of-mass energy of $\sqrt{s} = 14$ TeV using the CTEQ6L1 PDF set [344]. It was found in Ref. [249] that the choice of PDF influences the magnitude but not the acceptance of the rate, and therefore this different choice of PDF relative to our analytic calculations is not expected to influence the ratios we calculate. Contours in R_Λ, defined in the same way as in Section 5.6.2, were determined by counting the fraction of events that passed the condition $Q_{\rm tr} < \Lambda$, for both values of $Q_{\rm tr}$ defined in Appendix B.2.3. Events were simulated at DM masses of 10, 50, 100, 200, 300, 500, 1000 and 2000 GeV for a wide range of values of the cutoff scale Λ. The transverse momentum and rapidity of the jet are restricted to the ranges $(500 \leq p_{\rm T}/\text{GeV} \leq 2000)$ and $|\eta| \leq 2$ respectively, as in the analytic results from the previous section.

5.7 Conclusions

The search for DM is one of the main targets of LHC analysis. In this chapter we have continued our previous investigation to assess the validity of the EFT commonly used in interpreting such searches. Following Ref. [248], we have studied the quantity $R_\Lambda^{\rm tot}$ (see Eq.(5.31), which quantifies the error made when using effective operators to describe processes with very high momentum transfer. Our criterion indicates up to what cutoff

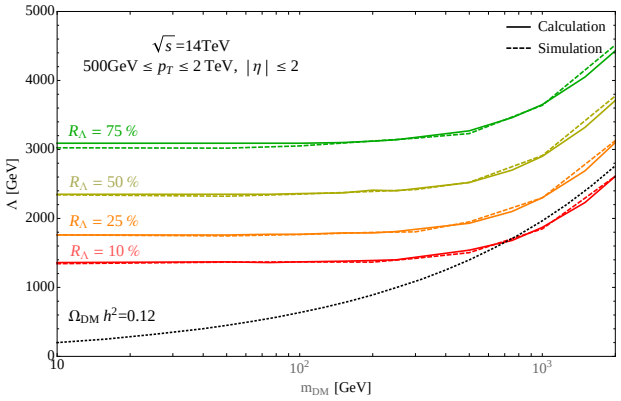

FIGURE 5.18: Comparison of the contour $R_\Lambda^{\text{tot}} = 50\%$ for the analytical calculation (solid line) and the simulation (dashed line). The dotted curve indicates the correct relic abundance.

energy scale the effective description is valid, depending on the DM mass and couplings. We have performed the analysis for the full list of EFT operators, connecting fermion DM particles and quarks or gluons, used by the ATLAS and CMS collaborations and originated from the exchange of heavy mediators in the s-channel. We have also extended our analysis to the case of $\sqrt{s} = 14$ TeV. Furthermore, we have validated our analytical results by performing numerical event simulations which reproduce the experimental situation in the closest possible way. Our results indicate that the range of validity of the EFT is significantly limited in the parameter space (Λ, m_{DM}).

Does it mean that the EFT is not the best tool to interpret the current LHC data of DM searches? The answer is yes and no. On the negative side, our results clearly cry out for an overcoming of the EFT, most possibly through identifying a handful of classes of models (able to reproduce the EFT operators in the heavy mediator limit); this would allow a consistent analysis of the current and future LHC data by consistently taking into account the role played by the mediator. On the positive side, keep working with the EFT allows to avoid the overwhelming model-dependence generated by the many DM models proposed so far. Nonetheless, as we have shown in section 5.5, the price to pay is a deterioration of the limits presented so far.

In the final section of this chapter 5.6 we have extended the investigation of the validity of the EFT approach for DM searches at the LHC. While in the first part of the chapter (sections (5.2,5.3,5.4 and 5.5)) our analysis has been focused on the case of the EFT operators generated by integrating out a heavy mediator in the s-channel, we have considered here the case of Dirac DM couplings to the standard model via the t-channel. Even though a t-channel operator can be expressed by a Fierz transformation as a sum of s-channel operators, our results as a function of Λ and DM mass (compared, for instance, to those of Fig. 5.4) indicate that one may not infer them from those of a single s-channel

operator, see Eq. (5.39). This is due to the inherently different kinematics of the s- and t-channel, in particular significant differences in the transferred momentum.

We have also computed the relic density over the parameter space of the model, assuming that the only interactions between DM and the SM are those mediated by the t-channel operator (5.36), and found that the region of EFT validity corresponds to an overly large relic density. This conclusion is rather general and may be evaded by assuming additional DM annihilation channels.

Similar to what happens in the s-channel case, our findings indicate that in the t-channel the range of validity of the EFT is significantly limited in the parameter space $(\Lambda, m_{\mathrm{DM}})$, reinforcing the need to go beyond the EFT at the LHC when looking for DM signals. This is especially true for light mediators as they can be singly produced in association with a DM particle, leading to a qualitatively new contribution to the mono-jet processes. Mediators can even be pair-produced at the LHC through both QCD processes and DM exchange processes. All of this rich dynamics leads to stronger signals (and therefore, in the absence thereof, to tighter bounds) than the EFT approach.

Chapter 6

Simplified Models

6.1 Introduction to Simplified Models

Many well-motivated extensions of the Standard Model (SM), such as the Minimal Supersymmetric SM (MSSM) [345], Large extra dimensions (LED) [105], little Higgs models with T-parity [346], etc. predict large missing energy signals at high-energy colliders. Often, the production of new particles associated with these extensions of the SM results in more than just missing energy signature, as is the case in the MSSM with the production of squarks and sleptons which cascade decay to the lightest supersymmetric partner (LSP). Such unusual events, with energetic leptons, jets, and large amounts of missing energy contain several discriminating features as compared with the SM and form the basis for powerful searches for new physics (see [347] for a recent example). At the same time, there are good reasons to develop searches that do not rely on extra discriminating features aside from large missing energy. Such searches, where large missing energy is the dominant signature of new physics, are the principal subject of this chapter.

The first strong motivation for missing energy searches is that the models mentioned above allow for the possibility of producing missing energy without it being accompanied by other unusual objects. The second reason is the overwhelming evidence for Dark Matter (DM) in the universe. If DM is a new fundamental particle, and if it interacts weakly but not too weakly with the SM, then the annihilation of SM particles into DM constitutes a new source of missing energy in colliders. The third reason is that such searches at colliders have a much more broad interpretation, and are sensitive to much more than just stable new particles. Such searches are sensitive also to any new, weakly interacting particle with a lifetime that exceeds about a microsecond since these would leave the detector before depositing their energy. It is therefore well worth the effort to

develop a comprehensive search strategy to look for events with large missing energy as their dominant discriminating signature.

In hadron colliders the observable quantity associated with undetected particles is of course only the momentum imbalance in the direction transverse to the beam, or the missing transverse momentum[1]. The simplest and best-known example of a search for large MET is the monojet search looking for a single QCD jet recoiling against nothing. It is now common to also include (or at least, not to exclude) multijet events recoiling against MET in the search for missing energy [238, 241, 348–350]. If nothing else this is useful because the probability of radiating a second jet from the initial state partons is large at LHC energies (discussed in e.g. [351]). In addition, as we discuss below, in some regions of the parameter space the underlying theoretical models often predict comparable signal in multijet events with missing energy as in the monojet signal.

Thus, missing energy signatures form a very wide net with which weakly interacting particles, not necessarily forming the dominant component of DM, can be efficiently searched for. The inclusive nature of these searches calls for the construction of equally broad theoretical models that can be used to interpret the experimental results in a comprehensive fashion. Over the past several years the Effective Field Theory (EFT) approach has gained in popularity since it allows one to focus on a minimal number of degrees-of-freedom, for example the initial partons involved in the reaction (quarks and gluons) and the DM candidate [70, 245, 311, 352–358]. It remains agnostic about heavier particles that may be present in a fully renormalizable model and thus allows for a fairly model-independent interpretation. However, as was recognized early on [70, 72, 313, 324, 325, 359, 360], and more recently in a quantitative way [248, 249, 319], the validity of this approach is often questionable at LHC energies where the momentum transfer involved in the reactions is comparable to the scale of non-renormalizable operator being constrained. In other words, the degrees-of-freedom that were assumed to generate these operators are important (in the parlance of EFTs, they should be "integrated-in"). The question then arises: *how do we amend the EFT approach and incorporate the effects of these other particles in the modeling of missing energy searches while continuing to work in a broad and inclusive theoretical framework?*

Simplified models [361–363] offer a powerful approach to address this issue by including in a minimal model the extra particles and interactions needed to reproduce the non-renormalizable operators. This should not be viewed as a step backwards. On the contrary: as is well-known from other studies, simplified models allow us to focus on the salient kinematical features of a process while ignoring differences among models

[1]Here and in what follows we will often abuse the terminology slightly and refer to searches utilizing this imbalance more generally as missing energy searches.

(such as helicity structure) that LHC measurements are anyways only weakly sensitive to. The DM-EFT operators are a case in point as many of the operators considered (e.g. $\bar{q}\gamma_\alpha q\ \bar{\chi}\gamma^\alpha\chi$ and $\bar{q}\gamma_5\gamma_\alpha q\ \bar{\chi}\gamma_5\gamma^\alpha\chi$) yield similar kinematical distributions at the LHC. Of course, these different operators yield very different behavior in direct- and indirect-detection experiments as we discuss below, but that is not pertinent for the purpose of presenting results from searches at the LHC[2]. Simplified models also bring to a sharp focus the importance of other searches at the LHC such as multi-jet+MET searches, which can provide complementary bounds on the underlying model. This is so because the new degrees-of-freedom included in the simplified model (which we henceforth refer to as *mediators*) can be produced on-shell and contribute significantly to processes other than the original ones considered within the EFT context. In sections 6.1.1, 6.1.2, and 6.1.3 we introduce and discuss the different simplified models.

Alongside missing energy searches at colliders, efforts for direct and indirect detection of DM offer complementary fronts where DM can be searched for (see for example ref. [364]). One of the advantages of the EFT approach is that it allows for a straightforward comparison of constraints coming from the different fronts. Simplified models maintain this advantage and allow for an equally straightforward comparison with direct detection experiments as was demonstrated for example in refs. [323, 335, 338, 365]. At the same time, simplified models avoid the pitfalls of the EFT approach by correctly modeling the weaker constraints on models with light mediators. We discuss these points further in the different sections where the simplified models are introduced.

6.1.1 S-channel models

Modeling the DM particle, χ, as a fermion we consider the dimension six operators of the form,

$$\mathcal{O}_6 = (\bar{q}\Gamma^m q)\ \ (\bar{\chi}\Gamma'_m\chi)\ . \tag{6.1}$$

These operators are the D1-D10 (and D1′-D4′) operators in the notation of Refs. [245, 249]. The simplest way of resolving four-fermion operators as in Eq. (6.1) is through a color-singlet boson, either a scalar or a vector, as shown in Fig. 6.1. The simplified model we describe assumes CP-conservation and contains a new scalar (pseudoscalar), S (S'), or a new vector (axial-vector), V_μ (V'_μ), with interactions,

$$\begin{aligned}\mathcal{L}_{\rm S} &\supset -\frac{1}{2}M^2_{\rm med}S^2 - y_\chi S\bar{\chi}\chi - y_q^{ij}S\bar{q}_i q_j + \text{h.c.}\,,\\ \mathcal{L}_{\rm S'} &\supset -\frac{1}{2}M^2_{\rm med}S'^2 - y'_\chi S'\bar{\chi}\gamma_5\chi - y_q'^{ij}S\bar{q}_i\gamma_5 q_j + \text{h.c.}\,,\end{aligned}$$

[2]However, it is important that the equivalency of these different choices for LHC phenomenology is clearly communicated so as to avoid misunderstandings with regard to the relevancy of the LHC results to other model choices and other experiments.

$$\begin{aligned}\mathcal{L}_{\mathrm{V}} &\supset \frac{1}{2}M_{\mathrm{med}}^2 V_\mu V^\mu - g_\chi V_\mu \bar{\chi}\gamma^\mu\chi - g_q^{ij} V_\mu \bar{q}_i\gamma^\mu q_j\,,\\ \mathcal{L}_{\mathrm{V}'} &\supset \frac{1}{2}M_{\mathrm{med}}^2 V'_\mu V'^\mu - g'_\chi V'_\mu \bar{\chi}\gamma^\mu\gamma_5\chi - g'^{ij}_q V'_\mu \bar{q}_i\gamma^\mu\gamma_5 q_j\,.\end{aligned} \tag{6.2}$$

where $q = u, d$ and $i, j = 1, 2, 3$ are flavor indices. Such simplified models have been considered in several past publications, see for example the early work of ref. [70, 313, 366] as well as more recent works [365, 367] and references therein. These Lagrangian terms generate the effective operators D1′, D4′, D5 and D8. Refs. [248, 249] find that the operators (D2′, D3′) and (D6, D7) have the same partonic level cross section as (D4′, D1′) and (D8, D5), respectively. We thus do not include the former in what follows. Note that a UV complete description of scalar theory would require $y_q \simeq m_q/M_{\mathrm{med}}$ (resulting in the operators D1-D4), but since the translation between these cases is simple, we find the use of Eqs. (6.2) sufficient for our purposes.

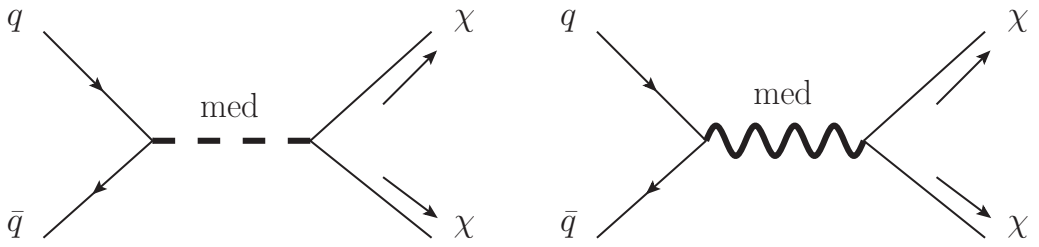

FIGURE 6.1: Two possible mediators. A massive scalar (left) and/or a massive vector-boson (right), resolving dimension-6 operators of the form, Eq. (6.12), through an s-channel exchange.

As concerns the mediator couplings to quarks, the existence of off-diagonal coupling is tightly constrained by various FCNC processes [368]. We do not study such couplings, taking $g_q^{ij} = g_q^i \delta^{ij}$. In the following we consider the scenario of flavor blind couplings to all quarks: $g_d^i = g_u^i \equiv g_q$ for $i = 1, 2, 3$. An interesting scenario, in which the mediator couples more strongly to the third generation is discussed below in Sec. 6.1.4. We further assume that the only available decay channels of the mediator are into quarks and DM particles.

The differential cross sections at the parton level (with respect to the pseudo-rapidity (η) and transverse momentum (p_{T}) of the final jet) for the s-channel process $f(p_1)+\bar{f}(p_2) \to \chi(p_3) + \chi(p_4) + g(k)$ are given in Eqs. (2.4)-(2.8) of ref. [249], where

$$\Lambda^4 = \frac{\left(Q_{\mathrm{tr}}^2 - M_{\mathrm{med}}^2\right)^2 + \Gamma^2 M_{\mathrm{med}}^2}{g_q^2 g_\chi^2}\,, \tag{6.3}$$

should be used to resolve the EFT operators.

As discussed earlier, the EFT approach, where integrating out a heavy mediator generates a tower of higher dimensional operators, is appropriate in processes with low energy transfer:

$$M_{\rm med} \gtrsim Q_{\rm tr} \geq 2m_\chi \,. \tag{6.4}$$

Refs. [248, 249, 319] discuss the limitations of the EFT approach for DM searches for an s-channel mediator exchange, and quantify the dependence of the errors resulting from the EFT approach on mediator and DM masses and couplings. At the partonic level the differences between the cross sections of the effective theory and the full theory are,

$$\left(\frac{{\rm d}^2\hat{\sigma}}{{\rm d}\eta{\rm d}p_{\rm T}}\right)_{\rm full} \Big/ \left(\frac{{\rm d}^2\hat{\sigma}}{{\rm d}\eta{\rm d}p_{\rm T}}\right)_{\rm EFT} = \frac{M_{\rm med}^4}{\left(Q_{\rm tr}^2 - M_{\rm med}^2\right)^2 + \Gamma^2 M_{\rm med}^2} \tag{6.5}$$

where $\Lambda = M_{Med}/\sqrt{g_q g_\chi}$ was used.

The authors of ref. [249] study the ratio between the EFT resulting cross section and the full theory at 8 TeV center of mass energy. They find that this ratio is smaller by 50% for both scalar and vector interactions if $\Lambda \gtrsim 2-3$ TeV and $m_\chi \lesssim 1$ TeV. In the following we explore the validity of the EFT approach as a function of the final jet p_T at $\sqrt{s} = 14$ TeV. For this high energy, the gluon initiated process is significant and contributes comparably to the quark initiated process, for high p_T cuts. We therefore present numeric results based on Monte Carlo simulated events. The events are generated using `MadGraph 5` [330] imposing a cut of $p_T \geq 200$ GeV and $|\eta| \leq 2.5$ on the final jet. To quantify the differences between the EFT and the simplified model approaches we use the ratio of partonic level cross-section with a single final state jet in addition to the DM pair. We expect next-to-leading order corrections, showering, hadronization, and detector effects to largely cancel in the ratio, and leave a more detailed analysis to future study.

Fig. 6.2 (6.3) shows the ratio between the interaction cross sections resulting from the simplified model and the effective theory for the scalar (vector) mediated interactions. At the top pane we present this ratio of the differential cross sections as a function of the jet $p_{\rm T}$, for several choices of DM and mediator masses. At the bottom pane we show the ratio between the total cross section as a function of the DM and mediator masses. It can be seen that the two approaches coincide for $M_{\rm med} \gg 2m_\chi, p_{\rm T}$. However, if this condition is not fulfilled, differences between the full theory and the EFT approach appear both in the total cross section and in the kinematical distribution of the two. It is thus necessary to go beyond the EFT study in order to correctly explore the region of parameter space where $M_{\rm med} \lesssim 2m_\chi$.

To find the most convenient and enlightening set of simplified models, one needs to study the sensitivity of the observables to the helicity structure of the mediator couplings. For

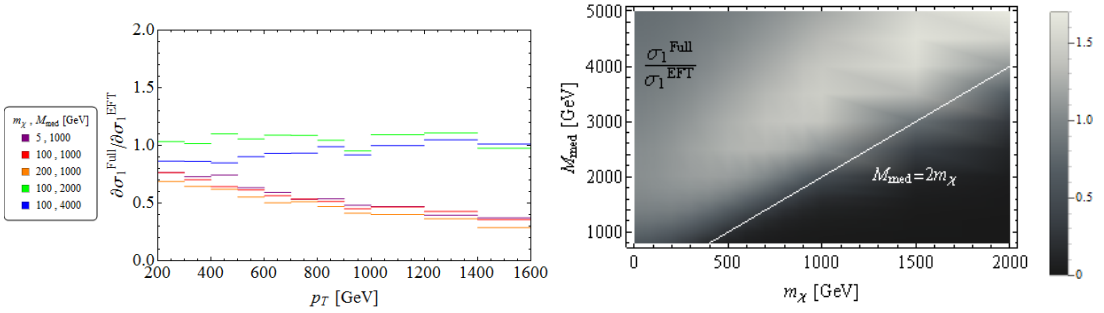

FIGURE 6.2: The ratio between the interaction cross section of the full theory and the EFT one in the case of scalar mediator. The top figure shows the ratio of differential cross sections, integrated over the jet rapidity $-2.5 \leq \eta \leq 2.5$. The ratio of the total cross section integrated over the jet transverse momentum $p_{\mathrm{T}} \geq 200$ GeV is plotted in the bottom figure. The events are generated using `MadGraph 5`.

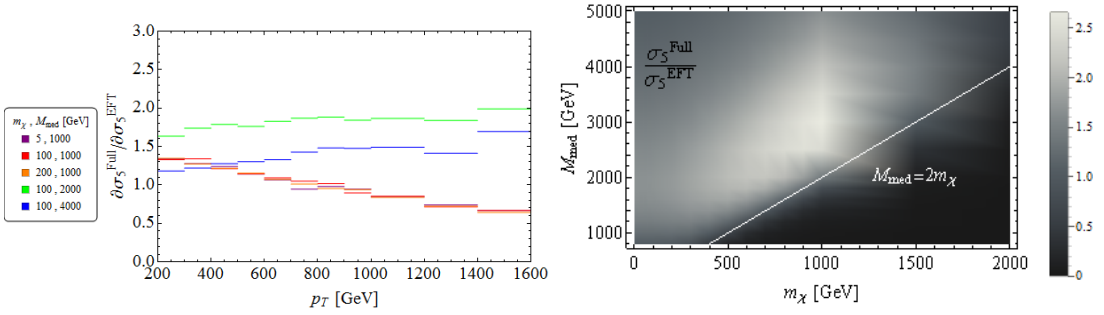

FIGURE 6.3: The same as Fig 6.2 but for a vector mediator.

the scalar and pseudoscalar interactions, Refs. [248, 249] find, at the parton level,

$$\left(\frac{\mathrm{d}^2\hat{\sigma}}{\mathrm{d}\eta\mathrm{d}p_{\mathrm{T}}}\right)_{D_1'} \Big/ \left(\frac{\mathrm{d}^2\hat{\sigma}}{\mathrm{d}\eta\mathrm{d}p_{\mathrm{T}}}\right)_{D_4'} = \left(1 - \frac{4m_{\mathrm{DM}}^2}{Q_{\mathrm{tr}}^2}\right), \tag{6.6}$$

while for vector couplings

$$\left(\frac{\mathrm{d}^2\hat{\sigma}}{\mathrm{d}\eta\mathrm{d}p_{\mathrm{T}}}\right)_{D_5} \Big/ \left(\frac{\mathrm{d}^2\hat{\sigma}}{\mathrm{d}\eta\mathrm{d}p_{\mathrm{T}}}\right)_{D_8} = \left(\frac{Q_{\mathrm{tr}}^2 + 2m_{\mathrm{DM}}^2}{Q_{\mathrm{tr}}^2 - 4m_{\mathrm{DM}}^2}\right). \tag{6.7}$$

In the limit that $Q_{\mathrm{tr}} \gg 2m_{\mathrm{DM}}$, the two differential cross sections share the same η and p_{T} distribution. However, these kinematical regions are suppressed by the parton distribution functions (PDFs).

To explore the impact of the different helicity structures we study the ratio between the cross sections arising from scalar (vector) and pseudoscalar (axial vector) mediators. The results, based on events generated using `MadGraph 5`, are shown in Figs. 6.4 and 6.5 for the scalar and vector cases, respectively. As above, we present this ratio for the differential cross section as a function of the jet p_{T} at the top, and as a function of the DM and mediator masses at the bottom. As expected, we find that the ratios between

each pair of cross sections (*i.e.* scalar vs. pseudoscalar, and vector vs. axial vector) have only weak dependence on the final jet p_{T}. The processes do however have different overall cross sections and thus will result in different number of signal events. Furthermore, this ratio has a nontrivial dependence on M_{med} for heavy DM particles, as a result of the PDFs. Since the scalar and axial vector interactions result in smaller cross-sections it is sufficient, as a first step, to explore the scalar and axial vector mediation resolving the s-channel DM pair-production at the LHC. If a signal is discovered, further analysis of the jet angular distribution could differentiate between the different particles mediating the DM production.

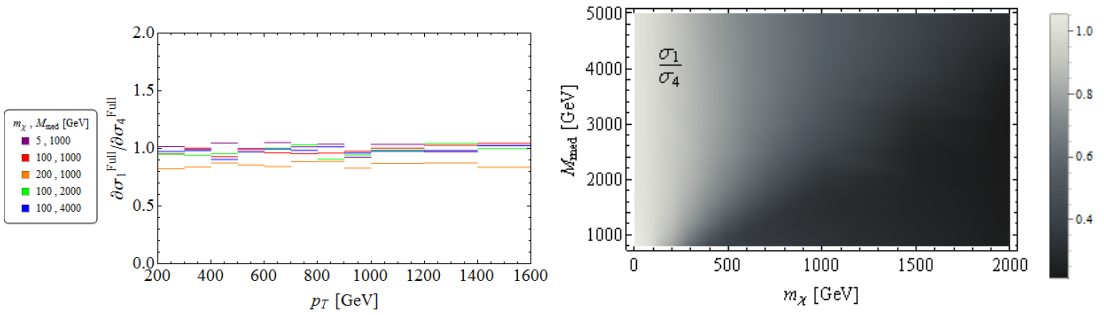

FIGURE 6.4: The ratio between the s channel interaction cross section mediated by a scalar and a pseudoscalar mediator. The top figure shows the ratio of differential cross sections, integrated over the jet rapidity $-2.5 \leq \eta \leq 2.5$. The ratio of total cross sections integrated over the jet transverse momentum $p_T \geq 100$ GeV is plotted in the bottom figure.

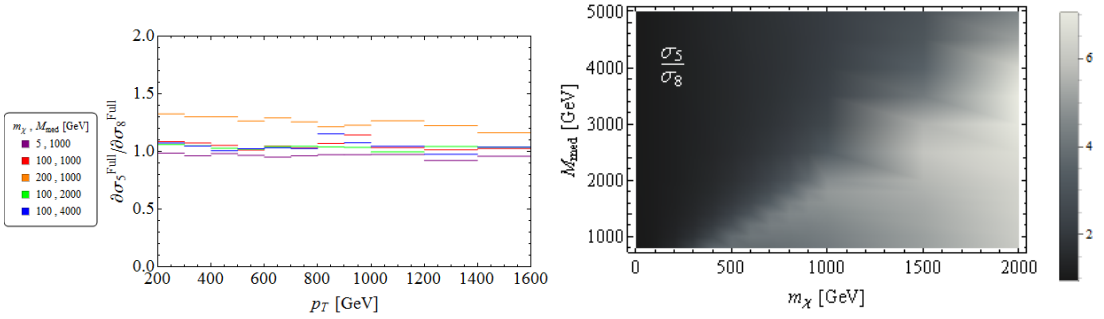

FIGURE 6.5: The same as Fig 6.4 but for a vector and an axial vector interactions.

Simplified models with s-channel mediator might also leave significant footprints in various experimental searches other than direct DM production at colliders. These are, for example, direct DM detection experiments and resonance searches in dijet production at the LHC. While it is important to consider these additional searches, this should be done with care since the reinterpretation of a set of constraints is model dependent. For instance, direct detection constraints are significantly weakened if the interaction is spin-dependent. Furthermore, since the collision energies are much lower ($1 - 100$ keV

range), direct detection may be entirely evaded if the dark spectrum is split by more than 100 keV or so, as is the case in inelastic DM models [369]. On the other hand such mass splittings are not a barrier at colliders and models of this kind can be searched for at the LHC (see further discussion in section 4.A of ref. [360]). This therefore provides another cogent example of the importance of a comprehensive program of complimentary DM searches. Here we briefly describe the constraints coming from dijet searches at the LHC.

The dijet narrow resonance searches, [370, 371], are relevant only for $\Gamma_{\rm med}/M_{\rm med} \lesssim 0.15$ in case of Gaussian shape or $\Gamma_{\rm med}/M_{\rm med} \lesssim 0.05$ for the Breit-Wigner case. In other cases the mediator will escape the direct searches. Therefore, the maximal couplings that may be probed by the narrow resonance searches with a Gaussian shape are

$$y_q < 1.1/\sqrt{N_q}\,, \qquad g_q < 1.4/\sqrt{N_q}\,. \tag{6.8}$$

For the Breit-Wigner case we find,

$$y_q < 0.65/\sqrt{N_q}\,, \qquad g_q < 0.79/\sqrt{N_q}\,. \tag{6.9}$$

Here we assume that the couplings to N_q quarks are equal to $y_q(g_q)$ for scalar and pseudoscalar (vector/axial vector) and both phase-space effects and the coupling to the DM candidate are neglected.

The CMS dijet angular distribution [372] and the ratio between the central and forward dijet cross-sections given by ATLAS [373] can be used to constrain models which can escape the narrow width searches. We note that the sensitivity of the angular distribution for relatively light mediators, $M_{\rm med} \lesssim 1\,\text{TeV}$, is limited because of the large contribution from gluon fusion. In that case, it may be that Tevatron data can be used to better constrain the relevant parameter space, as discussed in ref. [374] for example.

6.1.1.1 Expected Sensitivity for Monojet Search at 14 TeV

We present the expected sensitivity for a DM search in events with a monojet and MET ($\not{E}_T$) for the $\sqrt{s} = 14$ TeV run of the LHC and integrated luminosity of 300 fb^{-1}. The limits, shown in Fig. 6.6, are presented using simplified models with a scalar or axial vector mediator. Using Monte Carlo simulations for both background and signal, we derive prospective limits at 95% confidence-level (CL) on the product of mediator to DM and mediator to SM couplings, $y_\chi y_q$ ($g_\chi g_q$) for scalar (axial vector) mediator, for a range of DM and mediator masses. We assume flavor independent couplings to quarks and consider only part of the parameter space where predominantly off-shell production

of DM occurs, i.e. $M_{\text{med}} \lesssim 2m_\chi$. In this regime the cross section is expected to be independent of the mediator width, except for the region where $M_{\text{med}} \approx 2m_\chi$. In order to guarantee pertubativity of the models we only probe the parameter space for which,

$$g_{\chi/q}, y_{\chi/q} \leq 4\pi \tag{6.10}$$

and

$$\frac{\Gamma_{\text{med}}}{M_{\text{med}}} \lesssim 0.5. \tag{6.11}$$

In the region where the production cross section depends on $\Gamma_{\text{med}}/M_{\text{med}}$, we take the pertubative limit, $\Gamma_{\text{med}}/M_{\text{med}} = 0.5$. In the heavy DM mass region ($m_\chi \gtrsim 800$ GeV), where $y_\chi y_q \gtrsim 10.5$ for the scalar mediator and $g_\chi g_q \gtrsim 13$ for the axial vector mediator (which is outside our parameter space), one finds no sensitivity in the pertubative regime unless the mediator couples only to light quarks thereby suppressing $\Gamma_{\text{med}}/M_{\text{med}}$.

The main background processes are $Z \to \nu\bar{\nu}+jets$, $W \to \ell\nu+jets$, where $\ell = e, \mu, \tau$, and single boson production (Z, W) with the jet coming from Initial State Radiation (ISR). We consider these in the leading order approximation. Other background processes, such as di-boson and $t\bar{t}$ + single top were not taken into consideration, as their contribution to the background is smaller by orders of magnitude [240].

The background and signal events were generated using `MadGraph 5` generator [330] (with MSTW2008 PDF) for the hard process, and `Pythia` 6 [375] for showering and hadronization. For both signal and background we match the one and two jet samples. After the event generation, the interaction of the generated particles with the detector material and the detector response were simulated with `Delphes` 3.1.2 [376] and `ROOT` 5.3.4 [377], customized to the ATLAS detector geometry. All events were required to have $\not{E}_T > 120$ GeV, at least one jet with $p_{\text{T}} > 130$ GeV and $|\eta| < 2.0$. Events with more than two jets and events with a muon or an electron with $p_{\text{T}} > 30$ GeV and $|\eta| < 2.0$ were rejected. For signal and background events, the leading jet p_{T} distribution was drawn using the same binning as in the ATLAS monojet analysis [240]. The limit on the product of the coupling constants, $y_\chi y_q$ and $g_\chi g_q$, was calculated by requiring that the probability to find the background plus signal p_{T} distribution assuming the background only hypothesis gives a p-value of 0.05 using Poisson statistics. We leave a more detailed analysis including the case of on-shell production to a future study.

6.1.2 T-channel models

Modeling the WIMP χ as a fermion, we consider the dimension-6 operators of the form,

$$\mathcal{O}_6 = (\bar{q}\Gamma^m q) \quad (\bar{\chi}\Gamma'_m \chi) \tag{6.12}$$

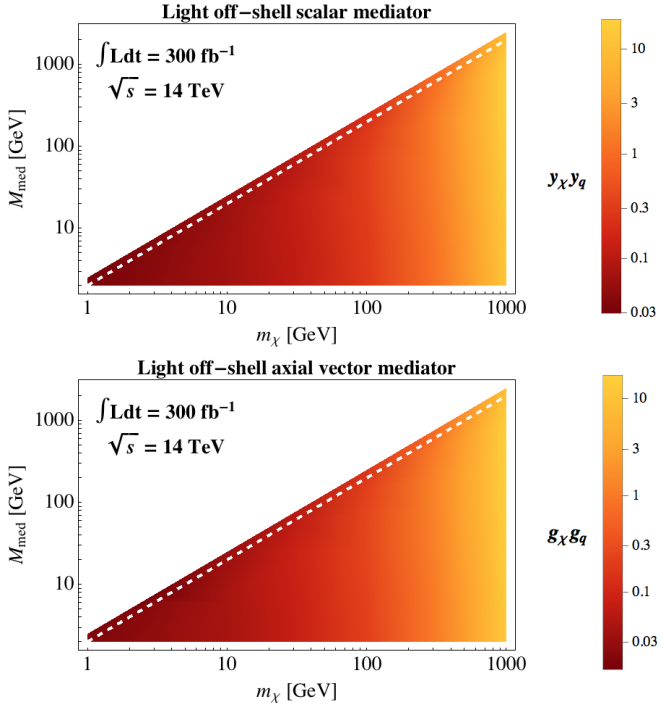

FIGURE 6.6: Expected sensitivity at 95% CL to the product of mediator coupling to DM and SM in the off-shell regime. The limits are derived for run II of the LHC at 14 TeV with 300 fb^{-1} of data, assuming a scalar (top) and an axial vector (bottom) mediator. The white dashed line indicates the boundary where $M_{\text{med}} = 2m_\chi$.

These are the D1-D10 operators in the notation of ref. [245]. These effective operators are generated through some new dynamics such as a particle mediating the interaction at tree level. In this section we consider a colored fermionic mediator with an interaction vertex between quarks and the WIMP resulting in a t-channel exchange as shown in Fig. 6.7. Similar to the s-channel case, this process can be searched for in events with large missing energy [3]. A concrete model is that of a squark exchange in supersymmetric models:

$$\mathcal{L} = \mathcal{L}_{SM} + g_M \sum_{i=1,2} \left(\widetilde{Q}_L^i \bar{Q}_L^i + \tilde{u}_R^i \bar{u}_R^i + \tilde{d}_R^i \bar{d}_R^i \right) \chi + \text{mass terms} + c.c. \tag{6.13}$$

where Q_L^i, u_R^i, d_R^i are the usual SM quarks, $\widetilde{Q}_L^i, \widetilde{u}_R^i, \widetilde{d}_R^i$ correspond to the respective squarks (from hereon the "mediators"), and i represents an index running over the first two generations, since we will not look at signals involving the third generation (see Sec. 6.1.4). Unlike the usual case in Superysmmetry, here the WIMP χ can be taken to be either Dirac or Majorana fermion. For simplicity we will take the mediator masses to be degenerate and focus on two different extreme cases: 1) all mediator flavors are

[3] One important difference between s- and t-channel mediators is that in the latter case colored radiation can originate from the mediator itself. See ref. [338] for the full set of leading order diagrams contributing to the process.

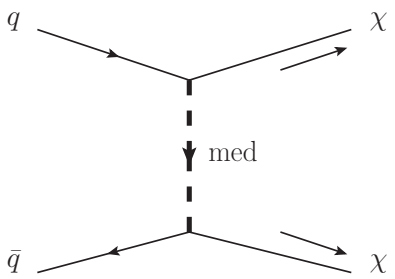

FIGURE 6.7: A massive scalar resolving dimension-6 operators of the form, Eq. (6.12), through a t-channel exchange. The MSSM with its squarks and neutralinos is an example of a full model exhibiting such a process.

present or 2) only $\tilde{d}_R^i$ are present. Simply due to multiplicity these two cases maximize and minimize the mediator production cross-section, respectively.

Since it is coupled to quarks, if kinematically possible the mediator can be produced on resonance at colliders. As discussed in Chapter 5, in this regime the EFT is no longer valid and the question is whether the actual limits are substantially changed. The largest production cross-section is associated with regions that are both at low center of mass energy (due to PDF effects), and on resonance [248, 317, 319, 334–337, 378, 379]. On the other hand, signal events at low $\sqrt{s}$ are strongly contaminated by SM backgrounds. As discussed in ref. [338], by comparing the EFT to the simplified model, one generally finds that the constraints from the simplified model are markedly different compared with those extracted from the EFT. If the mediator is kinematically accessible but sufficiently heavy, the correct bounds are stronger than those extracted from the EFT on account of resonant production [313]. If the mediator is light then the signal appears in the region contaminated by background and the EFT constraints are overly strong [323]. As in the case of s-channel discussed in Sec. (6.1.1) when the mediator is kinematically accessible one can directly search for it in other final states. Such searches may have a stronger impact than the monojet searches. For example, since the mediator couples to quarks and/or is a colored particle, this means that the mediator, rather than decaying only to DM, may be pair produced and be detected in multi-jet events with large missing energy [338]. As found in ref. [338], while monojet constraints on DD are relatively model independent in the EFT regime (which is not entered until the mediator is above 3 TeV in the s-channel case, and 1 TeV in the t-channel case and the DM is parametrically lighter), they rarely represent the true constraints, being either too weak (heavier mediator) or too strong (lighter mediator). The above Lagrangian, Eq. (6.13), induces a minimal decay width for each mediator

flavor given by the expression

$$\Gamma_{\text{med}}^{min} = \frac{g_M^2 M_{Med}}{16\pi}\left(1 - \frac{m_{DM}^2}{M_{Med}^2}\right)^2, \tag{6.14}$$

where M_{Med} is the mediator mass. The mediator width can be larger if additional states to which it can decay exist. These additional states are possibly constrained by LHC searches other than the ones considered herein. Since this involves more model dependency, we leave the mediator decay width as a free parameter in our results.

We now briefly review how multi-jet plus missing energy searches can probe the parameter space of this simplified model. Monojet analyses are cut-and-count based and involve signal regions defined by cuts on the transverse momentum of the jet and missing energy in the event. Limits are set independently for each signal region and the upper bound on the number of signal events is provided so that no further statistical analysis is necessary. By simulating the signal with different values of the coupling, g_M, one can find the maximal allowed couplings compatible with observations. We note that as the coupling increases, the width of the mediators must be taken at least as large as $\Gamma_{\text{med}}^{\text{min}}$, according to Eq. (6.14).

An important caveat to consider when performing a monojet analysis is that, despite the name, starting from analyses for the 8 TeV run of the LHC, no cuts on the p_T of the second leading jet are imposed. Simulating event samples without a second hard jet at parton level is therefore erroneous and would produce dramatically weaker constraints, as shown in ref. [338].

A second remark that applies both to monojet and multi-jet plus MET searches concerns the effect of the narrow width approximation (NWA). The standard procedure taken by ATLAS to extract limits on simplified models (for instance in the searches for gluinos or squarks) is to generate events for on-shell production of the heavier resonance, which later decays into the dark matter plus jets and missing energy. In doing so, one implicitly assumes that the cross-section is dominated by diagrams with mostly on-shell squarks and that their width is extremely narrow. On the other hand, the values of the coupling to which jets+MET searches are sensitive to force the squark widths to be comparable or larger than the p_T thresholds of the jets required by the analyses. Thus, finite width effects are important and once again we refer to ref. [338] for a quantitative discussion of these effects.

The parameter space for this colored-mediator + dark matter simplified model consists of three parameters only: the two masses M_{Med}, m_{DM} and the mediator-quark-dark matter coupling g_M. An intuitive and convenient way to visualize the results would be a color density plot in the M_{Med}, m_{DM} plane. In Figs. 6.8, 6.9 we report the exclusion bounds

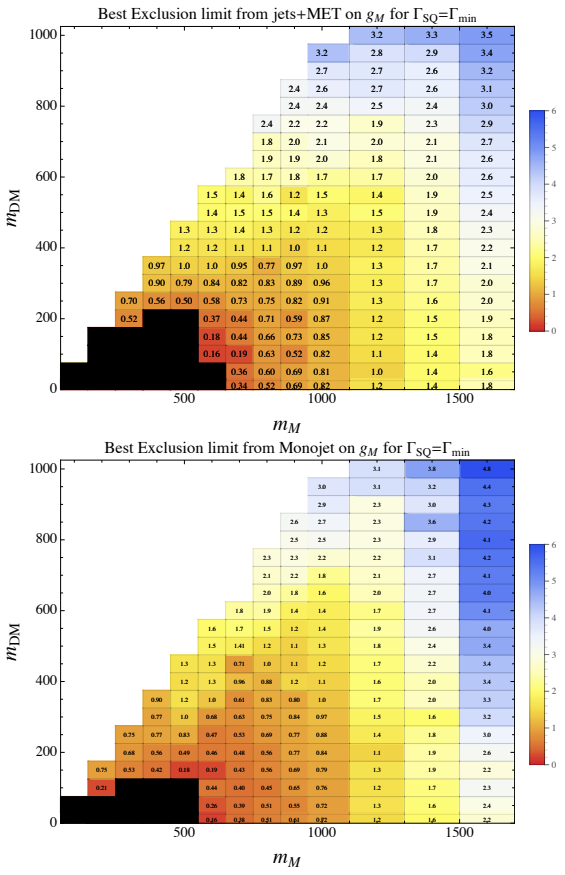

FIGURE 6.8: Limits from ref. [338] on g_M (for the case of mediator coupling to $\tilde{u}$, $\tilde{d}$, $\tilde{c}$, $\tilde{s}$, $L+R$) from (*left*) jets+MET, and (*right*) monojet, for a mediator decaying only to DM and a quark, with the natural width computed from Eq. (6.14). The black region in (a) is excluded from the pure QCD production of the mediator. Note that the mediator mass is denoted by m_M in these plots instead of M_{Med} as in the rest of the text.

for the simplified model with all mediator flavors, $\widetilde{Q}_L^i$, $\widetilde{u}_R^i$, and $\widetilde{d}_R^i$. The model with only $\tilde{d}_R^i$-type mediators can be treated in a similar manner and provides weaker constraints, owing to the smaller production cross section. From the plots we see that the interesting mass ranges are restricted to $100\text{GeV} \leq M_{Med} \leq 2\text{TeV}$, $100\text{GeV} \leq m_{DM} \leq 1\text{TeV}$. Outside this region the sensitivity of the jets+missing energy searches decreases until eventually the interpretation of the model as a tree level exchange of a heavy resonance is lost, either because $g_M \sim 4\pi$ or because $\Gamma_{\text{med}}^{min}(g_M) \sim M_{Med}$.[4]

[4]Except in the compressed case regime, the latter happens before the former.

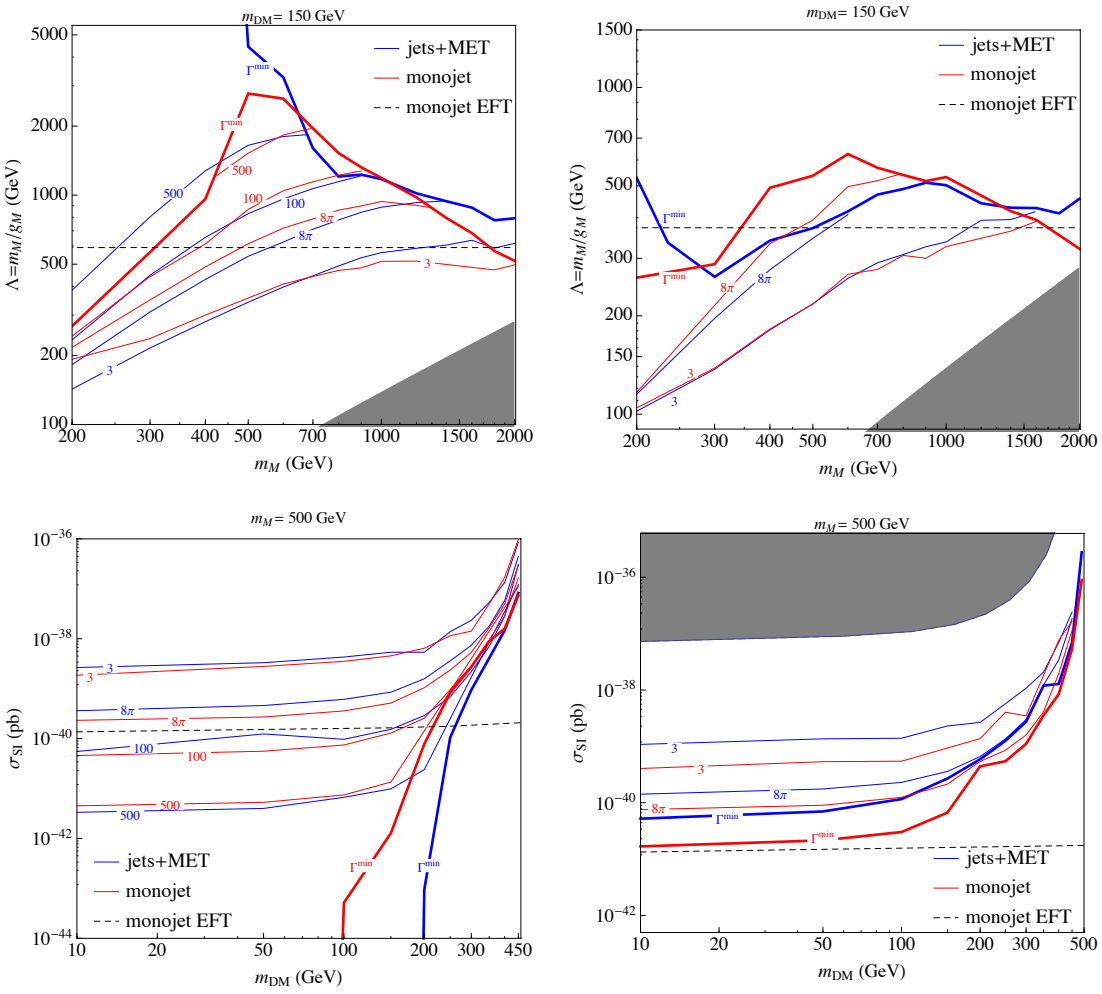

FIGURE 6.9: Examples of exclusion limits on $\Lambda = M_{Med}/g_M$ and direct detection cross section for two simplified models: $\widetilde{u}, \widetilde{d}, \widetilde{c}, \widetilde{s}$, L+R (left column); $\widetilde{d}_R, \widetilde{s}_R$ (right column). Figures taken from ref. [338]. Note that the mediator mass is denoted by m_M in these plots instead of M_{Med} as in the rest of the text.

6.1.3 Gauge Field Strengths models

We now move on to consider the EFT operators associated with gluons in the initial state, such as the CP conserving operators,

$$\frac{\alpha_s}{4\Lambda^3}\mathrm{tr}\left(G_{\mu\nu}G^{\mu\nu}\right)\bar{\chi}\chi, \quad \text{and} \quad \frac{i\alpha_s}{4\Lambda^3}\epsilon^{\mu\nu\alpha\beta}\mathrm{tr}\left(G_{\mu\nu}G_{\alpha\beta}\right)\bar{\chi}\gamma_5\chi \tag{6.15}$$

where α_s is the strong coupling and Λ denotes a high-energy scale. These are operators of the type D11-D14 of ref. [245] (similar models involving Elecroweak gauge bosons can be found here [380]). Simplified models for such dimension-7 operators are more complicated. In contrast to the simple resolutions we saw in sections 6.1.1 and 6.1.2, these operators cannot be resolved into two renormalizable operators glued by a single bosonic or fermionic mediators. Any resolution of these operators through a tree level exchange

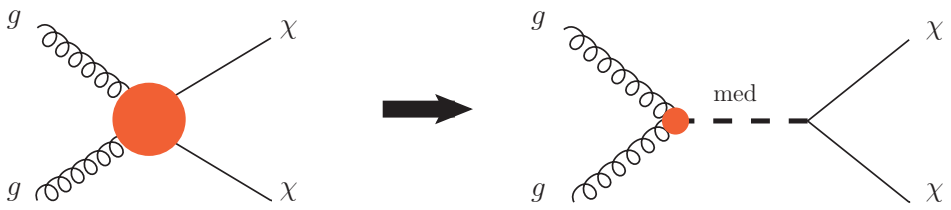

FIGURE 6.10: The dimension-7 operators contributing to processes such as $gg \to \chi\chi$ on the left can be resolved to lowest order via the diagram on the right with a scalar in the s-channel. The red blob in the scalar-gluon vertex on the right serves as a reminder that this is also a non-renormalizable interaction that has to be resolved at some energy scale.

of a mediator will itself involve at least one non-renormalizable operator. Alternatively these operators can be resolved through a loop of mediators. We begin by considering the tree level resolution as it is sufficiently simple to be used as a simplified model.

A tree-level resolution of the dimension-7 operators is shown in Fig. 6.10: a scalar (or pseudoscalar) that couples through a renormalizable Yukawa-type interaction to the WIMP (a fermion) and with higgs-like (or axion-like) coupling to the gluons (dimension-5) is exchanged through the s-channel. The interactions take the form,

$$\mathcal{L} \supset y_\chi S \bar{\chi}\chi + \frac{\alpha_s}{\Lambda_S} S G_{\alpha\beta} G^{\alpha\beta} \tag{6.16}$$

for the scalar and

$$\mathcal{L} \supset i y'_\chi S' \bar{\chi}\gamma_5\chi + \frac{\alpha_s}{\Lambda_{S'}} S' G_{\mu\nu} G_{\alpha\beta} \epsilon^{\mu\nu\alpha\beta} \tag{6.17}$$

for the pseudoscalar. Here Λ_S is some mass scale associated with the dimension-5 operator and the trace over the color indices has been left implicit. The scale that appears in the dimension-7 operators (D11-14) is given parameterically by,

$$\frac{\alpha_s}{4\Lambda^3} \sim \frac{1}{m_S^2} \frac{y_\chi \alpha_s}{\Lambda_S} \tag{6.18}$$

where m_S is the mass of the scalar S. A similar expression holds for the case of a pseudoscalar or for multiple scalars. Current collider constraints on the dimension-7 operators from missing energy searches (see e.g. [238]) give a bound of $\Lambda \gtrsim 350\,\text{GeV}$. This is such a low scale that one must seriously wonder whether this description is valid at LHC energies. Indeed, as was shown in ref. [249] the EFT approach for this operator breaks down and the limit $\Lambda \gtrsim 350\,\text{GeV}$ is invalid.

Resolving the dimension-7 operator through a scalar or pseudoscalar exchange ameliorate this problem. As is clear from Eq. (6.18) by having a sufficiently light scalar (small m_S)

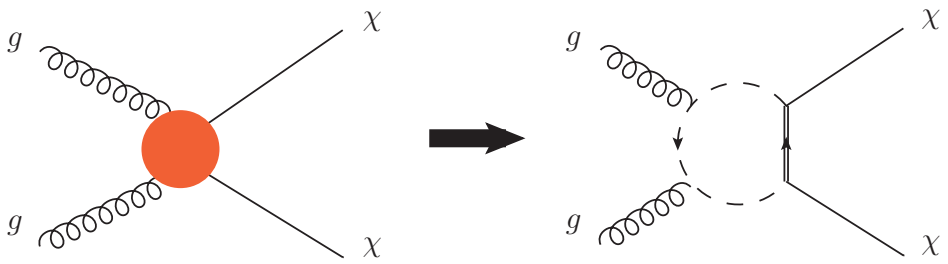

FIGURE 6.11: The dimension-7 operator contributing to processes such as $gg \to \chi\bar{\chi}$ on the left is resolved on the right in a model with new colored scalars (dashed line) and fermions (double line) that couple to the WIMP χ. Several other diagrams contribute aside from the one shown, see ref. [382] for details.

we can have very low effective scale Λ. Importantly, this can be done consistently by keeping the dimension-5 scale, Λ_S sufficiently heavy to avoid any unitarity issues with this operator (at sufficiently high energies even this operator must be resolved as we discuss below). The scalars can now be produced on-shell and the $gg \to \chi\bar{\chi}$ process is dominated by this production. The interactions in Eqs. (6.16) and (6.17) can be easily implemented in existing event generators. In fact, the case of a scalar is entirely analogous to a heavy higgs boson that is produced on-shell through the usual gluon-fusion process and decays dominantly into missing energy.

Resolving the dimension-5 operator $SG_{\alpha\beta}G^{\alpha\beta}$ can be done if the scalar S is coupled through Yukawa coupling to some new heavy colored states (this is completely analogous to the Higgs coupling to gluons via the top quark loop). In the limit of heavy mediators' mass the dimension-5 coupling is related to the heavy colored states' mass and coupling through [381]

$$\frac{\alpha_s}{\Lambda_S} \propto \frac{\alpha_s}{8\pi} \sum_f \left(\frac{y_f}{M_f} \right) \tag{6.19}$$

where the sum runs over all heavy colored fermions, y_f is the Yukawa coupling of these fermions to the scalar S, M_f is the heavy fermions f. A similar expression holds for the case of a pseudo-scalar. So, this model can be resolved into a fully renormalizable model by introducing new heavy (vector-like) quarks that couple to the scalar mediator. The relations of Eq. (6.19) and Eq. (6.18) require a mediator mass m_S which is not too heavy or the colored states are far too light and would have already been observed in searches for new colored states.

It is also possible to resolve the dimension-7 operators directly into renormalizable interactions with colored mediators as was done for example in refs. [382, 383] and is shown in Fig. 6.11. A simple example of such a model is one with new colored scalars and

fermions that couple to the WIMP through a Yukawa-type interaction. The coupling of the dimension-7 operator is then related to the mass and coupling of these new states through,

$$\frac{\alpha_s}{4\Lambda^3} \propto \frac{\alpha_s \lambda_\chi^2}{M_{\rm med}^3} \tag{6.20}$$

where $M_{\rm med}$ is the mass of the mediators and λ_χ is their coupling to the WIMP. Evidently, one needs fairly light mediators to generate the scale bounded by searches at the LHC, $\Lambda \sim 350\,\text{GeV}$ as in ref. [238]. Such new colored states are much easier to search for in other channels by producing them directly. Thus, this model is not very useful in providing a simplified framework to look for the process $gg \to \chi\bar{\chi}$.

To conclude this section we reiterate that resolving dimension-7 operators of the type discussed above (D11-D14 of ref. [245]) in terms of simplified models is not as straightforward as it is for operators associated with quarks (e.g. D1-D10). Because of their high dimensionality using these EFT operators at the LHC is particularly problematic as was recently shown in [249]. Perhaps the simplest way of making sense of such operators is through a new higgs-like scalar (or pseudoscalar) that couples directly to the WIMP through a Yukawa coupling and to gluons through a dimension five operator as in Eqs. (6.16) and (6.17).

6.1.4 Simplified models with Heavy Quarks

Models with dark matter coupled preferentially to third generation quarks have qualitatively different collider signals, including b-jets or higher multiplicity final states from top quarks. In the EFT approach, this corresponds to operators with flavor-dependent couplings. A flavor-safe way to treat this scenario is to assume minimal flavor violation, where the interaction strength for each flavor is proportional to the quark mass. The coefficients of the D1-D4 operators were parameterized to take this into account:

$$\mathcal{O}_{D1} = \sum_q \frac{m_q}{\Lambda^3} \bar{q} q \bar{\chi} \chi, \tag{6.21}$$

again assuming the DM is a fermion χ. It is also straightforward to allow for different overall coefficients in the coupling to up-type and down-type quarks [384].

The enhanced couplings to heavy quarks for these operators led Ref. [385] to consider the b-jet plus MET (mono-b) and $t\bar{t}$ plus MET collider signals. Despite the PDF suppression for producing these final states, it was found that limits could be improved significantly relative to the tree-level monojet limit. The irreducible background from V+jets was

also reduced due to the requirement of a b-tag. Furthermore, Ref. [386] pointed out that heavy quark loops lead to DM production through gluon fusion, which leads to much stronger monojet limits. However, in both cases the derived limit for light dark matter is $\Lambda \gtrsim 100$ GeV for the 8 TeV LHC run, in the case of the D1 operator as shown in Fig. 6.12. The limits are expected to increase to almost 300 GeV at 14 TeV [387].

We briefly comment on the validity of the EFT assumption, following the discussion in Chapter 5. Assuming an s-channel scalar mediator that couples primarily either to b-quarks or to top-quarks, the relation between the mediator mass M_{Med} and Λ for the D1 operator above is given by:

$$\Lambda = \left(\frac{m_q M_{Med}^2}{g_q g_\chi} \right)^{1/3}. \tag{6.22}$$

For $\Lambda = 100$ GeV and coupling to b-quarks, the condition on the momentum transfer in Eq. (5.5) becomes $Q_{\rm tr} < \sqrt{g_b g_\chi} \times 461$ GeV. Events passing mono-b cuts can only satisfy this requirement for large couplings $\sqrt{g_b g_\chi} \gtrsim 4$. The situation is worse for coupling to top quarks, which requires momentum transfer $Q_{\rm tr} < \sqrt{g_t g_\chi} \times 76$ GeV. Even with extreme couplings of 4π, the implied mediator mass is below 1 TeV, signaling the need for simplified models.

The simplest UV-complete possibility where DM couples to quarks proportional to their mass arises in Higgs-mediated models. Simplified s-channel mediator models introduce a new neutral scalar [388], pseudoscalar or vector [389] analogous to those discussed in Section 6.1.1, but the dominant interactions are with heavy quarks. For example, Refs. [390, 391] focused on a pseudoscalar, a, coupling primarily to b-quarks, which could arise through mixing with the pseudoscalar in a two-Higgs doublet model. The relevant interaction terms in this case are:

$$\mathcal{L} \supset i(g_\chi \bar{\chi}\gamma^5\chi + g_b \bar{b}\gamma^5 b)a \tag{6.23}$$

It was shown in Ref. [390] that both the mono-b and the sbottom search with two b-jets plus MET help to constrain the parameter space, depending on the a mass.

Simplified t-channel models also have collider signals with heavy quarks, for example if there is a sbottom-like scalar mediator $\tilde{B}$:

$$\mathcal{L} \supset -\lambda \tilde{B} \bar{b}_R \chi + \text{h.c.} \tag{6.24}$$

which could arise in flavored dark matter models [392]. Note that these interactions do not necessarily generate the scalar (D1) operator above, and in addition the assumption of minimal flavor violation does not require interaction strengths to be proportional to

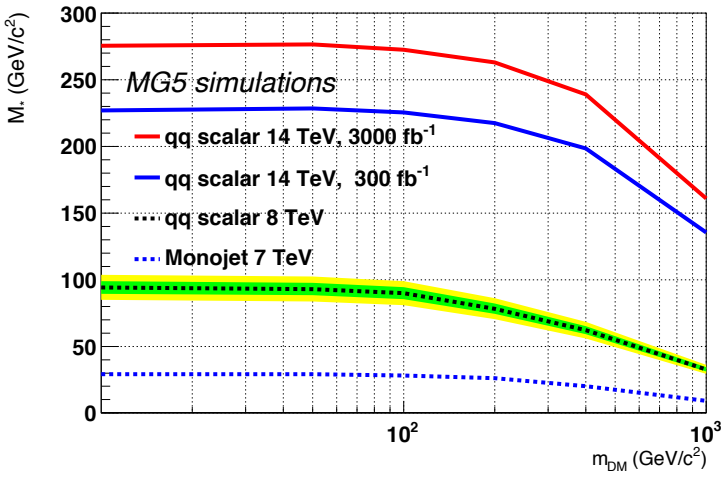

FIGURE 6.12: Expected 90% CL limits on the scalar operator D1 from a DM plus heavy quark search, including couplings to tops and bottoms. ATLAS 7 TeV limits come from [238].

mass. The sbottom search can be used to constrain the new mediator; however, when the coupling λ in Eq. (6.24) is large additional channels open up relative to the SUSY case, which changes the final state kinematics. Other t-channel models include instead DM coupling to the third generation left-handed doublet [334] or to right-handed top quarks [393, 394].

In the presence of additional flavor-violating structure, single top plus MET (mono-top) production is possible [384, 395, 396]. An example is the simplified t-channel model of fermion dark matter coupled to top quarks, when the scalar mediator also has RPV-like couplings to light quarks.

6.2 Constrains on Parameters space from Relic Density

6.2.1 Introduction

If DM consists of particles whose mass and interactions with SM particles are dictated by physics in the electroweak energy range, the DM abundance in our universe is likely to be fixed by the thermal freeze-out phenomenon: DM particles, initially present in our universe in thermal equilibrium abundance, annihilate with one another till chemical equilibrium is lost due to the expansion of the universe [35, 264, 342, 397]. The present-day relic density of these particles is predictable and, in the simple case of s-wave self-annihilation of DM in the early universe, it comes out to be (in units of the critical

energy density of the universe)

$$\Omega_{\rm DM}h^2 \simeq \frac{2 \times 2.4 \times 10^{-10}\,{\rm GeV}^{-2}}{\langle\sigma v\rangle_{\rm ann}}, \tag{6.25}$$

where $\langle\sigma v\rangle_{\rm ann}$ is the total thermally-averaged annihilation cross section, and the factor of 2 in the numerator is made explicit to emphasize the fact that we are assuming a non-self-conjugate DM particle. This abundance must match the one recently measured by the Planck collaboration, $\Omega^{\rm obs}_{\rm DM}h^2 = 0.1199 \pm 0.0027$ [66].

Now, a fundamental question which one should ask is the following: under the optimistic hypothesis that the next LHC run gives evidence for a new weakly interacting particle with a lifetime that exceeds about a microsecond, how confident can we be in claiming we have finally revealed the true nature of the DM?

The goal of this section is to investigate whether a new stable particle, within a given set of models, may be assigned the label of thermal relic DM by comparing the regions of the parameter space where the right abundance is attained with the exclusion regions for the forthcoming Run II at the LHC. The latter are a useful benchmark for evaluating the sensitivity of the analysis at 14 TeV. However, if DM is within the reach of the LHC, it is also useful to make the comparison with the 5σ discovery potential regions. Of course, one can also reverse the logic of this exercise and identify the regions of the parameter space of a given model where the DM abundance fits the observed one. This might be useful to set priorities for the LHC collaborations when comparing the future data with the plethora of models.

This is not to say that this analysis can exclude the possibility that a new stable particle can be DM. Rather, if the new particle is inconsistent with thermal-relic DM under our assumptions and in a particular model, then we learn that either: **1)** the model is not the correct model of DM, or **2)** one of the assumptions enumerated in Section 6.2.2 do not hold.

This section is structured as follows. In Subsection 6.2.2 we provide some general considerations and state our assumptions, along with a description of the model we consider. In Subsection 6.2.3 we compare ATLAS 14TeV sensitivity with the region of parameter space consistent with thermal relic DM. In Subsection 6.2.4 we extend this analysis to simplified models. Finally, we collect our concluding remarks in Subsection 6.2.5.

6.2.2 Working Assumptions

The goal of this Section is to provide some general considerations about the DM abundance and its link with collider searches and, above all, to list as clearly as possible the set of assumptions we are working with.

6.2.2.1 DM Abundance Considerations

Consider the general scenario where a DM candidate χ will eventually be efficiently pair-produced at the LHC. This implies that χ must interact with first-generation quarks, therefore one can define the thermally averaged DM annihilation cross section [5]

$$\langle \sigma v \rangle_* \equiv \langle \sigma v \rangle_{\chi\bar{\chi}\to u\bar{u}} + \langle \sigma v \rangle_{\chi\bar{\chi}\to d\bar{d}}, \tag{6.26}$$

which also sets a reference for DM production at the LHC. In the early universe, besides annihilations into quarks, there can be additional annihilation channels, so that the total DM annihilation cross section which is relevant for the relic abundance is

$$\langle \sigma v \rangle_{\rm ann} \geq \langle \sigma v \rangle_*. \tag{6.27}$$

So, by requiring that the particles χ and $\bar{\chi}$ compose the DM abundance, we find

$$\Omega^{\rm obs}_{\rm DM} h^2 \simeq \frac{2 \times 2.4 \times 10^{-10}\,{\rm GeV}^{-2}}{\langle \sigma v \rangle_{\rm ann}} \leq \frac{2 \times 2.4 \times 10^{-10}\,{\rm GeV}^{-2}}{\langle \sigma v \rangle_*}, \tag{6.28}$$

or

$$\langle \sigma v \rangle_* \lesssim 4.0 \times 10^{-9}\,{\rm GeV}^{-2}. \tag{6.29}$$

On the other hand, one can make the reasonable assumption that the dominant DM annihilation channel is to SM fermions and the coupling to the first generation of quarks is not less than the coupling to other SM fermions. This hypothesis follows from the requirement that the would-be DM particles are efficiently produced in the next Run II. We are the first to admit that this assumption is debatable, but we consider it as a working hypothesis. We will show later how weakening this assumption affects our results. In this case, we get

$$\langle \sigma v \rangle_{\rm ann} \leq \sum_{\rm quark\,gen.} \langle \sigma v \rangle_* + \sum_{\rm lepton\,gen.} \frac{1}{3} \langle \sigma v \rangle_* \simeq 4 \langle \sigma v \rangle_*, \tag{6.30}$$

and therefore

[5] Gluons and other quarks can of course contribute to DM production at the LHC, so the $_*$ subscript defines a reference channel rather than all possible channels of DM production at the LHC.

$$\Omega_{\rm DM}^{\rm obs} h^2 \simeq \frac{2 \times 2.4 \times 10^{-10}\,{\rm GeV}^{-2}}{\langle \sigma v \rangle_{\rm ann}} \gtrsim \frac{2 \times 6.0 \times 10^{-11}\,{\rm GeV}^{-2}}{\langle \sigma v \rangle_{*}}, \tag{6.31}$$

or

$$\langle \sigma v \rangle_{*} \gtrsim 1.0 \times 10^{-9}\,{\rm GeV}^{-2}. \tag{6.32}$$

Let us illustrate the relevance of these inequalities with a simple example. Assume that the interactions between DM and SM quarks are described within an Effective Field Theory (EFT), where the basic parameters are the DM mass $m_{\rm DM}$ and the UV scale Λ. Let us also imagine that the annihilation controlling the thermal abundance takes place in the s-wave. One therefore expects roughly that $\langle \sigma v \rangle_{*} \simeq 10^{-1} m_{\rm DM}^2/\Lambda^4$. We then obtain, from Eqs. (6.29) and (6.32),

$$0.7 \left(\frac{m_{\rm DM}}{10^2\,{\rm GeV}}\right)^{1/2} {\rm TeV} \lesssim \Lambda \lesssim 1.0 \left(\frac{m_{\rm DM}}{10^2\,{\rm GeV}}\right)^{1/2} {\rm TeV}. \tag{6.33}$$

This value of the UV scale needs to be compatible with the one needed to explain the positive DM signature at the LHC. For instance, if Λ turns out to be larger than the value of the lower bound, one concludes that the would-be DM particle has to annihilate in other channels which we do not have control of and therefore it would be difficult, if not impossible, to assign it the label "dark matter".

Curves corresponding to the correct relic abundance have been used as a benchmark or comparison for EFT constraints since the early usage of EFTs [245, 311]. However, these relic density constraints on thermal DM are usually considered not to be robust: for a given set of parameters, the relic density can be smaller if the cross section is enhanced by inclusion of other annihilation channels, such as annihilation to leptons; conversely, the true relic density can be larger if there is a larger dark sector including other types of DM. However, under a modest set of assumptions, these constraints can become substantially more powerful. Throughout this analysis, we will assume:

1. the DM candidate χ makes up 100% of the DM of the universe;
2. the DM annihilation rate is related to the observed density today via the standard thermal production mechanism;
3. the dominant annihilation channel is to SM fermions, via one dark mediator;
4. the DM couples to u, d quarks, so that it can be produced at the LHC;
5. the coupling to the first generation of quarks is no less than the coupling to other SM fermions.

In this situation, the relic density constraint gives a range within which the dark sector parameters should lie. It is clear that assumption 5 is by no means a certainty, and so we will show how our results are sensitive to relaxing this assumption. In the event of a signal, this assumption can instead be used to learn about the flavour structure of a thermal relic model that attempts to explain the signal. If the signal falls into the region where DM would be overproduced, then there must be enhanced couplings to other SM particles relative to u, d quarks in order to avoid overproduction, or alternatively, the DM is produced by some mechanism other than thermal production.

Assumption 2 can break down if either the DM was not produced thermally in the early universe, or if some other effect breaks the relationship between the DM density and annihilation rate. For example, unusual cosmologies between freezeout and today can influence the relic density of DM [398].

To summarize, under our generic assumptions 1-5 the DM production cross section must satisfy the bounds

$$1.0 \times 10^{-9}\,\mathrm{GeV}^{-2} \simeq \frac{1}{4}\langle\sigma v\rangle_{\mathrm{ann}} \leq \langle\sigma v\rangle_{*} \leq \langle\sigma v\rangle_{\mathrm{ann}} \simeq 4.0 \times 10^{-9}\,\mathrm{GeV}^{-2}\,, \tag{6.34}$$

where the value of the annihilation cross section is dictated by ensuring the correct relic abundance.

These tidy inequalities break down when we include the effect of the top quark mass, mediator widths, and a more accurate expression for the relic density later in the text, although the principle behind them remains the same. The two limits on the cross section describe two contours in the parameter space: if $\langle\sigma v\rangle_{*}$ is too large, then DM will be underproduced, we call this the *underproduction line*; if $\langle\sigma v\rangle_{*}$ is too small, then DM will be overproduced; this is called the *overproduction line*. This information is summarised in the table below, where $g_{(\mathrm{DM},f)}$ generically indicate the mediator couplings to DM and SM fermions, respectively.

Overproduction line	$\langle\sigma v\rangle_{\mathrm{ann}} \simeq 4\langle\sigma v\rangle_{*}$	**EFT:** Max Λ, min m_{DM}. **Simpl. mod.:** Max M, min $g_{(\mathrm{DM},f)}$, m_{DM}.
Underproduction line	$\langle\sigma v\rangle_{\mathrm{ann}} = \langle\sigma v\rangle_{*}$	**EFT:** Min Λ, max m_{DM}. **Simpl. mod.:** Min M, max $g_{(\mathrm{DM},f)}$, m_{DM}.

6.2.2.2 Models and cross sections

To illustrate our point, we focus on a class of simplified models where the DM is a Dirac particle annihilating to SM fermions in the s-channel via a Z'-type mediator. This

popular scenario has seen much attention, including searches by CDF [399], ATLAS [400] and CMS [401].

Working with simplified models is more timely than ever. For some years, the use of effective operators has been popular as a way to place general constraints on the dark sector [70, 245, 310–313, 352–357, 402]. However, there has always been concern that this approximation breaks down at some mediator mass scale and it is now clear that the effective operator assumption is not a good approximation at LHC energies unless the DM-SM coupling is very large [72, 248–250, 311, 313, 319, 324, 325, 360, 366]. On the other end of the spectrum, studies of specific well-motivated models such as supersymmetry [345] or extra dimensions [105] continue to play an important role, but the broad parameter space and specific assumptions required in these models make it difficult to draw general conclusions about the dark sector. Hence, simplified models have become the best way to constrain the DM parameter space [251, 363, 365, 403–405]. However, this parameter space is still broad, and it is usually unfeasible to constrain the entire space in just one analysis. This necessitates a specific choice for one or more parameters – for example the coupling-strength and mediator-mass may be constrained for a specific choice of the DM mass. Clearly this is sub-optimal, since we do not want our constraints to be valid only for one arbitrary choice of an unknown parameter. It is important to remember that the search for new neutral particles with electroweak couplings is motivated by the existence of dark matter, and so the requirement that these particles are a viable thermal relic DM candidate can be a powerful motivator for these arbitrary choices.

There are many other simplified models to choose from. For example, one could consider a model where dark matter couples to the standard model via s-channel exchange of a scalar mediator. In these models, the dark sector usually couples to the standard model via mixing between the new dark mediator and the Higgs. This leads to a Yukawa-type mediator-SM coupling, proportional to the SM fermion mass. This suppresses the production rate via u and d quarks at the LHC relative to top quark loop-induced production via gluon initial states. This suppression also applies to the annihilation rate, especially if annihilation to top quarks is kinematically (or otherwise) unavailable, resulting in very large DM masses and couplings and small mediator masses in order to reach the correct relic density. Hence we do not consider this model here. Another alternative is DM coupling to SM particles via exchange of a scalar mediator in the t-channel, as studied in e.g. [332, 334–337]. The phenomenology is a little different here, for example in the t-channel model the colored mediator can decay into a quark-DM pair [338]. Whilst this is an interesting model, we choose to study a Z'-type model as it has the best prospective LHC Run-II constraints with which to compare.

We consider the general interaction term in the Lagrangian for a vector mediator Z',

$$\mathcal{L} = -\sum_f Z'_\mu [\bar{f}\gamma^\mu (g_f^V - g_f^A \gamma_5) f] - Z'_\mu \, [\bar{\chi}\gamma^\mu (g_{\rm DM}^V - g_{\rm DM}^A \gamma_5)\chi], \tag{6.35}$$

where f is a generic SM fermion, the kinetic and gauge terms have been omitted, and the sum is over the quark and lepton flavours of choice (see e.g. Ref. [365]).

The LHC searches are only mildly sensitive to the ratios g_f^V/g_f^A and $g_{\rm DM}^V/g_{\rm DM}^A$, however the distinction is important for relic density calculations, and so we consider a pure vector coupling ($g_{f,\rm DM}^A = 0$). In the EFT limit, we also consider pure axial ($g_{f,\rm DM}^V = 0$) interactions. In the low-energy limit, the Lagrangian (6.35) leads to the effective operators

$$\mathcal{O}_V = \frac{1}{\Lambda^2}[\bar{\chi}\gamma^\mu\chi][\bar{f}\gamma_\mu f]\,, \qquad \text{(D5)} \tag{6.36}$$

$$\mathcal{O}_A = \frac{1}{\Lambda^2}[\bar{\chi}\gamma^\mu\gamma^5\chi][\bar{f}\gamma_\mu\gamma^5 f]\,. \qquad \text{(D8)} \tag{6.37}$$

The effective operators $\mathcal{O}_V$ and $\mathcal{O}_A$ correspond to the usual D5 and D8 operators respectively, defined in Ref. [245].

The process relevant for relic density calculations is the annihilation of DM particles of mass $m_{\rm DM}$ into SM fermions of mass m_f

$$\chi\bar{\chi} \to f\bar{f}. \tag{6.38}$$

In the effective operator limit, the relative cross sections per SM fermion flavour, expanded up to order v^2, are

$$(\sigma v)_*^V \simeq \frac{N_C m_{\rm DM}^2}{2\pi\Lambda^4}\left(\sqrt{1-\frac{m_f^2}{m_{\rm DM}^2}}\left(\frac{m_f^2}{m_{\rm DM}^2}+2\right) + v^2\frac{11m_f^4/m_{\rm DM}^4 + 2m_f^2/m_{\rm DM}^2 - 4}{24\sqrt{1-m_f^2/m_{\rm DM}^2}}\right) \tag{6.39}$$

$$(\sigma v)_*^A \simeq \frac{N_C}{2\pi\Lambda^4}\left(m_f^2\sqrt{1-\frac{m_f^2}{m_{\rm DM}^2}} + v^2\frac{23m_f^4/m_{\rm DM}^2 - 28m_f^2 + 8m_{\rm DM}^2}{24\sqrt{1-m_f^2/m_{\rm DM}^2}}\right). \tag{6.40}$$

where the colour factor N_C is equal to 3 for quarks and 1 for colourless fermions. The full expressions relative to the process (6.38) with Z' exchange, and the corresponding mediator widths, are reported in Appendix C.

6.2.3 Results: Effective operator limit

In the extreme EFT limit, for massless SM annihilation products, the annihilation cross section for a dimension-6 operator goes like $g_{\rm DM}^2 g_f^2 m_{\rm DM}^2/M^4 \equiv m_{\rm DM}^2/\Lambda^4$, where M is

the mediator mass, and g_f is its coupling with fermion species f. Thus, in general, the underproduction contour is a contour of maximum $g_{\rm DM}$, g_f, and $m_{\rm DM}$, and of minimum M, and vice-versa for the overproduction contour. Here we compare a range of constraints in the effective operator scenario, where the momentum carried by the mediator is assumed to be small relative to its mass and we define [6]

$$\Lambda \equiv \frac{M}{\sqrt{g_{\rm DM} g_f}}. \tag{6.41}$$

The LHC constraints in this scenario are generally valid in the range $\pi \lesssim \sqrt{g_{\rm DM} g_f} \lesssim 4\pi$ [331]. Since the annihilations relevant to relic density calculations take place when the DM is non-relativistic, the effective operator approximation is valid as long as $M \gg 2m_{\rm DM}$, or $\sqrt{g_{\rm DM} g_f} \gg 2m_{\rm DM}/\Lambda$, while direct detection constraints are valid across the entire parameter space of interest.

Our results in this limit are summarized in Fig. 6.13, where we compare the projected exclusion and discovery reach by ATLAS with the *under*- and *over*-production lines defined in the previous Section for the vector and axial-vector operator. In the following subsections we describe all the elements appearing in Fig. 6.13.

6.2.3.1 ATLAS reach

We use simulations of the exclusion and discovery reach of ATLAS at 14 TeV from Ref. [331]. This reference estimates the sensitivity of ATLAS to DM in the missing energy + jets channel. This is a powerful general-purpose channel which has led to strong constraints on DM by both ATLAS and CMS at 7 and 8 TeV [238, 349]. Searches for other final states such as mono-W/Z [332, 333, 406, 407], mono-photon [408, 409], mono-higgs [410, 411] and mono-top [395] can play a complementary role, especially when combined into mono-all searches. However, the monojet searches still give the strongest constraints [412], and thus represent a good choice for sensitivity studies.

The limits from Ref. [331] are only given for two DM masses, $m_{\rm DM} = \{50, 400\}$ GeV, however there is minimal variation in the constraint between the two masses, so we interpolate constraints on Λ between these two points.[7] These limits are determined for the vector operator, but are expected to be the same for the axial-vector operator [238].

The 1% and 5% labels indicate projected limits assuming a 1% or 5% systematic uncertainty in the SM background, respectively. Achieving 1% systematics may be overly

[6] The parameter Λ is sometimes called $M_\star$.

[7] We thank Steven Schramm for discussions on this point.

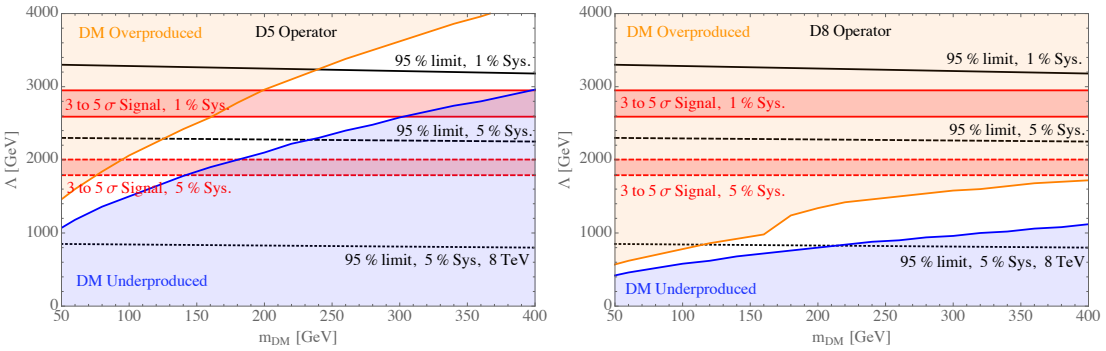

FIGURE 6.13: Blue and orange lines show the under- and over-production lines respectively, defined in the text, for the Vector (D5) (left) and Axial-Vector (D8) (right) operators. The black lines show prospective ATLAS exclusion limits for various energies and systematic uncertainties, and for luminosities of (3000, 300, 20) fb^{-1} from top to bottom. The red bands show the 3 to 5 σ discovery potential [331]. EFT approximation is valid for $\pi \lesssim \sqrt{g_{\rm DM} g_f} < 4\pi$ for ATLAS prospects, and $\sqrt{g_{\rm DM} g_f} \gg 2m_{\rm DM}/\Lambda$ for the relic density constraints. See text for more details. Direct detection constraints are not shown, but for the vector operator D5 they would rule out the entire visible space (cf. sect. 6.2.3.2).

optimistic, and can be considered a "best-case scenario". Other labels indicate the results at a given collision energy and integrated luminosity. The red bands indicate the potential significance of an observed signal, from 3σ to 5σ.

6.2.3.2 Direct Detection constraints

We use corrected versions of the equations from Ref. [245] to translate limits on the spin-dependent (SD) and spin-independent (SI) cross sections into limits on the effective operator parameter Λ. In this mass range, the strongest limits are currently from LUX [79] (SI cross section) and Xenon100 [413] (SD cross section). For our simplified models, constraints on Λ correspond to a constraint on $M/\sqrt{g_{\rm DM} g_f}$.

The vector operator $\mathcal{O}_V$ is subject to constraints on the spin-independent scattering cross section. These constraints are significantly stronger than prospective LHC bounds on this operator, ruling out the entire region displayed in Fig. 6.13 (left). However, the strength of direct detection constraints falls of quickly below $m_{\rm DM} \simeq 10$ GeV, while LHC constraints are expected to be relatively flat below $m_{\rm DM} = 50$ GeV. If the prospective LHC constraints in Fig. 6.13 (left) can be extrapolated down, they will become stronger than direct detection constraints at around $m_{\rm DM} = 10$ GeV. Conversely, the axial-vector operator $\mathcal{O}_A$ is subject to much weaker constraints on the spin-dependent scattering cross section. In this range they are barely distinguishable from the $\Lambda = 0$ line and thus are not shown.

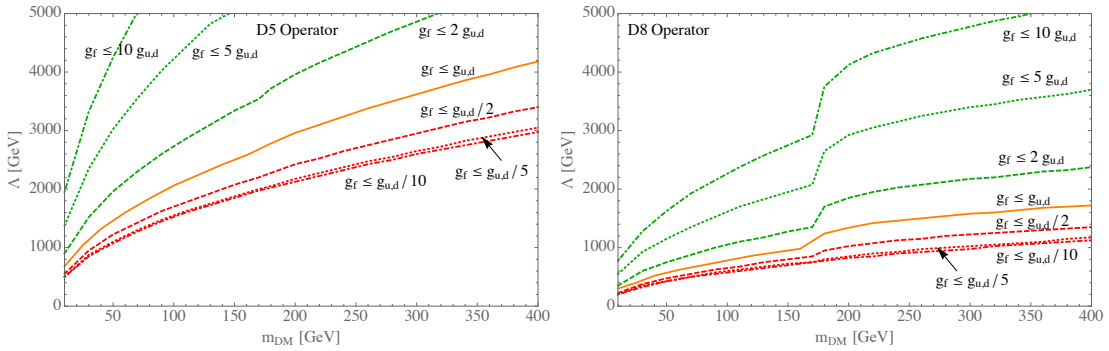

FIGURE 6.14: Analogues of the orange overproduction line in Fig. 6.14 (corresponding to $g_f \leq g_{u,d}$), changing the relative value of the coupling between u, d quarks and other SM fermions.

6.2.3.3 Relic Density Bounds

In Fig. 6.13, we show the *under*- and *over*-production lines defined in the previous Section, for the vector ($\mathcal{O}_V$, D5) and axial-vector ($\mathcal{O}_A$, D8) operator, under the assumptions 1-5 of Sect. 6.2.2.1. The range between the orange and blue lines shows the region of parameter space in which any observed χ can also be thermal relic DM. This marks a good starting point for WIMP searches. For example, we can see that pure vector DM will be difficult to observe for larger DM masses, and in any case it is ruled out by direct detection constraints. Conversely, axial-vector DM is unconstrained by direct detection, but it is already heavily constrained by 8 TeV collider bounds, and it is accessible to the 14 TeV searches even for DM masses above 500 GeV. The jump in the orange line is the point where annihilation into top quarks becomes kinematically allowed.

The overproduction lines in Fig. 6.13 rely on the assumption that the DM coupling to the first generation of quarks is not less than the coupling to other SM fermions ($g_f \leq g_{u,d}$), while the underproduction line only depends on the couplings $g_{u,d}$ to the first-generation quarks. Relaxing/strengthening the assumption 5 of Sect. 6.2.2.1 means allowing the couplings to other SM fermions to span over a wider/smaller range and correspondingly the upper limit is Eq. (6.32) is changed. The effect on the overproduction lines is shown in Fig. 6.14. We see that if the constraint on g_f is relaxed, the orange line of Fig. 6.13 gradually becomes too strong, and correspondingly the region in which to search for DM becomes broader (green curves of Fig. 6.14). In the event that a signal compatible with DM is observed, the region where it falls on the plot can be used to infer something about its nature. To be a credible DM candidate, it must either have a production mechanism aside from the usual thermal production, or its couplings to other SM particles can be inferred from where its parameters fall on this plot.

It is also interesting to note that in the EFT limit there exist simple expressions relating the DM parameters to the correct relic density. In fact, one can trade the annihilation

cross section for the relic abundance (see e.g. Eq. (6.25)). Then, using the Eqs. (6.39) and (6.40) for the annihilation cross section in the EFT limit, we can find a simple expression for a combination of the effective parameters in the low-energy theory

$$\frac{m_{\rm DM}^2}{\Lambda^4} \times \sum_i N_i^C \simeq 1 \times 10^{-8}\,{\rm GeV}^{-2} \quad (V), \tag{6.42}$$

$$\frac{m_f^2 + m_{\rm DM}^2 v^2/3}{\Lambda^4} \times \sum_i N_i^C \simeq 2.5 \times 10^{-8}\,{\rm GeV}^{-2} \quad (A), \tag{6.43}$$

where the sum is over the fermionic annihilation products and the colour factor N_i^C is 3 for coloured fermions and 1 for colourless fermions, and this equation assumes Λ is the same for all channels.

6.2.4 Results: Simplified models

We again consider the two scenarios discussed in the previous section: DM coupling to the minimum and maximum number of SM particles. Now we relax the assumptions leading to the effective operator approximation, and consider the simple UV-complete model described by the Lagrangian (6.35). This expands the relevant parameter space from just two parameters, $m_{\rm DM}$ and Λ, to the Simplified Models set of parameters $\{m_{\rm DM}, M, g_{\rm DM}^V, g_{\rm DM}^A, g_f^V, g_f^A\}$, where f runs over all SM fermions which the mediator can decay into. As already anticipated, we restrict our attention to the case of pure vector couplings, for which ATLAS projected limits exist [331]. Thus we consider $g_{\rm DM}^A = g_f^A = 0$, and we define $g_{\rm DM}^V \equiv g_{\rm DM}$, $g_f^V \equiv g_f$. The annihilation rates and mediator decay widths have been computed and are shown in Appendix C.

For the *overproduction line*, any change in parameters which decreases the cross section will lead to overproduction of DM. Similarly, for the *underproduction line*, any change in parameters which increases the cross section will lead to underproduction of DM.

In order to compare directly with prospective ATLAS constraints, in Figs. 6.15-6.16 we show lines for specific choices of $\sqrt{g_{\rm DM} g_f}$ =0.5, 1, π and $m_{\rm DM}$ =50, 400 GeV respectively. The ATLAS constraints are again from Ref. [331] and refer to a vector mediator model. These constraints have some degeneracy in M for low values of $\sqrt{g_{\rm DM} g_f}$, and so we do not show a line corresponding to $\sqrt{g_{\rm DM} g_f} = 0.5$ In order to compare with their prospective constraints, the relic density constraints assume the same (arbitrary) widths as ATLAS.

While the annihilation rate of DM particles only depends on the product $g_{\rm DM} g_f$, the mediator decay widths depend on each coupling individually. So we are forced to fix the ratio $g_f/g_{\rm DM}$, in addition to keeping the product $g_{\rm DM} g_f$ as a parameter,. For fixed values of the mediator width, a bound on the product $\sqrt{g_{\rm DM} g_f}$ can be recast into a bound on

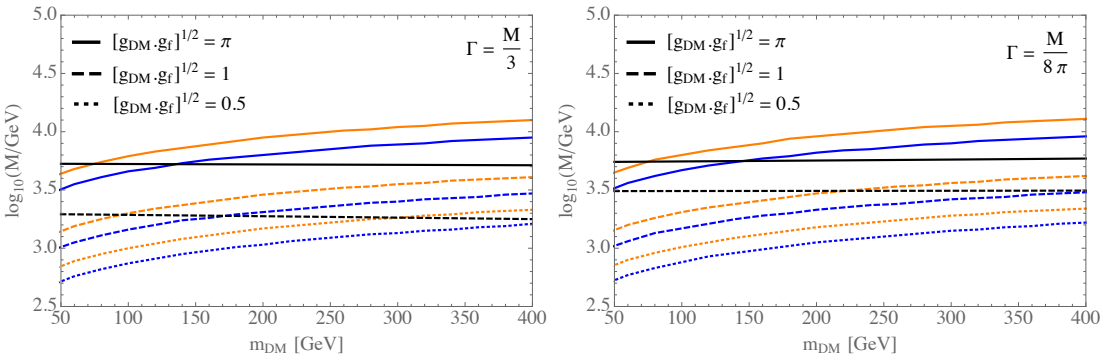

FIGURE 6.15: Over- (orange) and under- (blue) production boundary lines for thermal relic dark matter, for three different choices of the coupling strengths, and a Z'-type mediator with pure vector couplings. Black lines are ATLAS projected 95% lower bounds after 25 fb^{-1} at 14TeV, assuming 5% systematic uncertainties.

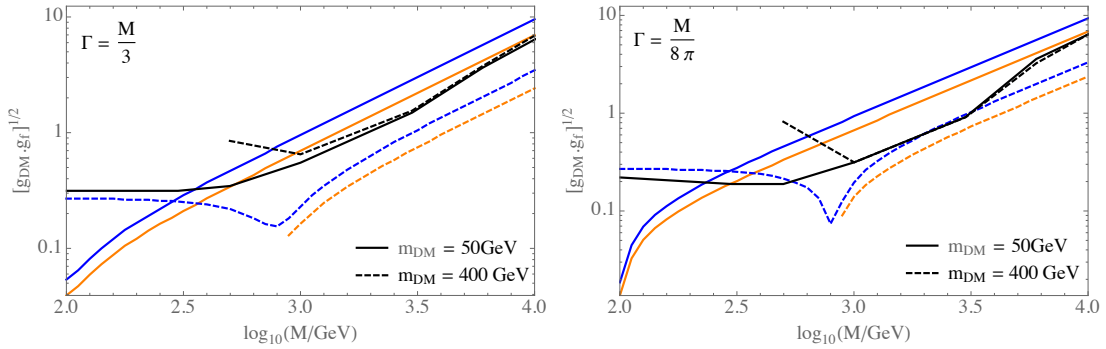

FIGURE 6.16: Over- (orange) and under- (blue) production boundary lines for thermal relic dark matter, compared with projected ATLAS reach (black), for two values of the dark matter mass, and a Z'-type mediator with pure vector couplings. Black lines are ATLAS projected 95% upper bounds after 25 fb^{-1} at 14TeV, assuming 5% systematic uncertainties.

the ratio $g_f/g_{\rm DM}$. The arbitrary widths used in Figs. 6.15-6.16 can be compared to the physical widths to fix the ratio $g_f/g_{\rm DM}$. This is shown in Fig. 6.17. In some regions there is no solution, and the width used by ATLAS is in fact not physical. For this reason we recommend to avoid the use of arbitrary mediator widths, and suggest instead that the widths are fixed to their minimal value given by the decay channels to SM particles and to DM particles.

6.2.5 Conclusions

The upcoming LHC searches for new weakly interacting stable particles may indeed provide some positive signal in the near future. Then, how confident can we be in claiming that the new particle actually accounts for the DM of the universe?

In this chapter we have stressed the importance of using relic density considerations in the searches for DM at the next LHC Run, not only regarded as a mere constraint but

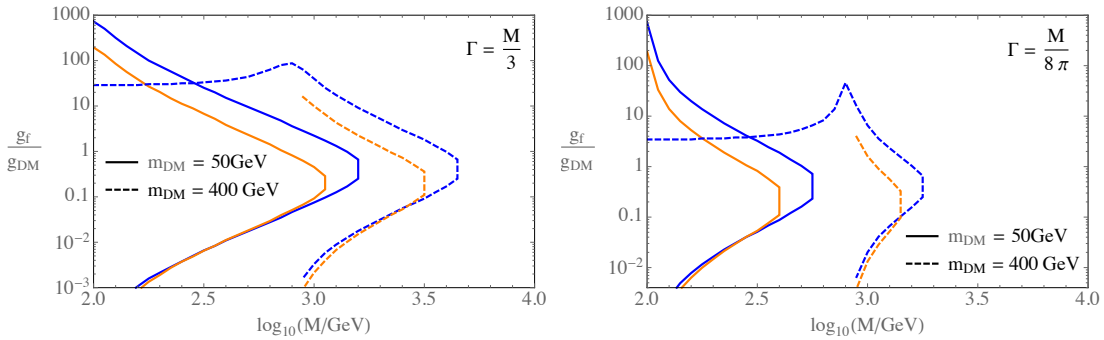

FIGURE 6.17: The solution to the ratio $g_f/g_{\rm DM}$ corresponding to the bounds on the product $g_f \cdot g_{\rm DM}$ combined with fixed mediator widths (as represented in Fig. 6.16). At large mediator masses, no solution exists and the widths are unphysical for the coupling strengths in Fig. 6.16.

also used as a powerful search tool. In fact, in order to reveal the true nature of DM, any future signal of a new weakly interacting particle possibly produced in the collider must be confronted with the requirement the new particle has a relic abundance compatible with observations before assigning it the label of thermal DM.

We have followed both the approach of effective operators (in terms of which most experimental analyses are carried out) and the approach of simplified models, for a reference case of a vector mediator. We have found that, in both situations, the forthcoming Run II of LHC has the potential to explore a large portion of the parameter space of thermal-relic DM, either in terms of claiming discovery or in terms ruling out models.

The results of this chapter are twofold. One the one hand, they can be used by LHC collaborations as a guidance into the parameter space of DM models; in fact, simple relic density considerations help to set priorities and parameter choices when analysing future data in terms of DM.

On the other hand, our results provide clear messages in case of observation of a new stable particle: if the new particle is not compatible with our thermal relic curves, either it is not the DM or one of our working assumptions is not valid. In any case, very interesting lessons about the nature of DM will be learned from LHC data.

Chapter 7

Conclusions

The focus of this work was to analyze possible issues and caveats in data analysis of experimental searches. The process going from raw data coming from the experiments to limits on new physics is a very delicate one that needs to account for a lot of effects. In Chapter 3 we have analyzed the effect of the evaporation of DM in the Sun on DM ID searches from neutrino from the Sun. This kind of search is an ID that is sensible to the DD parameter space $\sigma_p, m_{\rm DM}$. Our conclusion is that this is indeed true only above a certain DM mass $m_{\rm DM} = m_{min}(\sigma_p, \langle\sigma_{ann}v\rangle_\odot)$, of which we give accurate fitting functions.

It is know that positron excess could be due either annihilating DM or pulsars, and that the latter two generate two degenerate signals in the ID positron channel such that it is not possible to disentangle one from the other without using data from different channels. In Chapter 4 we have investigated if a possible antiproton channel signal could have the same problem, with annihilating DM signal being degenerate with astrophysical ones like SNR. Our answer is yes, so in case any antiproton signal will be detected (but this does not seem to be the case [184]), it will be necessary to make additional checks in other channels before claiming any conclusion out of it.

In Chapter 5 we have carefully analyzed one of the most relevant issues to take into account in DM collider searches. Collider searches at LHC were using EFT to predict expected signals as a function of the free parameters, and then impose bounds on the latter ones by comparing such expectations with experimental data. The resulting limits on the cut-off scales Λ were of the order of $300 \div 500\,\text{GeV}$. We have shown that such limits are not completely self-consistent, as for such low values of Λ EFT might not be an accurate description of BSM physics at LHC, being the mean energy of collisions around the same value. We have then developed a method to rescale experimental bounds to obtain new ones that reliably use EFT only with events that have a momentum transfer for which the EFT is valid, and we showed its results on actual limits. The validity

of EFT was investigated both in the case BSM particles would interact with SM ones through s-channel or t-channel mediator exchange. This problem attracted the attention of experimental collaborations as well, in fact in their latest published results they started to consider the issue of EFT validity, also using our approach.
Finally, in Chapter 6 we have made a brief introduction to Simplified Models, showing that such models not only solve any EFT validity issue, but also allow for a much wider range of searches for BSM physics, allowing a much richer phenomenology. Simplified Models has lately joined EFT (checked for its validity) as the preferred way to analyze experimental data among the scientific community [414, 415]. In my opinion the results obtained in this work are surely relevant to DM physics. Neutrinos from the Sun seem to be an interesting research field for the future. The huge solar mass (that makes it become a huge DD detector) and the improvements on understanding solar physics offer a great potential for DM search. Limits from neutrinos from the Sun are already competitive with DD ones. Because of this facts, it is interesting to analyze the effects of DM evaporation in the Sun, to understand the limits in this approach.
Recent results from charged cosmic rays do not show any significant excess with respect to SM. Moreover, any excess could also be due to astrophysical sources. ID looks like the DM search which has most uncertainties, especially resulting from our ignorance about the physics of our universe. Hopefully, this fact will be an additional reason for scientists to investigate and understand better this field of physics.
Finally, the search for DM at colliders, despite being limited by the maximum energy we can produce (13 TeV collisions at LHC have started recently), seems a very promising way to search for DM. The SM (Standard Model) of particle physics has proved to be very precise up to the TeV scale. Even though, from the theoretical point of view, SM could work up to any energy, higgs hierarchy problem suggests that there should be new physics around the TeV scale. At the end of LHC Run I, with collisions that reached an energy of 8 TeV, still no BSM physics has been found. Run II at LHC, operating at 13 TeV, has just started recently. To analyze the new collisions, experimental collaborations will use Simplified Models as well [416]. CMS and ATLAS have prepared a common strategy of using Simplified Models [417], so their results will be easily comparable. Hopefully, LHC Run II will finally let us access BSM physics!

Appendix A

Scattering and Evaporation Rates of DM in the Sun

A.1 Analytical calculation of scattering rate

In this appendix we present the calculation of the scattering rate per unit time $R^{\pm}(w \to v)$ at which a single DM particle of velocity w scatters to a final velocity between v and $v + \mathrm{d}v$, off a thermal distribution of nuclei with number density n_N, mass m_N and temperature T_N (for simplicity, throughout this appendix we drop the index i referring to a particular nucleus). We will use this result to compute the rates for capture and evaporation. This calculation was first performed by Gould in Ref. [265] and we reproduce it here, although in a different form. The differential scattering rate of a DM particle of initial speed w (in the lab frame) and final speed v on a nucleus of speed u is

$$Ct^2 s e^{-\kappa^2(2\mu\mu_+ t^2 + 2\mu_+ s^2)}\theta(w - |s-t|)\theta(s+t-w)\delta[v - (s^2+t^2-2zst)^{1/2}]\mathrm{d}z\mathrm{d}s\mathrm{d}t\,, \quad \text{(A.1)}$$

where s, t and κ are defined as

$$(1+\mu)s = |\vec{u} + \mu\vec{w}|\,, \qquad (1+\mu)t = |\vec{w} - \vec{u}|\,, \qquad \kappa = \sqrt{\frac{m_N}{2T_N}}\,, \quad \text{(A.2)}$$

$\mu, \mu_\pm$ are defined in (3.10) and C is a multiplicative factor

$$C = \frac{16\mu_+^4}{\sqrt{\pi}}\kappa^3 n_N \sigma \frac{e^{\kappa^2\mu w^2}}{w}\,. \quad \text{(A.3)}$$

The momentum conservation in the lab frame is obtained by integrating the following expression

$$\int_{-1}^{1} \delta[v - (s^2 + t^2 - 2zst)^{1/2}]\, \mathrm{d}z = \frac{v}{st}\theta(v - |s-t|)\theta(s+t-v)\,. \tag{A.4}$$

The integration domain is determined by the 4 θ-functions, that give us 4 inequalities

$$v - |s-t| \geq 0, \quad w - |s-t| \geq 0\,, \tag{A.5}$$

$$s + t - v \geq 0, \quad s + t - w \geq 0\,, \tag{A.6}$$

and we get that the new variables are subject to the constrains

$$x_1 = \frac{|v-w|}{2}\,, \qquad x_2 = \frac{v+w}{2}\,, \tag{A.7}$$

$$\begin{cases} x_1 \leq t \leq x_2\,, & \max[v,w] - t \leq s \leq \min[v,w] + t\,, \\ x_2 \leq t \leq \infty\,, & t - \min[v,w] \leq s \leq \min[v,w] + t\,. \end{cases} \tag{A.8}$$

The s integral is gaussian, thus we obtain (case $v > w$)

$$\begin{aligned} R^+(w \to v) &= Cv \int_{x_1}^{x_2} \mathrm{d}t \int_{v-t}^{w+t} \mathrm{d}s\, t e^{-\kappa^2(2\mu\mu_+ t^2 + 2\mu_+ s^2)} \\ &\quad + Cv \int_{x_2}^{\infty} \mathrm{d}t \int_{t-w}^{w+t} \mathrm{d}s\, t e^{-\kappa^2(2\mu\mu_+ t^2 + 2\mu_+ s^2)} \\ &= \frac{Cv}{\kappa\sqrt{2\mu_+}} \int_{x_1}^{x_2} \mathrm{d}t \chi(\kappa\sqrt{2\mu_+}(v-t), \kappa\sqrt{2\mu_+}(w+t)) t e^{-\kappa^2(2\mu\mu_+ t^2)} \\ &\quad + \frac{Cv}{\kappa\sqrt{2\mu_+}} \int_{x_2}^{\infty} \mathrm{d}t \chi(\kappa\sqrt{2\mu_+}(t-w), \kappa\sqrt{2\mu_+}(w+t)) t e^{-\kappa^2(2\mu\mu_+ t^2)}\,, \end{aligned} \tag{A.9}$$

where

$$\chi(a,b) \equiv \int_a^b \mathrm{d}y e^{-y^2} = \frac{\sqrt{\pi}}{2}\left[\mathrm{Erf}(b) - \mathrm{Erf}(a)\right]\,. \tag{A.10}$$

Using the fact that, for any real numbers a, b, c, d, e, A,

$$\begin{aligned} \int \mathrm{d}t \chi(bt+c, dt+e) t e^{-A^2 t^2} &= \frac{\sqrt{\pi} d}{4A^2} \frac{e^{-\frac{A^2 e^2}{A^2+d^2}} \mathrm{Erf}[\frac{de + A^2 t + d^2 t}{\sqrt{A^2+d^2}}]}{\sqrt{A^2+d^2}} - \frac{e^{-A^2 t^2}\chi(bt+c, dt+e)}{2A^2} \\ &\quad - \frac{\sqrt{\pi} b}{4A^2} \frac{e^{-\frac{A^2 c^2}{A^2+b^2}} \mathrm{Erf}[\frac{bc + A^2 t + b^2 t}{\sqrt{A^2+b^2}}]}{\sqrt{A^2+b^2}}\,, \end{aligned} \tag{A.11}$$

and defining $\alpha_\pm, \beta_\pm$ as in (3.10), we get the final result

$$R^+(w \to v) = \frac{2}{\sqrt{\pi}} n_N \sigma \frac{v}{w} \frac{\mu_+^2}{\mu} \left[\chi(\alpha_-, \alpha_+) + e^{-k^2\mu(v^2 - w^2)} \chi(\beta_-, \beta+)\right]\,. \tag{A.12}$$

The case $w > v$ can be done in the same way, and we get

$$R^-(w \to v) = \frac{2}{\sqrt{\pi}} n_N \sigma \frac{v}{w} \frac{\mu_+^2}{\mu} \left[\chi(-\alpha_-, \alpha_+) + e^{-k^2 \mu (v^2 - w^2)} \chi(-\beta_-, \beta_+) \right] . \tag{A.13}$$

The results in Eqs. (A.12)-(A.13) reproduce the expression in Eq. (3.9).

A.2 Analytical approximation of the evaporation rate

Using the identities in Ref. [265] to evaluate the integrals (3.11)-(3.12), one finds (for simplicity, throughout this appendix we drop the index i referring to a particular nucleus)

$$\begin{aligned} \Omega_{v_e}^{\pm}(w) \;=\; & \pm \frac{1}{2\sqrt{\pi}} \frac{2T_N}{m_N} \frac{1}{\mu^2} \frac{\sigma n_N}{w} \left[\mu \left(\pm \alpha_+ e^{-\alpha_-^2} - \alpha_- e^{-\alpha_+^2} \right) \right. \\ & + (\mu - 2\mu\alpha_+\alpha_- - 2\mu_+\mu_-)\, \chi(\pm\alpha_-, \alpha_+) \\ & \left. + 2\mu_+^2 e^{-\frac{m_\chi (v_e^2 - w^2)}{2T_N}} \chi(\pm\beta_-, \beta_+) \right] , \end{aligned} \tag{A.14}$$

where $\chi(a, b)$ is defined as in (A.10), and the evaporation rate per unit volume is defined as in Eq. (3.24)

$$\frac{\mathrm{d}E_\odot}{\mathrm{d}V} = \int_0^{v_e} f_0(w)\, \Omega_{v_e}^+(w) \mathrm{d}w \, . \tag{A.15}$$

This is a function of r, m_χ, σ. The analytical evaluation of this integral is possible (although lengthy) when f_0 is a thermal Maxwell-Boltzmann distribution as in (3.25), and the result is

$$\frac{\mathrm{d}E_\odot}{\mathrm{d}V} = \sigma A(r, m_\chi)\, n_N(r) n_0 e^{-m_\chi \phi(r)/T_\chi} e^{-(E_{\rm esc}(r) - E_{\rm esc}(0))/T_\chi} \frac{E_{\rm esc}(r)}{E_{\rm esc}(0)} \widetilde{R}(m_\chi) \, , \tag{A.16}$$

where $E_{\rm esc}(r) = (1/2) m_\chi v_e(r)^2$ is the escape energy at radius r, and

$$\widetilde{R}(m_\chi) \;=\; \frac{2}{\sqrt{\pi}} \sqrt{\frac{2T_\chi}{m_\chi}} \frac{E_{\rm esc}(0)}{T_\chi} e^{-E_{\rm esc}(0)/T_\chi} \, , \tag{A.17}$$

$$\begin{aligned} A(r, m_\chi) \;=\; & \frac{1}{\sqrt{\pi}} \left(\frac{T_N}{T_\chi} \right)^{3/2} \left\{ e^{-\frac{E_{\rm esc}(r)}{T_\chi} \frac{\mu T_N/T_\chi}{\mu_-^2 + \mu(T_N/T_\chi)}} \right. \\ & \times \left[\frac{T_\chi}{T_N} \frac{\mu_-}{\sqrt{\mu_-^2 + \mu T_N/T_\chi}} \left(1 + \frac{\mu_-^2}{\mu T_N/T_\chi} - \frac{\mu_-^2}{\mu} \right) \right. \\ & \left. \left. + \frac{\mu_+^3}{\mu \sqrt{\mu_-^2 + \mu T_N/T_\chi} \left(\frac{T_N}{T_\chi} - 1 \right)} \right] \chi(\gamma_-, \gamma_+) \right. \\ & \left. + \frac{T_\chi}{T_N} \left[\left(\frac{E_{\rm esc}(r)}{T_N} - \frac{1}{2\mu} + \frac{\mu_-^2}{\mu} \left(1 - \frac{T_\chi}{T_N} \right) \right) \chi(\alpha_-, \alpha_+) \right. \right. \end{aligned}$$

$$-\frac{\mu_+^2}{\mu}\frac{1}{1-\frac{T_\chi}{T_N}}\chi(\beta_-,\beta_+)$$
$$+2v_e(r)\sqrt{\frac{m_N}{2T_N}}\left(e^{-\mu^2 m_N v_e^2/(2T_N)}-\mu e^{-m_N v_e^2/(2T_N)}\right)\Big]\Big\}\,, \quad \text{(A.18)}$$

$$\gamma_\pm \equiv \sqrt{\frac{m_N}{2T_N}}v_e[\sqrt{\mu_-^2+\mu T_N/T_\chi}\pm\mu_-^2/\sqrt{\mu_-^2+\mu T_N/T_\chi}]\,. \quad \text{(A.19)}$$

For convenience, we kept separated in (A.16) the r-dependent and r-independent terms.

$$\begin{aligned} E_\odot(m_\chi,\sigma) &= \frac{\sigma\widetilde{R}(m_\chi)}{\int_{\rm Sun}e^{-m_\chi\phi(r)/T_\chi}{\rm d}^3r} \\ &\quad\times\int_{\rm Sun}{\rm d}^3r\left[A(r,m_\chi)\,n_N(r)e^{-m_\chi\phi(r)/T_\chi}e^{-(E_{\rm esc}(r)-E_{\rm esc}(0))/T_\chi}\frac{E_{\rm esc}(r)}{E_{\rm esc}(0)}\right] \\ &\equiv \frac{\sigma\widetilde{R}(m_\chi)}{\int_{\rm Sun}e^{-m_\chi\phi(r)/T_\chi}{\rm d}^3r}\times I(m_\chi)\,. \end{aligned} \quad \text{(A.20)}$$

This is the most general result for the evaporation rate, where the functions $\widetilde{R}$ and A are given by Eqs. (A.17) and (A.18), respectively. The underlying assumptions are: isotropic and velocity-independent cross section, thermal distributions of DM and nuclei.

A simple analytical approximation can be derived under the further hypothesis that $\bar{r}$ is very small (corresponding to a rather large m_χ/m_N). In this regime, Ref. [265] argues that the function A can be approximated as

$$A(r,m_\chi)\simeq\theta(T_\odot(r)-0.95T_\odot(\bar{r}))=\theta(T_\odot(r)-T_\odot(r_{95\%}))=\theta(r_{95\%}-r)\,, \quad \text{(A.21)}$$

being $T_\odot$ a monotonically decreasing function of r. The radius $r_{95\%}$ is defined as the radius where solar temperature has dropped to 95% of the DM temperatrure, i.e.

$$T_\odot(r_{95\%})=0.95\,T_\odot(\bar{r})\,, \quad \text{(A.22)}$$

and consequently, the number of nuclei within the radius $r_{95\%}$ is

$$N_N^{95\%}=\int_{\rm Sun}\theta(r_{95\%}-r)n_N(r){\rm d}^3r\,. \quad \text{(A.23)}$$

The theta function (A.21) forces the integrand in $I(m_\chi)$ to be evaluated for very small region of r close to the solar core, therefore the exponentials and the ratio of escape energies can be approximated with 1. It only remains

$$I(m_\chi)\simeq\int_{\rm Sun}\theta(r_{95\%}-r)n_N(r){\rm d}^3r=N_N^{95\%}\,. \quad \text{(A.24)}$$

This quantity, combined with the total DM-nucleus cross section σ, gives the evaporation cross section $\Sigma_{\rm evap}$, which is the sum of the scattering cross sections of all the nuclei

within a radius $r_{95\%}$

$$\Sigma_{\rm evap} = \sigma N_N^{95\%} \,. \tag{A.25}$$

Furthermore, within a small region the density can be taken as constant $\rho_\odot = \rho_\odot(\bar{r})$ and the gravitational potential reads $\phi(r) = (2\pi/3)\rho_\odot r^2 G_N$. Thus, the effective volume of DM is simply

$$\int_{\rm Sun} e^{-m_\chi \phi(r)/T_\chi} {\rm d}^3 r = \frac{3\sqrt{3}}{2\sqrt{2}} \left(\frac{T_\chi}{G_N \rho_\odot m_\chi}\right)^{3/2} , \tag{A.26}$$

while the mean DM orbit radius, the mean DM velocity and the escape energy at the solar center are

$$\bar{r} = \sqrt{\frac{6T_\odot(\bar{r})}{\pi^2 G_N \rho_\odot(\bar{r}) m_\chi}} \,, \qquad \bar{v} = \sqrt{\frac{8T_\odot(\bar{r})}{\pi m_\chi}} \,, \qquad E_{\rm esc}(0) = \frac{1}{2} m_\chi v_e(0)^2 \,. \tag{A.27}$$

Finally, the evaporation rate (A.20) can be re-written using Eqs. (A.24)-(A.27),

$$E_\odot \simeq E_\odot^{\rm approx} = \frac{8}{\pi^3} \frac{E_{\rm esc}(0)\bar{v}}{\bar{r}^3 T_\odot(\bar{r})} e^{-E_{\rm esc}(0)/T_\odot(\bar{r})} \Sigma_{\rm evap} \,, \tag{A.28}$$

which recovers Eq. (3.27).

Appendix B

Three-body Cross Sections

B.1 S Channel: Three-body Cross Sections

B.1.1 Generalities

In this Appendix we show the details of the calculations of the tree-level cross sections for the hard scattering process $f(p_1) + \bar{f}(p_2) \to \chi(p_3) + \chi(p_4) + g(k)$, where f is either a quark (operators D1-D10) or a gluon (D11-D14), and the final gluon is emitted from the initial state.

The differential cross section is generically given by

$$d\hat{\sigma} = \frac{\sum \overline{|\mathcal{M}|^2}}{4(p_1 \cdot p_2)} \mathrm{d}\Phi_3 \,, \tag{B.1}$$

where the three-body phase space is

$$\mathrm{d}\Phi_3 = (2\pi)^4 \delta^{(4)}(p_1 + p_2 - p_3 - p_4 - k) \frac{\mathrm{d}\mathbf{p}_3}{(2\pi)^3 2p_3^0} \frac{\mathrm{d}\mathbf{p}_4}{(2\pi)^3 2p_4^0} \frac{\mathrm{d}\mathbf{k}}{(2\pi)^3 2k^0} \,. \tag{B.2}$$

B.1.2 Matrix Elements

In the limit of massless light quarks, they have definite helicity and it makes no difference for the cross sections whether there is q or $\gamma^5 q$ in the operator. Therefore the following identifications between pairs of operators hold:

$$D1' \leftrightarrow D3', \qquad D2' \leftrightarrow D4', \qquad D5 \leftrightarrow D7, \qquad D6 \leftrightarrow D8, \qquad D9 \leftrightarrow D10 \,, \tag{B.3}$$

while the "primed" and "unprimed" operators are related as in Eq. (5.29). For definiteness, we choose to work with $D1', D4', D5, D8, D9$ and $D11 - D14$.

The amplitudes are given by

$$\begin{aligned}
\mathcal{M}_{D1'} &= -ig_s\frac{1}{\Lambda^2}\epsilon^{*a}_{\mu}(k)\left[\frac{\bar{v}(p_2)(\not{p}_1-\not{k})\gamma^{\mu}T^a u(p_1)}{(p_1-k)^2}-\frac{\bar{v}(p_2)\gamma^{\mu}T^a(\not{p}_2-\not{k})u(p_1)}{(p_2-k)^2}\right] \\
&\quad\times\bar{u}(p_3)v(p_4)\,, \qquad \text{(B.4)}\\
\mathcal{M}_{D4'} &= -ig_s\frac{1}{\Lambda^2}\epsilon^{*a}_{\mu}(k)\left[\frac{\bar{v}(p_2)\gamma^5(\not{p}_1-\not{k})\gamma^{\mu}T^a u(p_1)}{(p_1-k)^2}-\frac{\bar{v}(p_2)\gamma^{\mu}T^a(\not{p}_2-\not{k})\gamma^5 u(p_1)}{(p_2-k)^2}\right] \\
&\quad\times\bar{u}(p_3)\gamma^5 v(p_4)\,, \qquad \text{(B.5)}\\
\mathcal{M}_{D5} &= -ig_s\frac{g_{\nu\rho}}{\Lambda^2}\epsilon^{*a}_{\mu}(k)\left[\frac{\bar{v}(p_2)\gamma^{\nu}(\not{p}_1-\not{k})\gamma^{\mu}T^a u(p_1)}{(p_1-k)^2}-\frac{\bar{v}(p_2)\gamma^{\mu}T^a(\not{p}_2-\not{k})\gamma^{\nu}u(p_1)}{(p_2-k)^2}\right] \\
&\quad\times\bar{u}(p_3)\gamma^{\rho}v(p_4)\,, \qquad \text{(B.6)}\\
\mathcal{M}_{D8} &= -ig_s\frac{g_{\nu\rho}}{\Lambda^2}\epsilon^{*a}_{\mu}(k)\left[\frac{\bar{v}(p_2)\gamma^{\nu}\gamma^5(\not{p}_1-\not{k})\gamma^{\mu}T^a u(p_1)}{(p_1-k)^2}\right. \\
&\quad\left.-\frac{\bar{v}(p_2)\gamma^{\mu}T^a(\not{p}_2-\not{k})\gamma^{\nu}\gamma^5 u(p_1)}{(p_2-k)^2}\right]\bar{u}(p_3)\gamma^{\rho}\gamma^5 v(p_4)\,, \qquad \text{(B.7)}\\
\mathcal{M}_{D9} &= -i\frac{g_s}{16}\frac{g_{\mu\rho}g_{\nu\sigma}}{\Lambda^2}\epsilon^{*a}_{\alpha}(k)\left[\frac{\bar{v}(p_2)\sigma^{\mu\nu}(\not{p}_1-\not{k})\gamma^{\alpha}T^a u(p_1)}{(p_1-k)^2}\right. \\
&\quad\left.-\frac{\bar{v}(p_2)\gamma^{\alpha}T^a(\not{p}_2-\not{k})\sigma^{\mu\nu}u(p_1)}{(p_2-k)^2}\right]\bar{u}(p_3)\sigma^{\rho\sigma}v(p_4)\,, \qquad \text{(B.8)}\\
\mathcal{M}_{D11} &= \frac{g_s^3}{4\pi}\frac{1}{\Lambda^3}f_{abc}\epsilon_{\mu}(p_1)\epsilon_{\nu}(p_2)\epsilon^{*}_{\rho}(k)\bar{u}(p_3)v(p_4) \\
&\quad\left[\frac{((p_1-k)^{\nu}p_{2\sigma}-(p_1-k)\cdot p_2 g^{\nu}_{\sigma})}{(p_1-k)^2}\right. \\
&\qquad\times(g^{\mu\sigma}(2p_1-k)^{\rho}+g^{\rho\sigma}(2k-p_1)^{\mu}-g^{\mu\rho}(k+p_1)^{\sigma}) \\
&\quad-\frac{((p_2-k)^{\mu}p_{1\sigma}-(p_2-k)\cdot p_1 g^{\mu}_{\sigma})}{(p_2-k)^2} \\
&\qquad\times(g^{\nu\sigma}(2p_2-k)^{\rho}+g^{\rho\sigma}(2k-p_2)^{\nu}-g^{\nu\rho}(k+p_2)^{\sigma}) \\
&\quad-\frac{((p_1+p_2)^{\rho}k_{\sigma}-k\cdot(p_1+p_2)g^{\rho}_{\sigma})}{(p_1+p_2)^2} \\
&\qquad\times(g^{\mu\nu}(p_1-p_2)^{\sigma}+g^{\nu\sigma}(p_1+2p_2)^{\mu}-g^{\mu\sigma}(2p_1+p_2)^{\nu}) \\
&\quad\left.+g^{\mu\nu}(p_1-p_2)^{\rho}+g^{\nu\rho}(p_2+k)^{\mu}-g^{\mu\rho}(k+p_1)^{\nu}\right] \qquad \text{(B.9)}\\
\mathcal{M}_{D12} &= i\frac{g_s^3}{4\pi}\frac{1}{\Lambda^3}f_{abc}\epsilon_{\mu}(p_1)\epsilon_{\nu}(p_2)\epsilon^{*}_{\rho}(k)\bar{u}(p_3)\gamma^5 v(p_4) \\
&\quad\left[\frac{((p_1-k)^{\nu}p_{2\sigma}-(p_1-k)\cdot p_2 g^{\nu}_{\sigma})}{(p_1-k)^2}\right. \\
&\qquad\times(g^{\mu\sigma}(2p_1-k)^{\rho}+g^{\rho\sigma}(2k-p_1)^{\mu}-g^{\mu\rho}(k+p_1)^{\sigma}) \\
&\quad-\frac{((p_2-k)^{\mu}p_{1\sigma}-(p_2-k)\cdot p_1 g^{\mu}_{\sigma})}{(p_2-k)^2} \\
&\qquad\times(g^{\nu\sigma}(2p_2-k)^{\rho}+g^{\rho\sigma}(2k-p_2)^{\nu}-g^{\nu\rho}(k+p_2)^{\sigma}) \\
&\quad-\frac{((p_1+p_2)^{\rho}k_{\sigma}-k\cdot(p_1+p_2)g^{\rho}_{\sigma})}{(p_1+p_2)^2} \\
&\qquad\left.\times(g^{\mu\nu}(p_1-p_2)^{\sigma}+g^{\nu\sigma}(p_1+2p_2)^{\mu}-g^{\mu\sigma}(2p_1+p_2)^{\nu})\right.
\end{aligned}$$

$$+g^{\mu\nu}(p_1-p_2)^\rho + g^{\nu\rho}(p_2+k)^\mu - g^{\mu\rho}(k+p_1)^\nu] \ , \tag{B.10}$$

$$\begin{aligned}
\mathcal{M}_{D13} &= -\frac{g_s^3}{4\pi}\frac{1}{\Lambda^3} f_{abc}\epsilon_\mu(p_1)\epsilon_\nu(p_2)\epsilon^*_\rho(k)\bar{u}(p_3)v(p_4) \\
&\Bigg[\frac{(g^\mu_\sigma(2p_1-k)^\rho + g^\rho_\sigma(2k-p_1)^\mu - g^{\mu\rho}(k+p_1)_\sigma)(\epsilon^{\sigma\nu\eta\chi}p_{2\eta}(p_1-k)_\chi))}{(p_1-k)^2} \\
&+\frac{(g^\nu_\sigma(2p_2-k)^\rho + g^\rho_\sigma(2k-p_2)^\nu - g^{\nu\rho}(k+p_2)_\sigma)(\epsilon^{\sigma\mu\eta\chi}p_{1\eta}(p_2-k)_\chi)}{(p_2-k)^2} \\
&+\frac{(g^{\mu\nu}(p_1-p_2)_\sigma + g^\nu_\sigma(p_1+2p_2)^\mu - g^\mu_\sigma(2p_1+p_2)^\nu)(\epsilon^{\rho\eta\sigma\chi}k_\eta(p_1+p_2)_\chi)}{(p_1+p_2)^2} \\
&-\epsilon^{\mu\nu\rho\sigma}(p_1+p_2-k)_\sigma] \ ,
\end{aligned} \tag{B.11}$$

$$\begin{aligned}
\mathcal{M}_{D14} &= -i\frac{g_s^3}{4\pi}\frac{1}{\Lambda^3} f_{abc}\epsilon_\mu(p_1)\epsilon_\nu(p_2)\epsilon^*_\rho(k)\bar{u}(p_3)\gamma^5 v(p_4) \\
&\Bigg[\frac{(g^\mu_\sigma(2p_1-k)^\rho + g^\rho_\sigma(2k-p_1)^\mu - g^{\mu\rho}(k+p_1)_\sigma)(\epsilon^{\sigma\nu\eta\chi}p_{2\eta}(p_1-k)_\chi))}{(p_1-k)^2} \\
&+\frac{(g^\nu_\sigma(2p_2-k)^\rho + g^\rho_\sigma(2k-p_2)^\nu - g^{\nu\rho}(k+p_2)_\sigma)(\epsilon^{\sigma\mu\eta\chi}p_{1\eta}(p_2-k)_\chi)}{(p_2-k)^2} \\
&+\frac{(g^{\mu\nu}(p_1-p_2)_\sigma + g^\nu_\sigma(p_1+2p_2)^\mu - g^\mu_\sigma(2p_1+p_2)^\nu)(\epsilon^{\rho\eta\sigma\chi}k_\eta(p_1+p_2)_\chi)}{(p_1+p_2)^2} \\
&-\epsilon^{\mu\nu\rho\sigma}(p_1+p_2-k)_\sigma] \ .
\end{aligned} \tag{B.12}$$

where p_1, p_2 are the initial momenta, k the momenta of the gluon, and p_3, p_4 the momenta of the DM particle/antiparticle, g_s is the SU(3) gauge coupling and T^a are the SU(3) generators in the fundamental representation.

The corresponding squared amplitudes, averaged over initial states (color and spin) and summed over the final states are

$$\begin{aligned}
\sum\overline{|\mathcal{M}_{D1'}|^2} &= \frac{16}{9}\frac{g_s^2}{\Lambda^4}\frac{\left[(k\cdot(p_1+p_2))^2 - 2(p_1\cdot p_2)(k\cdot p_1 + k\cdot p_2 - p_1\cdot p_2)\right]}{(k\cdot p_1)(k\cdot p_2)} \\
&\quad\times[(p_3\cdot p_4) - m^2_{\rm DM}]
\end{aligned} \tag{B.13}$$

$$\begin{aligned}
\sum\overline{|\mathcal{M}_{D4'}|^2} &= \frac{16}{9}\frac{g_s^2}{\Lambda^4}\frac{\left[(k\cdot(p_1+p_2))^2 - 2(p_1\cdot p_2)(k\cdot p_1 + k\cdot p_2 - p_1\cdot p_2)\right]}{(k\cdot p_1)(k\cdot p_2)} \\
&\quad\times[(p_3\cdot p_4) + m^2_{\rm DM}]
\end{aligned} \tag{B.14}$$

$$\begin{aligned}
\sum\overline{|\mathcal{M}_{D5}|^2} &= -\frac{32}{9}\frac{g_s^2}{\Lambda^4}\Bigg[\frac{(k\cdot p_1)\left[(k\cdot p_1)+(k\cdot p_2)-3(p_1\cdot p_2)-m^2_{\rm DM}\right]}{(k\cdot p_2)} \\
&+\frac{(k\cdot p_2)\left[(k\cdot p_1)+(k\cdot p_2)-3(p_1\cdot p_2)-m^2_{\rm DM}\right]}{(k\cdot p_1)} - 4(p_1\cdot p_2) \\
&-2\frac{(p_1\cdot p_2)}{(k\cdot p_1)(k\cdot p_2)}\left[(k\cdot p_3)\left((p_1\cdot p_3)+(p_2\cdot p_3)\right)\right. \\
&\quad\left.+(p_1\cdot p_2)\left(m^2_{\rm DM}+(p_1\cdot p_2)\right) - 2(p_1\cdot p_3)(p_2\cdot p_3)\right] \\
&+2\frac{(k\cdot p_3)(p_1\cdot p_3) - (p_2\cdot p_3)(p_1\cdot p_3) + (p_2\cdot p_3)^2}{(k\cdot p_2)}
\end{aligned}$$

$$
\begin{aligned}
&+2\frac{(k\cdot p_3)(p_2\cdot p_3)-(p_1\cdot p_3)(p_2\cdot p_3)+(p_1\cdot p_3)^2}{(k\cdot p_1)}\\
&+\Big(2(p_1\cdot p_2)^2+m_{\rm DM}^2(p_1\cdot p_2)\Big)\Big(\frac{1}{k\cdot p_1}+\frac{1}{k\cdot p_2}\Big)\Big] \qquad \text{(B.15)}\\
\sum\overline{|\mathcal{M}_{D8}|^2} &= \frac{32}{9}\frac{g_s^2}{\Lambda^4}\Bigg[\frac{(k\cdot p_1)\left[(k\cdot p_1)+(k\cdot p_2)-3(p_1\cdot p_2)+m_{\rm DM}^2+2(p_3\cdot p_4)\right]}{(k\cdot p_2)}\\
&+\frac{(k\cdot p_2)\left[(k\cdot p_1)+(k\cdot p_2)-3(p_1\cdot p_2)+m_{\rm DM}^2+2(p_3\cdot p_4)\right]}{(k\cdot p_1)}-4(p_1\cdot p_2)\\
&+2\frac{(p_1\cdot p_2)}{(k\cdot p_1)(k\cdot p_2)}\left[(p_1\cdot p_2)\left(2(p_3\cdot p_4)+m_{\rm DM}^2\right)\right.\\
&\quad\left.+(k\cdot p_3)\left((p_1\cdot p_3)+(p_2\cdot p_3)\right)+2(p_1\cdot p_3)(p_2\cdot p_3)-(p_1\cdot p_2)^2\right]\\
&+2\frac{(p_1\cdot p_3)\left[-(k\cdot p_3)+(p_2\cdot p_3)\right]-(p_2\cdot p_3)^2}{(k\cdot p_2)}\\
&+2\frac{(p_2\cdot p_3)\left[-(k\cdot p_3)+(p_1\cdot p_3)\right]-(p_1\cdot p_3)^2}{(k\cdot p_1)}\\
&+(p_1\cdot p_2)\Big(2(p_1\cdot p_2)-m_{\rm DM}^2-2(p_3\cdot p_4)\Big)\Big(\frac{1}{k\cdot p_1}+\frac{1}{k\cdot p_2}\Big)\Bigg] \qquad \text{(B.16)}\\
\sum\overline{|\mathcal{M}_{D9}|^2} &= \frac{128}{9}\frac{g_s^2}{\Lambda^4}\left[-2[m_{\rm DM}^2-(k\cdot p_3)]\right.\\
&+\frac{(k\cdot p_1)\left[-(k\cdot p_3)+(p_1\cdot p_3)-(p_2\cdot p_3)+m_{\rm DM}^2\right]}{(k\cdot p_2)}\\
&-2\frac{(p_1\cdot p_2)\left[-2(k\cdot p_3)+(p_1\cdot p_3)+(p_2\cdot p_3)+m_{\rm DM}^2\right]}{(k\cdot p_2)}\\
&-4\frac{\left[(k\cdot p_3)-(p_2\cdot p_3)\right]\left[(p_1\cdot p_3)-(p_2\cdot p_3)\right]}{(k\cdot p_2)}\\
&+\frac{(k\cdot p_2)\left[-(k\cdot p_3)+(p_2\cdot p_3)-(p_1\cdot p_3)+m_{\rm DM}^2\right]}{(k\cdot p_1)}\\
&-2\frac{(p_1\cdot p_2)\left[-2(k\cdot p_3)+(p_1\cdot p_3)+(p_2\cdot p_3)+m_{\rm DM}^2\right]}{(k\cdot p_1)}\\
&-4\frac{\left[(k\cdot p_3)-(p_1\cdot p_3)\right]\left[(p_2\cdot p_3)-(p_1\cdot p_3)\right]}{(k\cdot p_1)}\\
&-2\frac{(p_1\cdot p_2)\left[(k\cdot p_3)-(p_1\cdot p_3)-(p_2\cdot p_3)\right]\left[2(k\cdot p_3)+(p_1\cdot p_2)\right]}{(k\cdot p_1)(k\cdot p_2)}\\
&+2\frac{(p_1\cdot p_2)\left[-4(p_1\cdot p_3)(p_2\cdot p_3)+m_{\rm DM}^2(p_1\cdot p_2)\right]}{(k\cdot p_1)(k\cdot p_2)}\Bigg] \qquad \text{(B.17)}\\
\sum\overline{|\mathcal{M}_{D11}|^2} &= \frac{3}{32\pi^2}\frac{g_s^6}{\Lambda^6}\left[(p_3\cdot p_4)-m_{\rm DM}^2\right]\left\{\frac{(k\cdot p_1)^3}{(k\cdot p_2)(p_1\cdot p_2)}+\frac{(k\cdot p_2)^3}{(k\cdot p_1)(p_1\cdot p_2)}\right.\\
&+\frac{(p_1\cdot p_2)^3}{(k\cdot p_1)(k\cdot p_2)}+3\frac{(k\cdot p_1)(k\cdot p_2)}{(p_1\cdot p_2)}\\
&+\frac{(k\cdot p_1)(p_1\cdot p_2)-(k\cdot p_1)^2}{(k\cdot p_2)}+\frac{(k\cdot p_2)(p_1\cdot p_2)-(k\cdot p_2)^2}{(k\cdot p_1)}\\
&-\frac{(k_-\cdot p_1)(k\cdot p_2)^3}{(k\cdot k_-)(k\cdot p_1)(p_1\cdot p_2)}-\frac{(k_-\cdot p_2)(k\cdot p_1)^3}{(k\cdot k_-)(k\cdot p_2)(p_1\cdot p_2)}
\end{aligned}
$$

$$
\begin{aligned}
&+\frac{(k_-\cdot p_1)}{(k\cdot k_-)(p_1\cdot p_2)}[(k\cdot p_1)^2+(k\cdot p_1)(k\cdot p_2)-(k\cdot p_2)^2]\\
&+\frac{(k_-\cdot p_2)}{(k\cdot k_-)(p_1\cdot p_2)}[(k\cdot p_2)^2+(k\cdot p_1)(k\cdot p_2)-(k\cdot p_1)^2]\\
&+2\frac{(k_-\cdot p_1)}{(k\cdot k_-)(k\cdot p_1)}[(k\cdot p_2)^2-(p_1\cdot p_2)(k\cdot p_2)]\\
&+2\frac{(k_-\cdot p_2)}{(k\cdot k_-)(k\cdot p_2)}[(k\cdot p_1)^2-(p_1\cdot p_2)(k\cdot p_1)]\\
&+2\frac{(k_-\cdot p_1)}{(k\cdot k_-)}[(p_1\cdot p_2)+(k\cdot p_1)-2(k\cdot p_2)]\\
&+2\frac{(k_-\cdot p_2)}{(k\cdot k_-)}[(p_1\cdot p_2)+(k\cdot p_2)-2(k\cdot p_1)]\\
&+(k\cdot p_1)+(k\cdot p_2)+6(p_1\cdot p_2)\}
\end{aligned}
\tag{B.18}
$$

$$
\begin{aligned}
\sum\overline{|\mathcal{M}_{D12}|^2} &= \frac{3}{32\pi^2}\frac{g_s^6}{\Lambda^6}\left[(p_3\cdot p_4)+m_{\rm DM}^2\right]\left\{\frac{(k\cdot p_1)^3}{(k\cdot p_2)(p_1\cdot p_2)}+\frac{(k\cdot p_2)^3}{(k\cdot p_1)(p_1\cdot p_2)}\right.\\
&+\frac{(p_1\cdot p_2)^3}{(k\cdot p_1)(k\cdot p_2)}+3\frac{(k\cdot p_1)(k\cdot p_2)}{(p_1\cdot p_2)}\\
&+\frac{(k\cdot p_1)(p_1\cdot p_2)-(k\cdot p_1)^2}{(k\cdot p_2)}+\frac{(k\cdot p_2)(p_1\cdot p_2)-(k\cdot p_2)^2}{(k\cdot p_1)}\\
&-\frac{(k_-\cdot p_1)(k\cdot p_2)^3}{(k\cdot k_-)(k\cdot p_1)(p_1\cdot p_2)}-\frac{(k_-\cdot p_2)(k\cdot p_1)^3}{(k\cdot k_-)(k\cdot p_2)(p_1\cdot p_2)}\\
&+\frac{(k_-\cdot p_1)}{(k\cdot k_-)(p_1\cdot p_2)}[(k\cdot p_1)^2+(k\cdot p_1)(k\cdot p_2)-(k\cdot p_2)^2]\\
&+\frac{(k_-\cdot p_2)}{(k\cdot k_-)(p_1\cdot p_2)}[(k\cdot p_2)^2+(k\cdot p_1)(k\cdot p_2)-(k\cdot p_1)^2]\\
&+2\frac{(k_-\cdot p_1)}{(k\cdot k_-)(k\cdot p_1)}[(k\cdot p_2)^2-(p_1\cdot p_2)(k\cdot p_2)]\\
&+2\frac{(k_-\cdot p_2)}{(k\cdot k_-)(k\cdot p_2)}[(k\cdot p_1)^2-(p_1\cdot p_2)(k\cdot p_1)]\\
&+2\frac{(k_-\cdot p_1)}{(k\cdot k_-)}[(p_1\cdot p_2)+(k\cdot p_1)-2(k\cdot p_2)]\\
&+2\frac{(k_-\cdot p_2)}{(k\cdot k_-)}[(p_1\cdot p_2)+(k\cdot p_2)-2(k\cdot p_1)]\\
&\left.+(k\cdot p_1)+(k\cdot p_2)+6(p_1\cdot p_2)\right\}
\end{aligned}
\tag{B.19}
$$

$$
\begin{aligned}
\sum\overline{|\mathcal{M}_{D13}|^2} &= \frac{3}{32\pi^2}\frac{g_s^6}{\Lambda^6}\left[(p_3\cdot p_4)-m_{\rm DM}^2\right]\left\{\frac{(k\cdot p_1)^3}{(k\cdot p_2)(p_1\cdot p_2)}+\frac{(k\cdot p_2)^3}{(k\cdot p_1)(p_1\cdot p_2)}\right.\\
&+\frac{(p_1\cdot p_2)^3}{(k\cdot p_1)(k\cdot p_2)}+3\frac{(k\cdot p_1)(k\cdot p_2)}{(p_1\cdot p_2)}\\
&+\frac{(k\cdot p_1)(p_1\cdot p_2)-(k\cdot p_1)^2}{(k\cdot p_2)}+\frac{(k\cdot p_2)(p_1\cdot p_2)-(k\cdot p_2)^2}{(k\cdot p_1)}\\
&-\frac{(k_-\cdot p_1)(k\cdot p_2)^3}{(k\cdot k_-)(k\cdot p_1)(p_1\cdot p_2)}-\frac{(k_-\cdot p_2)(k\cdot p_1)^3}{(k\cdot k_-)(k\cdot p_2)(p_1\cdot p_2)}\\
&\left.+\frac{(k_-\cdot p_1)}{(k\cdot k_-)(p_1\cdot p_2)}[(k\cdot p_1)^2-3(k\cdot p_1)(k\cdot p_2)+3(k\cdot p_2)^2]\right.
\end{aligned}
$$

$$
\begin{aligned}
&+\frac{(k_-\cdot p_2)}{(k\cdot k_-)(p_1\cdot p_2)}[(k\cdot p_2)^2-3(k\cdot p_1)(k\cdot p_2)+3(k\cdot p_1)^2]\\
&+2\frac{(k_-\cdot p_1)}{(k\cdot k_-)(k\cdot p_1)}[(k\cdot p_2)^2-(p_1\cdot p_2)(k\cdot p_2)]\\
&+2\frac{(k_-\cdot p_2)}{(k\cdot k_-)(k\cdot p_2)}[(k\cdot p_1)^2-(p_1\cdot p_2)(k\cdot p_1)]\\
&+2\frac{(k_-\cdot p_1)}{(k\cdot k_-)}[(p_1\cdot p_2)+(k\cdot p_1)-2(k\cdot p_2)]\\
&+2\frac{(k_-\cdot p_2)}{(k\cdot k_-)}[(p_1\cdot p_2)+(k\cdot p_2)-2(k\cdot p_1)]\\
&-3(k\cdot p_1)-3(k\cdot p_2)+2(p_1\cdot p_2)\}
\end{aligned}
\tag{B.20}
$$

$$
\begin{aligned}
\sum\overline{|\mathcal{M}_{D14}|^2} \;=\; &\frac{3}{32\pi^2}\frac{g_s^6}{\Lambda^6}\left[(p_3\cdot p_4)+m_{\rm DM}^2\right]\left\{\frac{(k\cdot p_1)^3}{(k\cdot p_2)(p_1\cdot p_2)}+\frac{(k\cdot p_2)^3}{(k\cdot p_1)(p_1\cdot p_2)}\right.\\
&+\frac{(p_1\cdot p_2)^3}{(k\cdot p_1)(k\cdot p_2)}+3\frac{(k\cdot p_1)(k\cdot p_2)}{(p_1\cdot p_2)}\\
&+\frac{(k\cdot p_1)(p_1\cdot p_2)-(k\cdot p_1)^2}{(k\cdot p_2)}+\frac{(k\cdot p_2)(p_1\cdot p_2)-(k\cdot p_2)^2}{(k\cdot p_1)}\\
&-\frac{(k_-\cdot p_1)(k\cdot p_2)^3}{(k\cdot k_-)(k\cdot p_1)(p_1\cdot p_2)}-\frac{(k_-\cdot p_2)(k\cdot p_1)^3}{(k\cdot k_-)(k\cdot p_2)(p_1\cdot p_2)}\\
&+\frac{(k_-\cdot p_1)}{(k\cdot k_-)(p_1\cdot p_2)}[(k\cdot p_1)^2-3(k\cdot p_1)(k\cdot p_2)+3(k\cdot p_2)^2]\\
&+\frac{(k_-\cdot p_2)}{(k\cdot k_-)(p_1\cdot p_2)}[(k\cdot p_2)^2-3(k\cdot p_1)(k\cdot p_2)+3(k\cdot p_1)^2]\\
&+2\frac{(k_-\cdot p_1)}{(k\cdot k_-)(k\cdot p_1)}[(k\cdot p_2)^2-(p_1\cdot p_2)(k\cdot p_2)]\\
&+2\frac{(k_-\cdot p_2)}{(k\cdot k_-)(k\cdot p_2)}[(k\cdot p_1)^2-(p_1\cdot p_2)(k\cdot p_1)]\\
&+2\frac{(k_-\cdot p_1)}{(k\cdot k_-)}[(p_1\cdot p_2)+(k\cdot p_1)-2(k\cdot p_2)]\\
&+2\frac{(k_-\cdot p_2)}{(k\cdot k_-)}[(p_1\cdot p_2)+(k\cdot p_2)-2(k\cdot p_1)]\\
&\left.-3(k\cdot p_1)-3(k\cdot p_2)+2(p_1\cdot p_2)\right\}\,.
\end{aligned}
\tag{B.21}
$$

where the polarization 4-vector is defined as $k_-\equiv P(k^\nu)/\sqrt{k^\mu\cdot P(k_\mu)}$, where P is the parity operation.

B.1.3 Cross sections

Now, the next step is to compute the cross sections in the lab frame. To this end we proceed by first evaluating the matrix elements and the phase space density in the center-of-mass frame and then boosting the result to the lab frame. In the center-of-mass

(c.o.m) frame, let us parametrize the four-momenta inolved in the process as

$$\begin{aligned} p_1 &= x\frac{\sqrt{s}}{2}(1,0,0,1)\,, \qquad p_2 = x\frac{\sqrt{s}}{2}(1,0,0,-1)\,, \qquad k = x\frac{\sqrt{s}}{2}(z_0, z_0\hat{k})\,, \\ p_3 &= x\frac{\sqrt{s}}{2}(1-y_0, \sqrt{(1-y_0)^2 - a^2}\hat{p}_3)\,, \\ p_4 &= x\frac{\sqrt{s}}{2}(1+y_0-z_0, \sqrt{(1+y_0-z_0)^2 - a^2}\hat{p}_4)\,, \end{aligned} \tag{B.22}$$

where the two colliding partons carry equal momentum fractions $x_1 = x_2 \equiv x$ of the incoming protons, $a \equiv 2m_{\rm DM}/(x\sqrt{s}) < 1$, $\hat{k} = (0, \sin\theta_0, \cos\theta_0)$, and θ_0 is the polar angle of $\hat{k}$ with respect to the beam line, in the c.o.m. frame.

$$\mathrm{d}\Phi_3 = \frac{1}{(4\pi)^3}\mathrm{d}E_3\,\mathrm{d}k\,\mathrm{d}\cos\theta_0 = \frac{1}{(4\pi)^3}\frac{x^2 s}{4}\mathrm{d}z_0\,\mathrm{d}y_0\,\mathrm{d}\cos\theta_0\,. \tag{B.23}$$

The kinematical domains of the variables y_0, z_0 are

$$\frac{z_0}{2}\left(1 - \sqrt{\frac{1-z_0-a^2}{1-z_0}}\right) \leq \quad y_0 \quad \leq \frac{z_0}{2}\left(1 + \sqrt{\frac{1-z_0-a^2}{1-z_0}}\right)\,, \tag{B.24}$$

$$0 \leq \quad z_0 \quad \leq 1 - a^2\,. \tag{B.25}$$

With the subscript $_0$ we will refer to quantities evaluated in the c.o.m. frame. The polarization 4-vector k_- in the c.o.m. frame simply reads $k_- = (1/\sqrt{2})(1, 0, -\sin\theta_0, -\cos\theta_0)$.

The conservation of three-momentum sets the angle $\theta_{0\,3j}$ between $\hat{p}_3$ and $\hat{k}$ as: $\cos\theta_{0\,3j} = (\mathbf{p}_4^2 - \mathbf{k}^2 - \mathbf{p}_3^2)/2|\mathbf{k}||\mathbf{p}_3|$. For the doubly-differential cross sections with respect to the energy and angle of the emitted gluon, in the c.o.m. frame, we obtain

$$\left.\frac{\mathrm{d}^2\hat{\sigma}}{\mathrm{d}z_0\mathrm{d}\cos\theta_0}\right|_{D1'} = \frac{\alpha_s}{36\pi^2}\frac{x^2 s}{\Lambda^4}\frac{\left[1 - z_0 - \frac{4m_{\rm DM}^2}{x^2 s}\right]^{3/2}}{\sqrt{1-z_0}}\frac{[1+(1-z_0)^2]}{z_0\sin^2\theta_0}\,, \tag{B.26}$$

$$\left.\frac{\mathrm{d}^2\hat{\sigma}}{\mathrm{d}z_0\mathrm{d}\cos\theta_0}\right|_{D4'} = \frac{\alpha_s}{36\pi^2}\frac{x^2 s}{\Lambda^4}\frac{\left[1 - z_0 - \frac{4m_{\rm DM}^2}{x^2 s}\right]^{1/2}}{\sqrt{1-z_0}}\frac{[1+(1-z_0)^2]}{z_0\sin^2\theta_0}\,, \tag{B.27}$$

$$\begin{aligned} \left.\frac{\mathrm{d}^2\hat{\sigma}}{\mathrm{d}z_0\mathrm{d}\cos\theta_0}\right|_{D5} &= \frac{\alpha_s}{108\pi^2}\frac{x^2 s}{\Lambda^4}\frac{\sqrt{1 - z_0 - \frac{4m_{\rm DM}^2}{x^2 s}}}{\sqrt{1-z_0}} \\ &\quad \times \frac{(1 - z_0 + \frac{2m_{\rm DM}^2}{x^2 s})(8 - 8z_0 + (3+\cos 2\theta_0)z_0^2)}{z_0\sin^2\theta_0}\,, \end{aligned} \tag{B.28}$$

$$\left.\frac{\mathrm{d}^2\hat{\sigma}}{\mathrm{d}z_0\mathrm{d}\cos\theta_0}\right|_{D8} = \frac{\alpha_s}{108\pi^2}\frac{x^2 s}{\Lambda^4}\frac{[1 - z_0 - \frac{4m_{\rm DM}^2}{x^2 s}]^{3/2}}{\sqrt{1-z_0}}\frac{8 - 8z_0 + (3+\cos 2\theta_0)z_0^2}{z_0\sin^2\theta_0}\,, \tag{B.29}$$

$$\left.\frac{\mathrm{d}^2\hat{\sigma}}{\mathrm{d}z_0\mathrm{d}\cos\theta_0}\right|_{D9} = \frac{\alpha_s}{27\pi^2}\frac{x^2 s}{\Lambda^4}\frac{\sqrt{1 - z_0 - \frac{4m_{\rm DM}^2}{x^2 s}}}{[1-z_0]^{3/2}} \tag{B.30}$$

$$\times \frac{(1-z_0+\frac{2m_{\rm DM}^2}{x^2 s})(4-8z_0+6z_0^2-(1+\cos 2\theta_0)z_0^3)}{z_0 \sin^2\theta_0}\,,$$

$$\left.\frac{\mathrm{d}^2\hat{\sigma}}{\mathrm{d}z_0 \mathrm{d}\cos\theta_0}\right|_{D11} = \frac{3\alpha_s^3 x^4 s^2}{32768\pi^2\Lambda^6}\frac{\left[1-z_0-\frac{4m_{\rm DM}^2}{x^2 s}\right]^{3/2}}{z_0\sqrt{1-z_0}\sin^2\theta_0}[128-128(1+\cos 2\theta_0)z_0$$
$$+(304+64\cos 2\theta_0+16\cos 4\theta_0)z_0^2-128(1+\cos 2\theta_0)z_0^3$$
$$+(79+44\cos 2\theta_0+5\cos 4\theta_0)z_0^4]\,, \tag{B.31}$$

$$\left.\frac{\mathrm{d}^2\hat{\sigma}}{\mathrm{d}z_0 \mathrm{d}\cos\theta_0}\right|_{D12} = \frac{3\alpha_s^3 x^4 s^2}{32768\pi^2\Lambda^6}\frac{\sqrt{1-z_0-\frac{4m_{\rm DM}^2}{x^2 s}}\sqrt{1-z_0}}{z_0\sin^2\theta_0}[128-128(1+\cos 2\theta_0)z_0$$
$$+(304+64\cos 2\theta_0+16\cos 4\theta_0)z_0^2-128(1+\cos 2\theta_0)z_0^3$$
$$+(79+44\cos 2\theta_0+5\cos 4\theta_0)z_0^4]\,, \tag{B.32}$$

$$\left.\frac{\mathrm{d}^2\hat{\sigma}}{\mathrm{d}z_0 \mathrm{d}\cos\theta_0}\right|_{D13} = \frac{3\alpha_s^3 x^4 s^2}{32768\pi^2\Lambda^6}\frac{\left[1-z_0-\frac{4m_{\rm DM}^2}{x^2 s}\right]^{3/2}}{z_0\sqrt{1-z_0}\sin^2\theta_0}[128-128(1+\cos 2\theta_0)z_0$$
$$+(240+128\cos 2\theta_0+16\cos 4\theta_0)z_0^2-16(11+4\cos 2\theta_0+\cos 4\theta_0)z_0^3$$
$$+(79+44\cos 2\theta_0+5\cos 4\theta_0)z_0^4]\,, \tag{B.33}$$

$$\left.\frac{\mathrm{d}^2\hat{\sigma}}{\mathrm{d}z_0 \mathrm{d}\cos\theta_0}\right|_{D14} = \frac{3\alpha_s^3 x^4 s^2}{32768\pi^2\Lambda^6}\frac{\sqrt{1-z_0-\frac{4m_{\rm DM}^2}{x^2 s}}\sqrt{1-z_0}}{z_0\sin^2\theta_0}[128-128(1+\cos 2\theta_0)z_0$$
$$+(240+128\cos 2\theta_0+16\cos 4\theta_0)z_0^2-16(11+4\cos 2\theta_0+\cos 4\theta_0)z_0^3$$
$$+(79+44\cos 2\theta_0+5\cos 4\theta_0)z_0^4]\,. \tag{B.34}$$

Eq. (B.26)-(B.29) agree with the findings in Refs. [314, 315], up to the factor of 1/9, as we are considering colored colliding particles.

To get the cross sections in the lab frame we perform a boost along the $\hat{z}$-axis, accounting for generic parton momentum fractions x_1, x_2, as in Eq. (5.10). The relations between the quantities z_0, θ_0 in the c.o.m. frame the the analog ones z, θ in the lab frame are

$$z_0 = z\frac{(x_1+x_2)^2+\cos\theta(x_2^2-x_1^2)}{4x_1x_2} \tag{B.35}$$

$$\sin^2\theta_0 = \frac{4x_1x_2}{[(x_1+x_2)+\cos\theta(x_2-x_1)]^2}\sin^2\theta \tag{B.36}$$

so that the cross section in the lab frame is simply

$$\frac{\mathrm{d}^2\hat{\sigma}}{\mathrm{d}z\mathrm{d}\cos\theta} = \frac{x_1+x_2}{x_1+x_2+\cos\theta(x_2-x_1)}\left.\frac{\mathrm{d}^2\hat{\sigma}}{\mathrm{d}z_0\mathrm{d}\cos\theta_0}\right|_{\substack{z_0\to z_0(z)\\ \theta_0\to\theta_0(\theta)}}\,. \tag{B.37}$$

Expressing the energy of the photon in terms of the transverse momentum and rapidity, $k^0 = p_{\rm T}\cosh\eta$, one finds

$$z = \frac{4p_{\rm T}\cosh\eta}{(x_1+x_2)\sqrt{s}}\,, \qquad \cos\theta = \tanh\eta\,, \tag{B.38}$$

which allows to express the differential cross sections with respect to the transverse momentum and pseudo-rapidity of the emitted photon,

$$\frac{\mathrm{d}^2\hat{\sigma}}{\mathrm{d}p_\mathrm{T}\mathrm{d}\eta} = \frac{4}{(x_1+x_2)\sqrt{s}\cosh\eta}\frac{\mathrm{d}^2\hat{\sigma}}{\mathrm{d}z\mathrm{d}\cos\theta}\,. \tag{B.39}$$

This way we get the translation of Eqs. (B.26)-(B.30) into the lab frame

$$\left.\frac{\mathrm{d}^2\hat{\sigma}}{\mathrm{d}p_\mathrm{T}\mathrm{d}\eta}\right|_{D1'} = \frac{\alpha_s}{36\pi^2}\frac{x_1x_2s}{\Lambda^4}\frac{1}{p_\mathrm{T}}\frac{\left[1-f-\frac{4m_\mathrm{DM}^2}{x_1x_2s}\right]^{3/2}\left[1+(1-f)^2\right]}{\sqrt{1-f}} \tag{B.40}$$

$$\left.\frac{\mathrm{d}^2\hat{\sigma}}{\mathrm{d}p_\mathrm{T}\mathrm{d}\eta}\right|_{D4'} = \frac{\alpha_s}{36\pi^2}\frac{x_1x_2s}{\Lambda^4}\frac{\sqrt{1-f}}{p_\mathrm{T}}\left[1-f-\frac{4m_\mathrm{DM}^2}{x_1x_2s}\right]^{1/2}\left[1+(1-f)^2\right] \tag{B.41}$$

$$\left.\frac{\mathrm{d}^2\hat{\sigma}}{\mathrm{d}p_\mathrm{T}\mathrm{d}\eta}\right|_{D5} = \frac{\alpha_s}{27\pi^2}\frac{x_1x_2s}{\Lambda^4}\frac{\sqrt{1-f-\frac{4m_\mathrm{DM}^2}{x_1x_2s}}\left[1-f+\frac{2m_\mathrm{DM}^2}{x_1x_2s}\right]}{\sqrt{1-f}}\frac{}{p_\mathrm{T}} \times\left[1+(1-f)^2-2\frac{p_\mathrm{T}^2}{x_1x_2s}\right] \tag{B.42}$$

$$\left.\frac{\mathrm{d}^2\hat{\sigma}}{\mathrm{d}p_\mathrm{T}\mathrm{d}\eta}\right|_{D8} = \frac{\alpha_s}{27\pi^2}\frac{x_1x_2s}{\Lambda^4}\frac{[1-f-\frac{4m_\mathrm{DM}^2}{x_1x_2s}]^{3/2}}{\sqrt{1-f}}\frac{1+(1-f)^2-2\frac{p_\mathrm{T}^2}{x_1x_2s}}{p_\mathrm{T}} \tag{B.43}$$

$$\left.\frac{\mathrm{d}^2\hat{\sigma}}{\mathrm{d}p_\mathrm{T}\mathrm{d}\eta}\right|_{D9} = \frac{2\alpha_s}{27\pi^2}\frac{x_1x_2s}{\Lambda^4}\frac{\sqrt{1-f-\frac{4m_\mathrm{DM}^2}{sx_1x_2}}(1-f+\frac{2m_\mathrm{DM}^2}{x_1x_2s})}{[1-f]^{3/2}}\frac{}{p_\mathrm{T}} \times\left[(1-f)(1+(1-f)^2)+f\frac{4p_\mathrm{T}^2}{x_1x_2s}\right] \tag{B.44}$$

$$\begin{aligned}\left.\frac{\mathrm{d}^2\hat{\sigma}}{\mathrm{d}p_\mathrm{T}\mathrm{d}\eta}\right|_{D11} = {}& \frac{3\alpha_s^3x_1^2x_2^2s^2}{256\pi^2\Lambda^6}\frac{(1-f-\frac{4m_\mathrm{DM}^2}{sx_1x_2})^{3/2}}{p_\mathrm{T}f^2\sqrt{1-f}}\left[16\frac{p_\mathrm{T}^4}{x_1^2x_2^2s^2}+8\frac{p_\mathrm{T}^2}{x_1x_2s}f\right.\\ &+(1-8\frac{p_\mathrm{T}^2}{x_1x_2s}+5\frac{p_\mathrm{T}^4}{x_1^2x_2^2s^2})f^2+(-2+8\frac{p_\mathrm{T}^2}{x_1x_2s})f^3\\ &\left.+(3-4\frac{p_\mathrm{T}^2}{x_1x_2s})f^4-2f^5+f^6\right]\end{aligned} \tag{B.45}$$

$$\begin{aligned}\left.\frac{\mathrm{d}^2\hat{\sigma}}{\mathrm{d}p_\mathrm{T}\mathrm{d}\eta}\right|_{D12} = {}& \frac{3\alpha_s^3x_1^2x_2^2s^2}{256\pi^2\Lambda^6}\frac{\sqrt{1-f-\frac{4m_\mathrm{DM}^2}{sx_1x_2}}\sqrt{1-f}}{p_\mathrm{T}f^2}\left[16\frac{p_\mathrm{T}^4}{x_1^2x_2^2s^2}+8\frac{p_\mathrm{T}^2}{x_1x_2s}f\right.\\ &+(1-8\frac{p_\mathrm{T}^2}{x_1x_2s}+5\frac{p_\mathrm{T}^4}{x_1^2x_2^2s^2})f^2\\ &\left.+(-2+8\frac{p_\mathrm{T}^2}{x_1x_2s})f^3+(3-4\frac{p_\mathrm{T}^2}{x_1x_2s})f^4-2f^5+f^6\right]\end{aligned} \tag{B.46}$$

$$\begin{aligned}\left.\frac{\mathrm{d}^2\hat{\sigma}}{\mathrm{d}p_\mathrm{T}\mathrm{d}\eta}\right|_{D13} = {}& \frac{3\alpha_s^3x_1^2x_2^2s^2}{256\pi^2\Lambda^6}\frac{(1-f-\frac{4m_\mathrm{DM}^2}{sx_1x_2})^{3/2}}{p_\mathrm{T}f^2\sqrt{1-f}}\left[16\frac{p_\mathrm{T}^4}{x_1^2x_2^2s^2}\right.\\ &+8(\frac{p_\mathrm{T}^2}{x_1x_2s}-2\frac{p_\mathrm{T}^4}{x_1^2x_2^2s^2})f+(1-12\frac{p_\mathrm{T}^2}{x_1x_2s}+5\frac{p_\mathrm{T}^4}{x_1^2x_2^2s^2})f^2\\ &\left.+(-2+8\frac{p_\mathrm{T}^2}{x_1x_2s})f^3+(3-4\frac{p_\mathrm{T}^2}{x_1x_2s})f^4-2f^5+f^6\right]\end{aligned} \tag{B.47}$$

$$\left.\frac{\mathrm{d}^2\hat{\sigma}}{\mathrm{d}p_{\mathrm{T}}\mathrm{d}\eta}\right|_{D14} = \frac{3\alpha_s^3 x_1^2 x_2^2 s^2}{256\pi^2\Lambda^6}\frac{\sqrt{1-f-\frac{4m_{\mathrm{DM}}^2}{sx_1x_2}}\sqrt{1-f}}{p_{\mathrm{T}}f^2}\left[16\frac{p_{\mathrm{T}}^4}{x_1^2x_2^2s^2}\right. \\ +8(\frac{p_{\mathrm{T}}^2}{x_1x_2s}-2\frac{p_{\mathrm{T}}^4}{x_1^2x_2^2s^2})f+(1-12\frac{p_{\mathrm{T}}^2}{x_1x_2s}+5\frac{p_{\mathrm{T}}^4}{x_1^2x_2^2s^2})f^2 \\ \left.+(-2+8\frac{p_{\mathrm{T}}^2}{x_1x_2s})f^3+(3-4\frac{p_{\mathrm{T}}^2}{x_1x_2s})f^4-2f^5+f^6\right] \tag{B.48}$$

where we have defined

$$f(p_{\mathrm{T}},\eta,x_1,x_2)\equiv\frac{p_{\mathrm{T}}(x_1e^{-\eta}+x_2e^{\eta})}{x_1x_2\sqrt{s}}\,. \tag{B.49}$$

For the emission of a photon, rather than a gluon, from a quark with charge Q_q one simply replaces $(4/3)\,\alpha_s \to Q_q^2\alpha$ in Eqs. (B.40)-(B.44). From these expressions one reproduces the results reported in Eqs. (5.18)-(5.26).

B.2 T Channel: Three-body Cross Sections

In this Appendix we show the details of the calculations of the tree-level cross sections for the hard scattering processes $q(p_1)+\bar{q}(p_2)\to\chi(p_3)+\chi(p_4)+g(k)$ and $q(p_1)+g(p_2)\to\chi(p_3)+\chi(p_4)+q(k)$, computed using the effective Lagrangian of Eq. 5.36.

B.2.1 Matrix Elements

The amplitudes for the process we are interested in are described, at leading order, by the Feyman diagrams in figure 5.11. In the EFT limit they are given by

$$\mathcal{M}_g = -i\frac{g^2g_s}{M^2}\epsilon_\mu^* T_{ij}^a\times\left\{\frac{\bar{u}(p_3)P_L(\not{p}_1-\not{p}_2)\gamma^\mu u(p_1)\bar{v}(p_2)P_Rv(p_4)}{(p_1-k)^2}\right. \\ \left.-\frac{\bar{u}(p_3)P_Lu(p_1)\bar{v}(p_2)P_R\gamma^\mu(\not{p}_2-\not{k})v(p_4)}{(p_2-k)^2}\right\} \\ \mathcal{M}_q = -i\frac{g^2g_s}{M^2}\epsilon_\mu T_{ij}^a\times\left\{\frac{\bar{u}(k)P_Rv(p_3)\bar{u}(p_4)P_L(\not{p}_1+\not{p}_2)\gamma^\mu u(p_1)}{(p_1+p_2)^2}\right. \\ \left.-\frac{\bar{u}(k)\gamma^\mu(\not{p}_2-\not{k})P_Rv(p_3)\bar{u}(p_4)P_Lu(p_1)}{(p_2-k)^2}\right\} \\ \mathcal{M}_{\bar{q}} = -i\frac{g^2g_s}{M^2}\epsilon_\mu T_{ij}^a\times\left\{\frac{\bar{v}(k)P_Lu(p_3)\bar{v}(p_4)P_R(\not{p}_1+\not{p}_2)\gamma^\mu v(p_1)}{(p_1+p_2)^2}\right. \\ \left.-\frac{\bar{v}(k)\gamma^\mu(\not{p}_2-\not{k})P_Lu(p_3)\bar{v}(p_4)P_Rv(p_1)}{(p_2-k)^2}\right\} \tag{B.50}$$

for the gluon, quark and anti-quark emission processes respectively. Here we denote the gluon polarization vector by ϵ_μ and the left and right projectors $(1-\gamma_5)/2$ and $(1+\gamma_5)/2$

with P_L and P_R respectively. The matrix T^a_{ij} stands for the standard QCD Gell-Mann matrices. Notice that we work in the massless quark limit. The anti-quark matrix element is simply obtained from the quark one by exchanging quarks with anti-quarks and left with right projectors. The parton level cross sections for the two processes are thus the same, so here we only show the explicit derivation of the quark one. The squared amplitudes, averaged over initial states (spin and colour) and summed over the final states, are given by

$$\begin{aligned}
|\mathcal{M}_g|^2 &= \frac{1}{9}\frac{g_s^2}{\Lambda^4}\frac{1}{(k\cdot p_1)(k\cdot p_2)}\times \\
&\Big\{p_1\cdot p_3\Big[(k\cdot p_4)(k\cdot p_1)-(k\cdot p_4)(p_1\cdot p_2)-(k\cdot p_2)(p_1\cdot p_4)\Big]+ \\
&+p_2\cdot p_4\Big[(k\cdot p_3)(k\cdot p_2)-(k\cdot p_3)(p_1\cdot p_2)-(k\cdot p_1)(p_2\cdot p_3)\Big]+ \\
&+(p_1\cdot p_3)(p_2\cdot p_4)\Big[2p_1\cdot p_2-k\cdot p_1-k\cdot p_2\Big]\Big\}
\end{aligned} \tag{B.51}$$

$$\begin{aligned}
|\mathcal{M}_q|^2 &= \frac{1}{6}\frac{g_s^2}{\Lambda^4}\frac{1}{(k\cdot p_1)(k\cdot p_2)}\times \\
&\Big\{p_1\cdot p_4\Big[(k\cdot p_2)(p_1\cdot p_3)-(k\cdot p_1)(p_2\cdot p_3)+ \\
&\qquad +(k\cdot p_2)(k\cdot p_3)+(k\cdot p_1)(k\cdot p_3)-(p_1\cdot p_2)(k\cdot p_3)\Big]+ \\
&+p_2\cdot p_2\Big[(p_1\cdot p_4)(p_2\cdot p_3)-(k\cdot p_4)(k\cdot p_3)\Big]+ \\
&+(k\cdot p_3)\Big[(k\cdot p_1)(p_1\cdot p_4)+(k\cdot p_1)(p_2\cdot p_4)+(k\cdot p_2)(p_2\cdot p_4)\Big]\Big\}
\end{aligned} \tag{B.52}$$

with $\Lambda^2 = M^2/g^2$.

B.2.2 Cross sections

The simplest way to compute the cross section in the lab frame is to first evaluate the matrix elements and the phase space density in the center-of-mass (c.o.m.) frame, and then boost the result to the lab frame. In the c.o.m. frame, let us parametrize the four-momenta inolved in the process as

$$\begin{aligned}
p_1 &= x\frac{\sqrt{s}}{2}(1,0,0,1)\,, \qquad p_2 = x\frac{\sqrt{s}}{2}(1,0,0,-1)\,, \qquad k = x\frac{\sqrt{s}}{2}(z_0, z_0\hat{k})\,, \\
p_3 &= x\frac{\sqrt{s}}{2}(1-y_0, \sqrt{(1-y_0)^2-a^2}\hat{p}_3)\,, \\
p_4 &= x\frac{\sqrt{s}}{2}(1+y_0-z_0, \sqrt{(1+y_0-z_0)^2-a^2}\hat{p}_4)\,,
\end{aligned} \tag{B.53}$$

where the two colliding partons carry equal momentum fractions $x_1 = x_2 \equiv x$ of the incoming protons, $a \equiv 2m_{\mathrm{DM}}/(x\sqrt{s}) < 1$, $\hat{k} = (0, \sin\theta_0, \cos\theta_0)$, and θ_0 is the polar angle of $\hat{k}$ with respect to the beam line, in the c.o.m. frame. The subscript $_0$ denotes quantities evaluated in the c.o.m. frame.

The differential cross section is generically given by

$$d\hat{\sigma} = \frac{\sum \overline{|\mathcal{M}|^2}}{4(p_1 \cdot p_2)} \mathrm{d}\Phi_3 \,, \tag{B.54}$$

where the three-body phase space is

$$\mathrm{d}\Phi_3 = (2\pi)^4 \, \delta(E_1+E_2-E_3-E_4-E_k) \, \delta^{(3)}(\vec{p}_1+\vec{p}_2-\vec{p}_3-\vec{p}_4-\vec{k}) \frac{\mathrm{d}^3 p_3}{(2\pi)^3 2E_3} \frac{\mathrm{d}^3 p_4}{(2\pi)^3 2E_4} \frac{\mathrm{d}^3 k}{(2\pi)^3 2E_k}. \tag{B.55}$$

Using the three-momentum delta function, we can integrate away $\mathrm{d}^3 p_4$; the energy delta function instead fixes the angle $\theta_{0\,3\mathrm{j}}$ between $\hat{p}_3$ and the jet $\hat{k}$ as: $\cos\theta_{0\,3\mathrm{j}} = (\mathbf{p}_4^2 - \mathbf{k}^2 - \mathbf{p}_3^2)/2|\mathbf{k}||\mathbf{p}_3|$. Integration over the azimuthal angle ϕ_0 of the outgoing jet simply gives a factor of 2π, while the matrix element does depend on the azimuthal angle of the three-momentum $\vec{p}_3$ with respect to $\vec{k}$, $\phi_{0\,3\mathrm{j}}$, and so it can not be integrated over at this stage, contrary to the s-channel case. Taking all of this into account, the phase space density simplifies to

$$\mathrm{d}\Phi_3 = \frac{1}{8(2\pi)^4} \, \mathrm{d}E_3 \, \mathrm{d}|\vec{k}| \, \mathrm{d}\cos\theta_0 \, \mathrm{d}\phi_{0\,3\mathrm{j}} = \frac{x^2 s}{32(2\pi)^4} \, \mathrm{d}y_0 \, \mathrm{d}z_0 \, \mathrm{d}\cos\theta_0 \, \mathrm{d}\phi_{0\,3\mathrm{j}}. \tag{B.56}$$

The kinematical domains of y_0, z_0 and $\phi_{0\,3\mathrm{j}}$ are

$$\frac{z_0}{2}\left(1 - \sqrt{\frac{1-z_0-a^2}{1-z_0}}\right) \leq \quad y_0 \quad \leq \frac{z_0}{2}\left(1 + \sqrt{\frac{1-z_0-a^2}{1-z_0}}\right) \tag{B.57}$$

$$0 \leq \quad z_0 \quad \leq 1 - a^2 \tag{B.58}$$

$$0 \leq \quad \phi_{0\,3\mathrm{j}} \quad \leq 2\pi \tag{B.59}$$

The variables y_0 and $\phi_{0\,3\mathrm{j}}$ refer to the momentum $\vec{p}_3$ of an invisible DM particle; they are therefore not measurable, and we integrate over them. For our present purpose, finding the total integrated cross section is useless, since these variables enter our definition of the momentum transfer Q_{tr}, and the condition $Q_{\mathrm{tr}} < \Lambda$ which we used to define the ratio R_Λ.

With the matrix elements of Eqns. B.51 and B.52, and the phase space density B.56, we get the differential cross sections in the c.o.m. frame:

$$\left.\frac{\mathrm{d}^4\hat{\sigma}}{\mathrm{d}z_0 \, \mathrm{d}\cos\theta_0 \, \mathrm{d}y_0 \, \mathrm{d}\phi_{0\,3\mathrm{j}}}\right|_g = \frac{1}{4608\pi^4} \frac{g_s^2}{\Lambda^4} \frac{1-z_0}{z_0^4}$$

$$
\begin{aligned}
&\Big\{ 4x(2-z_0)\csc\theta_0\cos\phi_{0\,3\mathrm{j}}(\cos\theta_0(z_0-2y_0)+z_0) \\
&\qquad \times\sqrt{s\left(sx^2y_0(z_0-1)(y_0-z_0)-m_{\mathrm{DM}}^2z_0^2\right)}-8m_{\mathrm{DM}}^2z_0^2\cos^2\phi_{0\,3\mathrm{j}} \\
&+sx^2((z_0-2)z_0+2)\left(\sec^2(\theta_0/2)\,y_0^2+\csc^2(\theta_0/2)\,(y_0-z_0)^2\right) \\
&-2sx^2y_0^2((z_0-6)z_0+6)+4sx^2y_0(z_0-1)(y_0-z_0)\cos(2\phi_{0\,3\mathrm{j}}) \\
&+2sx^2y_0((z_0-6)z_0+6)z_0-sx^2z_0^2((z_0-2)z_0+2)\Big\},
\end{aligned}
\tag{B.60}
$$

$$
\begin{aligned}
\left.\frac{\mathrm{d}^4\hat{\sigma}}{\mathrm{d}z_0\,\mathrm{d}\cos\theta_0\,\mathrm{d}y_0\,\mathrm{d}\phi_{0\,3\mathrm{j}}}\right|_q &= \frac{1}{98304\pi^4}\frac{g_s^2}{\Lambda^4}\frac{1-z_0}{z_0^3\cos^2\frac{\theta_0}{2}} \\
&\Big\{ 8x\sqrt{s}\left[z_0(z_0-y_0-1)-\left(z_0^2-(1+y_0)z_0+2y_0\right)\cos\theta_0\right]\cos\phi_{0\,3\mathrm{j}}\sin\theta_0\times \\
&\qquad \times\sqrt{sx^2y_0(z_0-y_0)(1-z_0)-m_{\mathrm{DM}}^2z_0^2} \\
&-2(1-\cos(2\theta_0))m_{\mathrm{DM}}^2z_0^2+4\Big[sx^2y_0(z_0-y_0)(1-z_0)-m_{\mathrm{DM}}^2z_0^2\Big]\cos(2\phi_{0\,3\mathrm{j}})\sin^2\theta_0 \\
&+sx^2\Big[11z_0^4-(6+22y_0)z_0^3+(11y_0^2+8y_0+3)z_0^2-2y_0(1+y_0)z_0+2y_0^2\Big] \\
&+sx^2\Big[z_0^4-2(1+y_0)z_0^3+(y_0^2+8y_0+1)z_0^2-6y_0(1+y_0)z_0+6y_0^2\Big]\cos(2\theta_0) \\
&-4sx^2z_0\Big[z_0^3-2(1+y_0)z_0^2+(y_0^2+4y_0+1)z_0-2y_0(1+y_0)\Big]\cos\theta_0\Big\}.
\end{aligned}
\tag{B.61}
$$

To get the cross sections in the lab frame we perform a boost in the $\hat{z}$ axis, accounting for the generic parton momentum fractions x_1, x_2. The velocity of the c.o.m. of the colliding particles with respect to the lab frame is given by

$$
\beta_{\mathrm{c.o.m.}}=\frac{x_1-x_2}{x_1+x_2},
\tag{B.62}
$$

so that the relations between the quantities z_0, θ_0 and the analogous ones z, θ in the lab frame are

$$
\begin{aligned}
z_0 &= \frac{(x_1+x_2)^2+(x_2^2-x_1^2)\cos\theta}{4x_1x_2}z \\
\sin^2\theta_0 &= \frac{4x_1x_2}{[(x_1+x_2)+(x_2-x_1)\cos\theta]^2}\sin^2\theta.
\end{aligned}
\tag{B.63}
$$

The Jacobian factor to transform $\mathrm{d}z_0\,\mathrm{d}\cos\theta_0 \to \mathrm{d}z\,\mathrm{d}\cos\theta$ is simply obtained using equations B.63; the cross section in the lab frame is then

$$
\frac{\mathrm{d}^4\hat{\sigma}}{\mathrm{d}z\,\mathrm{d}\cos\theta\,\mathrm{d}y_0\,\mathrm{d}\phi_{0\,3\mathrm{j}}}=\frac{x_1+x_2}{x_1+x_2+(x_1-x_2)\cos\theta}\left.\frac{\mathrm{d}^4\hat{\sigma}}{\mathrm{d}z_0\,\mathrm{d}\cos\theta_0\,\mathrm{d}y_0\,\mathrm{d}\phi_{0\,3\mathrm{j}}}\right|_{\substack{z_0\to z_0(z)\\ \theta_0\to\theta_0(\theta)}}.
\tag{B.64}
$$

Expressing the energy of the emitted gluon or (anti-)quark in terms of the transverse momentum and rapidity, $k^0 = p_{\rm T}\cosh\eta$, one finds

$$z = \frac{4p_{\rm T}\cosh\eta}{(x_1+x_2)\sqrt{s}}, \qquad \cos\theta = \tanh\eta \tag{B.65}$$

which allows us to express the differential cross sections with respect to the transverse momentum and pseudo-rapidity of the emitted jet:

$$\frac{{\rm d}^4\hat{\sigma}}{{\rm d}p_{\rm T}\,{\rm d}\eta\,{\rm d}y_0\,{\rm d}\phi_{0\,3{\rm j}}} = \frac{4}{(x_1+x_2)\sqrt{s}\cosh\eta}\,\frac{{\rm d}^4\hat{\sigma}}{{\rm d}z\,{\rm d}\cos\theta\,{\rm d}y_0\,{\rm d}\phi_{0\,3{\rm j}}}\bigg|_{\substack{z\,\to\,z(p_{\rm T},\,\eta)\\ \theta\,\to\,\theta(p_{\rm T},\,\eta)}} . \tag{B.66}$$

B.2.3 Transferred momentum

As is clear from our arguments, the key ingredient to quantify the validity of the EFT approximation is the value of the transferred momentum of the process. Since each process of interest here is given (at tree level) by the contribution of two Feynman diagrams, there will also be two expressions for the transferred momentum for both gluon and (anti-)quark emission, which we report here:

$$\begin{aligned}
Q^2_{\rm tr,g1} &= (p_1-k-p_3)^2 \\
&= m^2_{\rm DM} + \sqrt{s}x_2e^{\eta}p_{\rm T} - \frac{e^{2\eta}(1+y)(x_1x_2^2s)}{x_1+e^{2\eta}x_2} - \frac{x_1^2x_2^2e^{\eta}s^{3/2}y\left(x_1-e^{2\eta}x_2\right)}{p_{\rm T}(x_1+e^{2\eta}x_2)^2} \\
&\quad -\frac{2e^{\eta}x_1x_2\sqrt{s}\cos\phi_{0\,3{\rm j}}}{p_{\rm T}(x_1+e^{2\eta}x_2)^2}\Big[-m^2_{\rm DM}p_{\rm T}^2\left(x_1+e^{2\eta}x_2\right)^2 \\
&\quad -sx_1x_2y\left(e^{\eta}\sqrt{s}x_1x_2-p_{\rm T}\left(x_1+e^{2\eta}x_2\right)\right)\left(e^{\eta}\sqrt{s}x_1x_2y-p_{\rm T}\left(x_1+e^{2\eta}x_2\right)\right)\Big]^{1/2}\Bigg\},
\end{aligned} \tag{B.67}$$

$$\begin{aligned}
Q^2_{\rm tr,g2} &= (p_1-p_3)^2 \\
&= m^2_{\rm DM} + \frac{x_1x_2s(x_1-e^{2\eta}x_2)}{x_1+e^{2\eta}x_2} - \frac{(1-y)(x_1^2x_2s)}{x_1+e^{2\eta}x_2} - \frac{x_1^2x_2^2e^{\eta}s^{3/2}y(x_1-e^{2\eta}x_2)}{p_{\rm T}(x_1+e^{2\eta}x_2)^2} \\
&\quad -\frac{2e^{\eta}x_1x_2\sqrt{s}\cos\phi_{0\,3{\rm j}}}{p_{\rm T}(x_1+e^{2\eta}x_2)^2}\Big[-m^2_{\rm DM}p_{\rm T}^2\left(x_1+e^{2\eta}x_2\right)^2 \\
&\quad -sx_1x_2y\left(e^{\eta}\sqrt{s}x_1x_2-p_{\rm T}\left(x_1+e^{2\eta}x_2\right)\right)\left(e^{\eta}\sqrt{s}x_1x_2y-p_{\rm T}\left(x_1+e^{2\eta}x_2\right)\right)\Big]^{1/2}\Bigg\},
\end{aligned} \tag{B.68}$$

$$\begin{aligned}
Q^2_{\rm tr,q1} &= (p_3+k)^2 \\
&= m^2_{\rm DM} + p_{\rm T}\sqrt{s}\left(e^{-\eta}x_1+e^{\eta}x_2\right) - x_1x_2s\,y,
\end{aligned} \tag{B.69}$$

$$\begin{aligned}
Q^2_{\rm tr,q2} &= (p_1-p_3-k)^2 \\
&= m^2_{\rm DM} + \sqrt{s}x_1e^{-\eta}p_{\rm T} - \frac{(1+y)(x_1^2x_2s)}{x_1+e^{2\eta}x_2} + \frac{x_1^2x_2^2e^{\eta}s^{3/2}y(x_1-e^{2\eta}x_2)}{p_{\rm T}(x_1+e^{2\eta}x_2)^2} \\
&\quad -\frac{2e^{\eta}x_1x_2\sqrt{s}\cos\phi_{0\,3{\rm j}}}{p_{\rm T}(x_1+e^{2\eta}x_2)^2}\Big[-m^2_{\rm DM}p_{\rm T}^2\left(x_1+e^{2\eta}x_2\right)^2
\end{aligned} \tag{B.70}$$

$$-sx_1x_2y\left(e^{\eta}\sqrt{s}x_1x_2 - p_{\mathrm{T}}\left(x_1 + e^{2\eta}x_2\right)\right)\left(e^{\eta}\sqrt{s}x_1x_2y - p_{\mathrm{T}}\left(x_1 + e^{2\eta}x_2\right)\right)\Big]^{1/2}.$$

The notation g, q stands for gluon or quark emission; the indices $1, 2$ refer to emission from each of the initial state particles.

Appendix C

Two Body Annihilation Cross Sections and Widths

C.1 Introduction

In this Appendix we collect the results of cross sections calculations for the process of DM annihilation into SM fermions

$$\chi\bar{\chi} \to f\bar{f} \tag{C.1}$$

We performed the calculation at zero temperature in the lab frame where χ is at rest, and the center of mass energy $s = 2m_{\rm DM}^2\left(\frac{1}{\sqrt{1-v^2}}+1\right)$. This is equivalent to performing the calculation in the Moeller frame, and is the correct frame for the relic density calculations [264].

C.1.1 Relic density general formalism

Our technique to compute the abundance and notation follow Refs. [264] and [342]. First we find the freezeout temperature by solving

$$e^{x_F} = \frac{\sqrt{\frac{45}{8}}g_{\rm DoF}m_{\rm DM}M_{\rm Pl}c(c+2)\langle\sigma v\rangle}{2\pi^3 g_\star^{1/2}\sqrt{x_F}}, \tag{C.2}$$

where $x = m_{\rm DM}/T$ and subscript F denotes the value at freezeout, $g_{\rm DoF} = 2$ is the number of degrees of freedom of the DM particle, c is a matching constant usually taken to be $1/2$, $g_\star$ is the number of relativistic degrees of freedom, $M_{\rm Pl} = 1/\sqrt{G_N}$ is

the Planck mass. Usually, it is safe to expand in powers of the velocity and use the approximation

$$\langle\sigma v\rangle = a + b\langle v^2\rangle + \mathcal{O}(\langle v^4\rangle) \simeq a + 6b/x_F. \tag{C.3}$$

However, when the mediator width is small, this approximation can down near the s-channel resonance in the annihilation rate at $M \simeq 2m_{\rm DM}$ [31, 264, 418] if the width is small. Around this point it becomes more accurate to use the full expression,

$$\langle\sigma v\rangle = \frac{x}{8m_{\rm DM}^5 K_2^2[x]} \int_{4m_{\rm DM}^2}^{\infty} {\rm d}s\, \sigma(s - 4m_{\rm DM}^2)\sqrt{s}K_1[\sqrt{s}\, x/m_{\rm DM}]. \tag{C.4}$$

With this information, one can calculate the relic abundance,

$$\Omega_{\rm DM}h^2 = \Omega_\chi h^2 + \Omega_{\bar\chi}h^2 = \frac{2 \times 1.04 \times 10^9\,{\rm GeV}^{-1} m_{\rm DM}}{M_{\rm Pl}\int_{T_0}^{T_F} g_\star^{1/2}\langle\sigma v\rangle {\rm d}T}, \tag{C.5}$$

where the factor of 2 is for Dirac DM. When the non-relativistic approximation to the annihilation rate holds, this simplifies to

$$\Omega_{\rm DM}h^2 = \frac{2 \times 1.04 \times 10^9\,{\rm GeV}^{-1} x_F}{\overline{g_\star}^{1/2}\, M_{\rm Pl}\,(a + 3b/x_F)} \tag{C.6}$$

where $\overline{g_\star}^{1/2}$ is a typical value of $g_\star^{1/2}(T)$ in the range $T_0 \le T \le T_F$. We have tested the validity of this approximation and find that there is a negligible difference to the full relativistic calculation, since the widths we consider are relatively large. If the physical widths are used, then care should be taken that this approximation still holds when the width becomes small, especially when the annihilation rate has a larger p-wave component.

C.2 Results

C.2.1 Full expressions

$$\begin{aligned}(\sigma v)_V \;=\; & \frac{N_C (g_f^V)^2 (g_{\rm DM}^V)^2}{2\pi} \frac{\sqrt{1 - m_f^2/m_{\rm DM}^2}}{(M^2 - 4m_{\rm DM}^2)^2 + \Gamma^2 M^2}\Big[(m_f^2 + 2m_{\rm DM}^2) + \\ & v^2\Big(\frac{11m_f^4 + 2m_f^2 m_{\rm DM}^2 - 4m_{\rm DM}^4}{24m_{\rm DM}^2(1 - \frac{m_f^2}{m_{\rm DM}^2})} + 2\frac{m_{\rm DM}^2(m_f^2 + 2m_{\rm DM}^2)(M^2 - 4m_{\rm DM}^2)}{(M^2 - 4m_{\rm DM}^2)^2 + \Gamma^2 M^2}\Big)\Big],\end{aligned} \tag{C.7}$$

$$(\sigma v)_A \;=\; \frac{N_C (g_f^A)^2 (g_{\rm DM}^A)^2}{2\pi} \frac{\sqrt{1 - m_f^2/m_{\rm DM}^2}}{(M^2 - 4m_{\rm DM}^2)^2 + \Gamma^2 M^2}\Big[\Big(1 - 4\frac{m_{\rm DM}^2}{M^2}\Big)^2 m_f^2 +$$

$$v^2\Bigg(\Big(\frac{2m_f^2 m_{\rm DM}^2}{M^4}+\frac{2m_{\rm DM}^2}{M^2}-\frac{3m_f^2}{M^2}+\frac{23m_f^2}{24m_{\rm DM}^2}-\frac{7}{6}\Big)\frac{m_f^2}{(1-m_f^2/m_{\rm DM}^2)}$$
$$+\frac{m_{\rm DM}^2}{3(1-m_f^2/m_{\rm DM}^2)}+\frac{2(M^2-4m_{\rm DM}^2)^3 m_{\rm DM}^2 m_f^2}{M^4\left((M^2-4m_{\rm DM}^2)^2+\Gamma^2M^2\right)}\Bigg)\Bigg]. \tag{C.8}$$

C.2.2 Limit $m_f \to 0$

$$(\sigma v)_V = \frac{N_C (g_f^V)^2 (g_{\rm DM}^V)^2}{\pi}\frac{m_{\rm DM}^2}{(M^2-4m_{\rm DM}^2)^2+\Gamma^2M^2} \times\left[1+v^2\left(-\frac{1}{12}+\frac{2m_{\rm DM}^2(M^2-4m_{\rm DM}^2)}{(M^2-4m_{\rm DM}^2)^2+\Gamma^2M^2}\right)\right], \tag{C.9}$$

$$(\sigma v)_A = \frac{N_C (g_f^A)^2 (g_{\rm DM}^A)^2}{6\pi}\frac{m_{\rm DM}^2}{(M^2-4m_{\rm DM}^2)^2+\Gamma^2M^2}v^2. \tag{C.10}$$

C.2.3 Effective Operator Approximation

$$(\sigma v)_V = \frac{N_C m_{\rm DM}^2}{2\pi\Lambda^4}\sqrt{1-\frac{m_f^2}{m_{\rm DM}^2}}\left[\left(\frac{m_f^2}{m_{\rm DM}^2}+2\right) +v^2\frac{11m_f^4/m_{\rm DM}^4+2m_f^2/m_{\rm DM}^2-4}{24(1-m_f^2/m_{\rm DM}^2)}\right], \tag{C.11}$$

$$(\sigma v)_A = \frac{N_C}{2\pi\Lambda^4}\sqrt{1-\frac{m_f^2}{m_{\rm DM}^2}}\left[m_f^2+v^2\frac{23m_f^4/m_{\rm DM}^2-28m_f^2+8m_{\rm DM}^2}{24(1-m_f^2/m_{\rm DM}^2)}\right]. \tag{C.12}$$

C.2.4 Widths

The widths for the vector mediator decay to a pair of fermions are given by

$$\Gamma_V = \frac{N_C (g_f^V)^2 (M^2+2m_f^2)\sqrt{1-4m_f^2/M^2}}{12\pi M}, \tag{C.13}$$

$$\Gamma_A = \frac{N_C (g_f^A)^2 M(1-4m_f^2/M^2)^{3/2}}{12\pi}. \tag{C.14}$$

Bibliography

[1] **CMS** Collaboration, S. Chatrchyan *et al.*, "Observation of a new boson at a mass of 125 GeV with the CMS experiment at the LHC," *Phys.Lett.* **B716** (2012) 30–61, arXiv:1207.7235 [hep-ex].

[2] **ATLAS** Collaboration, G. Aad *et al.*, "Observation of a new particle in the search for the Standard Model Higgs boson with the ATLAS detector at the LHC," *Phys.Lett.* **B716** (2012) 1–29, arXiv:1207.7214 [hep-ex].

[3] **Super-Kamiokande Collaboration** Collaboration, Y. Fukuda *et al.*, "Evidence for oscillation of atmospheric neutrinos," *Phys.Rev.Lett.* **81** (1998) 1562–1567, arXiv:hep-ex/9807003 [hep-ex].

[4] J. L. Feng, "Dark Matter Candidates from Particle Physics and Methods of Detection," *Ann.Rev.Astron.Astrophys.* **48** (2010) 495–545, arXiv:1003.0904 [astro-ph.CO].

[5] **SNO Collaboration** Collaboration, Q. Ahmad *et al.*, "Direct evidence for neutrino flavor transformation from neutral current interactions in the Sudbury Neutrino Observatory," *Phys.Rev.Lett.* **89** (2002) 011301, arXiv:nucl-ex/0204008 [nucl-ex].

[6] C. Baker, D. Doyle, P. Geltenbort, K. Green, M. van der Grinten, *et al.*, "An Improved experimental limit on the electric dipole moment of the neutron," *Phys.Rev.Lett.* **97** (2006) 131801, arXiv:hep-ex/0602020 [hep-ex].

[7] **WMAP** Collaboration, G. Hinshaw *et al.*, "Nine-Year Wilkinson Microwave Anisotropy Probe (WMAP) Observations: Cosmological Parameter Results," *Astrophys.J.Suppl.* **208** (2013) 19, arXiv:1212.5226 [astro-ph.CO].

[8] **WMAP Collaboration** Collaboration, E. Komatsu *et al.*, "Seven-Year Wilkinson Microwave Anisotropy Probe (WMAP) Observations: Cosmological Interpretation," *Astrophys.J.Suppl.* **192** (2011) 18, arXiv:1001.4538 [astro-ph.CO].

[9] **WMAP** Collaboration, C. Bennett *et al.*, "Nine-Year Wilkinson Microwave Anisotropy Probe (WMAP) Observations: Final Maps and Results," *Astrophys.J.Suppl.* **208** (2013) 20, arXiv:1212.5225 [astro-ph.CO].

[10] D. Larson, J. Dunkley, G. Hinshaw, E. Komatsu, M. Nolta, *et al.*, "Seven-Year Wilkinson Microwave Anisotropy Probe (WMAP) Observations: Power Spectra and WMAP-Derived Parameters," *Astrophys.J.Suppl.* **192** (2011) 16, arXiv:1001.4635 [astro-ph.CO].

[11] **Particle Data Group** Collaboration, J. Beringer *et al.*, "Review of Particle Physics (RPP)," *Phys.Rev.* **D86** (2012) 010001.

[12] R. Massey, T. Kitching, and J. Richard, "The dark matter of gravitational lensing," *Rept.Prog.Phys.* **73** (2010) 086901, arXiv:1001.1739 [astro-ph.CO].

[13] M. Kamionkowski, "Possible relics from new physics in the early universe: Inflation, the cosmic microwave background, and particle dark matter," arXiv:astro-ph/9809214 [astro-ph].

[14] K. Begeman, A. Broeils, and R. Sanders, "Extended rotation curves of spiral galaxies: Dark haloes and modified dynamics," *Mon.Not.Roy.Astron.Soc.* **249** (1991) 523.

[15] A. Klypin, H. Zhao, and R. S. Somerville, "Lambda CDM-based models for the Milky Way and M31 I: Dynamical models," *Astrophys.J.* **573** (2002) 597–613, arXiv:astro-ph/0110390 [astro-ph].

[16] M. Milgrom, "The MOND paradigm," arXiv:0801.3133 [astro-ph].

[17] B. Famaey and S. McGaugh, "Modified Newtonian Dynamics (MOND): Observational Phenomenology and Relativistic Extensions," *Living Rev.Rel.* **15** (2012) 10, arXiv:1112.3960 [astro-ph.CO].

[18] D. Clowe, M. Bradac, A. H. Gonzalez, M. Markevitch, S. W. Randall, *et al.*, "A direct empirical proof of the existence of dark matter," *Astrophys.J.* **648** (2006) L109–L113, arXiv:astro-ph/0608407 [astro-ph].

[19] M. Markevitch, A. Gonzalez, L. David, A. Vikhlinin, S. Murray, *et al.*, "A Textbook example of a bow shock in the merging galaxy cluster 1E0657-56," *Astrophys.J.* **567** (2002) L27, arXiv:astro-ph/0110468 [astro-ph].

[20] D. Clowe, A. Gonzalez, and M. Markevitch, "Weak lensing mass reconstruction of the interacting cluster 1E0657-558: Direct evidence for the existence of dark matter," *Astrophys.J.* **604** (2004) 596–603, arXiv:astro-ph/0312273 [astro-ph].

[21] **2DFGRS Collaboration** Collaboration, M. Colless *et al.*, "The 2dF Galaxy Redshift Survey: Spectra and redshifts," *Mon.Not.Roy.Astron.Soc.* **328** (2001) 1039, arXiv:astro-ph/0106498 [astro-ph].

[22] **SDSS Collaboration** Collaboration, M. Tegmark *et al.*, "The 3-D power spectrum of galaxies from the SDSS," *Astrophys.J.* **606** (2004) 702–740, arXiv:astro-ph/0310725 [astro-ph].

[23] V. Springel, S. D. White, A. Jenkins, C. S. Frenk, N. Yoshida, *et al.*, "Simulating the joint evolution of quasars, galaxies and their large-scale distribution," *Nature* **435** (2005) 629–636, arXiv:astro-ph/0504097 [astro-ph].

[24] C. Tao, "Astrophysical Constraints on Dark Matter," *EAS Publ.Ser.* **53** (2012) 97–104, arXiv:1110.0298 [astro-ph.CO].

[25] M. Viel, J. Lesgourgues, M. G. Haehnelt, S. Matarrese, and A. Riotto, "Can sterile neutrinos be ruled out as warm dark matter candidates?," *Phys.Rev.Lett.* **97** (2006) 071301, arXiv:astro-ph/0605706 [astro-ph].

[26] M. Viel, J. Lesgourgues, M. G. Haehnelt, S. Matarrese, and A. Riotto, "Constraining warm dark matter candidates including sterile neutrinos and light gravitinos with WMAP and the Lyman-alpha forest," *Phys.Rev.* **D71** (2005) 063534, arXiv:astro-ph/0501562 [astro-ph].

[27] D. Fixsen, E. Cheng, J. Gales, J. C. Mather, R. Shafer, *et al.*, "The Cosmic Microwave Background spectrum from the full COBE FIRAS data set," *Astrophys.J.* **473** (1996) 576, arXiv:astro-ph/9605054 [astro-ph].

[28] D. Fixsen, "The Temperature of the Cosmic Microwave Background," *Astrophys.J.* **707** (2009) 916–920, arXiv:0911.1955 [astro-ph.CO].

[29] **Supernova Search Team** Collaboration, A. G. Riess *et al.*, "Observational evidence from supernovae for an accelerating universe and a cosmological constant," *Astron.J.* **116** (1998) 1009–1038, arXiv:astro-ph/9805201 [astro-ph].

[30] **Supernova Cosmology Project** Collaboration, S. Perlmutter *et al.*, "Measurements of Omega and Lambda from 42 high redshift supernovae," *Astrophys.J.* **517** (1999) 565–586, arXiv:astro-ph/9812133 [astro-ph].

[31] K. Griest and M. Kamionkowski, "Unitarity Limits on the Mass and Radius of Dark Matter Particles," *Phys.Rev.Lett.* **64** (1990) 615.

[32] A. Zentsova and A. Chernin, "Evolution of entropy perturbations in the post-recombination epoch. i. linear stage," *Astrophysics* **15** no. 3, (1979) 317–323. http://dx.doi.org/10.1007/BF01004377.

[33] H.-Y. Chiu, "Symmetry between particle and anti-particle populations in the universe," *Phys.Rev.Lett.* **17** (1966) 712.

[34] G. Steigman, "Cosmology Confronts Particle Physics," *Ann.Rev.Nucl.Part.Sci.* **29** (1979) 313–338.

[35] R. J. Scherrer and M. S. Turner, "On the Relic, Cosmic Abundance of Stable Weakly Interacting Massive Particles," *Phys.Rev.* **D33** (1986) 1585.

[36] R. Peccei, "The Strong CP problem and axions," *Lect.Notes Phys.* **741** (2008) 3–17, arXiv:hep-ph/0607268 [hep-ph].

[37] R. Peccei and H. R. Quinn, "CP Conservation in the Presence of Instantons," *Phys.Rev.Lett.* **38** (1977) 1440–1443.

[38] J. E. Kim and G. Carosi, "Axions and the Strong CP Problem," *Rev.Mod.Phys.* **82** (2010) 557–602, arXiv:0807.3125 [hep-ph].

[39] J. E. Kim, "Weak Interaction Singlet and Strong CP Invariance," *Phys.Rev.Lett.* **43** (1979) 103.

[40] M. A. Shifman, A. Vainshtein, and V. I. Zakharov, "Can Confinement Ensure Natural CP Invariance of Strong Interactions?," *Nucl.Phys.* **B166** (1980) 493.

[41] M. Dine, W. Fischler, and M. Srednicki, "A Simple Solution to the Strong CP Problem with a Harmless Axion," *Phys.Lett.* **B104** (1981) 199.

[42] A. Zhitnitsky, "On Possible Suppression of the Axion Hadron Interactions. (In Russian)," *Sov.J.Nucl.Phys.* **31** (1980) 260.

[43] G. G. Raffelt, "Astrophysical axion bounds," *Lect.Notes Phys.* **741** (2008) 51–71, arXiv:hep-ph/0611350 [hep-ph].

[44] L. Rosenberg and K. van Bibber, "Searches for invisible axions," *Phys.Rept.* **325** (2000) 1–39.

[45] K. J. Bae, J.-H. Huh, and J. E. Kim, "Update of axion CDM energy," *JCAP* **0809** (2008) 005, arXiv:0806.0497 [hep-ph].

[46] S. Chang, C. Hagmann, and P. Sikivie, "Studies of the motion and decay of axion walls bounded by strings," *Phys.Rev.* **D59** (1999) 023505, arXiv:hep-ph/9807374 [hep-ph].

[47] C. Hagmann, S. Chang, and P. Sikivie, "Axion radiation from strings," *Phys.Rev.* **D63** (2001) 125018, arXiv:hep-ph/0012361 [hep-ph].

[48] R. Battye and E. Shellard, "Axion string constraints," *Phys.Rev.Lett.* **73** (1994) 2954–2957, arXiv:astro-ph/9403018 [astro-ph].

[49] M. Yamaguchi, M. Kawasaki, and J. Yokoyama, "Evolution of axionic strings and spectrum of axions radiated from them," *Phys.Rev.Lett.* **82** (1999) 4578–4581, arXiv:hep-ph/9811311 [hep-ph].

[50] A. D. Linde, "Inflation and Axion Cosmology," *Phys.Lett.* **B201** (1988) 437.

[51] M. Tegmark, A. Aguirre, M. Rees, and F. Wilczek, "Dimensionless constants, cosmology and other dark matters," *Phys.Rev.* **D73** (2006) 023505, arXiv:astro-ph/0511774 [astro-ph].

[52] D. H. Weinberg, J. S. Bullock, F. Governato, R. K. de Naray, and A. H. G. Peter, "Cold dark matter: controversies on small scales," arXiv:1306.0913 [astro-ph.CO].

[53] G. D. Starkman, A. Gould, R. Esmailzadeh, and S. Dimopoulos, "Opening the Window on Strongly Interacting Dark Matter," *Phys.Rev.* **D41** (1990) 3594.

[54] J. Kang, M. A. Luty, and S. Nasri, "The Relic abundance of long-lived heavy colored particles," *JHEP* **0809** (2008) 086, arXiv:hep-ph/0611322 [hep-ph].

[55] D. N. Spergel and P. J. Steinhardt, "Observational evidence for selfinteracting cold dark matter," *Phys.Rev.Lett.* **84** (2000) 3760–3763, arXiv:astro-ph/9909386 [astro-ph].

[56] B. D. Wandelt, R. Dave, G. R. Farrar, P. C. McGuire, D. N. Spergel, *et al.*, "Selfinteracting dark matter," arXiv:astro-ph/0006344 [astro-ph].

[57] M. Vogelsberger, J. Zavala, and A. Loeb, "Subhaloes in Self-Interacting Galactic Dark Matter Haloes," *Mon.Not.Roy.Astron.Soc.* **423** (2012) 3740, arXiv:1201.5892 [astro-ph.CO].

[58] M. Rocha, A. H. Peter, J. S. Bullock, M. Kaplinghat, S. Garrison-Kimmel, *et al.*, "Cosmological Simulations with Self-Interacting Dark Matter I: Constant Density Cores and Substructure," *Mon.Not.Roy.Astron.Soc.* **430** (2013) 81–104, arXiv:1208.3025 [astro-ph.CO].

[59] A. H. Peter, M. Rocha, J. S. Bullock, and M. Kaplinghat, "Cosmological Simulations with Self-Interacting Dark Matter II: Halo Shapes vs. Observations," *Mon.Not.Roy.Astron.Soc.* **430** (2013) 105, arXiv:1208.3026 [astro-ph.CO].

[60] J. Zavala, M. Vogelsberger, and M. G. Walker, "Constraining Self-Interacting Dark Matter with the Milky Way's dwarf spheroidals," *Monthly Notices of the Royal Astronomical Society: Letters* **431** (2013) L20–L24, arXiv:1211.6426 [astro-ph.CO].

[61] M. Vogelsberger, J. Zavala, C. Simpson, and A. Jenkins, "Dwarf galaxies in CDM and SIDM with baryons: observational probes of the nature of dark matter," *Mon.Not.Roy.Astron.Soc.* **444** (2014) 3684, arXiv:1405.5216 [astro-ph.CO].

[62] O. D. Elbert, J. S. Bullock, S. Garrison-Kimmel, M. Rocha, J. Oñorbe, *et al.*, "Core Formation in Dwarf Halos with Self Interacting Dark Matter: No Fine-Tuning Necessary," arXiv:1412.1477 [astro-ph.GA].

[63] M. Markevitch, A. Gonzalez, D. Clowe, A. Vikhlinin, L. David, *et al.*, "Direct constraints on the dark matter self-interaction cross-section from the merging galaxy cluster 1E0657-56," *Astrophys.J.* **606** (2004) 819–824, arXiv:astro-ph/0309303 [astro-ph].

[64] S. W. Randall, M. Markevitch, D. Clowe, A. H. Gonzalez, and M. Bradac, "Constraints on the Self-Interaction Cross-Section of Dark Matter from Numerical Simulations of the Merging Galaxy Cluster 1E 0657-56," *Astrophys.J.* **679** (2008) 1173–1180, arXiv:0704.0261 [astro-ph].

[65] K. Petraki and R. R. Volkas, "Review of asymmetric dark matter," *Int.J.Mod.Phys.* **A28** (2013) 1330028, arXiv:1305.4939 [hep-ph].

[66] **Planck Collaboration** Collaboration, P. Ade *et al.*, "Planck 2013 results. XVI. Cosmological parameters," *Astron.Astrophys.* **571** (2014) A16, arXiv:1303.5076 [astro-ph.CO].

[67] A. B. McDonald, "Neutrino oscillation measurements: Past and present,".

[68] J. McDonald, "Simultaneous Generation of WIMP Miracle-like Densities of Baryons and Dark Matter," *Phys.Rev.* **D84** (2011) 103514, arXiv:1108.4653 [hep-ph].

[69] Y. Cui, L. Randall, and B. Shuve, "A WIMPy Baryogenesis Miracle," *JHEP* **1204** (2012) 075, arXiv:1112.2704 [hep-ph].

[70] Y. Bai, P. J. Fox, and R. Harnik, "The Tevatron at the Frontier of Dark Matter Direct Detection," *JHEP* **1012** (2010) 048, arXiv:1005.3797 [hep-ph].

[71] M. R. Buckley, "Asymmetric Dark Matter and Effective Operators," *Phys.Rev.* **D84** (2011) 043510, arXiv:1104.1429 [hep-ph].

[72] P. J. Fox, R. Harnik, R. Primulando, and C.-T. Yu, "Taking a Razor to Dark Matter Parameter Space at the LHC," *Phys.Rev.* **D86** (2012) 015010, arXiv:1203.1662 [hep-ph].

[73] **DAMA Collaboration** Collaboration, R. Bernabei *et al.*, "First results from DAMA/LIBRA and the combined results with DAMA/NaI," *Eur.Phys.J.* **C56** (2008) 333–355, arXiv:0804.2741 [astro-ph].

[74] **DAMA Collaboration, LIBRA Collaboration** Collaboration, R. Bernabei *et al.*, "New results from DAMA/LIBRA," *Eur.Phys.J.* **C67** (2010) 39–49, arXiv:1002.1028 [astro-ph.GA].

[75] **CoGeNT collaboration** Collaboration, C. Aalseth *et al.*, "Results from a Search for Light-Mass Dark Matter with a P-type Point Contact Germanium Detector," *Phys.Rev.Lett.* **106** (2011) 131301, arXiv:1002.4703 [astro-ph.CO].

[76] C. Aalseth, P. Barbeau, J. Colaresi, J. Collar, J. Diaz Leon, *et al.*, "Search for an Annual Modulation in a P-type Point Contact Germanium Dark Matter Detector," *Phys.Rev.Lett.* **107** (2011) 141301, arXiv:1106.0650 [astro-ph.CO].

[77] G. Angloher, M. Bauer, I. Bavykina, A. Bento, C. Bucci, *et al.*, "Results from 730 kg days of the CRESST-II Dark Matter Search," *Eur.Phys.J.* **C72** (2012) 1971, arXiv:1109.0702 [astro-ph.CO].

[78] **CDMS Collaboration** Collaboration, R. Agnese *et al.*, "Silicon Detector Dark Matter Results from the Final Exposure of CDMS II," *Phys.Rev.Lett.* **111** (2013) 251301, arXiv:1304.4279 [hep-ex].

[79] **LUX Collaboration** Collaboration, D. Akerib *et al.*, "First results from the LUX dark matter experiment at the Sanford Underground Research Facility," *Phys.Rev.Lett.* **112** no. 9, (2014) 091303, arXiv:1310.8214 [astro-ph.CO].

[80] R. Foot, "Implications of the DAMA and CRESST experiments for mirror matter type dark matter," *Phys.Rev.* **D69** (2004) 036001, arXiv:hep-ph/0308254 [hep-ph].

[81] R. Foot, "A comprehensive analysis of the dark matter direct detection experiments in the mirror dark matter framework," *Phys.Rev.* **D82** (2010) 095001, arXiv:1008.0685 [hep-ph].

[82] R. Foot, "Mirror and hidden sector dark matter in the light of new CoGeNT data," *Phys.Lett.* **B703** (2011) 7–13, arXiv:1106.2688 [hep-ph].

[83] R. Foot, "Direct detection experiments explained with mirror dark matter," *Phys.Lett.* **B728** (2014) 45–50, arXiv:1305.4316 [astro-ph.CO].

[84] R. Foot, "Hidden sector dark matter explains the DAMA, CoGeNT, CRESST-II and CDMS/Si experiments," *Phys.Rev.* **D88** no. 2, (2013) 025032, arXiv:1209.5602 [hep-ph].

[85] N. Fornengo, P. Panci, and M. Regis, "Long-Range Forces in Direct Dark Matter Searches," *Phys.Rev.* **D84** (2011) 115002, arXiv:1108.4661 [hep-ph].

[86] R. Foot, H. Lew, and R. Volkas, "A Model with fundamental improper space-time symmetries," *Phys.Lett.* **B272** (1991) 67–70.

[87] R. Foot, H. Lew, and R. Volkas, "Possible consequences of parity conservation," *Mod.Phys.Lett.* **A7** (1992) 2567–2574.

[88] R. Foot and R. Volkas, "Neutrino physics and the mirror world: How exact parity symmetry explains the solar neutrino deficit, the atmospheric neutrino anomaly and the LSND experiment," *Phys.Rev.* **D52** (1995) 6595–6606, arXiv:hep-ph/9505359 [hep-ph].

[89] T. Lee and C.-N. Yang, "Question of Parity Conservation in Weak Interactions," *Phys.Rev.* **104** (1956) 254–258.

[90] M. Pavsic, "External inversion, internal inversion, and reflection invariance," *Int.J.Theor.Phys.* **9** (1974) 229–244, arXiv:hep-ph/0105344 [hep-ph].

[91] S. Blinnikov and M. Y. Khlopov, "ON POSSIBLE EFFECTS OF 'MIRROR' PARTICLES," *Sov.J.Nucl.Phys.* **36** (1982) 472.

[92] S. Blinnikov and M. Khlopov, "Possible astronomical effects of mirror particles," *Sov.Astron.* **27** (1983) 371–375.

[93] Z. Berezhiani, D. Comelli, and F. L. Villante, "The Early mirror universe: Inflation, baryogenesis, nucleosynthesis and dark matter," *Phys.Lett.* **B503** (2001) 362–375, arXiv:hep-ph/0008105 [hep-ph].

[94] A. Y. Ignatiev and R. Volkas, "Mirror dark matter and large scale structure," *Phys.Rev.* **D68** (2003) 023518, arXiv:hep-ph/0304260 [hep-ph].

[95] R. Foot and R. Volkas, "Was ordinary matter synthesized from mirror matter? An Attempt to explain why Omega(Baryon) approximately equal to 0.2 Omega(Dark)," *Phys.Rev.* **D68** (2003) 021304, arXiv:hep-ph/0304261 [hep-ph].

[96] R. Foot and R. Volkas, "Explaining Omega(Baryon) approximately 0.2 Omega(Dark) through the synthesis of ordinary matter from mirror matter: A More general analysis," *Phys.Rev.* **D69** (2004) 123510, arXiv:hep-ph/0402267 [hep-ph].

[97] Z. Berezhiani, P. Ciarcelluti, D. Comelli, and F. L. Villante, "Structure formation with mirror dark matter: CMB and LSS," *Int.J.Mod.Phys.* **D14** (2005) 107–120, arXiv:astro-ph/0312605 [astro-ph].

[98] P. Ciarcelluti, "Cosmology with mirror dark matter. 1. Linear evolution of perturbations," *Int.J.Mod.Phys.* **D14** (2005) 187–222, arXiv:astro-ph/0409630 [astro-ph].

[99] P. Ciarcelluti, "Cosmology with mirror dark matter. 2. Cosmic microwave background and large scale structure," *Int.J.Mod.Phys.* **D14** (2005) 223–256, arXiv:astro-ph/0409633 [astro-ph].

[100] Z. Berezhiani, S. Cassisi, P. Ciarcelluti, and A. Pietrinferni, "Evolutionary and structural properties of mirror star MACHOs," *Astropart.Phys.* **24** (2006) 495–510, arXiv:astro-ph/0507153 [astro-ph].

[101] S. Nussinov, "TECHNOCOSMOLOGY: COULD A TECHNIBARYON EXCESS PROVIDE A 'NATURAL' MISSING MASS CANDIDATE?," *Phys.Lett.* **B165** (1985) 55.

[102] S. M. Barr, R. S. Chivukula, and E. Farhi, "Electroweak Fermion Number Violation and the Production of Stable Particles in the Early Universe," *Phys.Lett.* **B241** (1990) 387–391.

[103] O. Klein, "Quantum Theory and Five-Dimensional Theory of Relativity. (In German and English)," *Z.Phys.* **37** (1926) 895–906.

[104] T. Appelquist, H.-C. Cheng, and B. A. Dobrescu, "Bounds on universal extra dimensions," *Phys.Rev.* **D64** (2001) 035002, arXiv:hep-ph/0012100 [hep-ph].

[105] N. Arkani-Hamed, S. Dimopoulos, and G. Dvali, "The Hierarchy problem and new dimensions at a millimeter," *Phys.Lett.* **B429** (1998) 263–272, arXiv:hep-ph/9803315 [hep-ph].

[106] I. Antoniadis, N. Arkani-Hamed, S. Dimopoulos, and G. Dvali, "New dimensions at a millimeter to a Fermi and superstrings at a TeV," *Phys.Lett.* **B436** (1998) 257–263, arXiv:hep-ph/9804398 [hep-ph].

[107] N. Arkani-Hamed, S. Dimopoulos, and G. Dvali, "Phenomenology, astrophysics and cosmology of theories with submillimeter dimensions and TeV scale quantum gravity," *Phys.Rev.* **D59** (1999) 086004, arXiv:hep-ph/9807344 [hep-ph].

[108] S. Cullen, M. Perelstein, and M. E. Peskin, "TeV strings and collider probes of large extra dimensions," *Phys.Rev.* **D62** (2000) 055012, arXiv:hep-ph/0001166 [hep-ph].

[109] G. F. Giudice, R. Rattazzi, and J. D. Wells, "Quantum gravity and extra dimensions at high-energy colliders," *Nucl.Phys.* **B544** (1999) 3–38, arXiv:hep-ph/9811291 [hep-ph].

[110] R. Franceschini, P. P. Giardino, G. F. Giudice, P. Lodone, and A. Strumia, "LHC bounds on large extra dimensions," *JHEP* **1105** (2011) 092, arXiv:1101.4919 [hep-ph].

[111] C. Hoyle, D. Kapner, B. R. Heckel, E. Adelberger, J. Gundlach, *et al.*, "Sub-millimeter tests of the gravitational inverse-square law," *Phys.Rev.* **D70** (2004) 042004, arXiv:hep-ph/0405262 [hep-ph].

[112] J. C. Long, H. W. Chan, A. B. Churnside, E. A. Gulbis, M. C. Varney, *et al.*, "New experimental limits on macroscopic forces below 100 microns," arXiv:hep-ph/0210004 [hep-ph].

[113] G. F. Giudice, T. Plehn, and A. Strumia, "Graviton collider effects in one and more large extra dimensions," *Nucl.Phys.* **B706** (2005) 455–483, arXiv:hep-ph/0408320 [hep-ph].

[114] G. Servant and T. M. Tait, "Is the lightest Kaluza-Klein particle a viable dark matter candidate?," *Nucl.Phys.* **B650** (2003) 391–419, arXiv:hep-ph/0206071 [hep-ph].

[115] H.-C. Cheng, J. L. Feng, and K. T. Matchev, "Kaluza-Klein dark matter," *Phys.Rev.Lett.* **89** (2002) 211301, arXiv:hep-ph/0207125 [hep-ph].

[116] G. Altarelli and D. Meloni, "A non supersymmetric SO(10) grand unified model for all the physics below M_{GUT}," *JHEP* **1308** (2013) 021, arXiv:1305.1001.

[117] S. Dodelson and L. M. Widrow, "Sterile-neutrinos as dark matter," *Phys.Rev.Lett.* **72** (1994) 17–20, arXiv:hep-ph/9303287 [hep-ph].

[118] A. Strumia and F. Vissani, "Neutrino masses and mixings and...," arXiv:hep-ph/0606054 [hep-ph].

[119] A. Kusenko, "Sterile neutrinos: The Dark side of the light fermions," *Phys.Rept.* **481** (2009) 1–28, arXiv:0906.2968 [hep-ph].

[120] **EROS** Collaboration, C. Afonso *et al.*, "Limits on galactic dark matter with 5 years of EROS SMC data," *Astron.Astrophys.* **400** (2003) 951–956, arXiv:astro-ph/0212176 [astro-ph].

[121] **EROS** Collaboration, C. Afonso *et al.*, "Bulge microlensing optical depth from EROS 2 observations," *Astron.Astrophys.* **404** (2003) 145–156, arXiv:astro-ph/0303100 [astro-ph].

[122] **EROS-2** Collaboration, P. Tisserand *et al.*, "Limits on the Macho Content of the Galactic Halo from the EROS-2 Survey of the Magellanic Clouds," *Astron.Astrophys.* **469** (2007) 387–404, arXiv:astro-ph/0607207 [astro-ph].

[123] **MACHO** Collaboration, D. Bennett *et al.*, "The MACHO project dark matter search," *ASP Conf.Ser.* **88** (1996) 95, arXiv:astro-ph/9510104 [astro-ph].

[124] **MACHO** Collaboration, C. Alcock *et al.*, "The MACHO project: Microlensing results from 5.7 years of LMC observations," *Astrophys.J.* **542** (2000) 281–307, arXiv:astro-ph/0001272 [astro-ph].

[125] **MACHO** Collaboration, P. Popowski *et al.*, "Microlensing optical depth towards the galactic bulge using clump giants from the MACHO survey," *Astrophys.J.* **631** (2005) 879–905, arXiv:astro-ph/0410319 [astro-ph].

[126] L. Wyrzykowski, S. Kozlowski, J. Skowron, A. Udalski, M. Szymanski, *et al.*, "The OGLE View of Microlensing towards the Magellanic Clouds. III. Ruling out sub-solar MACHOs with the OGLE-III LMC data," *Mon.Not.Roy.Astron.Soc.* **413** (2011) 493, arXiv:1012.1154 [astro-ph.GA].

[127] L. Wyrzykowski, J. Skowron, S. Kozlowski, A. Udalski, M. Szymanski, *et al.*, "The OGLE View of Microlensing towards the Magellanic Clouds. IV. OGLE-III SMC Data and Final Conclusions on MACHOs," *Mon.Not.Roy.Astron.Soc.* **416** (2011) 2949, arXiv:1106.2925 [astro-ph.GA].

[128] G. Jungman, M. Kamionkowski, and K. Griest, "Supersymmetric dark matter," *Phys.Rept.* **267** (1996) 195–373, arXiv:hep-ph/9506380 [hep-ph].

[129] A. Drukier and L. Stodolsky, "Principles and Applications of a Neutral Current Detector for Neutrino Physics and Astronomy," *Phys.Rev.* **D30** (1984) 2295.

[130] M. W. Goodman and E. Witten, "Detectability of Certain Dark Matter Candidates," *Phys.Rev.* **D31** (1985) 3059.

[131] L. Baudis, "Direct dark matter detection: The next decade," *Physics of the Dark Universe* **1** (Nov., 2012) 94–108, arXiv:1211.7222 [astro-ph.IM].

[132] J. Engel, S. Pittel, and P. Vogel, "Nuclear physics of dark matter detection," *Int.J.Mod.Phys.* **E1** (1992) 1–37.

[133] J. Lewin and P. Smith, "Review of mathematics, numerical factors, and corrections for dark matter experiments based on elastic nuclear recoil," *Astropart.Phys.* **6** (1996) 87–112.

[134] M. T. Ressell, M. B. Aufderheide, S. D. Bloom, K. Griest, G. J. Mathews, *et al.*, "Nuclear shell model calculations of neutralino - nucleus cross-sections for Si-29 and Ge-73," *Phys.Rev.* **D48** (1993) 5519–5535.

[135] V. Dimitrov, J. Engel, and S. Pittel, "Scattering of weakly interacting massive particles from Ge-73," *Phys.Rev.* **D51** (1995) 291–295, arXiv:hep-ph/9408246 [hep-ph].

[136] J. Engel, M. Ressell, I. Towner, and W. Ormand, "Response of mica to weakly interacting massive particles," *Phys.Rev.* **C52** (1995) 2216–2221, arXiv:hep-ph/9504322 [hep-ph].

[137] J. Engel and P. Vogel, "Spin dependent cross-sections of weakly interacting massive particles on nuclei," *Phys.Rev.* **D40** (1989) 3132–3135.

[138] M. Ressell and D. Dean, "Spin dependent neutralino - nucleus scattering for A approximately 127 nuclei," *Phys.Rev.* **C56** (1997) 535–546, arXiv:hep-ph/9702290 [hep-ph].

[139] E. Holmlund, M. Kortelainen, T. Kosmas, J. Suhonen, and J. Toivanen, "Microscopic calculation of the LSP detection rates for the Ga-71, Ge-73 and I-127 dark-matter detectors," *Phys.Lett.* **B584** (2004) 31–39.

[140] P. Toivanen, M. Kortelainen, J. Suhonen, and J. Toivanen, "Large-scale shell-model calculations of elastic and inelastic scattering rates of lightest supersymmetric particles (LSP) on I-127, Xe-129, Xe-131, and Cs-133 nuclei," *Phys.Rev.* **C79** (2009) 044302.

[141] J. Menendez, D. Gazit, and A. Schwenk, "Spin-dependent WIMP scattering off nuclei," *Phys.Rev.* **D86** (2012) 103511, arXiv:1208.1094 [astro-ph.CO].

[142] E. Epelbaum, H.-W. Hammer, and U.-G. Meissner, "Modern Theory of Nuclear Forces," *Rev.Mod.Phys.* **81** (2009) 1773–1825, arXiv:0811.1338 [nucl-th].

[143] T. Park, L. Marcucci, R. Schiavilla, M. Viviani, A. Kievsky, *et al.*, "Parameter free effective field theory calculation for the solar proton fusion and hep processes," *Phys.Rev.* **C67** (2003) 055206, arXiv:nucl-th/0208055 [nucl-th].

[144] A. M. Green, "Astrophysical uncertainties on direct detection experiments," *Mod.Phys.Lett.* **A27** (2012) 1230004, arXiv:1112.0524 [astro-ph.CO].

[145] M. Pato, L. Baudis, G. Bertone, R. Ruiz de Austri, L. E. Strigari, *et al.*, "Complementarity of Dark Matter Direct Detection Targets," *Phys.Rev.* **D83** (2011) 083505, arXiv:1012.3458 [astro-ph.CO].

[146] A. Drukier, K. Freese, and D. Spergel, "Detecting Cold Dark Matter Candidates," *Phys.Rev.* **D33** (1986) 3495–3508.

[147] K. Freese, J. A. Frieman, and A. Gould, "Signal Modulation in Cold Dark Matter Detection," *Phys.Rev.* **D37** (1988) 3388–3405.

[148] D. N. Spergel, "The Motion of the Earth and the Detection of Wimps," *Phys.Rev.* **D37** (1988) 1353.

[149] C. J. Copi, J. Heo, and L. M. Krauss, "Directional sensitivity, WIMP detection, and the galactic halo," *Phys.Lett.* **B461** (1999) 43–48, arXiv:hep-ph/9904499 [hep-ph].

[150] C. Savage, K. Freese, and P. Gondolo, "Annual Modulation of Dark Matter in the Presence of Streams," *Phys.Rev.* **D74** (2006) 043531, arXiv:astro-ph/0607121 [astro-ph].

[151] M. J. Lewis and K. Freese, "The Phase of the annual modulation: Constraining the WIMP mass," *Phys.Rev.* **D70** (2004) 043501, arXiv:astro-ph/0307190 [astro-ph].

[152] G. Heusser, "Low-radioactivity background techniques," *Ann.Rev.Nucl.Part.Sci.* **45** (1995) 543–590.

[153] J. Billard, L. Strigari, and E. Figueroa-Feliciano, "Implication of neutrino backgrounds on the reach of next generation dark matter direct detection experiments," *Phys.Rev.* **D89** no. 2, (2014) 023524, arXiv:1307.5458 [hep-ph].

[154] **DAMIC Collaboration** Collaboration, A. A. Aguilar-Arevalo *et al.*, "DAMIC: a novel dark matter experiment," arXiv:1310.6688 [astro-ph.IM].

[155] M. Felizardo, T. Girard, T. Morlat, A. Fernandes, A. Ramos, *et al.*, "Final Analysis and Results of the Phase II SIMPLE Dark Matter Search," *Phys.Rev.Lett.* **108** (2012) 201302, arXiv:1106.3014 [astro-ph.CO].

[156] **COUPP Collaboration** Collaboration, E. Behnke *et al.*, "First Dark Matter Search Results from a 4-kg CF_3I Bubble Chamber Operated in a Deep Underground Site," *Phys.Rev.* **D86** no. 5, (2012) 052001, arXiv:1204.3094 [astro-ph.CO].

[157] D. Y. Akimov, H. Araujo, E. Barnes, V. Belov, A. Bewick, *et al.*, "WIMP-nucleon cross-section results from the second science run of ZEPLIN-III," *Phys.Lett.* **B709** (2012) 14–20, arXiv:1110.4769 [astro-ph.CO].

[158] **EDELWEISS Collaboration** Collaboration, E. Armengaud *et al.*, "Final results of the EDELWEISS-II WIMP search using a 4-kg array of cryogenic germanium detectors with interleaved electrodes," *Phys.Lett.* **B702** (2011) 329–335, arXiv:1103.4070 [astro-ph.CO].

[159] **EDELWEISS Collaboration** Collaboration, E. Armengaud *et al.*, "A search for low-mass WIMPs with EDELWEISS-II heat-and-ionization detectors," *Phys.Rev.* **D86** (2012) 051701, arXiv:1207.1815 [astro-ph.CO].

[160] **CDMS-II Collaboration** Collaboration, Z. Ahmed *et al.*, "Dark Matter Search Results from the CDMS II Experiment," *Science* **327** (2010) 1619–1621, arXiv:0912.3592 [astro-ph.CO].

[161] **CDMS-II Collaboration** Collaboration, Z. Ahmed *et al.*, "Results from a Low-Energy Analysis of the CDMS II Germanium Data," *Phys.Rev.Lett.* **106** (2011) 131302, arXiv:1011.2482 [astro-ph.CO].

[162] **SuperCDMS Collaboration** Collaboration, R. Agnese *et al.*, "Search for Low-Mass Weakly Interacting Massive Particles Using Voltage-Assisted Calorimetric Ionization Detection in the SuperCDMS Experiment," *Phys.Rev.Lett.* **112** no. 4, (2014) 041302, arXiv:1309.3259 [physics.ins-det].

[163] **XENON10 Collaboration** Collaboration, J. Angle *et al.*, "A search for light dark matter in XENON10 data," *Phys.Rev.Lett.* **107** (2011) 051301, arXiv:1104.3088 [astro-ph.CO].

[164] **XENON100 Collaboration** Collaboration, E. Aprile *et al.*, "Dark Matter Results from 225 Live Days of XENON100 Data," *Phys.Rev.Lett.* **109** (2012) 181301, arXiv:1207.5988 [astro-ph.CO].

[165] **CoGeNT Collaboration** Collaboration, C. Aalseth *et al.*, "CoGeNT: A Search for Low-Mass Dark Matter using p-type Point Contact Germanium Detectors," *Phys.Rev.* **D88** no. 1, (2013) 012002, arXiv:1208.5737 [astro-ph.CO].

[166] P. Cushman, C. Galbiati, D. McKinsey, H. Robertson, T. Tait, *et al.*, "Working Group Report: WIMP Dark Matter Direct Detection," arXiv:1310.8327 [hep-ex].

[167] M. Cirelli, "Indirect Searches for Dark Matter: a status review," *Pramana* **79** (2012) 1021–1043, arXiv:1202.1454 [hep-ph].

[168] G. Gelmini and P. Gondolo, "DM Production Mechanisms," arXiv:1009.3690 [astro-ph.CO].

[169] A. Boyarsky, O. Ruchayskiy, and M. Shaposhnikov, "The Role of sterile neutrinos in cosmology and astrophysics," *Ann.Rev.Nucl.Part.Sci.* **59** (2009) 191–214, arXiv:0901.0011 [hep-ph].

[170] L. J. Hall, K. Jedamzik, J. March-Russell, and S. M. West, "Freeze-In Production of FIMP Dark Matter," *JHEP* **1003** (2010) 080, arXiv:0911.1120 [hep-ph].

[171] M. Cirelli, P. Panci, G. Servant, and G. Zaharijas, "Consequences of DM/antiDM Oscillations for Asymmetric WIMP Dark Matter," *JCAP* **1203** (2012) 015, arXiv:1110.3809 [hep-ph].

[172] S. Tulin, H.-B. Yu, and K. M. Zurek, "Oscillating Asymmetric Dark Matter," *JCAP* **1205** (2012) 013, arXiv:1202.0283 [hep-ph].

[173] **PAMELA Collaboration** Collaboration, O. Adriani *et al.*, "An anomalous positron abundance in cosmic rays with energies 1.5-100 GeV," *Nature* **458** (2009) 607–609, arXiv:0810.4995 [astro-ph].

[174] **PAMELA** Collaboration, O. Adriani *et al.*, "Cosmic-Ray Positron Energy Spectrum Measured by PAMELA," *Phys.Rev.Lett.* **111** (2013) 081102, arXiv:1308.0133 [astro-ph.HE].

[175] **HEAT Collaboration** Collaboration, S. Barwick *et al.*, "Measurements of the cosmic ray positron fraction from 1-GeV to 50-GeV," *Astrophys.J.* **482** (1997) L191–L194, arXiv:astro-ph/9703192 [astro-ph].

[176] **AMS-01 Collaboration** Collaboration, M. Aguilar *et al.*, "Cosmic-ray positron fraction measurement from 1 to 30-GeV with AMS-01," *Phys.Lett.* **B646** (2007) 145–154, arXiv:astro-ph/0703154 [ASTRO-PH].

[177] **Fermi LAT Collaboration** Collaboration, M. Ackermann *et al.*, "Measurement of separate cosmic-ray electron and positron spectra with the Fermi Large Area Telescope," *Phys.Rev.Lett.* **108** (2012) 011103, arXiv:1109.0521 [astro-ph.HE].

[178] O. Adriani, G. Barbarino, G. Bazilevskaya, R. Bellotti, M. Boezio, *et al.*, "A new measurement of the antiproton-to-proton flux ratio up to 100 GeV in the cosmic radiation," *Phys.Rev.Lett.* **102** (2009) 051101, arXiv:0810.4994 [astro-ph].

[179] **PAMELA Collaboration** Collaboration, O. Adriani *et al.*, "PAMELA results on the cosmic-ray antiproton flux from 60 MeV to 180 GeV in kinetic energy," *Phys.Rev.Lett.* **105** (2010) 121101, arXiv:1007.0821 [astro-ph.HE].

[180] O. Adriani, G. Bazilevskaya, G. Barbarino, R. Bellotti, M. Boezio, *et al.*, "Measurement of the flux of primary cosmic ray antiprotons with energies of 60-MeV to 350-GeV in the PAMELA experiment," *JETP Lett.* **96** (2013) 621–627.

[181] **Fermi LAT Collaboration** Collaboration, A. A. Abdo *et al.*, "Measurement of the Cosmic Ray e+ plus e- spectrum from 20 GeV to 1 TeV with the Fermi Large Area Telescope," *Phys.Rev.Lett.* **102** (2009) 181101, arXiv:0905.0025 [astro-ph.HE].

[182] **HESS Collaboration** Collaboration, F. Aharonian *et al.*, "The energy spectrum of cosmic-ray electrons at TeV energies," *Phys.Rev.Lett.* **101** (2008) 261104, arXiv:0811.3894 [astro-ph].

[183] **AMS** Collaboration, C. Corti, "The cosmic ray electron and positron spectra measured by AMS-02," arXiv:1402.0437 [physics.ins-det].

[184] G. Giesen, M. Boudaud, Y. Genolini, V. Poulin, M. Cirelli, *et al.*, "AMS-02 antiprotons, at last! Secondary astrophysical component and immediate implications for Dark Matter," arXiv:1504.04276 [astro-ph.HE].

[185] T. Delahaye, F. Donato, N. Fornengo, J. Lavalle, R. Lineros, *et al.*, "Galactic secondary positron flux at the Earth," *Astron.Astrophys.* **501** (2009) 821–833, arXiv:0809.5268 [astro-ph].

[186] P. D. Serpico, "On the possible causes of a rise with energy of the cosmic ray positron fraction," *Phys.Rev.* **D79** (2009) 021302, arXiv:0810.4846 [hep-ph].

[187] P. D. Serpico, "Astrophysical models for the origin of the positron 'excess'," *Astropart.Phys.* **39-40** (2012) 2–11, arXiv:1108.4827 [astro-ph.HE].

[188] M. Cirelli, G. Corcella, A. Hektor, G. Hutsi, M. Kadastik, *et al.*, "PPPC 4 DM ID: A Poor Particle Physicist Cookbook for Dark Matter Indirect Detection," *JCAP* **1103** (2011) 051, arXiv:1012.4515 [hep-ph].

[189] P. Meade, M. Papucci, A. Strumia, and T. Volansky, "Dark Matter Interpretations of the e+- Excesses after FERMI," *Nucl.Phys.* **B831** (2010) 178–203, arXiv:0905.0480 [hep-ph].

[190] M. Cirelli, M. Kadastik, M. Raidal, and A. Strumia, "Model-independent implications of the e+-, anti-proton cosmic ray spectra on properties of Dark Matter," *Nucl.Phys.* **B813** (2009) 1–21, arXiv:0809.2409 [hep-ph].

[191] M. Kachelriess and P. Serpico, "Model-independent dark matter annihilation bound from the diffuse γ ray flux," *Phys.Rev.* **D76** (2007) 063516, arXiv:0707.0209 [hep-ph].

[192] P. Ciafaloni, D. Comelli, A. Riotto, F. Sala, A. Strumia, *et al.*, "Weak Corrections are Relevant for Dark Matter Indirect Detection," *JCAP* **1103** (2011) 019, arXiv:1009.0224 [hep-ph].

[193] P. Ciafaloni, M. Cirelli, D. Comelli, A. De Simone, A. Riotto, *et al.*, "On the Importance of Electroweak Corrections for Majorana Dark Matter Indirect Detection," *JCAP* **1106** (2011) 018, arXiv:1104.2996 [hep-ph].

[194] M. Cirelli and G. Giesen, "Antiprotons from Dark Matter: Current constraints and future sensitivities," *JCAP* **1304** (2013) 015, arXiv:1301.7079 [hep-ph].

[195] A. Abdo, M. Ackermann, M. Ajello, W. Atwood, L. Baldini, *et al.*, "Fermi LAT Search for Photon Lines from 30 to 200 GeV and Dark Matter Implications," *Phys.Rev.Lett.* **104** (2010) 091302, arXiv:1001.4836 [astro-ph.HE].

[196] **LAT Collaboration** Collaboration, M. Ackermann *et al.*, "Fermi LAT Search for Dark Matter in Gamma-ray Lines and the Inclusive Photon Spectrum," *Phys.Rev.* **D86** (2012) 022002, arXiv:1205.2739 [astro-ph.HE].

[197] **Fermi-LAT Collaboration** Collaboration, A. Abdo *et al.*, "Observations of Milky Way Dwarf Spheroidal galaxies with the Fermi-LAT detector and constraints on Dark Matter models," *Astrophys.J.* **712** (2010) 147–158, arXiv:1001.4531 [astro-ph.CO].

[198] **Fermi-LAT collaboration** Collaboration, M. Ackermann *et al.*, "Constraining Dark Matter Models from a Combined Analysis of Milky Way Satellites with the Fermi Large Area Telescope," *Phys.Rev.Lett.* **107** (2011) 241302, arXiv:1108.3546 [astro-ph.HE].

[199] **Fermi-LAT Collaboration** Collaboration, A. Abdo *et al.*, "Constraints on Cosmological Dark Matter Annihilation from the Fermi-LAT Isotropic Diffuse

Gamma-Ray Measurement," *JCAP* **1004** (2010) 014, arXiv:1002.4415 [astro-ph.CO].

[200] M. Ackermann, M. Ajello, A. Allafort, L. Baldini, J. Ballet, *et al.*, "Constraints on Dark Matter Annihilation in Clusters of Galaxies with the Fermi Large Area Telescope," *JCAP* **1005** (2010) 025, arXiv:1002.2239 [astro-ph.CO].

[201] **LAT collaboration** Collaboration, M. Ackermann *et al.*, "Constraints on the Galactic Halo Dark Matter from Fermi-LAT Diffuse Measurements," *Astrophys.J.* **761** (2012) 91, arXiv:1205.6474 [astro-ph.CO].

[202] **Fermi LAT Collaboration** Collaboration, M. Ackermann *et al.*, "Search for Dark Matter Satellites using the FERMI-LAT," *Astrophys.J.* **747** (2012) 121, arXiv:1201.2691 [astro-ph.HE].

[203] **Fermi-LAT Collaboration** Collaboration, A. Cuoco *et al.*, "Anisotropies in the diffuse gamma-ray background measured by Fermi LAT," *Nucl.Instrum.Meth.* **A692** (2012) 127–131, arXiv:1110.1047 [astro-ph.HE].

[204] **HESS Collaboration** Collaboration, F. Aharonian *et al.*, "H.E.S.S. observations of the Galactic Center region and their possible dark matter interpretation," *Phys.Rev.Lett.* **97** (2006) 221102, arXiv:astro-ph/0610509 [astro-ph].

[205] **HESS Collaboration** Collaboration, F. Aharonian *et al.*, "Discovery of very-high-energy gamma-rays from the galactic centre ridge," *Nature* **439** (2006) 695–698, arXiv:astro-ph/0603021 [astro-ph].

[206] **H.E.S.S.Collaboration** Collaboration, A. Abramowski *et al.*, "Search for a Dark Matter annihilation signal from the Galactic Center halo with H.E.S.S," *Phys.Rev.Lett.* **106** (2011) 161301, arXiv:1103.3266 [astro-ph.HE].

[207] **HESS Collaboration** Collaboration, A. Abramowski *et al.*, "H.E.S.S. observations of the globular clusters NGC 6388 and M 15 and search for a Dark Matter signal," *Astrophys.J.* **735** (2011) 12, arXiv:1104.2548 [astro-ph.HE].

[208] **HESS Collaboration** Collaboration, . F. Aharonian, "Observations of the Sagittarius Dwarf galaxy by the H.E.S.S. experiment and search for a Dark Matter signal," *Astropart.Phys.* **29** (2008) 55–62, arXiv:0711.2369 [astro-ph].

[209] **HESS Collaboration** Collaboration, A. Abramowski *et al.*, "H.E.S.S. constraints on Dark Matter annihilations towards the Sculptor and Carina Dwarf Galaxies," *Astropart.Phys.* **34** (2011) 608–616, arXiv:1012.5602 [astro-ph.HE].

[210] **HESS Collaboration** Collaboration, F. Aharonian, "A search for a dark matter annihilation signal towards the Canis Major overdensity with H.E.S.S," *Astrophys.J.* **691** (2009) 175–181, arXiv:0809.3894 [astro-ph].

[211] **HESS** Collaboration, A. Abramowski *et al.*, "Search for Dark Matter Annihilation Signals from the Fornax Galaxy Cluster with H.E.S.S," *Astrophys.J.* **750** (2012) 123, arXiv:1202.5494 [astro-ph.HE].

[212] **HESS Collaboration** Collaboration, F. Aharonian *et al.*, "Search for Gamma-rays from Dark Matter annihilations around Intermediate Mass Black Holes with the H.E.S.S. experiment," *Phys.Rev.* **D78** (2008) 072008, arXiv:0806.2981 [astro-ph].

[213] M. Cirelli, P. Panci, and P. D. Serpico, "Diffuse gamma ray constraints on annihilating or decaying Dark Matter after Fermi," *Nucl.Phys.* **B840** (2010) 284–303, arXiv:0912.0663 [astro-ph.CO].

[214] **IceCube Collaboration** Collaboration, R. Abbasi *et al.*, "The IceCube Neutrino Observatory IV: Searches for Dark Matter and Exotic Particles," arXiv:1111.2738 [astro-ph.HE].

[215] **IceCube Collaboration** Collaboration, R. Abbasi *et al.*, "Search for Dark Matter from the Galactic Halo with the IceCube Neutrino Observatory," *Phys.Rev.* **D84** (2011) 022004, arXiv:1101.3349 [astro-ph.HE].

[216] W. H. Press and D. N. Spergel, "Capture by the sun of a galactic population of weakly interacting massive particles," *Astrophys.J.* **296** (1985) 679–684.

[217] A. Gould, "Resonant Enhancements in WIMP Capture by the Earth," *Astrophys.J.* **321** (1987) 571.

[218] I. Lopes, P. Panci, and J. Silk, "Helioseismology with long range dark matter-baryon interactions," *Astrophys.J.* **795** (2014) 162, arXiv:1402.0682 [astro-ph.SR].

[219] I. Lopes, K. Kadota, and J. Silk, "Constraint on Light Dipole Dark Matter from Helioseismology," *Astrophys.J.Lett.* **780** (2014) L15, arXiv:1310.0673 [astro-ph.SR].

[220] A. C. Vincent, P. Scott, and A. Serenelli, "Possible Indication of Momentum-Dependent Asymmetric Dark Matter in the Sun," *Phys.Rev.Lett.* **114** no. 8, (2015) 081302, arXiv:1411.6626 [hep-ph].

[221] A. C. Vincent, A. Serenelli, and P. Scott, "Generalised form factor dark matter in the Sun," arXiv:1504.04378 [hep-ph].

[222] **SNO Collaboration** Collaboration, Q. Ahmad *et al.*, "Measurement of the rate of $\nu_e + d \to p + p + e^-$ interactions produced by ^8B solar neutrinos at the Sudbury Neutrino Observatory," *Phys.Rev.Lett.* **87** (2001) 071301, arXiv:nucl-ex/0106015 [nucl-ex].

[223] D. Seckel, T. Stanev, and T. K. Gaisser, "Signatures of cosmic-ray interactions on the solar surface," *ApJ* **382** (Dec., 1991) 652–666.

[224] **ICECUBE Collaboration** Collaboration, R. Abbasi *et al.*, "Limits on a muon flux from neutralino annihilations in the Sun with the IceCube 22-string detector," *Phys.Rev.Lett.* **102** (2009) 201302, arXiv:0902.2460 [astro-ph.CO].

[225] G. Wikström and J. Edsjö, "Limits on the WIMP-nucleon scattering cross-section from neutrino telescopes," *JCAP* **4** (Apr., 2009) 9, arXiv:0903.2986 [astro-ph.CO].

[226] M. Blennow, J. Edsjo, and T. Ohlsson, "Neutrinos from WIMP annihilations using a full three-flavor Monte Carlo," *JCAP* **0801** (2008) 021, arXiv:0709.3898 [hep-ph].

[227] T. Bruch, A. H. Peter, J. Read, L. Baudis, and G. Lake, "Dark Matter Disc Enhanced Neutrino Fluxes from the Sun and Earth," *Phys.Lett.* **B674** (2009) 250–256, arXiv:0902.4001 [astro-ph.HE].

[228] A. Gould, "Gravitational diffusion of solar system WIMPs," *ApJ* **368** (Feb., 1991) 610–615.

[229] **Super-Kamiokande Collaboration** Collaboration, S. Desai *et al.*, "Search for dark matter WIMPs using upward through-going muons in Super-Kamiokande," *Phys.Rev.* **D70** (2004) 083523, arXiv:hep-ex/0404025 [hep-ex].

[230] **IceCube Collaboration** Collaboration, R. Abbasi *et al.*, "Multi-year search for dark matter annihilations in the Sun with the AMANDA-II and IceCube detectors," *Phys.Rev.* **D85** (2012) 042002, arXiv:1112.1840 [astro-ph.HE].

[231] **IceCube collaboration** Collaboration, M. Aartsen *et al.*, "Search for dark matter annihilations in the Sun with the 79-string IceCube detector," *Phys.Rev.Lett.* **110** no. 13, (2013) 131302, arXiv:1212.4097 [astro-ph.HE].

[232] **Super-Kamiokande Collaboration** Collaboration, T. Tanaka *et al.*, "An Indirect Search for WIMPs in the Sun using 3109.6 days of upward-going muons in Super-Kamiokande," *Astrophys.J.* **742** (2011) 78, arXiv:1108.3384 [astro-ph.HE].

[233] **Super-Kamiokande** Collaboration, K. Choi *et al.*, "Search for neutrinos from annihilation of captured low-mass dark matter particles in the Sun by Super-Kamiokande," *Phys.Rev.Lett.* **114** no. 14, (2015) 141301, arXiv:1503.04858 [hep-ex].

[234] **ANTARES Collaboration** Collaboration, S. Adrian-Martinez *et al.*, "First results on dark matter annihilation in the Sun using the ANTARES neutrino telescope," *JCAP* **1311** (2013) 032, arXiv:1302.6516 [astro-ph.HE].

[235] **ANTARES** Collaboration, P. Fermani, "Indirect Dark Matter search with large neutrino telescopes," *Frascati Phys.Ser.* **56** (2012) 244–257, arXiv:1307.2402 [astro-ph.HE].

[236] **ANTARES** Collaboration, J. Zornoza and G. Lambard, "Results and prospects of dark matter searches with ANTARES," *Nucl.Instrum.Meth.* **A742** (2014) 173–176, arXiv:1404.0148 [astro-ph.HE].

[237] M. Boliev, S. Demidov, S. Mikheyev, and O. Suvorova, "Search for muon signal from dark matter annihilations inthe Sun with the Baksan Underground Scintillator Telescope for 24.12 years," *JCAP* **1309** (2013) 019, arXiv:1301.1138 [astro-ph.HE].

[238] **ATLAS Collaboration** Collaboration, G. Aad *et al.*, "Search for dark matter candidates and large extra dimensions in events with a jet and missing transverse momentum with the ATLAS detector," *JHEP* **1304** (2013) 075, arXiv:1210.4491 [hep-ex].

[239] **CMS Collaboration** Collaboration, S. Chatrchyan *et al.*, "Search for New Physics with a Mono-Jet and Missing Transverse Energy in pp Collisions at $\sqrt{s} = 7$ TeV," *Phys.Rev.Lett.* **107** (2011) 201804, arXiv:1106.4775 [hep-ex].

[240] **ATLAS Collaboration** Collaboration, T. A. collaboration, "Search for New Phenomena in Monojet plus Missing Transverse Momentum Final States using 10fb-1 of pp Collisions at sqrts=8 TeV with the ATLAS detector at the LHC,".

[241] **CMS Collaboration** Collaboration, S. Chatrchyan *et al.*, "Search for new physics in monojet events in pp collisions at sqrt(s)= 8 TeV,".

[242] **ATLAS Collaboration** Collaboration, G. Aad *et al.*, "Jet energy measurement with the ATLAS detector in proton-proton collisions at $\sqrt{s} = 7$ TeV," *Eur.Phys.J.* **C73** no. 3, (2013) 2304, arXiv:1112.6426 [hep-ex].

[243] **ATLAS** Collaboration, G. Aad *et al.*, "Luminosity Determination in pp Collisions at $\sqrt{s} = 7$ TeV Using the ATLAS Detector at the LHC," *Eur.Phys.J.* **C71** (2011) 1630, arXiv:1101.2185 [hep-ex].

[244] **ATLAS** Collaboration, T. A. collaboration, "Luminosity Determination in pp Collisions at sqrt(s) = 7 TeV using the ATLAS Detector in 2011,".

[245] J. Goodman, M. Ibe, A. Rajaraman, W. Shepherd, T. M. Tait, *et al.*, "Constraints on Dark Matter from Colliders," *Phys.Rev.* **D82** (2010) 116010, arXiv:1008.1783 [hep-ph].

[246] G. Busoni, A. De Simone, and W.-C. Huang, "On the Minimum Dark Matter Mass Testable by Neutrinos from the Sun," *JCAP* **1307** (2013) 010, arXiv:1305.1817 [hep-ph].

[247] V. Pettorino, G. Busoni, A. De Simone, E. Morgante, A. Riotto, *et al.*, "Can AMS-02 discriminate the origin of an anti-proton signal?," *JCAP* **1410** no. 10, (2014) 078, arXiv:1406.5377 [hep-ph].

[248] G. Busoni, A. De Simone, E. Morgante, and A. Riotto, "On the Validity of the Effective Field Theory for Dark Matter Searches at the LHC," *Phys.Lett.* **B728** (2014) 412–421, arXiv:1307.2253 [hep-ph].

[249] G. Busoni, A. De Simone, J. Gramling, E. Morgante, and A. Riotto, "On the Validity of the Effective Field Theory for Dark Matter Searches at the LHC, Part II: Complete Analysis for the s-channel," *JCAP* **1406** (2014) 060, arXiv:1402.1275 [hep-ph].

[250] G. Busoni, A. De Simone, T. Jacques, E. Morgante, and A. Riotto, "On the Validity of the Effective Field Theory for Dark Matter Searches at the LHC Part III: Analysis for the t-channel," arXiv:1405.3101 [hep-ph].

[251] J. Abdallah, A. Ashkenazi, A. Boveia, G. Busoni, A. De Simone, *et al.*, "Simplified Models for Dark Matter and Missing Energy Searches at the LHC," arXiv:1409.2893 [hep-ph].

[252] G. Busoni, A. De Simone, T. Jacques, E. Morgante, and A. Riotto, "Making the Most of the Relic Density for Dark Matter Searches at the LHC 14 TeV Run," *JCAP* **1503** no. 03, (2015) 022, arXiv:1410.7409 [hep-ph].

[253] C. Rott, J. M. Siegal-Gaskins, and J. F. Beacom, "New sensitivity to solar WIMP annihilation using low-energy neutrinos," *Phys.Rev.D* **88** no. 5, (Sept., 2013) 055005, arXiv:1208.0827 [astro-ph.HE].

[254] N. Bernal, J. Martín-Albo, and S. Palomares-Ruiz, "A novel way of constraining WIMPs annihilations in the Sun: MeV neutrinos," *JCAP* **1308** (2013) 011, arXiv:1208.0834 [hep-ph].

[255] P. Vogel and J. F. Beacom, "Angular distribution of neutron inverse beta decay, anti-neutrino(e) + p —¿ e+ + n," *Phys.Rev.* **D60** (1999) 053003, arXiv:hep-ph/9903554 [hep-ph].

[256] H. Yuksel, S. Horiuchi, J. F. Beacom, and S. Ando, "Neutrino Constraints on the Dark Matter Total Annihilation Cross Section," *Phys.Rev.* **D76** (2007) 123506, arXiv:0707.0196 [astro-ph].

[257] S. Palomares-Ruiz and S. Pascoli, "Testing MeV dark matter with neutrino detectors," *Phys.Rev.* **D77** (2008) 025025, arXiv:0710.5420 [astro-ph].

[258] D. E. Kaplan, M. A. Luty, and K. M. Zurek, "Asymmetric Dark Matter," *Phys.Rev.* **D79** (2009) 115016, arXiv:0901.4117 [hep-ph].

[259] R. Allahverdi and B. Dutta, "Natural GeV Dark Matter and the Baryon-Dark Matter Coincidence Puzzle," *Phys.Rev.* **D88** no. 2, (2013) 023525, arXiv:1304.0711 [hep-ph].

[260] J. Kumar, J. G. Learned, S. Smith, and K. Richardson, "Tools for Studying Low-Mass Dark Matter at Neutrino Detectors," *Phys.Rev.* **D86** (2012) 073002, arXiv:1204.5120 [hep-ph].

[261] K. Griest and D. Seckel, "Cosmic Asymmetry, Neutrinos and the Sun," *Nucl.Phys.* **B283** (1987) 681.

[262] A. M. Serenelli, S. Basu, J. W. Ferguson, and M. Asplund, "New Solar Composition: The Problem with Solar Models Revisited," *ApJ* **705** (Nov., 2009) L123–L127, arXiv:0909.2668 [astro-ph.SR].

[263] R. Kappl and M. W. Winkler, "New Limits on Dark Matter from Super-Kamiokande," *Nucl.Phys.* **B850** (2011) 505–521, arXiv:1104.0679 [hep-ph].

[264] P. Gondolo and G. Gelmini, "Cosmic abundances of stable particles: Improved analysis," *Nucl.Phys.* **B360** (1991) 145–179.

[265] A. Gould, "WIMP Distribution in and Evaporation From the Sun," *Astrophys.J.* **321** (1987) 560.

[266] G. Eder, *Nuclear Forces: Introduction to Theoretical Nuclear Physics.* M.I.T. Press, 1968.

[267] R. H. Helm, "Inelastic and Elastic Scattering of 187-Mev Electrons from Selected Even-Even Nuclei," *Phys.Rev.* **104** (1956) 1466–1475.

[268] G. Duda, A. Kemper, and P. Gondolo, "Model Independent Form Factors for Spin Independent Neutralino-Nucleon Scattering from Elastic Electron Scattering Data," *JCAP* **0704** (2007) 012, arXiv:hep-ph/0608035 [hep-ph].

[269] A. Gould, "EVAPORATION OF WIMPs WITH ARBITRARY CROSS-SECTIONS," *Astrophys. J.* **356** (1990) 302–309.

[270] R. L. Gilliland, J. Faulkner, W. H. Press, and D. N. Spergel, "Solar models with energy transport by weakly interacting particles," *ApJ* **306** (July, 1986) 703–709.

[271] M. Nauenberg, "Energy Transport and Evaporation of Weakly Interacting Particles in the Sun," *Phys.Rev.* **D36** (1987) 1080.

[272] **AMS Collaboration** Collaboration, M. Aguilar *et al.*, "First Result from the Alpha Magnetic Spectrometer on the International Space Station: Precision Measurement of the Positron Fraction in Primary Cosmic Rays of 0.5-350 GeV," *Phys.Rev.Lett.* **110** (2013) 141102.

[273] A. R. Bell, "The Acceleration of cosmic rays in shock fronts. I," *Mon.Not.Roy.Astron.Soc.* **182** (1978) 147–156.

[274] R. Blandford and D. Eichler, "Particle Acceleration at Astrophysical Shocks: A Theory of Cosmic Ray Origin," *Phys.Rept.* **154** (1987) 1–75.

[275] A. Berlin, P. Gratia, D. Hooper, and S. D. McDermott, "Hidden Sector Dark Matter Models for the Galactic Center Gamma-Ray Excess," *Phys.Rev.* **D90** no. 1, (2014) 015032, arXiv:1405.5204 [hep-ph].

[276] M. Cirelli, "Indirect Searches for Dark Matter: a status review," *Pramana* **79** (2012) 1021–1043, arXiv:1202.1454 [hep-ph].

[277] A. De Simone, A. Riotto, and W. Xue, "Interpretation of AMS-02 Results: Correlations among Dark Matter Signals," *JCAP* **1305** (2013) 003, arXiv:1304.1336 [hep-ph].

[278] N. Fornengo, L. Maccione, and A. Vittino, "Constraints on particle dark matter from cosmic-ray antiprotons," *JCAP* **1404** (2014) 003, arXiv:1312.3579 [hep-ph].

[279] P. Ciafaloni, M. Cirelli, D. Comelli, A. De Simone, A. Riotto, *et al.*, "Initial State Radiation in Majorana Dark Matter Annihilations," *JCAP* **1110** (2011) 034, arXiv:1107.4453 [hep-ph].

[280] P. Ciafaloni, D. Comelli, A. De Simone, A. Riotto, and A. Urbano, "Electroweak Bremsstrahlung for Wino-Like Dark Matter Annihilations," *JCAP* **1206** (2012) 016, arXiv:1202.0692 [hep-ph].

[281] J. Lavalle, J. Pochon, P. Salati, and R. Taillet, "Clumpiness of dark matter and positron annihilation signal: computing the odds of the galactic lottery," *Astron.Astrophys.* **462** (2007) 827–848, arXiv:astro-ph/0603796 [astro-ph].

[282] J. Lavalle, Q. Yuan, D. Maurin, and X. Bi, "Full Calculation of Clumpiness Boost factors for Antimatter Cosmic Rays in the light of Lambda-CDM N-body simulation results. Abandoning hope in clumpiness enhancement?," *Astron.Astrophys.* **479** (2008) 427–452, arXiv:0709.3634 [astro-ph].

[283] M. Ibe, H. Murayama, and T. Yanagida, "Breit-Wigner Enhancement of Dark Matter Annihilation," *Phys.Rev.* **D79** (2009) 095009, arXiv:0812.0072 [hep-ph].

[284] D. Feldman, Z. Liu, and P. Nath, "PAMELA Positron Excess as a Signal from the Hidden Sector," *Phys.Rev.* **D79** (2009) 063509, arXiv:0810.5762 [hep-ph].

[285] A. Sommerfeld, "Über die beugung und bremsung der elektronen," *Annalen der Physik* **403** no. 3, (1931) 257–330. http://dx.doi.org/10.1002/andp.19314030302.

[286] J. Hisano, S. Matsumoto, and M. M. Nojiri, "Explosive dark matter annihilation," *Phys.Rev.Lett.* **92** (2004) 031303, arXiv:hep-ph/0307216 [hep-ph].

[287] J. Hisano, S. Matsumoto, M. M. Nojiri, and O. Saito, "Non-perturbative effect on dark matter annihilation and gamma ray signature from galactic center," *Phys.Rev.* **D71** (2005) 063528, arXiv:hep-ph/0412403 [hep-ph].

[288] J. Hisano, S. Matsumoto, M. Nagai, O. Saito, and M. Senami, "Non-perturbative effect on thermal relic abundance of dark matter," *Phys.Lett.* **B646** (2007) 34–38, arXiv:hep-ph/0610249 [hep-ph].

[289] M. Cirelli, A. Strumia, and M. Tamburini, "Cosmology and Astrophysics of Minimal Dark Matter," *Nucl.Phys.* **B787** (2007) 152–175, arXiv:0706.4071 [hep-ph].

[290] M. Cirelli, R. Franceschini, and A. Strumia, "Minimal Dark Matter predictions for galactic positrons, anti-protons, photons," *Nucl.Phys.* **B800** (2008) 204–220, arXiv:0802.3378 [hep-ph].

[291] N. Arkani-Hamed, D. P. Finkbeiner, T. R. Slatyer, and N. Weiner, "A Theory of Dark Matter," *Phys.Rev.* **D79** (2009) 015014, arXiv:0810.0713 [hep-ph].

[292] M. Lattanzi and J. I. Silk, "Can the WIMP annihilation boost factor be boosted by the Sommerfeld enhancement?," *Phys.Rev.* **D79** (2009) 083523, arXiv:0812.0360 [astro-ph].

[293] F. Aharonian, A. Atoyan, and H. Volk, "High energy electrons and positrons in cosmic rays as an indicator of the existence of a nearby cosmic tevatron," *Astron.Astrophys.* **294** (1995) L41–L44.

[294] D. Hooper, P. Blasi, and P. D. Serpico, "Pulsars as the Sources of High Energy Cosmic Ray Positrons," *JCAP* **0901** (2009) 025, arXiv:0810.1527 [astro-ph].

[295] **FERMI-LAT Collaboration** Collaboration, D. Grasso *et al.*, "On possible interpretations of the high energy electron-positron spectrum measured by the Fermi Large Area Telescope," *Astropart.Phys.* **32** (2009) 140–151, arXiv:0905.0636 [astro-ph.HE].

[296] M. Pato, M. Lattanzi, and G. Bertone, "Discriminating the source of high-energy positrons with AMS-02," *JCAP* **1012** (2010) 020, arXiv:1010.5236 [astro-ph.HE].

[297] P. Blasi, "The origin of the positron excess in cosmic rays," *Phys.Rev.Lett.* **103** (2009) 051104, arXiv:0903.2794 [astro-ph.HE].

[298] P. Blasi and P. D. Serpico, "High-energy antiprotons from old supernova remnants," *Phys.Rev.Lett.* **103** (2009) 081103, arXiv:0904.0871 [astro-ph.HE].

[299] M. Kachelriess, S. Ostapchenko, and R. Tomas, "Antimatter production in supernova remnants," *Astrophys.J.* **733** (2011) 119, arXiv:1103.5765 [astro-ph.HE].

[300] L. Tan and L. Ng, "PARAMETRIZATION OF ANTI-P INVARIANT CROSS-SECTION IN P P COLLISIONS USING A NEW SCALING VARIABLE," *Phys.Rev.* **D26** (1982) 1179–1182.

[301] L. Tan and L. Ng, "CALCULATION OF THE EQUILIBRIUM ANTI-PROTON SPECTRUM," *J.Phys.* **G9** (1983) 227–242.

[302] T. Bringmann and P. Salati, "The galactic antiproton spectrum at high energies: Background expectation vs. exotic contributions," *Phys.Rev.* **D75** (2007) 083006, arXiv:astro-ph/0612514 [astro-ph].

[303] C. Evoli, I. Cholis, D. Grasso, L. Maccione, and P. Ullio, "Antiprotons from dark matter annihilation in the Galaxy: astrophysical uncertainties," *Phys.Rev.* **D85** (2012) 123511, arXiv:1108.0664 [astro-ph.HE].

[304] C. Evoli, D. Gaggero, D. Grasso, and L. Maccione, "Cosmic-Ray Nuclei, Antiprotons and Gamma-rays in the Galaxy: a New Diffusion Model," *JCAP* **0810** (2008) 018, arXiv:0807.4730 [astro-ph].

[305] J. F. Navarro, C. S. Frenk, and S. D. White, "The Structure of cold dark matter halos," *Astrophys.J.* **462** (1996) 563–575, arXiv:astro-ph/9508025 [astro-ph].

[306] **Fermi-LAT Collaboration** Collaboration, M. Ackermann *et al.*, "Dark matter constraints from observations of 25 Milky Way satellite galaxies with the Fermi Large Area Telescope," *Phys.Rev.* **D89** no. 4, (2014) 042001, arXiv:1310.0828 [astro-ph.HE].

[307] S. Ting, "slides of the talk at spacepart12, cern," 5-7 november, 2012. http://indico.cern.ch/event/197799/page/1.

[308] M. Pato, D. Hooper, and M. Simet, "Pinpointing Cosmic Ray Propagation With The AMS-02 Experiment," *JCAP* **1006** (2010) 022, arXiv:1002.3341 [astro-ph.HE].

[309] I. Cholis and D. Hooper, "Constraining the origin of the rising cosmic ray positron fraction with the boron-to-carbon ratio," *Phys.Rev.* **D89** no. 4, (2014) 043013, arXiv:1312.2952 [astro-ph.HE].

[310] M. Beltran, D. Hooper, E. W. Kolb, Z. A. Krusberg, and T. M. Tait, "Maverick dark matter at colliders," *JHEP* **1009** (2010) 037, arXiv:1002.4137 [hep-ph].

[311] J. Goodman, M. Ibe, A. Rajaraman, W. Shepherd, T. M. Tait, *et al.*, "Constraints on Light Majorana dark Matter from Colliders," *Phys.Lett.* **B695** (2011) 185–188, arXiv:1005.1286 [hep-ph].

[312] A. Rajaraman, W. Shepherd, T. M. Tait, and A. M. Wijangco, "LHC Bounds on Interactions of Dark Matter," *Phys.Rev.* **D84** (2011) 095013, arXiv:1108.1196 [hep-ph].

[313] P. J. Fox, R. Harnik, J. Kopp, and Y. Tsai, "Missing Energy Signatures of Dark Matter at the LHC," *Phys.Rev.* **D85** (2012) 056011, arXiv:1109.4398 [hep-ph].

[314] H. Dreiner, M. Huck, M. Krämer, D. Schmeier, and J. Tattersall, "Illuminating Dark Matter at the ILC," *Phys.Rev.* **D87** no. 7, (2013) 075015, arXiv:1211.2254 [hep-ph].

[315] Y. J. Chae and M. Perelstein, "Dark Matter Search at a Linear Collider: Effective Operator Approach," *JHEP* **1305** (2013) 138, arXiv:1211.4008 [hep-ph].

[316] A. De Simone, A. Monin, A. Thamm, and A. Urbano, "On the effective operators for Dark Matter annihilations," *JCAP* **1302** (2013) 039, arXiv:1301.1486 [hep-ph].

[317] H. Dreiner, D. Schmeier, and J. Tattersall, "Contact Interactions Probe Effective Dark Matter Models at the LHC," *Europhys.Lett.* **102** (2013) 51001, arXiv:1303.3348 [hep-ph].

[318] J.-Y. Chen, E. W. Kolb, and L.-T. Wang, "Dark matter coupling to electroweak gauge and Higgs bosons: an effective field theory approach," *Phys.Dark Univ.* **2** (2013) 200–218, arXiv:1305.0021 [hep-ph].

[319] O. Buchmueller, M. J. Dolan, and C. McCabe, "Beyond Effective Field Theory for Dark Matter Searches at the LHC," *JHEP* **1401** (2014) 025, arXiv:1308.6799 [hep-ph].

[320] H. Dreiner, M. Huck, M. Krämer, D. Schmeier, and J. Tattersall, "Illuminating Dark Matter at the ILC," *Phys.Rev.* **D87** no. 7, (2013) 075015, arXiv:1211.2254 [hep-ph].

[321] R. Cotta, J. Hewett, M. Le, and T. Rizzo, "Bounds on Dark Matter Interactions with Electroweak Gauge Bosons," *Phys.Rev.* **D88** (2013) 116009, arXiv:1210.0525 [hep-ph].

[322] P. J. Fox and C. Williams, "Next-to-Leading Order Predictions for Dark Matter Production at Hadron Colliders," *Phys.Rev.* **D87** no. 5, (2013) 054030, arXiv:1211.6390 [hep-ph].

[323] H. An, X. Ji, and L.-T. Wang, "Light Dark Matter and Z' Dark Force at Colliders," *JHEP* **1207** (2012) 182, arXiv:1202.2894 [hep-ph].

[324] I. M. Shoemaker and L. Vecchi, "Unitarity and Monojet Bounds on Models for DAMA, CoGeNT, and CRESST-II," *Phys.Rev.* **D86** (2012) 015023, arXiv:1112.5457 [hep-ph].

[325] P. J. Fox, R. Harnik, J. Kopp, and Y. Tsai, "LEP Shines Light on Dark Matter," *Phys.Rev.* **D84** (2011) 014028, arXiv:1103.0240 [hep-ph].

[326] A. Martin, W. Stirling, R. Thorne, and G. Watt, "Parton distributions for the LHC," *Eur.Phys.J.* **C63** (2009) 189–285, arXiv:0901.0002 [hep-ph].

[327] S. Alekhin, S. Alioli, R. D. Ball, V. Bertone, J. Blumlein, *et al.*, "The PDF4LHC Working Group Interim Report," arXiv:1101.0536 [hep-ph].

[328] R. Barbieri, G. Isidori, J. Jones-Perez, P. Lodone, and D. M. Straub, "$U(2)$ and Minimal Flavour Violation in Supersymmetry," *Eur.Phys.J.* **C71** (2011) 1725, arXiv:1105.2296 [hep-ph].

[329] R. Barbieri, D. Buttazzo, F. Sala, and D. M. Straub, "Flavour physics from an approximate $U(2)^3$ symmetry," *JHEP* **1207** (2012) 181, arXiv:1203.4218 [hep-ph].

[330] J. Alwall, M. Herquet, F. Maltoni, O. Mattelaer, and T. Stelzer, "MadGraph 5 : Going Beyond," *JHEP* **1106** (2011) 128, arXiv:1106.0522 [hep-ph].

[331] T. A. collaboration, "Sensitivity to WIMP Dark Matter in the Final States Containing Jets and Missing Transverse Momentum with the ATLAS Detector at 14 TeV LHC," Tech. Rep. ATL-PHYS-PUB-2014-007, CERN, Geneva, Jun, 2014.

[332] N. F. Bell, J. B. Dent, A. J. Galea, T. D. Jacques, L. M. Krauss, *et al.*, "Searching for Dark Matter at the LHC with a Mono-Z," *Phys.Rev.* **D86** (2012) 096011, arXiv:1209.0231 [hep-ph].

[333] **ATLAS Collaboration** Collaboration, G. Aad *et al.*, "Search for dark matter in events with a Z boson and missing transverse momentum in pp collisions at $\sqrt{s}$=8 TeV with the ATLAS detector," *Phys.Rev.* **D90** no. 1, (2014) 012004, arXiv:1404.0051 [hep-ex].

[334] S. Chang, R. Edezhath, J. Hutchinson, and M. Luty, "Effective WIMPs," *Phys.Rev.* **D89** no. 1, (2014) 015011, arXiv:1307.8120 [hep-ph].

[335] H. An, L.-T. Wang, and H. Zhang, "Dark matter with t-channel mediator: a simple step beyond contact interaction," *Phys.Rev.* **D89** no. 11, (2014) 115014, arXiv:1308.0592 [hep-ph].

[336] Y. Bai and J. Berger, "Fermion Portal Dark Matter," *JHEP* **1311** (2013) 171, arXiv:1308.0612 [hep-ph].

[337] A. DiFranzo, K. I. Nagao, A. Rajaraman, and T. M. Tait, "Simplified Models for Dark Matter Interacting with Quarks," *JHEP* **1311** (2013) 014, arXiv:1308.2679 [hep-ph].

[338] M. Papucci, A. Vichi, and K. M. Zurek, "Monojet versus the rest of the world I: t-channel models," *JHEP* **1411** (2014) 024, arXiv:1402.2285 [hep-ph].

[339] M. Garny, A. Ibarra, S. Rydbeck, and S. Vogl, "Majorana Dark Matter with a Coloured Mediator: Collider vs Direct and Indirect Searches," *JHEP* **1406** (2014) 169, arXiv:1403.4634 [hep-ph].

[340] N. F. Bell, J. B. Dent, T. D. Jacques, and T. J. Weiler, "W/Z Bremsstrahlung as the Dominant Annihilation Channel for Dark Matter," *Phys.Rev.* **D83** (2011) 013001, arXiv:1009.2584 [hep-ph].

[341] A. Martin, W. Stirling, R. Thorne, and G. Watt, "Parton distributions for the LHC," 2009. http://mstwpdf.hepforge.org/.

[342] G. Bertone, D. Hooper, and J. Silk, "Particle dark matter: Evidence, candidates and constraints," *Phys.Rept.* **405** (2005) 279–390, arXiv:hep-ph/0404175 [hep-ph].

[343] N. D. Christensen and C. Duhr, "FeynRules - Feynman rules made easy," *Comput.Phys.Commun.* **180** (2009) 1614–1641, arXiv:0806.4194 [hep-ph].

[344] J. Pumplin, D. Stump, J. Huston, H. Lai, P. M. Nadolsky, *et al.*, "New generation of parton distributions with uncertainties from global QCD analysis," *JHEP* **0207** (2002) 012, arXiv:hep-ph/0201195 [hep-ph].

[345] D. Chung, L. Everett, G. Kane, S. King, J. D. Lykken, *et al.*, "The Soft supersymmetry breaking Lagrangian: Theory and applications," *Phys.Rept.* **407** (2005) 1–203, arXiv:hep-ph/0312378 [hep-ph].

[346] M. Schmaltz and D. Tucker-Smith, "Little Higgs review," *Ann.Rev.Nucl.Part.Sci.* **55** (2005) 229–270, arXiv:hep-ph/0502182 [hep-ph].

[347] **ATLAS** Collaboration, G. Aad *et al.*, "Search for supersymmetry at $\sqrt{s}$=8 TeV in final states with jets and two same-sign leptons or three leptons with the ATLAS detector," *JHEP* **1406** (2014) 035, arXiv:1404.2500 [hep-ex].

[348] **ATLAS Collaboration** Collaboration, G. Aad *et al.*, "Search for new phenomena with the monojet and missing transverse momentum signature using the ATLAS detector in $\sqrt{s} = 7$ TeV proton-proton collisions," *Phys.Lett.* **B705** (2011) 294–312, arXiv:1106.5327 [hep-ex].

[349] **CMS** Collaboration, S. Chatrchyan *et al.*, "Search for dark matter and large extra dimensions in monojet events in pp collisions at $\sqrt{s} = 7$ TeV," *JHEP* **1209** (2012) 094, arXiv:1206.5663 [hep-ex].

[350] **ATLAS** Collaboration, J. Abdallah, "Searches for monojets and monophotons with the ATLAS detector," *EPJ Web Conf.* **60** (2013) 17004.

[351] U. Haisch, F. Kahlhoefer, and E. Re, "QCD effects in mono-jet searches for dark matter," *JHEP* **1312** (2013) 007, arXiv:1310.4491 [hep-ph].

[352] Q.-H. Cao, C.-R. Chen, C. S. Li, and H. Zhang, "Effective Dark Matter Model: Relic density, CDMS II, Fermi LAT and LHC," *JHEP* **1108** (2011) 018, arXiv:0912.4511 [hep-ph].

[353] K. Cheung, P.-Y. Tseng, and T.-C. Yuan, "Cosmic Antiproton Constraints on Effective Interactions of the Dark Matter," *JCAP* **1101** (2011) 004, arXiv:1011.2310 [hep-ph].

[354] J.-M. Zheng, Z.-H. Yu, J.-W. Shao, X.-J. Bi, Z. Li, *et al.*, "Constraining the interaction strength between dark matter and visible matter: I. fermionic dark matter," *Nucl.Phys.* **B854** (2012) 350–374, arXiv:1012.2022 [hep-ph].

[355] K. Cheung, P.-Y. Tseng, and T.-C. Yuan, "Gamma-ray Constraints on Effective Interactions of the Dark Matter," *JCAP* **1106** (2011) 023, arXiv:1104.5329 [hep-ph].

[356] Z.-H. Yu, J.-M. Zheng, X.-J. Bi, Z. Li, D.-X. Yao, *et al.*, "Constraining the interaction strength between dark matter and visible matter: II. scalar, vector and spin-3/2 dark matter," *Nucl.Phys.* **B860** (2012) 115–151, arXiv:1112.6052 [hep-ph].

[357] J. Fan, M. Reece, and L.-T. Wang, "Non-relativistic effective theory of dark matter direct detection," *JCAP* **1011** (2010) 042, arXiv:1008.1591 [hep-ph].

[358] A. L. Fitzpatrick, W. Haxton, E. Katz, N. Lubbers, and Y. Xu, "The Effective Field Theory of Dark Matter Direct Detection," *JCAP* **1302** (2013) 004, arXiv:1203.3542 [hep-ph].

[359] **CDF** Collaboration, T. Aaltonen *et al.*, "A Search for dark matter in events with one jet and missing transverse energy in $p\bar{p}$ collisions at $\sqrt{s} = 1.96$ TeV," *Phys.Rev.Lett.* **108** (2012) 211804, arXiv:1203.0742 [hep-ex].

[360] N. Weiner and I. Yavin, "How Dark Are Majorana WIMPs? Signals from MiDM and Rayleigh Dark Matter," *Phys.Rev.* **D86** (2012) 075021, arXiv:1206.2910 [hep-ph].

[361] N. Arkani-Hamed, P. Schuster, N. Toro, J. Thaler, L.-T. Wang, *et al.*, "MARMOSET: The Path from LHC Data to the New Standard Model via On-Shell Effective Theories," arXiv:hep-ph/0703088 [HEP-PH].

[362] J. Alwall, P. Schuster, and N. Toro, "Simplified Models for a First Characterization of New Physics at the LHC," *Phys.Rev.* **D79** (2009) 075020, arXiv:0810.3921 [hep-ph].

[363] **LHC New Physics Working Group** Collaboration, D. Alves *et al.*, "Simplified Models for LHC New Physics Searches," *J.Phys.* **G39** (2012) 105005, arXiv:1105.2838 [hep-ph].

[364] P. Salati, "Indirect and direct dark matter detection," *PoS* **CARGESE2007** (2007) 009.

[365] O. Buchmueller, M. J. Dolan, S. A. Malik, and C. McCabe, "Characterising dark matter searches at colliders and direct detection experiments: Vector mediators," *JHEP* **1501** (2015) 037, arXiv:1407.8257 [hep-ph].

[366] J. Goodman and W. Shepherd, "LHC Bounds on UV-Complete Models of Dark Matter," arXiv:1111.2359 [hep-ph].

[367] M. Abdullah, A. DiFranzo, A. Rajaraman, T. M. Tait, P. Tanedo, *et al.*, "Hidden on-shell mediators for the Galactic Center γ-ray excess," *Phys.Rev.* **D90** no. 3, (2014) 035004, arXiv:1404.6528 [hep-ph].

[368] G. Isidori, Y. Nir, and G. Perez, "Flavor Physics Constraints for Physics Beyond the Standard Model," *Ann.Rev.Nucl.Part.Sci.* **60** (2010) 355, arXiv:1002.0900 [hep-ph].

[369] D. Tucker-Smith and N. Weiner, "Inelastic dark matter," *Phys.Rev.* **D64** (2001) 043502, arXiv:hep-ph/0101138 [hep-ph].

[370] **ATLAS** Collaboration, G. Aad *et al.*, "Search for New Physics in the Dijet Mass Distribution using 1 fb^{-1} of pp Collision Data at $\sqrt{s} = 7$ TeV collected by the ATLAS Detector," *Phys.Lett.* **B708** (2012) 37–54, arXiv:1108.6311 [hep-ex].

[371] **ATLAS** Collaboration, G. Aad *et al.*, "Search for new phenomena in the dijet mass distribution using $p - p$ collision data at $\sqrt{s} = 8$ TeV with the ATLAS detector," *Phys.Rev.* **D91** no. 5, (2015) 052007, arXiv:1407.1376 [hep-ex].

[372] **CMS** Collaboration, S. Chatrchyan *et al.*, "Search for quark compositeness in dijet angular distributions from pp collisions at $\sqrt{s} = 7$ TeV," *JHEP* **1205** (2012) 055, arXiv:1202.5535 [hep-ex].

[373] **ATLAS** Collaboration, G. Aad *et al.*, "Search for New Physics in Dijet Mass and Angular Distributions in pp Collisions at $\sqrt{s} = 7$ TeV Measured with the ATLAS Detector," *New J.Phys.* **13** (2011) 053044, arXiv:1103.3864 [hep-ex].

[374] B. A. Dobrescu and F. Yu, "Coupling-mass mapping of dijet peak searches," *Phys.Rev.* **D88** no. 3, (2013) 035021, arXiv:1306.2629 [hep-ph].

[375] T. Sjostrand, S. Mrenna, and P. Z. Skands, "PYTHIA 6.4 Physics and Manual," *JHEP* **0605** (2006) 026, arXiv:hep-ph/0603175 [hep-ph].

[376] S. Ovyn, X. Rouby, and V. Lemaitre, "DELPHES, a framework for fast simulation of a generic collider experiment," arXiv:0903.2225 [hep-ph].

[377] I. Antcheva, M. Ballintijn, B. Bellenot, M. Biskup, R. Brun, *et al.*, "ROOT: A C++ framework for petabyte data storage, statistical analysis and visualization," *Comput.Phys.Commun.* **180** (2009) 2499–2512.

[378] F. J. Petriello, S. Quackenbush, and K. M. Zurek, "The Invisible Z' at the CERN LHC," *Phys.Rev.* **D77** (2008) 115020, arXiv:0803.4005 [hep-ph].

[379] Y. Gershtein, F. Petriello, S. Quackenbush, and K. M. Zurek, "Discovering hidden sectors with mono-photon Z'o searches," *Phys.Rev.* **D78** (2008) 095002, arXiv:0809.2849 [hep-ph].

[380] A. Crivellin, U. Haisch, and A. Hibbs, "LHC constraints on gauge boson couplings to dark matter," arXiv:1501.00907 [hep-ph].

[381] A. Djouadi, "The Anatomy of electro-weak symmetry breaking. I: The Higgs boson in the standard model," *Phys.Rept.* **457** (2008) 1–216, arXiv:hep-ph/0503172 [hep-ph].

[382] N. Weiner and I. Yavin, "UV completions of magnetic inelastic and Rayleigh dark matter for the Fermi Line(s)," *Phys.Rev.* **D87** no. 2, (2013) 023523, arXiv:1209.1093 [hep-ph].

[383] M. T. Frandsen, U. Haisch, F. Kahlhoefer, P. Mertsch, and K. Schmidt-Hoberg, "Loop-induced dark matter direct detection signals from gamma-ray lines," *JCAP* **1210** (2012) 033, arXiv:1207.3971 [hep-ph].

[384] J. F. Kamenik and J. Zupan, "Discovering Dark Matter Through Flavor Violation at the LHC," *Phys.Rev.* **D84** (2011) 111502, arXiv:1107.0623 [hep-ph].

[385] T. Lin, E. W. Kolb, and L.-T. Wang, "Probing dark matter couplings to top and bottom quarks at the LHC," *Phys.Rev.* **D88** no. 6, (2013) 063510, arXiv:1303.6638 [hep-ph].

[386] U. Haisch, F. Kahlhoefer, and J. Unwin, "The impact of heavy-quark loops on LHC dark matter searches," *JHEP* **1307** (2013) 125, arXiv:1208.4605 [hep-ph].

[387] G. Artoni, T. Lin, B. Penning, G. Sciolla, and A. Venturini, "Prospects for collider searches for dark matter with heavy quarks," arXiv:1307.7834 [hep-ex].

[388] R. C. Cotta, A. Rajaraman, T. M. P. Tait, and A. M. Wijangco, "Particle Physics Implications and Constraints on Dark Matter Interpretations of the CDMS Signal," *Phys.Rev.* **D90** no. 1, (2014) 013020, arXiv:1305.6609 [hep-ph].

[389] A. Berlin, D. Hooper, and S. D. McDermott, "Simplified Dark Matter Models for the Galactic Center Gamma-Ray Excess," *Phys.Rev.* **D89** no. 11, (2014) 115022, arXiv:1404.0022 [hep-ph].

[390] E. Izaguirre, G. Krnjaic, and B. Shuve, "The Galactic Center Excess from the Bottom Up," *Phys.Rev.* **D90** no. 5, (2014) 055002, arXiv:1404.2018 [hep-ph].

[391] S. Ipek, D. McKeen, and A. E. Nelson, "A Renormalizable Model for the Galactic Center Gamma Ray Excess from Dark Matter Annihilation," *Phys.Rev.* **D90** no. 5, (2014) 055021, arXiv:1404.3716 [hep-ph].

[392] P. Agrawal, B. Batell, D. Hooper, and T. Lin, "Flavored Dark Matter and the Galactic Center Gamma-Ray Excess," *Phys.Rev.* **D90** no. 6, (2014) 063512, arXiv:1404.1373 [hep-ph].

[393] A. Kumar and S. Tulin, "Top-flavored dark matter and the forward-backward asymmetry," *Phys.Rev.* **D87** no. 9, (2013) 095006, arXiv:1303.0332 [hep-ph].

[394] B. Batell, T. Lin, and L.-T. Wang, "Flavored Dark Matter and R-Parity Violation," *JHEP* **1401** (2014) 075, arXiv:1309.4462 [hep-ph].

[395] J. Andrea, B. Fuks, and F. Maltoni, "Monotops at the LHC," *Phys.Rev.* **D84** (2011) 074025, arXiv:1106.6199 [hep-ph].

[396] J.-L. Agram, J. Andrea, M. Buttignol, E. Conte, and B. Fuks, "Monotop phenomenology at the Large Hadron Collider," *Phys.Rev.* **D89** no. 1, (2014) 014028, arXiv:1311.6478 [hep-ph].

[397] M. Srednicki, R. Watkins, and K. A. Olive, "Calculations of Relic Densities in the Early Universe," *Nucl.Phys.* **B310** (1988) 693.

[398] G. B. Gelmini and P. Gondolo, "Neutralino with the right cold dark matter abundance in (almost) any supersymmetric model," *Phys.Rev.* **D74** (2006) 023510, arXiv:hep-ph/0602230 [hep-ph].

[399] **CDF** Collaboration, T. Aaltonen *et al.*, "Search for new particles decaying into dijets in proton-antiproton collisions at s**(1/2) = 1.96-TeV," *Phys.Rev.* **D79** (2009) 112002, arXiv:0812.4036 [hep-ex].

[400] **ATLAS** Collaboration, G. Aad *et al.*, "Search for high-mass resonances decaying to dilepton final states in pp collisions at s**(1/2) = 7-TeV with the ATLAS detector," *JHEP* **1211** (2012) 138, arXiv:1209.2535 [hep-ex].

[401] **CMS** Collaboration, S. Chatrchyan *et al.*, "Search for narrow resonances using the dijet mass spectrum in pp collisions at $\sqrt{s}$=8??TeV," *Phys.Rev.* **D87** no. 11, (2013) 114015, arXiv:1302.4794 [hep-ex].

[402] **CMS** Collaboration, S. Lowette, "Search for Dark Matter at CMS," arXiv:1410.3762 [hep-ex].

[403] S. Malik, C. McCabe, H. Araujo, A. Belyaev, C. Boehm, *et al.*, "Interplay and Characterization of Dark Matter Searches at Colliders and in Direct Detection Experiments," arXiv:1409.4075 [hep-ex].

[404] P. Harris, V. V. Khoze, M. Spannowsky, and C. Williams, "Constraining Dark Sectors at Colliders: Beyond the Effective Theory Approach," *Phys.Rev.* **D91** no. 5, (2015) 055009, arXiv:1411.0535 [hep-ph].

[405] M. R. Buckley, D. Feld, and D. Goncalves, "Scalar Simplified Models for Dark Matter," *Phys.Rev.* **D91** no. 1, (2015) 015017, arXiv:1410.6497 [hep-ph].

[406] L. M. Carpenter, A. Nelson, C. Shimmin, T. M. Tait, and D. Whiteson, "Collider searches for dark matter in events with a Z boson and missing energy," *Phys.Rev.* **D87** no. 7, (2013) 074005, arXiv:1212.3352.

[407] T. A. collaboration, "Search for dark matter pair production in events with a hadronically decaying W or Z boson and missing transverse momentum in pp collision data at $\sqrt{s} = 8$ TeV with the ATLAS detector,".

[408] **ATLAS Collaboration** Collaboration, G. Aad *et al.*, "Search for dark matter candidates and large extra dimensions in events with a photon and missing transverse momentum in pp collision data at $\sqrt{s} = 7$ TeV with the ATLAS detector," *Phys.Rev.Lett.* **110** (2013) 011802, arXiv:1209.4625 [hep-ex].

[409] **CMS Collaboration** Collaboration, S. Chatrchyan *et al.*, "Search for Dark Matter and Large Extra Dimensions in pp Collisions Yielding a Photon and Missing Transverse Energy," *Phys.Rev.Lett.* **108** (2012) 261803, arXiv:1204.0821 [hep-ex].

[410] A. A. Petrov and W. Shepherd, "Searching for dark matter at LHC with Mono-Higgs production," *Phys.Lett.* **B730** (2014) 178–183, arXiv:1311.1511 [hep-ph].

[411] L. Carpenter, A. DiFranzo, M. Mulhearn, C. Shimmin, S. Tulin, *et al.*, "Mono-Higgs-boson: A new collider probe of dark matter," *Phys.Rev.* **D89** no. 7, (2014) 075017, arXiv:1312.2592 [hep-ph].

[412] N. Zhou, D. Berge, and D. Whiteson, "Mono-everything: combined limits on dark matter production at colliders from multiple final states," *Phys.Rev.* **D87** no. 9, (2013) 095013, arXiv:1302.3619 [hep-ex].

[413] **XENON100** Collaboration, E. Aprile *et al.*, "Limits on spin-dependent WIMP-nucleon cross sections from 225 live days of XENON100 data," *Phys.Rev.Lett.* **111** no. 2, (2013) 021301, arXiv:1301.6620 [astro-ph.CO].

[414] **ATLAS Collaboration** Collaboration, G. Aad *et al.*, "Search for new phenomena in final states with an energetic jet and large missing transverse momentum in pp collisions at $\sqrt{s} = 8$ TeV with the ATLAS detector," arXiv:1502.01518 [hep-ex].

[415] U. Haisch and E. Re, "Simplified dark matter top-quark interactions at the LHC," arXiv:1503.00691 [hep-ph].

[416] J. Abdallah, H. Araujo, A. Arbey, A. Ashkenazi, A. Belyaev, *et al.*, "Simplified Models for Dark Matter Searches at the LHC," arXiv:1506.03116 [hep-ph].

[417] D. Abercrombie, N. Akchurin, E. Akilli, J. A. Maestre, B. Allen, *et al.*, "Dark Matter Benchmark Models for Early LHC Run-2 Searches: Report of the ATLAS/CMS Dark Matter Forum," arXiv:1507.00966 [hep-ex].

[418] K. Griest and D. Seckel, "Three exceptions in the calculation of relic abundances," *Phys.Rev.* **D43** (1991) 3191–3203.